

Technical University of Denmark



Georgios I. Koutsouris, s091211

Energy Integral Equation Models for Use in Room Acoustic Predictions

Master's Thesis, September 2011

Georgios I. Koutsouris, s091211

Energy Integral Equation Models for Use in Room Acoustic Predictions

Master's Thesis, September 2011

This report was prepared by
Georgios I. Koutsouris, s091211

Supervisors

Assoc. Prof. Jonas Brunskog
Assist. Prof. Cheol-Ho Jeong
Assoc. Prof. Finn Jacobsen

Release date: 29 July 2011
Category: 1 (public)
Edition: First
Comments: This report is part of the requirements to achieve the Master of Science in Engineering (M.Sc.Eng.) at the Technical University of Denmark. This report represents 30 ECTS points.
Rights: ©Georgios I. Koutsouris, 2011

Department of Electrical Engineering
Acoustic Technology (AC)
Technical University of Denmark
Orstedes Plads, building 352
DK-2800 Kgs. Lyngby
Denmark

www.dtu.dk/centre/act
Tel: (+45) 45 25 39 49
E-mail: info@elektro.dtu.dk

Preface

This thesis is the final project for the Master of Science in Engineering Acoustics at the Technical University of Denmark (DTU). The project was conducted at the Acoustic Technology sector, at the Electrical Engineering department, from February to July 2011, under the supervision of Assoc. Prof. Jonas Brunskog, Assist. Prof. Cheol-Ho Jeong and Assoc. Prof. Finn Jacobsen. The study reports an investigation in energy integral equation models for use in room acoustic predictions.

Acknowledgments

I would like to thank all my supervisors: Assoc. Prof. Jonas Brunskog, Assist. Prof. Cheol-Ho Jeong and Assoc. Prof. Finn Jacobsen for their valuable help in preparing this thesis, and especially Jonas Brunskog for involving me in this fascinating project.

My studies in the MSc Engineering Acoustics were funded by the *Alexander S. Onassis Public Benefit Foundation* and I am indebted to the people who accredited my scholarship.

Special thanks to Brady Peters, PhD student in the Royal Danish Academy of Fine Arts, School of Architecture, for borrowing me his prototype scattering surfaces.

Last but not least, I would like to thank my parents and my sister for all the things they have offered to me, and of course my dear girlfriend Stelina for her unfailing support while studying abroad.

Abstract

A combined model for room acoustic predictions is developed. The model aims to treat both diffuse and specular reflections in a unified way. Two well known methods are incorporated: acoustical radiosity, accounting for the diffuse part and the image source method, accounting for the specular part. The model is based on the conservation of the acoustical energy. Losses are taken into account by the energy absorption coefficient and the diffuse reflections are controlled via the scattering coefficient, which defines the portion of energy that has been diffusely reflected.

The model is optimized for impulse response predictions in arbitrary polyhedral rooms and it is deterministic, compared to other room acoustic models, such as ray tracing, which is based on stochastic simulation. The resolution of the impulse response is high and from this common room acoustic parameters can be predicted.

The predictions are validated by measurements in a scale model room and by comparison with published measurement data for a real music studio hall. Despite a few deviations in some of the parameters, the model seems promising for a commercial application, with high accuracy. Like all geometrical acoustic models, the presented one suffers from the coarse assumption that a wave can be replaced by a ray and it is valid for frequencies above Schroeder's large room limit.

Contents

Preface	i
Acknowledgments	iii
Abstract	v
Contents	vii
1 Introduction	1
1.1 Geometrical Room Acoustics	1
1.2 Specular and Diffuse Reflections	2
1.3 Review of Geometrical Room Acoustic Models	3
1.4 Energy Considerations in a Room	4
1.4.1 Mean Free Path	4
1.4.2 Energy Decay	5
1.5 Layout of the Thesis	7
2 Energy Integral Equation	9
2.1 Assumptions and Features	9
2.2 Formulation of the Energy Integral Equation	10
2.2.1 Energy at the Receiver	11
2.3 Discretization	12
2.3.1 Energy at the Receiver	13
2.4 Evaluation of the Form Factors	13
2.4.1 Area to Area Integration	14
2.4.2 Semi-analytical Formulation	16
2.4.3 Basis Functions in Form Factors	17
2.5 Studied Rooms	18
3 Image Source Model	23
3.1 Assumptions and Features	23
3.2 The ISM in a Rectangular Room	24
3.3 The ISM in a Polyhedral Room	26
3.3.1 Interrupt Criteria	26
3.3.2 The Algorithm Structure	29
4 Combined Model	31
4.1 Formulation of the Problem	31
4.1.1 Scattering Coefficient	32
4.1.2 Image Sources	33
4.1.3 Image Elements	34

4.1.4	Energy at the receiver	38
4.2	Algorithm Implementation	40
4.2.1	Impulsive Original Source	41
4.2.2	Discretizing Time	41
4.2.3	Primary Step	42
4.2.4	Main Algorithm - Iterations	43
4.2.5	Full Algorithm – Iterations	53
4.2.6	Energy at the Receiver	56
4.2.7	Reciprocity of Image Elements	56
5	Investigation of the Combined Model	61
5.1	Energy Conservation	61
5.2	On the Degree of Scattering	65
5.3	Rectangular Room with High Absorption at the Ceiling	69
5.4	Prediction of Flutter Echo	74
5.5	Performance of the CARISM	75
5.6	Room Acoustic Parameters	77
5.6.1	Irregular room with uniform absorption	79
5.6.2	Irregular room with non-uniform absorption	80
5.7	Investigation of the Full Algorithm	81
6	Experimental Validation	91
6.1	Time Resolution	91
6.2	Irregular Room Measurements	91
6.2.1	Results	94
6.3	Round Robin III Music Studio	100
6.3.1	First Phase	102
6.3.2	Second Phase	104
6.3.3	Computational Performance	113
7	Conclusion	123
7.1	Summary and Discussion	123
7.2	Future Work	125
	Bibliography	127
	Appendix	131
A	Room Acoustic Parameters	131
A.1	Energy Decay Curve	131
A.2	Clarity	131
A.3	Definition	132
A.4	Center Time	132
A.5	Sound Strength	132
	Index	133

List of Symbols

Start

α	Energy absorption coefficient
ρ	Energy reflection Coefficient
a_m	Air absorption exponent
B	Radiation density
B_d	Radiation density in the diffuse model
B_Q	Radiation density directly by the source
B_w	Radiation density of a wall
B_s	Radiation density in the specular model
c	Sound speed
E_Q	Energy density directly by the source
F_{ijm}	Form factor between element i and image element jm .
F_{ij}	Form factor between element i and element j .
H_{iq}	Solid angle between an element and a source
i	Receiving element in an energy exchange
j	Source element in an energy exchange
jm	image element m of source element j
K	Total number of image sources from the original source Q
k	Indexing of image sources
M	Total number of image elements from element j
N	Number of elements on the boundary of a room
n	Discrete time step
N_w	Total number of walls defining room
o	Order of image source
P	Receiver

Q	Original source in the room
q_k	Image source of the original source ($q_0 \equiv Q$)
r_q	Source factor
$R_{i,jm}$	Distance between element i and image element jm
$R_{i,j}$	Distance between element i and element j
$R_{i,q}$	Distance between element i and image source q
s	Energy scattering coefficient
S_i	Area of element i
S_w	Area of wall w
T	Time steps of the discretized impulse response length
$T_{i,jm}$	Time steps between any image element jm and element i
$T_{i,j}$	Time steps between any element j and element i
$T_{i,Q}$	Time steps between the original source and element i
$T_{i,q}$	Time steps between an image source and element i
t_{max}	Length of the impulse response
$T_{P,jm}$	Time steps between image element jm and the receiver
$T_{P,j}$	Time steps between element j the receiver
$T_{P,Q}$	Time steps between the original source and the receiver
$T_{P,q}$	Time steps between an image source and the receiver
$T_{w,Q}$	Time steps between the original source and the center of a wall
$T_{w,q}$	Time steps between an image source and the center of a wall
w	Indexing of walls
W_Q	Power of the original source
End	

Acronyms

AR	Acoustical Radiosity
BRDF	Bidirectional Reflectance Distribution Function
CARISM	Combined Model of Acoustical Radiosity and Image Source Method
EIE	Energy Integral Equation
ISM	Image Source Model
IRM	Image Receiver Model
IRIE	Impulse Response due to Image Elements
PR	Progressive Radiosity

Chapter 1

Introduction

1.1 Geometrical Room Acoustics

Sound fields in rooms are extremely complicated in general, except from a few rather simple cases, such as a spherical or a rectangular room. But even in such simply shaped rooms, the acoustic behavior can be difficult to predict, due to numerous factors that influence the propagation of sound inside them, apart from the geometry. Three of the most important are the absorption and roughness of the walls, as well as the dissipation of energy in the air.

Room sound field predictions can be divided roughly into two categories: 1) wave acoustics and 2) geometrical acoustics. The former works with solutions of the wave equation analytically for simple cases or numerically for complicated ones. The Green's function is one of the basic tools for such models, providing the impulse response at a receiving position, due to a Dirac-impulse source. In the same category, Finite Element or Boundary Element methods can be included, attempting to solve the wave equation numerically for complicated room shapes, by subdividing the interior domain into solid elements or the boundary into surface elements, respectively. An eigenmode analysis is possible with such methods, as long as the room is not large and the frequency is low. Otherwise the required subdivision becomes very high, raising abruptly the computational effort. The major feature of this category is the inclusion of phase information in the sound field, and this is the reason why an eigenmode analysis is feasible.

The second category of room acoustic predictions makes an important simplification. The sound waves are replaced by rays [1], following the notion used in optics for light waves. With this assumption, almost all the literature from optics can be applied in acoustics, with one distinct difference: The time dependence. Light propagates with a very high speed, so that the problem can be assumed independent of time, for all engineering applications. In contrast, sound propagates very slowly and the acoustic problem remains a time-dependent one. The major goal in geometrical room acoustics is the estimation of the impulse response at a receiving position for arbitrary shaped rooms, of any size. Phase information can be included in some models, allowing simulation of pressure impulse responses and eigenmode analysis. A pressure impulse response is very useful for performing auralizations. But, models without phase information work well for certain areas of interest. They are used for a fast and as reliable as possible prediction of room acoustic parameters [1, 2], which are of great value for design or optimization purposes for auditoriums, classrooms, concert halls, theaters and so on. Most of the room acoustic parameters are nothing else than energy ratios between different parts of the response (such as early-late)

and thus they are based on the squared pressure impulse response. However, a frequency dependence is still preserved in this category by allowing the absorption on the walls and in the air to be frequency dependent.

In this study we often deal with the so called *reflectograms* (or *echograms*) which are graphs showing the strength of the reflections as a function of their arrival times, t , at a receiver, after the direct contribution. The direct contribution is by definition placed at $t = 0$. A reflectogram is pretty similar to a squared pressure impulse response (energy impulse response), since both graphs represent the response of the room.

Obviously, geometrical acoustic models are realized by computer modeling which has been greatly developed from the 1960s and is now the major tool for application and research purposes in room acoustics. A variety of commercial software exists for this, tending to replace gradually the need for scale models in the design of new halls [2]. The assumption of geometrical rays – instead of waves – is valid at high frequencies for which the wavelength becomes comparable with the room dimensions. Apart from that, the assumptions of the geometrical acoustic models are valid for frequencies above Schroeder’s large room limit [3]:

$$f_{sch} \approx 2000 \sqrt{\frac{T_{60}}{V}} \quad (1.1)$$

where T_{60} is the reverberation time in the room and V is its volume. Above f_{sch} there is strong modal overlap, so that eigenmodes are hardly distinguishable and results from geometrical acoustic methods can be accepted. Apparently, an eigenfrequency analysis is useless for this area. For small rooms Schroeder’s frequency becomes high, so that the valid region for geometrical modeling is quite limited. But, as the room becomes larger, Schroeder’s frequency decreases, making the prediction reliable in the common range of interest.

1.2 Specular and Diffuse Reflections

The absorption coefficients of the walls in a room are of great importance for the geometrical acoustic models, since they represent the dissipation of energy. However, the way the total energy in a room is dissipated depends also on the kind of reflection occurring on each wall. The two extreme cases of reflection is the *specular* and *diffuse* (Fig. 1.1). In the first case the angle of a reflected sound ray is the same with the angle of the incident ray. In the second case, an incident ray gives rise to a bundle of other rays towards randomly distributed directions. This second case occurs on surfaces with prominent roughness. The notion of the diffuse reflection can hold only macroscopically, so that the rough surfaces can be treated as flat in computer models. Of course if we were able to zoom in and model all the surface irregularities by numerous planes, we could probably treat the diffuse reflection as specular, but the computational effort would become intolerable for our existing computational power. Hence, modeling the scattering surfaces as flat and attaching a scattering coefficient (see Sec. 1.4) provides a very practical tool for room acoustic modeling.

One can see the optical analogy for the two kinds of reflections by considering a mirror as a specular surface for light and a typical flat gypsum board as a scattering one. However, due to the different nature of sound and light waves, a gypsum board cannot be considered as a scattering surface for sound waves, in the same degree as for light waves. This is because of the different wavelength. Audible sound exists at much longer wavelengths than visible light. So, the roughness of the surface should be higher for sound in order for a prominent scattering to take place.

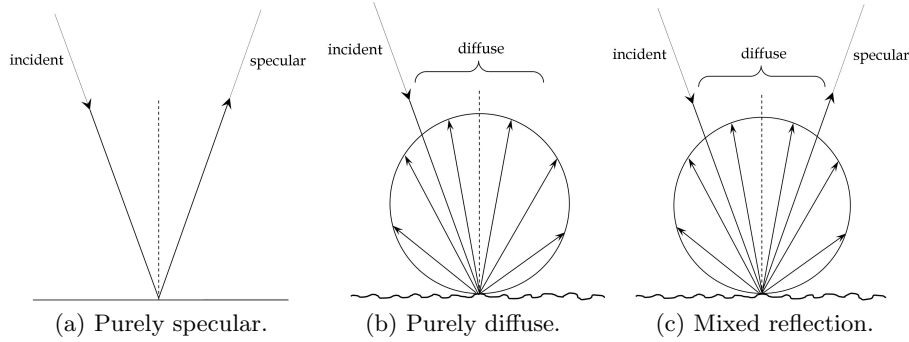


Figure 1.1: Specular and diffuse reflection.

Diffuse reflection is memoryless, that is, the reflected ray can be determined without knowledge of the incident. In contrast, when specular reflection takes place, the history of the incident ray must be known for the determination of the reflected ray.

In real walls, neither specular or diffuse reflection occurs. The situation is a semi-diffuse (or semi-specular) reflection. This mixed case is usually treated as a combination of purely specular and purely diffuse reflection in different proportions, as illustrated in Figure 1.1. The ultimate goal of this thesis is to effectively treat the mixed case.

1.3 Review of Geometrical Room Acoustic Models

By replacing sound waves by rays, most of the sound propagation laws degenerate to simple geometrical tasks. The direct contribution from a source to a receiver is represented by a straight connecting line, while a reflection can be represented by the total path connecting the source to the reflecting point and subsequently this point to the receiver. This is the basis for all geometrical acoustic models.

Probably the most known model is *ray tracing*. It is an efficient combination of geometrical acoustics and stochastic simulation. Introduced in acoustics by Krokstadt [4], it has been experienced considerable development over the past 40 years, because of its efficiency and its simple implementation. The principle of the model is the emission of a large number of rays from a source towards all directions that are consistent with its directivity pattern. The rays can be emitted randomly or uniformly, but since their number is not infinite, the simulation involves statistical errors that are reduced as the number of rays is increased. Each ray is reflected specularly at the room surfaces many times and the whole path is recorded. If the ray passes around the proximity of a point receiver, a contribution is added, according to the present strength of the ray. The proximity around the receiver usually is defined by a small sphere or another solid body that is called *tracer*. Intersection of the ray with the body results in a contribution. A ray is aborted from the recording list if its energy has become smaller than a predefined limit. A maximum number of reflections can also be used as a stop criterion. In some ray tracing models the tracer expands as time is increased [5, 6], in order to account for the increasing number of reflections as a function of time and the expansion of the wave fronts as they propagate away from the source. Two variants of the ray-tracing, accounting for this expansion, are the *beam* and *cone tracing* [6]. Evidently, the way the rays are emitted and traced by the receiver involves a stochastic simulation, because we

are never absolutely sure that all the relevant reflections have been detected, and on the other hand, many rays are detected “around” the receiver and not at its center. Ray-tracing and its variations were initially based on specular reflections, but recently some modifications allow the treatment of diffuse reflections as well [6]. In the usual way, every time a ray hits a diffusing surface, a random number is generated, determining the new direction of the ray. In Dalenbäck’s approach [6], a secondary source is created emitting new rays omnidirectionally towards the half-space defined by the surface.

Similar to ray-tracing is the *sonel mapping technique* [7] where, instead of rays, waves are represented by sound particles, carrying a portion of the total energy supplied by the source. The method uses the same principles as the *photon mapping technique*, in computer graphics [8]. The particles are again detected by a tracer around the receiver and the relevant contribution is added. Both specular and diffuse reflections can be treated. The model is again a stochastic one.

Possibly the only full deterministic geometrical acoustic model is the image source model, **ISM**, [9, 10, 11, 12], described extensively in Chapter 3. It is a perfectly specular-reflection based model. Every reflection can be represented by an image source. Hence, the total path, from the original source to the receiver via the reflection, can be seen as the distance from the image source to the receiver. Each image source generates other image sources with respect to the walls, corresponding to a higher order of reflection. This process is repeated until a desired upper limit of reflections have been reached. Once the image sources have been located in the space around the room, its walls can be fully neglected and the contributions from the generated sources are calculated at the receiver. As will become apparent in Chapter 3, the method does not suffer from statistical errors. One of the major drawbacks is the nonlinear increase of the computational load with the length of the desired impulse response, because of the exponential growth of the number of sources. On the contrary, in ray-tracing the computation time increases only linearly with the length of the impulse response, since the number of rays is fixed. However this is the reason why the **ISM** results in a far better resolution in the impulse response than ray-tracing does. Recently a hybrid model between ray-tracing and **ISM** have been used [5, 13], incorporating the best parts of both methods.

The only model that effectively simulates perfectly diffuse reflections in a room is acoustical radiosity **AR**, based on an energy integral equation. Since this model is the basis of our study –together with the **ISM**– it will be described in detail in Chapter 2. **AR** models the diffuse reflections with much better accuracy than the ray-tracing models do. The method is linked somehow to the Boundary Element methods, since the room surfaces are subdivided into a number of elements and the energy exchange between them is calculated.

1.4 Energy Considerations in a Room

1.4.1 Mean Free Path

One of the most basic terms in room acoustics is the *mean free path* [1], which is defined as the ratio of the total distance that a sound particle has traveled to the total number of reflections, K , it has undergone, $\langle R \rangle = ct/K$. It essentially represents the average distance the sound particle travels between two subsequent reflections. For rooms with diffuse sound field the mean free path for any sound

particle is given by the simple formula [14]:

$$\langle R \rangle = \frac{4V}{S} \quad (1.2)$$

where V is the volume of the room and S is its entire surface.

1.4.2 Energy Decay

When a source in the room emits a Dirac impulse at time $t = 0$, a direct contribution reaches the receiver, followed by subsequent early reflections from the walls. Under the assumption of specular reflections, the reflection density is increased according to a quadratic function of time [15]. This means that soon the early distinct reflections have been converted into a group of hardly distinguishable ones, that usually are referred as the reverberant tail of the response [1]. In reality, the reflections are not purely specular, except from the very early part of the room response. Any scattering surface in the room converts the initially specularly reflected energy into diffusely reflected and after a while, the reverberant tail consist of almost purely diffuse reflections.

Under the diffuse sound field assumption, the energy decay follows an exponential law. According to Eyring's reverberation theory the energy decay as a function of time is given by [1]:

$$E(t) = E_0 \exp \left[\frac{cS}{4V} t \ln(1 - \bar{\alpha}) \right] \quad (1.3)$$

where E_0 is the initial energy, c is the speed of sound and $\bar{\alpha}$ is the average absorption coefficient. The natural logarithm in eq. (1.3) can be expanded into a series [1]:

$$\ln(1 - \bar{\alpha}) = -\bar{\alpha} - \frac{\bar{\alpha}^2}{2} - \frac{\bar{\alpha}^3}{3} + \dots \quad (1.4)$$

If the average absorption coefficient is considered small compared with unity, only the first term can be kept, $\ln(1 - \bar{\alpha}) \simeq -\bar{\alpha}$, so that the energy decay can now be expressed according to Sabine's reverberation theory:

$$E(t) = E_0 \exp \left[\frac{-cS}{4V} \bar{\alpha} t \right] \quad (1.5)$$

The two expressions give similar results as long as $\bar{\alpha}$ is small enough, and they are valid for a perfectly diffuse field. The reverberation time according to Eyring's theory is:

$$T = -\frac{55.3V}{cS \ln(1 - \bar{\alpha})} \quad (1.6)$$

while according to Sabine's theory it is:

$$T = \frac{55.3V}{cS\bar{\alpha}} \quad (1.7)$$

When $\bar{\alpha}$ is large, the reverberation time given by eq. (1.6) is longer than that given by eq. (1.7).

In general, the simulated energy decay in a room very much depends on the kind of reflections assumed. Even if the absorption on the walls is the same, the energy is distributed differently when only specular or diffuse reflections are taken into account. Hodgson [16] states that the sound decay is nonlinear on a logarithmic scale for rooms with purely specularly reflecting surfaces. This means that the exponential

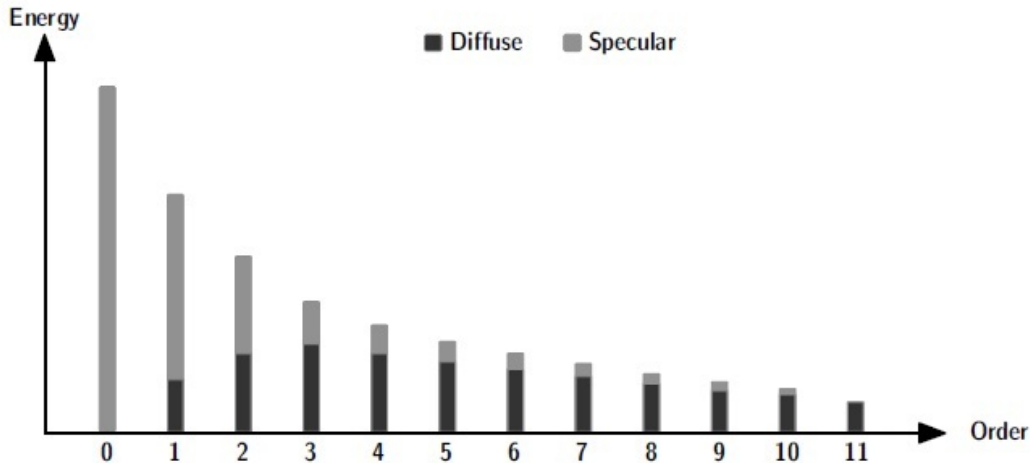


Figure 1.2: Conversion from specularly into diffusely reflected energy. General trend, illustrated by Kuttruff [20]. Taken from [5].

law is not valid. The slope of the decay curve becomes smaller at the end. But the way the energy decays is highly dependent on the room shape. Irregular shapes tend to distribute the energy more than regular shapes –like rectangular rooms– so that the energy decay approaches the exponential law [16, 17]. As will become apparent in Sec. 3.2, regular rooms tend to maintain highly symmetric reflection patterns which decay much slower than the asymmetrical ones. A very common example in rectangular rooms is the *flutter echo* phenomenon, where two parallel highly reflective surfaces lead to repeatable reflections between them. However, when some of the surfaces in the room reflect sound in a diffuse manner the slope of the decay curve is very close to the one predicted by eq. (1.3), even for regular or symmetrical rooms [17].

For the characterization of diffuse reflections, the *scattering coefficient*, s , has been introduced [18], representing the fraction of the energy that is diffusely reflected by a surface. Hanyu [19] presents a theoretical framework for describing the degree of diffusion in a room. He introduces the concept of *average scattering coefficient*, \bar{s} , in analogy to the average absorption coefficient. Hanyu considers the absorption and scattering coefficients as probabilities that a sound particle is absorbed or is diffusely reflected, respectively.

All of the present discussion is based on a very important fact: The conversion of specular sound energy into diffuse sound energy is irreversible [20]. This means that once a ray has been split up to a bundle of other rays, during a diffuse reflection, it is impossible that these rays can be concentrated to form again one single ray. In this way, less and less portion of energy is carried by a ray of the bundle after a sequence of diffuse reflections. Thus, even a small amount of diffusion in a room is able to convert all the specular energy into diffuse and to bring the decay curve close to that obtained when perfectly diffuse wall reflections are assumed [17, 20].

Figure 1.2 illustrates a classical example by Kuttruff about the conversion of specularly reflected sound energy to diffusely reflected. In this example the absorption coefficient is uniform, 0.2, and at every reflection, 25% of the impinging energy is scattered, while 75% is reflected specularly. Just after the first reflection 25% of the energy has been diffusely reflected. Soon, the diffusely reflected portion of energy is larger than the specularly reflected one. Summing up the “diffuse” and “specular” energies at every reflection, we get the total energy in the room. The

reflections are assumed to be equally spaced in time. Consequently, similar graphs are expected in time-domain too, as were the examples presented by Hanyu [19].

1.5 Layout of the Thesis

The scope of this thesis is to develop a computational model for room acoustic predictions based on a unified treatment of diffuse and specular reflections. The model is intended for energy impulse response predictions, thus for transient sound fields. However, modifying the model for steady state predictions is quite straightforward. The content of the thesis can be summarized as follows:

In Chapter 2, the energy integral equation method –acoustical radiosity (AR)– is presented both in an analytical and in a numerical version. The evaluation of the form factors, that appear in the numerical version, is discussed and a simple algorithm is proposed for the form factors between a pair of triangular elements.

In Chapter 3, the principles of the image source model (ISM) are presented both for rectangular and for arbitrary polyhedral rooms. The so important validation criteria for the image sources are described and the structure of a typical ISM algorithm is presented.

Chapter 4, is the central part of the thesis, where AR and the ISM are combined in a unified model that handles diffuse and specular reflections. Initially, the discretized form of the energy integral equation is reformulated to include specular reflections. Afterwards, an algorithm that implements the generalized energy integral equation is developed and several variations of it are discussed.

The algorithm is investigated theoretically in Chapter 5. The conservation of energy, according to Sec. 1.4.2, is discussed through several room case studies. In addition, the variation of room acoustic parameters as a function of the scattering coefficient is investigated.

In Chapter 6 the combined model is validated with measurements in a room scale model and with published data from the music studio in the German National Metrology Institute (PTB). The room corresponds to the third phase of the Round Robin process¹ [21, 22], which aims to help room acousticians to evaluate their prediction software.

Discussion about the advantages, disadvantages, assumptions and potential of the proposed model is kept for the last chapter of the thesis. Possible future work is also presented.

¹<http://www.ptb.de/en/org/1/16/163/roundrobin/roundrob3.1.htm>

Chapter 2

Energy Integral Equation

When the reflections in a room are assumed to be purely diffuse, an energy based method, known as *Energy Integral Equation Method* (**EIE**) or *Acoustical Radiosity* (**AR**), can be used. The term Acoustical Radiosity is an extension of the classical *radiosity* method, widely used in computer graphics [23]. The major difference between the classical radiosity method and **AR** is the time dependence. The former deals with light, whose speed can be assumed to be infinite, so that the whole method is time-independent. The latter deals with sound, whose speed is finite, converting the method into a time-dependent one. Except from computer graphics and acoustics, a similar method is used in thermal radiation heat transfer [24].

AR is based on an energy integral equation derived by Kuttruff in the early 1970s [1]. This equation describes the flow of energy on the whole boundary of a room. In almost all cases the equation should be solved numerically, which involves discretization of the boundary into elements. For this reason **AR** is often referred to as an intensity-based boundary element method [25]. The prediction of a sound field using **AR** is implemented usually in two parts. In the first part, the energy history is computed for every element on the boundary. The energy on each element is a combination of the energy arriving directly from the source and the interactions with the other elements due to the diffuse reflections. In the second part, the energy at the receiver is calculated by extracting the contribution from each element. In computer graphics the first part is named *rendering* and the second is named *gathering*. We shall adopt these terms for our **AR** approach.

2.1 Assumptions and Features

AR is an energy-based method, so that any phase information is lost. Thus, the sound waves are assumed uncorrelated. One of the main assumptions for **AR** is that only diffuse reflections occur in a room. This is of course less restrictive than the assumption of a diffuse field [20, 26]. In addition, some properties of the sound field seem not to be affected much by a change from specular to diffuse reflection. The *Lambert's* scattering law is adopted for describing the diffuse reflections in **AR**. According to this, the value of the intensity of a scattered ray, $I(\theta, R)$, at distance R , from the point of reflection, is dependent on the reflection angle [1]:

$$I(\theta, R) = I(0, R) \cos \theta \quad (2.1)$$

where $I(0, R)$ is the intensity normal to the surface. Definitely, Lambert's law is one way for describing diffuse reflections, but it is not unique. Other distributions of the scattered energy could happen in real situations, but the Lambert's law is

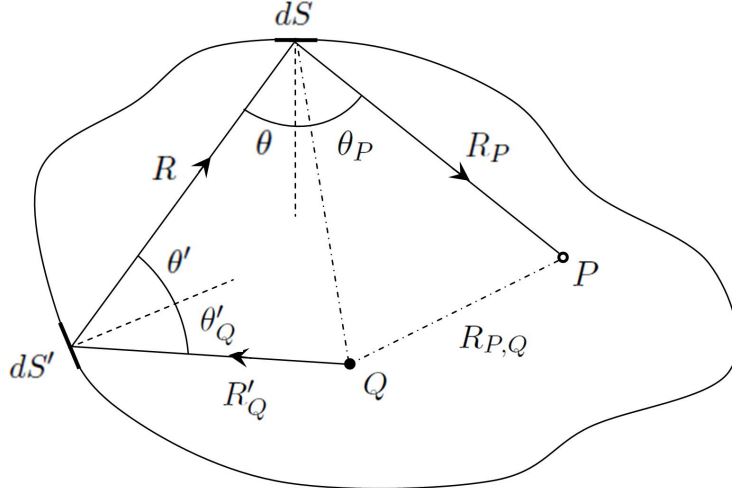


Figure 2.1: Geometry for the energy integral equation.

probably the most known and it has been extensively applied in a variety of fields – such as computer graphics – not only in acoustics. It is the major tool for including scattering in commercial room acoustic prediction software. However, there is no physical background behind it. Instead, it is based on empirical observations [27].

As discussed in Sec. 1.4, certain studies about the energy decay in a room have concluded that initially only specular reflections may occur but soon the energy is converted to diffusely reflected [20]. Thus, AR seems to be suitable for predicting the late part of the energy decay.

Since in AR the reflections are memoryless, the *gathering* process is not view-dependent. This means that no directional information is required at the receiver and the *rendering* and *gathering* processes can be separated. If specular reflections were involved, they should be computed simultaneously, as it happens in our combined model, in Chapter 4. This feature of AR makes it quite competitive, since once the room is rendered, the contribution at the receiver can be calculated with very low computational cost, allowing walk-through simulations and real-time auralizations [28].

The most prominent drawback of AR is the high computational effort for the rendering part, because of the large number of elements used in a large room simulation. In contrast, radiosity in graphic applications is very efficient because of the time independence.

All the (energy) absorption coefficients in this study are taken to be independent of the incident angle. For the development of the theory in this and the next two chapters, no reference to frequency dependence is made. It will be included during the final validation.

2.2 Formulation of the Energy Integral Equation

Figure 2.1 illustrates an arbitrary room boundary with two elements dS and dS' marked on it. Following Nosal *et al.*, [28] we denote the position vectors for these elements by \mathbf{r} and \mathbf{r}' . The vector connecting the elements dS and dS' is denoted by \mathbf{R} and the corresponding distance by R . The angles formed by \mathbf{R} and the dS , dS' normals are θ and θ' respectively. The source in the room is denoted by Q and the receiver by P .

In the following, B denotes the *radiation density*, that is, the rate of energy, leaving a unit area of a surface [1, 28]. The radiation density should not be confused with the radiation intensity, even if they have the same units [W/m^2]. The latter is angle dependent while the former is not. The radiation density of a point results by integration of the intensity, I , over a hemisphere, h , of radius R , surrounding the point [28]:

$$B\left(\mathbf{r}', t - \frac{R}{c}\right) dS' = \int_h I(\theta', R, t) dS \quad (2.2)$$

and by applying Lambert's law:

$$B\left(\mathbf{r}', t - \frac{R}{c}\right) dS' = I(0, R, t) \int_h \cos \theta' dS \quad (2.3)$$

For the present formulation the air absorption is neglected. It will be included in the discretized form, in the next section. When only diffuse reflections are taken into account, the radiation density at a point \mathbf{r} on the boundary, at a particular time is the sum of the contributions from all surface differential areas dS' and the direct contribution from the source. If the last is denoted by B_Q , the resulting radiation density at the point \mathbf{r} is given by Kuttruff's energy integral equation [1, 26]:

$$B(\mathbf{r}, t) = \int_S \rho(\mathbf{r}) K(\mathbf{r}, \mathbf{r}') B\left(\mathbf{r}', t - \frac{R}{c}\right) dS' + B_Q(\mathbf{r}, t) \quad (2.4)$$

where the term R/c accounts for the corresponding time delay between points \mathbf{r} and \mathbf{r}' . $\rho(\mathbf{r})$ is the (energy) reflection coefficient at \mathbf{r} and $K(\mathbf{r}, \mathbf{r}')$ is the *reflection Kernel* between points \mathbf{r} and \mathbf{r}' [26]. Assuming that the diffuse reflections are described by the Lambert's law, the reflection kernel reads:

$$K(\mathbf{r}, \mathbf{r}') = \frac{\cos \theta \cos \theta'}{\pi R^2} \quad (2.5)$$

If the source Q is omnidirectional and has power W_Q , the direct contribution to the elements on the boundary is given by:

$$B_Q(\mathbf{r}, t) = W_Q \left(t - \frac{R_Q}{c}\right) \frac{\cos \theta_Q}{4\pi R_Q^2} \rho(\mathbf{r}) \quad (2.6)$$

where now R_Q is the distance between the source and point \mathbf{r} on element dS and R_Q/c represents the corresponding delay.

2.2.1 Energy at the Receiver

Once the rendering part has been finished, i.e., $B(\mathbf{r}, t)$ is known for all positions \mathbf{r} as a function of time, the energy density at the receiver can be calculated by collecting all the information from the boundary:

$$E(t) = \frac{1}{\pi c} \int_S B\left(\mathbf{r}, t - \frac{R_P}{c}\right) \frac{\cos \theta_P}{R_P^2} dS + E_Q(t) \quad (2.7)$$

where the direct contribution from the source reads:

$$E_Q(t) = \frac{1}{4\pi c R_{P,Q}^2} W_Q \left(t - \frac{R_{P,Q}}{c}\right) \quad (2.8)$$

2.3 Discretization

Except from a few cases, such as the spherical or flat room, described by Kuttruff [1], eq. (2.4) does not have a closed form solution and needs to be solved numerically. For that purpose, the boundary of the room is subdivided into planar elements i , each of area S_i . The elements should be small enough to justify the assumption that the radiation density remains constant within each element [20]. Let the total number of elements be N . According to Nosal *et al.* [28], eq. (2.4) can be discretized in space as:

$$B_i(t) = \rho_i \sum_{j=1}^N B_j \left(t - \frac{R_{i,j}}{c} \right) F_{ij} + B_{i,Q}(t) \quad (2.9)$$

where $R_{i,j}$ is the distance between the centroids of i and j and $B_{i,Q}(t)$ is the direct contribution from the source. The reflection kernel, given by eq. (2.5), is now integrated over both surfaces S_i and S_j . This double surface integral is called *form factor* between the elements, i and j :

$$F_{i,j} = \frac{1}{S_i} \int_{S_i} \int_{S_j} K(\mathbf{r}, \mathbf{r}') dS' dS \quad (2.10)$$

The form factor represents the portion of energy that leaves element i and is received by element j . As a consequence, summing up all the form factors from element i to all the other elements of the room boundary should give one, in order for the conservation of energy to apply:

$$\sum_{j=1}^N F_{ij} = 1 \quad (2.11)$$

This is one of the fundamental properties of the (diffuse) form factors. Another more trivial fact is that coplanar elements do not interact with each other so that their form factor is zero. This is a direct consequence of the Lambert's law, but physically it is not totally correct, because *grazing incidence* [1] cannot be modeled. The reciprocity property also holds for the form factors:

$$S_i F_{i,j} = S_j F_{j,i} \quad (2.12)$$

The factor $1/S_i$ in eq. (2.10) implies an averaging over the area of element i . If the integrand in eq. (2.10) is assumed to vary very little over element i , the area-to-area form factor can be approximated by a differential area-to-finite area form factor:

$$F_{i,j} \simeq F_{di,j} = \int_{S_j} K(\mathbf{r}, \mathbf{r}') dS' \quad (2.13)$$

This formula is called *configuration factor* [23] and it is widely employed in computer graphics, for reducing the computational cost of the rendering algorithms. The configuration factor is usually evaluated by a method called *hemi-cube*, very popular in computer graphics for its efficiency [23].

The energy is assumed to be attenuated exponentially when the sound travels the distance R in the air. The air absorption is represented by the factor $e^{-\alpha_m R}$, where α_m is the air absorption exponent. Some typical values are given in Table 2.1. Including this in the discretized form of eq. (2.4), we get:

$$B_i(t) = \rho_i \sum_{j=1}^N B_j \left(t - \frac{R_{i,j}}{c} \right) F_{ij} e^{-\alpha_m R_{i,j}} + B_{i,Q}(t) \quad (2.14)$$

Relative humidity (%)	Frequency (Hz)						
	500	1000	2000	3000	4000	6000	8000
40	0.60	1.07	2.58	5.03	8.40	17.71	30.00
50	0.63	1.08	2.28	4.20	6.84	14.26	24.29
60	0.64	1.11	2.14	3.72	5.91	12.08	20.52
70	0.64	1.15	2.08	3.45	5.32	10.62	17.91

Table 2.1: Air absorption exponent, a_m in 10^{-3} m^{-1} . From [1].

The direct contribution from the source to element i is obtained by eq. (2.6), with air absorption taken into account:

$$B_{i,Q}(t) = \frac{\rho_i}{4\pi S_i} W_Q \left(t - \frac{R_{i,Q}}{c} \right) H_{i,Q} e^{-\alpha_m R_{i,Q}} \quad (2.15)$$

where $H_{i,Q}$ is the integral over the solid angle, $\Omega_{i,Q}$, subtended by the element i at the source Q :

$$H_{i,Q} = \int_{S_i} d\Omega_{i,Q} = \int_{S_i} \frac{\cos \theta_Q}{R_Q^2} dS \quad (2.16)$$

Throughout the present study, the integrals over solid angles are evaluated using the *spherical triangle method*, a very simple, fast and accurate approach, proposed by Nosal *et al.* [28].

2.3.1 Energy at the Receiver

As in Sec. 2.2.1 once the energy on the meshed boundary has been calculated, the energy reaching the receiver can be found by spatially discretizing eq. (2.7):

$$E(t) = \frac{1}{\pi c} \sum_{j=1}^N \int_{S_j} B_j \left(t - \frac{R_{P,j}}{c} \right) H_{P,j} e^{-\alpha_m R_{P,j}} + E_Q(t) e^{-\alpha_m R_{P,Q}} \quad (2.17)$$

where

$$H_{P,j} = \int_{S_j} \frac{\cos \theta_P}{R_{P,j}^2} dS \quad (2.18)$$

is the integral over the solid angle subtended by the element j at the receiver P . $E_Q(t)$ is the direct contribution from the source, given by eq. (2.8).

2.4 Evaluation of the Form Factors

The double surface integral in eq. (2.10) is very difficult to evaluate analytically for an arbitrary pair of elements i and j . However there exist some analytical formulas for specific configurations, such as a pair of rectangular elements [29]. The form factor literature is quiet extensive especially in computer graphics and thermal radiation heat transfer. Many properties and well-known formulas originate from these fields, but can be directly used in acoustics as well.

The boundary discretization of an arbitrary polyhedral room can be performed by subdivision into polygonal elements. Schröder and Hanrahan proposed an analytical solution for general polygon-to-polygon form factors [30]. The formulation is non-elementary, since it is based on the *dilogarithm* [31]. The proposed formulas

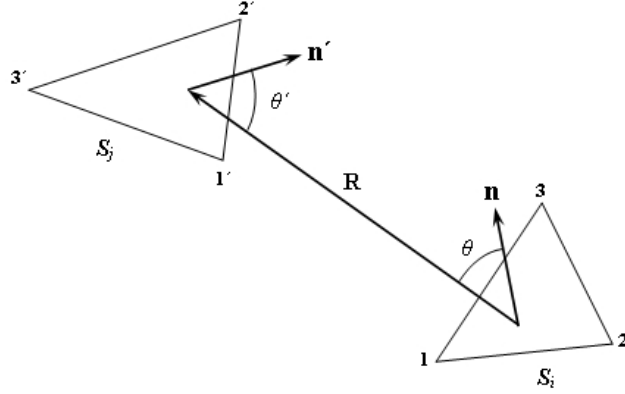


Figure 2.2: A pair of triangular elements over which the form factor is calculated.

seem unnecessarily complicated for our purpose. Instead, since we are going to subdivide the room boundary into *triangular elements*, we present a simple numerical approach for the form factors between two arbitrary oriented triangles.

The method is based on the parametric equation of a planar surface, that is transformed into a parametric equation for a planar triangle. Then, an analytical expression for the configuration factor between a differential area and a planar polygon is incorporated to reduce the order of the initial four-pole integration. The last expression is taken directly from the literature. The final combined formula gives accurate and fast results.

2.4.1 Area to Area Integration

Starting from the parametric plane equation we can make a simple transform to generate the parametric equation for a planar triangle. Then the double surface integral of the form factor expression becomes a four-fold integral of the four triangle parameters. A Gauss-Legendre numerical integration scheme is used.

The form factor expression between two elements i, j :

$$F_{ij} = \frac{1}{S_i} \int_{S_i} \int_{S_j} \frac{\cos \theta \cos \theta'}{\pi \mathbf{R}^2} ds' ds \quad (2.19)$$

can be rewritten using vector notation (Fig. 2.2):

$$F_{ij} = \frac{1}{S_i} \int_{S_i} \int_{S_j} \frac{\mathbf{n} \cdot \mathbf{R}}{|\mathbf{n}| |\mathbf{R}|} \frac{-\mathbf{n}' \cdot \mathbf{R}}{|\mathbf{n}'| |\mathbf{R}|} \frac{1}{\pi |\mathbf{R}|^2} ds' ds \quad (2.20)$$

where S_i, S_j are the areas of the elements, \mathbf{n}, \mathbf{n}' are the normal vectors to the triangles and \mathbf{R} is the vector between two points on them:

$$\mathbf{R} = (x - x')\mathbf{i} + (y - y')\mathbf{j} + (z - z')\mathbf{k} \quad (2.21)$$

The vertices of each triangle are denoted by the index 1,2 and 3 counterclockwise, so that the normal vector points inwards to the domain between the two triangles.

Three points are necessary for defining a plane and we have them already from the triangle vertices. A point on the plane can be described by the following parametric

expressions:

$$\begin{aligned}x &= x_1 + (x_2 - x_1)s + (x_3 - x_1)t \\y &= y_1 + (y_2 - y_1)s + (y_3 - y_1)t \\z &= z_1 + (z_2 - z_1)s + (z_3 - z_1)t\end{aligned}\tag{2.22}$$

and the vector defining the point is therefore:

$$\mathbf{r} = x\mathbf{i} + y\mathbf{j} + z\mathbf{k}\tag{2.23}$$

where s and t are the parameters varying from $-\infty$ to $+\infty$. For $(s, t) = (0, 0)$, $(x, y, z) = (x_1, y_1, z_1)$. For $(s, t) = (1, 0)$, $(x, y, z) = (x_2, y_2, z_2)$ and for $(s, t) = (0, 1)$, $(x, y, z) = (x_3, y_3, z_3)$. These limiting cases lead us to the conclusion that the entire region of the triangle, bounded by the points 1,2 and 3, is described by eq. (2.22) when the sum of the two parameters goes from 0 to 1. Hence a new parameter is introduced, $h = s + t$, that varies from 0 to 1. At the same time one of the initial parameters, lets say s , should vary from 0 to h . The remaining t parameter is the dependent one, given by $t = s - h$. The triple of equations (2.22) is now transformed into:

$$\begin{aligned}x &= x_1 + (x_2 - x_3)s + (x_3 - x_1)h \\y &= y_1 + (y_2 - y_3)s + (y_3 - y_1)h \\z &= z_1 + (z_2 - z_3)s + (z_3 - z_1)h\end{aligned}\tag{2.24}$$

which fully define a triangle. The double surface integral of eq. (2.20) can now be written, according to the surface integral theory, with respect to the parameters s and h as:

$$F_{ij} = \frac{1}{\pi S_i} \int_0^1 \int_0^h \int_0^1 \int_0^{h'} \frac{(\mathbf{n} \cdot \mathbf{R})(-\mathbf{n}' \cdot \mathbf{R})}{|\mathbf{R}|^4} |\mathbf{r}_s \times \mathbf{r}_h| |\mathbf{r}_{s'} \times \mathbf{r}_{h'}| ds' dh' ds dh\tag{2.25}$$

where \mathbf{r}_s is the partial derivative of \mathbf{r} with respect to s and so on. Due to linearity of equations (2.24), the vectors \mathbf{r}_s and \mathbf{r}_h become constants, so that their cross products are constants too and can be removed outside from the integration. For example:

$$\begin{aligned}\mathbf{r}_s &= (x_2 - x_3)\mathbf{i} + (y_2 - y_3)\mathbf{j} + (z_2 - z_3)\mathbf{k} \\ \mathbf{r}_h &= (x_3 - x_1)\mathbf{i} + (y_3 - y_1)\mathbf{j} + (z_3 - z_1)\mathbf{k}\end{aligned}\tag{2.26}$$

which gives a constant cross product. Similarly for $\mathbf{r}_{s'}$ and $\mathbf{r}_{h'}$. Note that now \mathbf{R} , as given by eq. (2.21) is considered as a function of s , h , s' and h' . Finally, the remaining four-folded integral to be evaluated is:

$$F_{ij} = \frac{|\mathbf{r}_s \times \mathbf{r}_h| |\mathbf{r}_{s'} \times \mathbf{r}_{h'}|}{\pi S_i} \int_0^1 \int_0^h \int_0^1 \int_0^{h'} \frac{(\mathbf{n} \cdot \mathbf{R})(-\mathbf{n}' \cdot \mathbf{R})}{|\mathbf{R}|^4} ds' dh' ds dh\tag{2.27}$$

The cross product for each triangle can be evaluated prior to the computation of the form factors and stored in a look up table, saving a significant amount of time.

The advantage of the method is that it is extremely simple in its formulation and can be used directly for any configuration of a pair of triangles, distant or tangent ones. The only drawback is the four dimensional integration that should be evaluated with a nested numerical rule. The Gauss-Legendre rule is one option.

Whatever rule is applied, care has to be taken for the integration with respect to the s and s' variables, since the corresponding integration limits vary from 0 to h

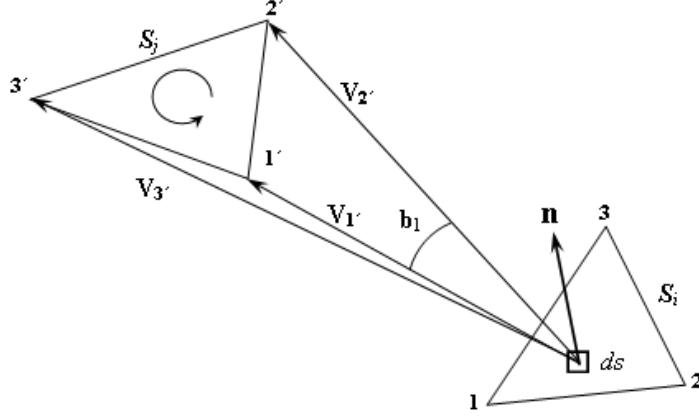


Figure 2.3: Differential area to triangle geometry.

and from 0 to h' , respectively. Consequently, it will be inefficient to keep the same number of evaluation points the four variables in eq. (2.27). First we should decide on the number of points for the variables with constant limits, these being h and h' . Then, we can keep their spacing to decide the number of points for the variables s and s' up to the upper limits h and h' . The evaluation points are then evenly distributed over the whole triangle area.

The present method can be efficiently used also for arbitrary placed rectangular elements or parallelograms, just by employing directly eq. (2.22) with s and t from 0 to 1, which results to constant limits of integration.

2.4.2 Semi-analytical Formulation

The inner double integral of eq. (2.25) can be replaced by an analytical expression for the calculation of the form factor between a differential area ds , lying on element i , and a polygonal element j , with N vertices [24, 32]. Let us denote by \mathbf{V}_e and \mathbf{V}_{e+1} the vectors from the differential area ds to two subsequent vertices e and $e+1$ of the polygon. The cross-product vector between them is $\mathbf{V}_e \times \mathbf{V}_{e+1}$ and by scaling it so that its magnitude equals the angle between the vectors we get:

$$\begin{aligned} \mathbf{b}_e &= \frac{(\mathbf{V}_e \times \mathbf{V}_{e+1})}{|\mathbf{V}_e \times \mathbf{V}_{e+1}|} \left[\frac{\pi}{2} - \tan^{-1} \left(\frac{\mathbf{V}_e \cdot \mathbf{V}_{e+1}}{|\mathbf{V}_e \times \mathbf{V}_{e+1}|} \right) \right] \\ &= \frac{(\mathbf{V}_e \times \mathbf{V}_{e+1})}{|\mathbf{V}_e \times \mathbf{V}_{e+1}|} \tan^{-1} \left(\frac{|\mathbf{V}_e \times \mathbf{V}_{e+1}|}{\mathbf{V}_e \cdot \mathbf{V}_{e+1}} \right) \end{aligned} \quad (2.28)$$

The form factor is obtained by:

$$F_{di,j} = \frac{1}{2\pi} \sum_{e=1}^N \mathbf{b}_e \cdot \mathbf{n} \quad (2.29)$$

The vector \mathbf{b}_e is normal to the plane defined by the vertices e and $e+1$ and the point on the differential area ds . Evidently, $\mathbf{V}_{N+1} = \mathbf{V}_1$. As before, \mathbf{n} is the normal vector of element i . When $|\mathbf{V}_e \times \mathbf{V}_{e+1}|$ equals zero, the whole term in the sum can be nullified manually and the summation can be continued for the next pair.

Equation (2.29) is very simple in its implementation. The computation of the cross product between \mathbf{V}_e and \mathbf{V}_{e+1} is the most heavy computational task, that requires six multiplications and three additions, for each edge. But considering

triangular elements, only three terms are required in the sum, and the ensemble of calculations is much smaller than in the direct integration, for the same accuracy. Combining now eq. (2.25) and eq. (2.29) and proceeding as for eq. (2.27), we obtain the final formula:

$$F_{ij} = \frac{|\mathbf{r}_s \times \mathbf{r}_h|}{2\pi S_i} \int_0^1 \int_0^h \sum_{e=1}^N \mathbf{b}_e \cdot \mathbf{n} ds dh \quad (2.30)$$

During the double numerical integration, for every new value of the parameters h and s a new point on element i is specified, using eq. (2.24) and the vectors \mathbf{V}_e and \mathbf{V}_{e+1} are determined.

The method is fast and very accurate with a three-point Gauss-Legendre rule. Only a deviation of around 0.1% is observed. For a room with 1070 elements the form factors of all combinations were 1144900 and the time required was 3 minutes in MATLAB¹. When the full formula –eq. (2.27)– was employed, the required time was about 5 minutes, i.e., about 1.5 times longer. In any case, the computation time is halved when the reciprocity relation by eq. (2.12) is applied. This means that we do not need to calculate the whole N by N matrix, but only its upper or lower triangular parts. For such a calculation, the i elements are run through, from 1 to N , but the j elements are run from i to N . The concept will be mentioned again and illustrated in Section 4.2.7.

In all classical AR algorithms, the form factors are computed prior to the energy calculations and stored in a look up table, since they do not depend at all on the conditions in the room, but only on its geometry. This strategy is followed in this study as well.

2.4.3 Basis Functions in Form Factors

So far, we have made the assumption that the energy does not vary over an element. But it is possible to apply a non-constant basis function in the form factor expression, so that the energy variations over the element are taken into account. The form factor expression is modified as:

$$F_{ij} = \frac{1}{S_i} \int_{S_i} \int_{S_j} M_i(\mathbf{r}) M_j(\mathbf{r}') \frac{\cos \theta \cos \theta'}{\pi \mathbf{R}^2} ds' ds \quad (2.31)$$

where $M_i(\mathbf{r})$, $M_j(\mathbf{r}')$ are the basis functions and \mathbf{r} , \mathbf{r}' define the points on elements i and j , respectively. Usually the basis functions are chosen to be simple polynomials, whose boundary conditions are satisfied by the adjacency of an element with its neighbor elements. For the case of constant basis functions, $M_i(\mathbf{r}) = M_j(\mathbf{r}') = 1$.

This technique is rather new in computer graphics, borrowed by finite element method and leads to a smoother rendering than with constant functions [33]. In that way, the need for interpolation between the elements after the initial rendering is eliminated. However, it is important to notice that in computer graphics the result of the calculation is the rendering itself, i.e., radiosity is used for visualizing the distribution of light at the walls. So, it is indeed very important to obtain a fine and smooth solution in terms of elements. On the other hand, in AR the information at the receiver –not at the walls– is the ultimate goal. Moreover, people’s ability to identify spatial sound differences is much more limited than their visual detection ability. From these, it seems useless to further complicate AR by employing such basis functions. Hence, in the this study we assume constant basis functions, which leads to the simple form factor expression, given by eq. (2.19).

¹MATLAB is a registered trademark of the Math Works, Inc.

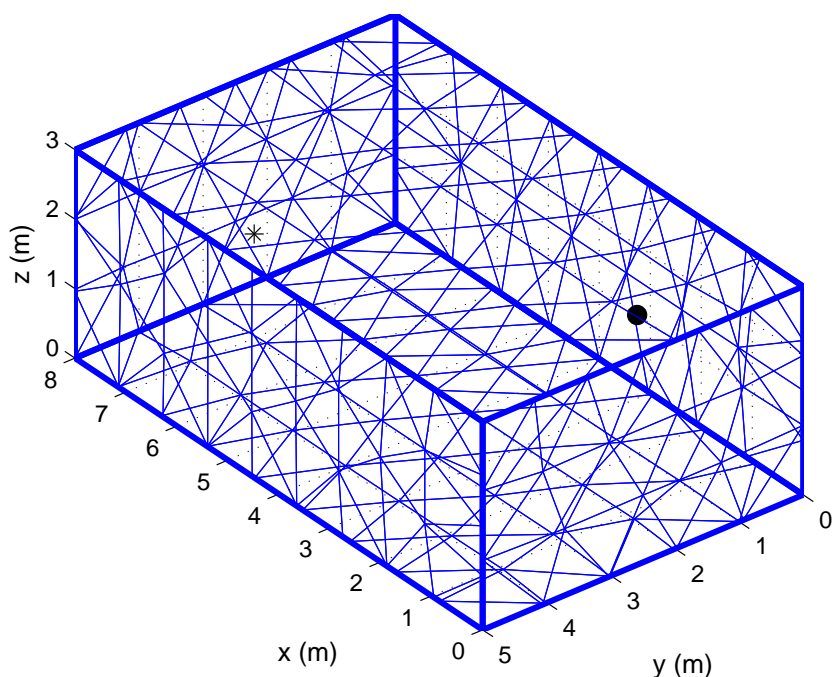


Figure 2.4: An example of a meshed rectangular room, with $N=406$ triangular elements. Length: 8 m. Width: 5 m. Height: 3 m.

2.5 Studied Rooms

The theoretical development in the next chapters will be illustrated by examples from two simple rooms: One rectangular and one irregularly polyhedral. Henceforth, we will refer at the rooms simply with the names *rectangular* and *irregular*. The rooms are meshed using a two-dimensional mesh generator, developed by Per-Olof Persson and Gilbert Strang in the Department of Mathematics at MIT. The program is called `DistMesh` and is written in MATLAB². This code is able to subdivide a surface into triangular elements but it is not a general surface mesh generator, i.e., it does not account for the orientation of the surface. Thus, another code was constructed to treat the three-dimensional case of the room. The code rotates the coordinate system of each wall, using its rotation matrix, so that the wall coincides with the xy plane. The mesh generator is then applied and the elements are produced according to this plane. All the corresponding nodes are finally rotated back to the initial coordinate system, using the inverse rotation matrix.

Two examples of the meshed rooms are illustrated in Figures 2.4 and 2.5. The first room is a hypothetical rectangular one, while the second one is a representation of a real scale model with 7 totally reflective walls and a volume of 0.452 m^3 . This room is made from acrylic glass and represents a reverberation chamber, for 1/10 scale measurements. It is available in the Acoustic Technology laboratory, at the department of DTU Electrical Engineering. However, in this study we are interested in modeling the behavior of the room and not in obtaining actual results. The scaling factor of the room can thus be ignored and the room can be treated just as a very small full scale one.

²<http://persson.berkeley.edu/distmesh/>, <http://math.mit.edu/~persson/mesh>.

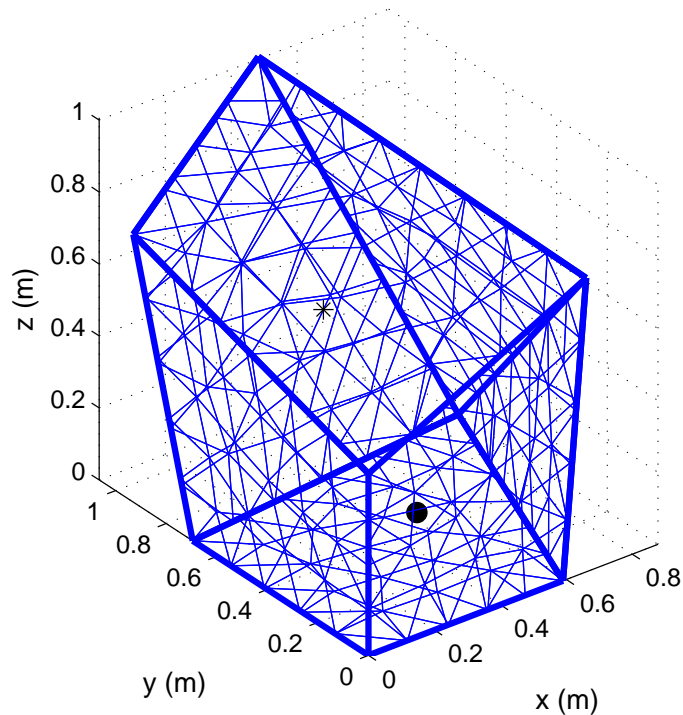


Figure 2.5: An example of a meshed polyhedral room, with $N=338$ triangular elements. The illustration corresponds to a scale model, available in the Acoustic Technology laboratory, at the department of DTU Electrical Engineering.

	x (m)	y (m)	z (m)
Q_{rec}	3.0	2.5	2.0
P_{rec}	6.0	1.5	2.0
Q_{irr}	0.3	0.2	0.2
P_{irr}	0.4	0.7	0.5

Table 2.2: Source-receiver positions for the rectangular and the irregular room.

The rectangular room can be easily subdivided directly into rectangular elements, without using the `DistMesh` function. The work by Miles [34] is based on rectangular rooms and it provides simple expressions for the form factors, between rectangular elements, that can be easily integrated numerically. An analytical expression for the integrals over solid angles is derived as well. Miles was one of the first using `AR` for room acoustic predictions and his study covered both the steady and transient states. The numerical integration of the form factors by Miles can be easily validated with the analytical formulas by Gross *et al.* [29]. The agreement is very high, depending on the numerical integration method used.

Calculated energy decay curves for the two rooms are illustrated in Figures 2.6 and 2.7, as an example, for uniform absorption coefficient equal to 0.4. The energy decay curve is obtained by Schroeder integration (see App. A). The upper axis shows how many mean free paths are included at the respective time of the lower axis, i.e., it shows the average number of reflections up to time t , given by the dimensionless number $tc/\langle R \rangle$. Source and receiver are placed according to Table 2.2.

For the rectangular room two calculations were performed. In the first one,

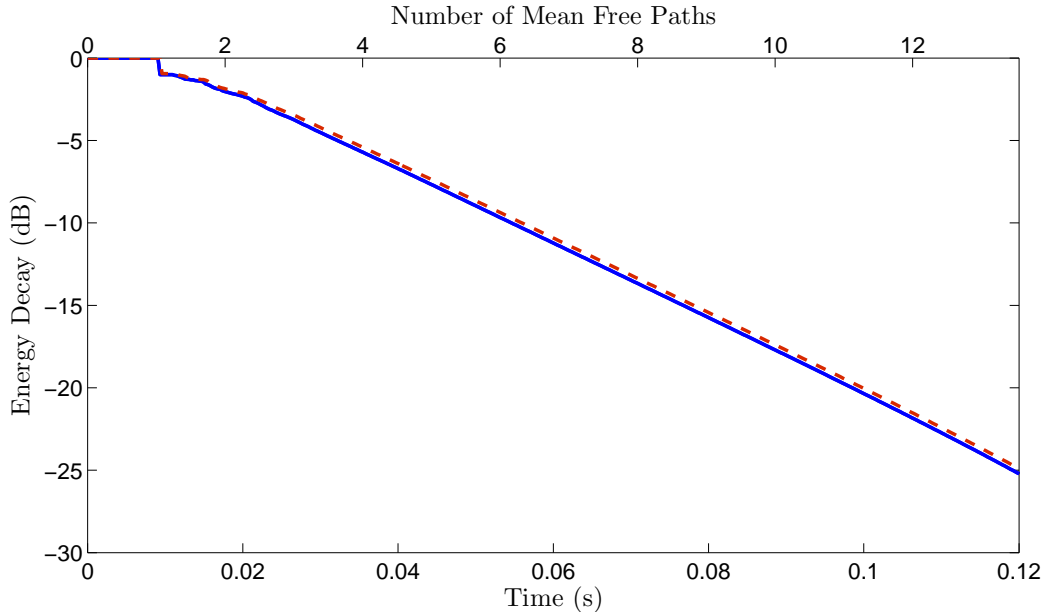


Figure 2.6: Rectangular room. Decay curve predicted by **AR** for source-receiver positions from Table 2.2. **—**: Analytical evaluation of form factors and integrals over solid angles. **- - -**: Numerical evaluation of form factors and integrals over solid angles.

$N = 486$ rectangular elements were used. The form factors were calculated analytically by the formulas from Gross and the integrals over solid angles were calculated according to Miles. In the second calculation $N = 406$ triangular elements were used, applying the `DistMesh` function, as illustrated in Fig. 2.4. The form factors were calculated according to Sec. 2.4 and the integrals over solid angles were calculated with the spherical triangle method. The time discretization in both calculations were performed with a sampling frequency of 4000 Hz. The decay curves are very close to each other. The form factor evaluation, according to Sec. 2.4, and the spherical triangle method seem to approximate well the analytical expressions by Gross and Miles, respectively.

The calculations in the irregular room were performed with $N = 338$ triangular elements. The form factors were evaluated according to Sec. 2.4 and the integrals over solid angles with the spherical triangle method. The calculation time for the form factors was 17 s.

After a transition time, the curves follow an exponential decay in both rooms, as expected for a diffusely reflecting boundary [20, 26, 34]. The exponential decay is translated into a straight line in logarithmic scale. The reverberation time can be evaluated by this straight part of the curve. For the rectangular room the estimated reverberation time by Sabine’s formula is 0.31 s and by Eyring’s formula 0.24 s. Evaluating directly the slope of the curve, we obtain reverberation time 0.27 s. For the irregular room the estimated reverberation time by Sabine’s formula is 51.7 ms, by Eyring’s 40.5 ms, while by direct evaluation of the slope of the curve we get 45.6 ms. The dashed red and dashed-dotted green straight lines in Fig. 2.7 indicate the energy decay according to Sabine’s and Eyring’s theory, respectively. For better visualizing the difference in the slope, Sabine’s and Eyring’s lines were chosen to intersect the **AR** decay curve at -5 dB level, where it has become also a straight line. For that reason, the reverberation time derived by the straight part of the **AR** curve

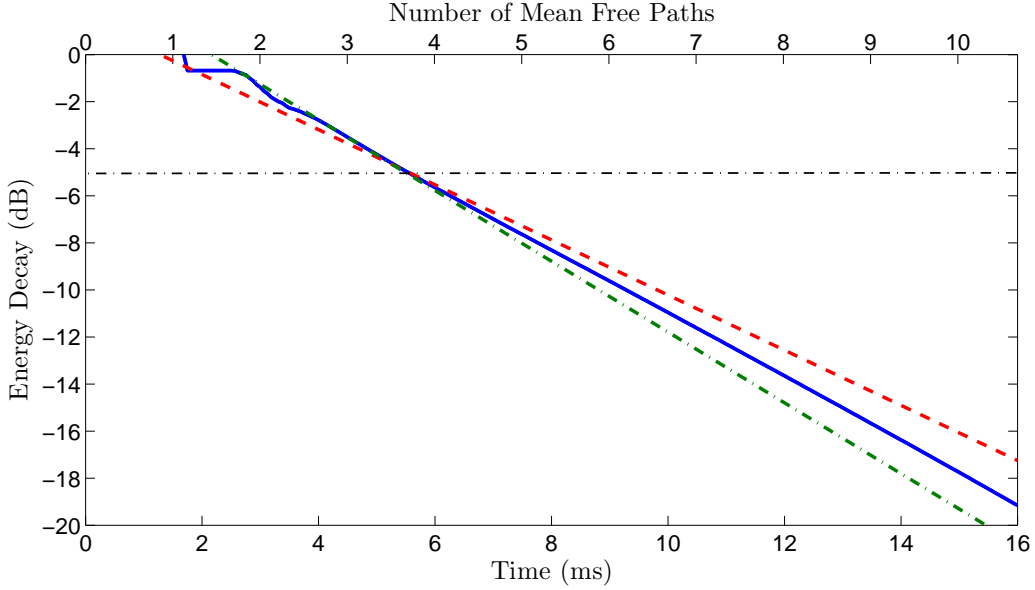


Figure 2.7: Irregular room. —: Decay curve predicted by AR for source-receiver positions from Table 2.2. - - -: Decay curve according to Sabine’s theory. - · - · -: Decay curve according to Eyring’s theory. All curves intersect each other at -5 dB level, where the AR curve has become a straight line.

coincides with the T_{30} value (see App. A).

As expected, according to Sec. 1.4.2, the reverberation time by Sabine’s formula is much longer than from Eyring’s in both the rectangular and the irregular room, because the average absorption coefficient is quite large. The prediction by AR lies between these two theoretical values. AR assumes diffuse reflections but not diffuse field. Consequently, the resulting reverberation time is expected to be longer than the one predicted by the perfectly diffuse-field theory (Eyring’s theory). On the other hand, the assumption for the Sabine’s theory by eq. (1.4) is not valid for the large α applied this case, leading to far longer reverberation time, even than that predicted by AR. The execution time of the foregoing simulations was 19 s for the rectangular room and 16 s for the irregular room.

A picture of the AR computational performance is given in Figures 2.8 and 2.9, as a function of the number of elements and the sampling frequency, respectively. The calculations were performed in the irregular room with uniform absorption 0.4 and source-receiver positions from Tab. 2.2. According to equations (2.9) and (2.10) the execution time of the AR algorithm is proportional to the squared number of elements, N^2 , and directly proportional to the sampling frequency. In the first figure, simulations were run with $N = 254, 276, 338, 387, 459, 565, 699$ elements and fixed sampling frequency at 10 kHz for a 40 ms impulse response length. The execution time increases linearly with N^2 . In the same figure, the variation of the predicted reverberation time T_{30} and the early decay time EDT is also shown. It can be seen that the parameters are only slightly affected by the boundary subdivision.

In the second figure, the number of elements was fixed at 338. The impulse response length was again 40 ms and the sampling frequency varied from 2.5 to 25 kHz. Clearly, the computational time increases linearly, while the T_{30} and EDT parameters are overestimated at low sampling frequencies, converging towards the final values after 15 kHz.

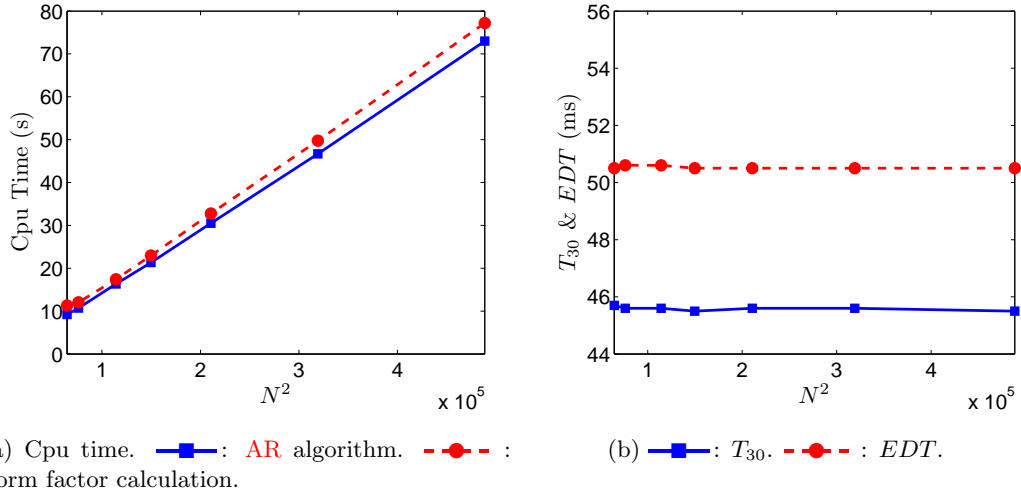


Figure 2.8: Execution time and T_{30} , EDT values at P_{irr} , as a function of the squared number of elements. $N = 254, 276, 338, 387, 459, 565, 699$ elements were used.

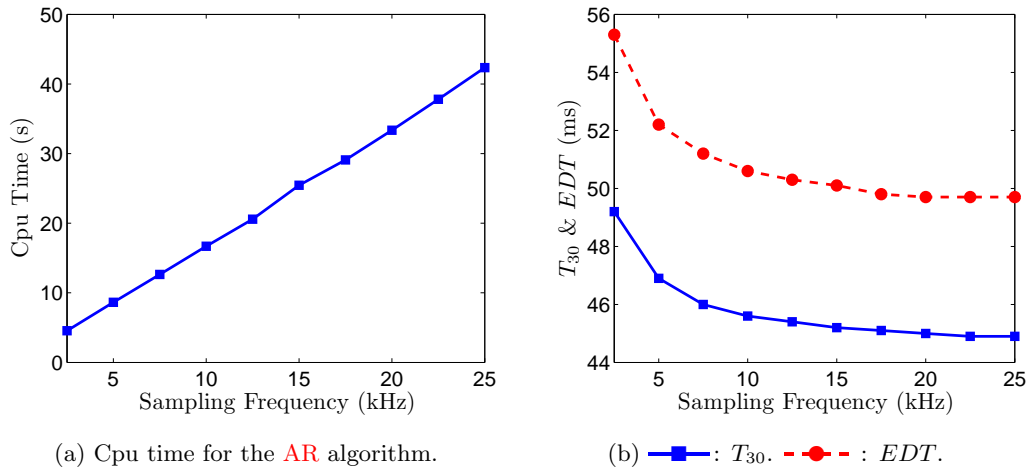


Figure 2.9: Execution time and T_{30} , EDT values at P_{irr} , as a function of the sampling frequency.

Chapter 3

Image Source Model

A well documented approach for the study of pure specular reflections in a room is the Image Source Model, **ISM**. In its principle, the reflection path of a sound ray is replaced by a straight line connecting the receiver to the corresponding image source [10, 12].

Let us denote by $Q = [x_Q \ y_Q \ z_Q]$ the original source in the room, with power W_Q . Every image source will be defined by q . We consider a room consisting of planar walls. Initially, the original source is mirrored at every wall. This results to the first order image sources. Every image source can now suffer a new mirroring at all walls, except from the wall that created the image source. This will result to the second order image sources. The same process is repeated as many times as we want, until a desired maximum order of reflection is achieved. It is convenient to call *daughter source* every new image source and *mother source* its predecessor. In this chapter, each image source is characterized by a sequence of indices corresponding to the walls involved in its production.

The **ISM** is mainly used for sound pressure calculations. It is a really useful tool, since phase shifts can be included, resulting to an impulse response that can be directly used for room auralizations. However, the calculations can be also performed in terms of energy, similarly to **AR**. Apparently, the phase information is lost. Since the ultimate goal of this study is to combine the **ISM** with **AR**, only the energy approach is considered.

Every time a source is mirrored back from a wall, its power is attenuated by the reflection coefficient, ρ , of the wall. In an image source sequence, the power of the last image source has been attenuated by the product of all reflection coefficients of the precedent reflections. This product is called *source factor*.

3.1 Assumptions and Features

The most important assumption of the **ISM** is that all reflections are treated as purely specular. This involves errors in application to real cases, because almost nowhere can somebody find a purely specular surface. But even with the assumption of specular surfaces, the **ISM** is an exact method only if the walls are hard, that is, totally reflective. As long as the walls are absorbent, the **ISM** remains an approximation of the sound field, with analytically definable errors in the elementary process of reflection of a sound wave from a surface [11].

As happens with most geometrical acoustic models, the **ISM** does not take into account the expansion of the wave front as it travels away from the source. Thus, the wave nature of sound is not properly modeled. Moreover, even if some algorithms

of the **ISM** take phase into account, they usually have to simplify the problem by adopting angle independent reflection coefficients, leading to further errors. In this study, the reflection coefficients are also considered angle independent.

On the other hand the **ISM** is a really useful tool for investigating the acoustics in complicated rooms, giving highly detailed impulse responses. The model is fully deterministic, because all possible reflections from the source can be predicted without statistical means, as is the case for ray tracing.

Handling all possible reflections can be a very time consuming task for arbitrary polyhedral rooms. The number of image sources grows exponentially with the order of reflection. The computational cost of the method is very high, because each source has to be checked whether it is valid or not (see Sec. 3.3).

3.2 The ISM in a Rectangular Room

The application of the **ISM** in a rectangular room is quite straightforward and very efficient, since the positions of the image sources follow a regular pattern that can be easily calculated. Let us denote the room dimensions by L_x , L_y and L_z . In compact form, the image source positions are usually described as:

$$(x, y, z) = (\pm x_Q + 2lL_x, \pm y_Q + 2mL_y, \pm z_Q + 2nL_z) \quad (3.1)$$

where $l, m, n = 0, 1, 2, \dots$. All combinations given by (3.1) lead to valid reflection paths and thus the time consuming visibility tests can be omitted. The expression in eq.(3.1) can be transformed to a more convenient form [35]:

$$x = (-1)^l x_Q + \left[l + \frac{1 - (-1)^l}{2} \right] L_x, \quad (3.2)$$

$$y = (-1)^m y_Q + \left[m + \frac{1 - (-1)^m}{2} \right] L_y, \quad (3.3)$$

$$z = (-1)^n z_Q + \left[n + \frac{1 - (-1)^n}{2} \right] L_z \quad (3.4)$$

where again $l, m, n = 0, 1, 2, \dots$. The source factor of each image source is given by:

$$r_q = \rho_{x1}\rho_{x2}\rho_{y1}\rho_{y2}\rho_{z1}\rho_{z2} \quad (3.5)$$

where

$$\rho_{x1} = \rho_{x=0}^{|\frac{1}{2}l - \frac{1}{4} + \frac{1}{4}(-1)^l|}, \quad \rho_{x2} = \rho_{x=L_x}^{|\frac{1}{2}l + \frac{1}{4} - \frac{1}{4}(-1)^l|} \quad (3.6)$$

is the reflection coefficients for sides $x = 0$ and $x = L_x$, and similarly for the other two dimensions. Except from the lack of validation checks, the **ISM** in a rectangular room is facilitated by the fact that no mother sources should be stored for the creation of the daughter sources. In Figure 3.1 a typical reflectogram has been computed using this algorithm, for the rectangular room and source-receiver position described in Section 2.5. The regular pattern of the image sources is obvious in the late part of the response, where groups of equally spaced bins are present. The energy is specularly reflected between the parallel planes of the room in a repeatable way. Hence, the decay has a lower slope at the late part, than in the beginning, as illustrated in Figure 3.2, in consistent with the analysis in Sec. 1.4. The lower slope appears after the “knee” point at 0.1 s.

In Chapter 4 the algorithm for **ISM** in rectangular rooms is used for validating the more complicated algorithm for the **ISM** in arbitrary polyhedral rooms.

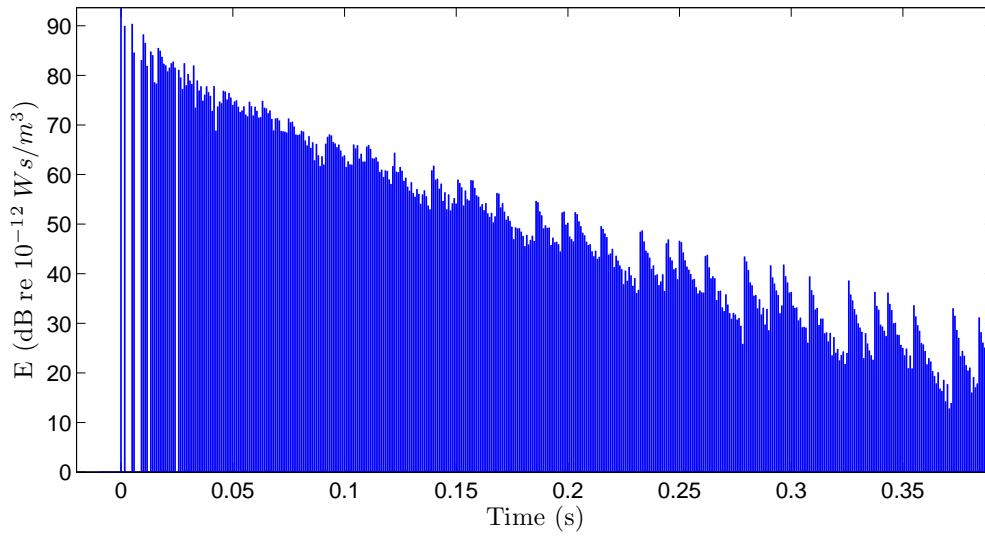


Figure 3.1: Reflectogram predicted by **ISM** for the rectangular room described in Sec. 2.5. Uniform absorption coefficient equal to 0.4. Source-receiver from Tab. 2.2.

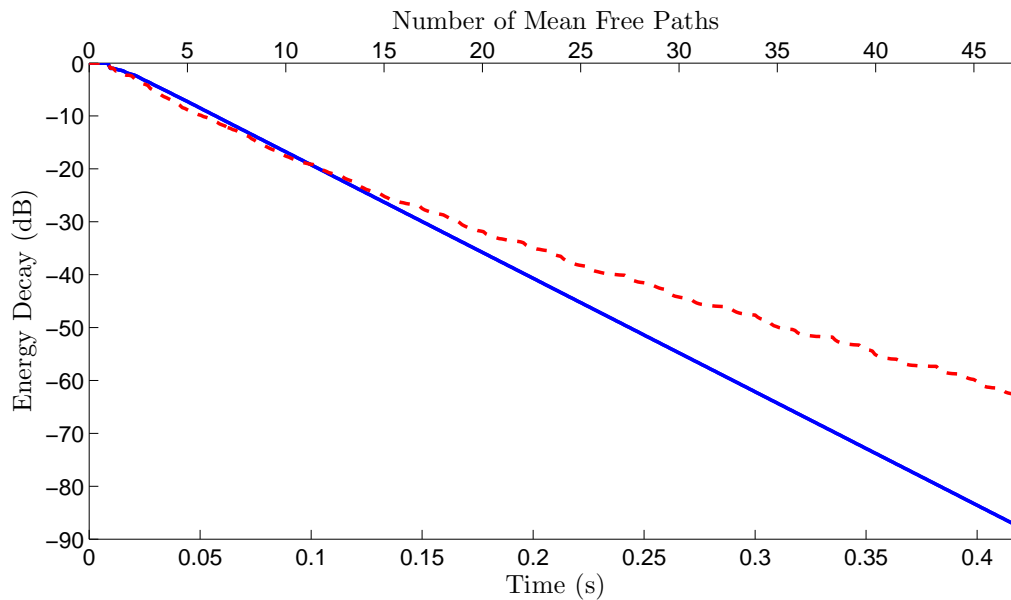


Figure 3.2: Decay curves predicted by **AR** and **ISM** for the rectangular room described in Sec. 2.5. —: **AR**. - - -: **ISM**. Uniform absorption coefficient equal to 0.4. Source-receiver from Tab. 2.2.

3.3 The ISM in a Polyhedral Room

In the general case of an arbitrary polyhedral room, the **ISM** proves to be very time consuming when a long impulse response is to be predicted. The number of image sources follows an exponential growth, with increasing order. If the number of walls in the room is N_w , the number of image sources up to order o is [1]:

$$N_q = N_w \frac{(N_w - 1)^o - 1}{N_w - 2} \quad (3.7)$$

For example, a room with 8 walls would require almost 156864 image sources for 6 orders of reflections. However, only a small part from the ensemble of image sources contributes to the impulse response. Most of the calculated image sources are not valid, i.e., they do not correspond to a feasible reflection path. Therefore, the most consuming task in the general **ISM** is to filter out all the unwanted image sources.

Figure 3.3 illustrates the validity test for two second order image sources, as described compactly in [10, 13]. Let us focus on the image source q_{12} . Its indices reveal that the last mirroring was performed on the 2nd wall. First, the line connecting P and q_{12} is formed. The intersection point, x , of this line and the plane defining wall No 2 is inside the actual polygon that defines the wall. Subsequently, the line connecting x with the first order image source, q_1 is formed. The intersection point, y , of the line and the plane defining wall No 1 is again inside the corresponding polygon. Since all the intersection points of the image chain up to q_{12} are inside the corresponding walls, the image source q_{12} can be said to be *valid* or in other words *visible*. The same task should be performed for any image source, starting from the last reflection towards the receiver and going back to the previous reflections – mother image sources – and the corresponding intersection points, until the chain is finished. If at least one intersection point is out of the wall edges, the tested image source should be discarded. This is the case for the image source q_{21} . The first line from P to q_{21} intersects the plane of wall No 1 at point z , out of the wall boundaries. As a result the reflection cannot be formed and the image source should be omitted.

3.3.1 Interrupt Criteria

The foregoing validity test is probably the most known among programmers of the **ISM**. However, it is apparent that all the image sources of a reflection path have to be created first before the validity test is applied. Consequently, a quiet large number of combinations should be created and only a small portion of them are feasible.

Vorländer in the late 1980s [13] introduced the use of ray-tracing in finding the valid image sources. The concept is that when emitting a large number of rays from the source, some of them are detected by a sphere around the receiver. The captured rays correspond to feasible reflections, therefore to valid image sources. As a result, only the valid image source combinations are generated. Once all the significant image sources have been detected, the ray-tracing program is no more used and the impulse response is calculated directly via the **ISM**. This method, that was given the name *hybrid method* [5], became very popular for its efficiency and commercial softwares, were based on it. The well known commercial software ODEON uses a modified version of the hybrid method ¹.

Mechel [11] proposed a number of checking operations that facilitate the generation of sources, so that only valid combinations are created, without use of ray-

¹<http://www.odeon.dk/pdf/OdeonManual10.pdf>

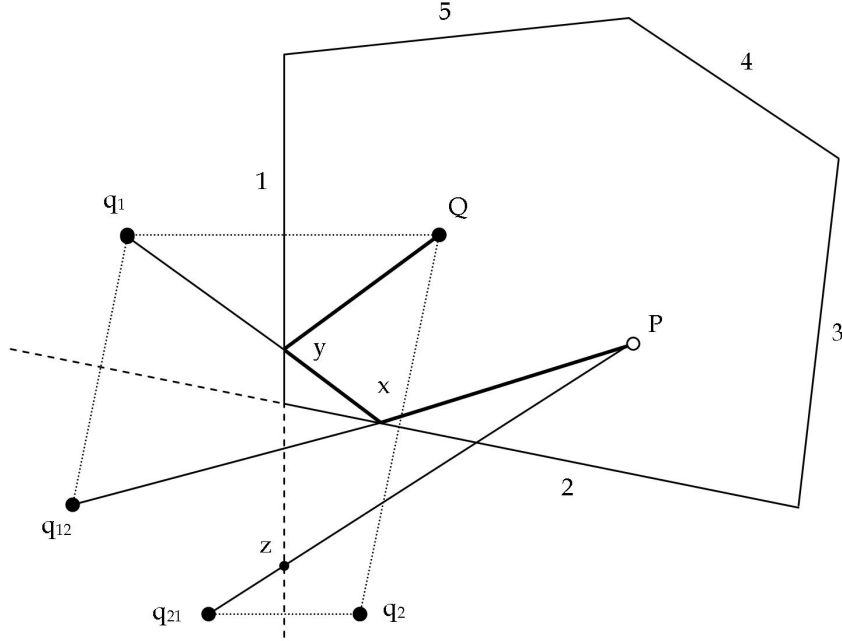


Figure 3.3: An example of valid and non-valid image sources. The images q_1 , q_2 and q_{12} are valid ones, while the image q_{21} is not. The bold crooked line denotes the feasible reflection path.

tracing. Mechel performs these checking operations by a list of *interrupt criteria*. He argues that with the application of such criteria the computational load can be reduced dramatically and many orders of reflections can be handled, even in rooms with many walls. According to Mechel, the **ISM** deserves more attention in room acoustic simulations, because of its deterministic nature. Some of the Mechel's interrupt criteria, had been proposed by Borish [10], some time ago. The main interrupt criteria, partly used in this study are listed below:

Inside Criterion Every mother source should always be mirrored outside from the reflecting walls. As a result, the daughter sources are placed further and further away from the original room walls. A direct consequence of the inside criterion is that a mother source can never be mirrored back to the wall that was used to create it. The inside region is defined by the direction of the normal vector of the wall.

Visibility Criterion This is the most important criterion in the determination of valid image sources and in the creation of new ones. It actually works both for the receiver P and the walls. Referring again to Figure 3.3, the receiver is visible from the source q_{12} , since the straight line from the source towards the receiver passes through the wall boundaries. The image source can be said to be *effective* for the receiver. In the same way, the wall No 2 is visible from the image source q_1 . If a wall is not visible from a source no reflections can be produced on this wall and thus no daughter image source. This is a very important consideration, because instead of storing both q_1 and q_{12} and checking the validity of the final path, a wall visibility test can be applied for q_1 , before generating q_{12} .

An *effective polyhedron* can be employed, defined by the planes that pass through the point image source and the edges of the wall where it was reflected. The effective polyhedron is similar to the *polygonal pyramid*, used by Mechel and defines the valid

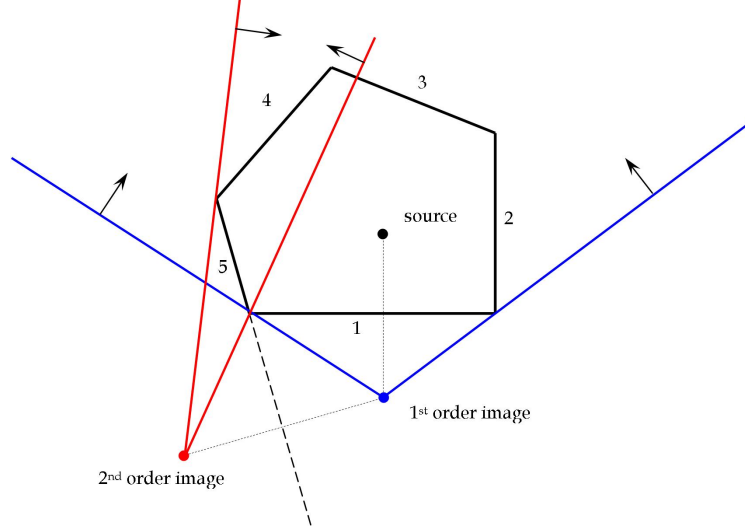


Figure 3.4: Two effective polyhedra as they appear in a ground plan of a room. —: For the first order image source. —: For the second order image source. The normal vectors define the inside region.

region of an image source, so that every receiver inside this, is affected by the source. In Figure 3.4 an example of two effective polyhedra is illustrated. The drawing represents a ground plan of a room, with the first order image source for the mirror wall No 1 and its daughter image source with respect to the mirror wall No 5. The effective polyhedron for the first image source is defined by the blue lines and it is apparent that the whole room domain and walls are visible by the source. In contrast, only wall No 4 is fully visible by the second image source, while wall No 3 is only partly visible. The inside region of the polyhedron is defined by the directions of the plane normal vectors. An effective polyhedron can be fully represented by the plane equations of the surfaces bounding the polyhedron. Hence it is enough to store all the four plane parameters of the surfaces.

According to Fig. 3.4, the 2nd order mother source will produce daughter sources only behind walls No 3 and 4. Apparently, a problem arises for the partly visible wall No 3. Even if a source is produced for it, this is not valid for all the wall region. As a consequence, later reflections from this source would be problematic. A dilemma arises now, whether to accept or not this image source. According to Mechel, an accurate solution implies that the wall should be subdivided into two new walls, so that the valid region of the image source will be restricted by the visible part of the wall. Of course this dynamical definition of the walls would raise the computational load. Mechel proposes a compromise between efficiency and accuracy by considering only the centroid of the wall. If it is inside the effective polyhedron, then the wall is considered visible. Another more flexible approach is to check whether the visible part of the wall exceeds some size limit, in order to be accepted. This size limit could be a preset portion of the full wall. In Chapter 4 some variations of these approaches are employed.

It is important to note that an image source chain is terminated when a wall is not visible by the mother source, but is not terminated when the source is not effective for the receiver. It is likely that one of its descendants will be effective.

Proximity Criterion The desired duration of the impulse response corresponds to a specific distance when multiplied with the speed of sound. Borish [10] suggests

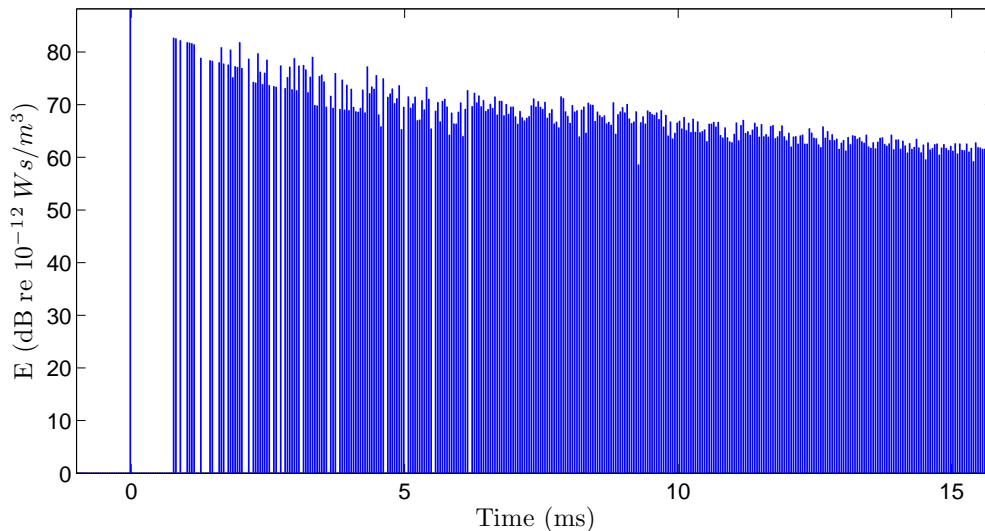


Figure 3.5: Reflectogram predicted by **ISM** for the irregular room described in Sec. 2.5. Uniform absorption coefficient equal to 0.4. Source-receiver from Tab. 2.2.

to check if the distance between the generated image source and the receiver is larger than the impulse response distance, so that image sources beyond this can be omitted.

Source Factor Criterion Mechel [11] suggests to neglect any image source whose source factor is less than a preset limit. This means that the power of the source is not able any more to contribute significantly at the impulse response.

3.3.2 The Algorithm Structure

In 1988, Lee and Lee [12] proposed an algorithm for the **ISM**, based on mirroring the whole room and not only the source, behind each wall. A transformation matrix is generated for each wall that links the original coordinate system to the coordinate system of the corresponding image room. The writers claim that employing this matrix there is no need for storing the mother sources. Actually, this seems not to be so beneficial, since the high computation load compensates for the required storage.

According to Mechel [11] the standard **ISM** can be implemented in three for-loops. The outer most loop runs over the order of reflection, o , up to a maximum limit, o_{max} . The middle loop runs over the mother sources of the previous reflection order and the innermost loop runs over the walls of the room. In this loop all the mirroring and checking operations are included. The generated valid sources are stored in a table, that is looked up during the next order, for creating the daughter sources. Obviously, the length of table is progressively increased. Even if a source is not effective for the receiver, it should be stored. In this standard algorithm, the whole ensemble of image sources, for all orders is stored in a final table, which is accessed afterwards for calculating the contributions at the receiver.

Application of the **ISM** algorithm to the irregular room introduced in Sec. 2.5 gives the response of Figure 3.5. The absorption coefficient and source-receiver positions are the same as in Sec. 2.5. The corresponding energy decay curve is

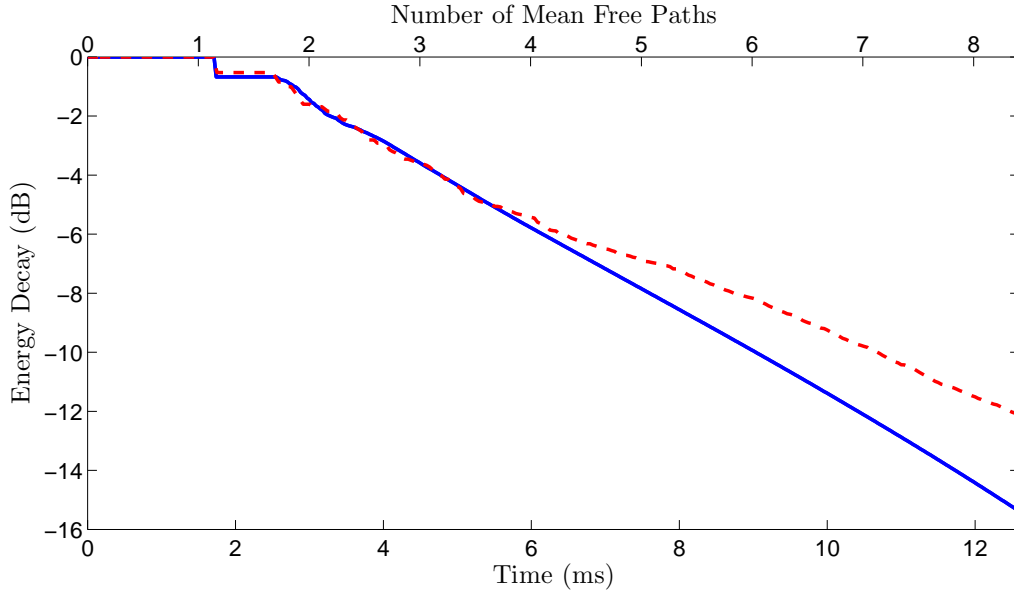


Figure 3.6: Decay curves predicted by AR and ISM for the irregular room described in Sec. 2.5. —: AR. - - -: ISM. Uniform absorption coefficient equal to 0.4. Source-receiver from Tab. 2.2.

presented in Figure 3.6, where it is compared with the corresponding curve by AR (Fig. 2.7).

Up to 6 ms, the decay follows the exponential law predicted by AR. After that time the slope becomes lower, as in the rectangular room. Even if the room has an irregular shape, the fact that only specularly reflecting surfaces are used prevents the decay to be exponential to the end.

The fluctuations in the curve are justified both by the specular nature of the ISM but also by the way the valid image sources are generated. According to Sec. 3.3.1 we have to compromise between efficiency and accuracy by choosing an approximate way of accepting or discarding a reflecting wall for generating a new image source. This involves some errors by choosing either less or more image sources than the “actual” number. We will return again to this important topic in Chapter 4.

Chapter 4

Combined Model

In reality, neither purely diffuse nor purely specular reflections occur in rooms. Indeed the situation is a mixture of these two extremes. Thus there has been a need for developing room acoustic models that are able to handle successfully this mixed case.

Several authors have presented hybrid models to this direction. In 1993, Lewers [36] proposed a combination of beam tracing and AR. In 1996, Dalenbäck [6] applied an approximate cone tracing to a multipass algorithm that accounts for the diffuse reflection by the notion of *secondary sources*. Later on, in 2000, Kuttruff [37] used the ISM to account for the specular reflections in AR and he solved the problem analytically for a stationary field in a flat room. But actually, before Kuttruff's article, two other researchers, Baines in 1983 [38] and Korany in 2000 [39] had proposed the idea of a combined ISM and AR method for predicting the sound field in a rectangular room.

A more recent approach for an integrated treatment of diffuse and specular reflections is based on the *bidirectional reflectance distribution functions* (BRDFs), a term taken directly from computer graphics. The approach was proposed by Siltanen [40]. The BRDFs describe the directional reflected pattern of a surface as a function of the incoming angle (Fig. 4.1). By discretizing the directional information into a number of solid angles, the specular relations between the elements in a meshed boundary can be studied. Of course, this discretization of the outgoing angles involves errors in the approximation and an increasing number of discretized angles is needed for a high accuracy. The detection of the specular components by a point receiver employs ray tracing over a sphere around the receiver.

4.1 Formulation of the Problem

The combination of the ISM and AR is the basis for our approach. However, unlike the previous attempts, our goal is to derive an algorithm that will be able to handle arbitrary polyhedral rooms. We adopt the name CARISM (Combined Acoustical Radiosity - Image Source Model) for the proposed method. The exponential growth of the number of image sources, with increasing order of reflection, as described in Sec. 3.3, has prevented many acousticians to apply the ISM for practical purposes. However, as described in Sec. 3.3.1, careful handling of the valid image sources and their subsequent reflections, leads to a very low number of effective image sources and can drastically reduce the computational load. The ISM gives a full deterministic solution and it is irreplaceable when high resolution in the echogram is desired.

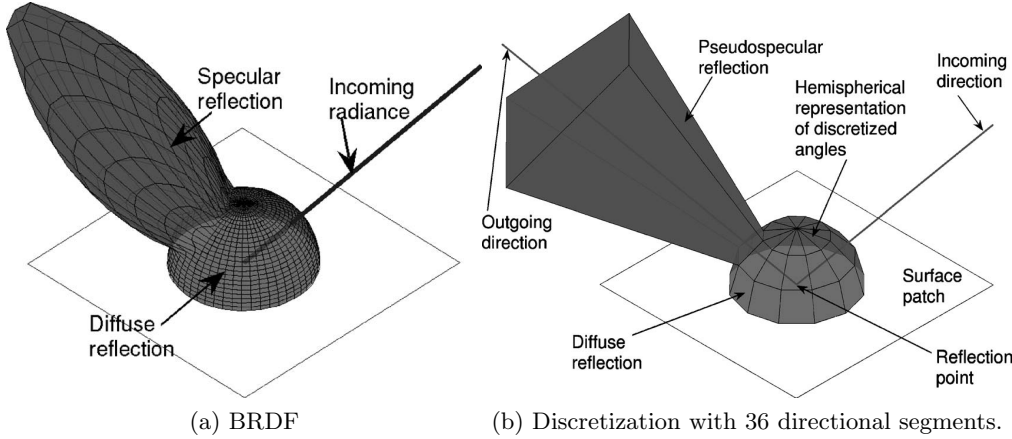


Figure 4.1: A typical BRDF graph with its discretized version used in Siltanen’s algorithm [40].

4.1.1 Scattering Coefficient

The starting point of all relevant existing algorithms is the division of reflected energy from a surface into specular and diffuse components. When a ray, carrying some energy, hits a surface, a portion is absorbed and the remaining is reflected. As usual, the absorbed energy is described by the *absorption coefficient*, α , while the reflected is represented by the *reflection coefficient*, $\rho = 1 - \alpha$. This reflected portion of energy can be further separated to a diffuse part, characterized by the *scattering coefficient*, s , and a specular part $(1 - s)$. As a result, the diffusely reflected energy is a fraction of $s(1 - \alpha)$ with respect to the impinging energy, while the specular is a fraction of $(1 - s)(1 - \alpha)$ [18]. Conservation of energy implies that:

$$\alpha + s(1 - \alpha) + (1 - s)(1 - \alpha) = 1 \quad (4.1)$$

The foregoing tactic is followed in our study, even though its validity is not fully justified and remains a coarse interpretation of the complicated reflection phenomena, taking place on a surface. It should be noted that this division is artificial. The reflection pattern can be whatever, from a perfect circle (diffuse Lambert’s law) to one line (specular reflection) and is better described by the **BRDFs**. However, the only available data providing diffuse information for materials are the scattering coefficients. There is a long literature of papers and standards on measuring the scattering coefficients [18] and on some numerical methods as well, providing theoretical values [41]. For these reasons, in this study we adopt the notion of scattering coefficient as a practical way to think of diffuse reflections. Note that eq. (4.1) is feasible as long as sound absorption and sound scattering are independent of each other [19].

Figure 4.2 illustrates all combinations between ideally diffuse and ideally specular reflections. These are the primitive cases that when combined can give various complicated reflection paths. The first case describes two subsequent specular reflections and it is the main block of the **ISM**. The last case represents only diffuse reflections which are implemented by **AR**. The mixed cases, in the middle, can be handled by the combination of **AR** and the **ISM**. It should be clear that the energy is irreversibly transferred from the specular model to the diffuse one. This means that an incident sound ray is possible to be converted into a bundle of diffuse rays, but the reflection of diffuse energy can never re-form a single sound ray [20].

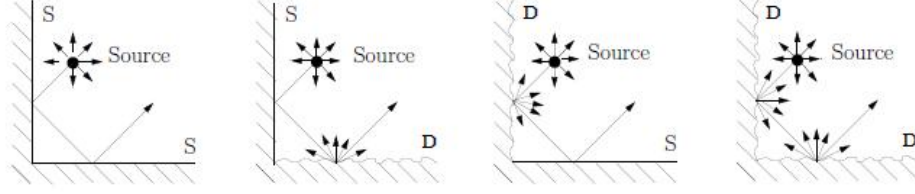


Figure 4.2: The four possible reflection combinations, when we assume that the real case is a mixture of ideally specular and ideally diffuse reflections. **S**: specular reflecting surface. **D**: diffuse reflecting surface. Picture taken from [27], after Dalenbäck [6].

4.1.2 Image Sources

Let us consider first the original source, Q , in the room and a receiver P . The source produces specular reflections at the walls that can be accounted for by creating all image sources up to a desired order. Every time a ray from the original source hits a wall, its energy is reduced by $(1 - s)\rho$. If o denotes the order of the image source under consideration and l denotes the intermediate reflections up to order o , then each reflecting wall can be represented by w_l , which takes values from 1 to the total number of walls. With this nomenclature, the source factor, r_{q_k} , of an image source, q_k , is given by:

$$r_{q_k} = (1 - s_{w_0})\rho_{w_0} \cdot (1 - s_{w_1})\rho_{w_1} \cdots (1 - s_{w_o})\rho_{w_o} = \prod_{l=0}^o (1 - s_{w_l})\rho_{w_l} \quad (4.2)$$

The special product $(1 - s_{w_0})\rho_{w_0} = 1$ symbolizes the direct contribution, so that the original source, Q has a source factor of 1. The subindex $k = 1, 2, \dots$ denotes the numbering of the image source. When $k = 0$, we define $q_0 \equiv Q$. The purely specular energy density reaching any receiver P in the room is computed as the sum of the contributions from all sources, original and image:

$$E_{q_k}(t) = \frac{1}{4\pi c} \sum_{k=0}^K \frac{r_{q_k}}{R_{P,q_k}^2} W_Q \left(q_k, t - \frac{R_{P,q_k}}{c} \right) e^{-a_m R_{P,q_k}} \quad (4.3)$$

where $W_Q(t)$ is the power of the original source and R_{P,q_k} is the distance between any source and the receiver, that results to a time delay, $t = R_{P,q_k}/c$. The upper limit of the sum K is the total number of image sources.

The boundary of the room is meshed into elements, in order for the radiosity to be applied. Each of the elements acts as a new receiver of specular reflected energy from the image sources. The specular component of the radiation density for each element, together with the direct contribution from the source, is thus:

$$B_{q_k,i}(t) = \frac{s_i \rho_i}{4\pi S_i} \sum_{k=0}^K r_{q_k} W_Q \left(q_k, t - \frac{R_{i,q_k}}{c} \right) H_{i,q_k} e^{-a_m R_{i,q_k}} \quad (4.4)$$

where S_i is the area of the element, R_{i,q_k} is the distance between the source and the element and:

$$H_{i,q_k} = \int_{S_i} \frac{\cos \theta_k}{R_{i,q_k}^2} dS \quad (4.5)$$

is the integral over the solid angle subtended by the element at the source. As in Section 2.3, the exponential factor accounts for the air absorption. At this point it

should be stressed that the indexing k and the total number K of the image sources might not be the same in both equations (4.3) and (4.4), since different sources are effective for the receiver and different for each element. The notation $\sum_{k=0}^K$ is adopted just to symbolize the *ensemble* of image sources for any receiver, without further complicating the nomenclature.

4.1.3 Image Elements

Dalenbäck clearly states that every diffuse reflection can be represented by a new source which sends out rays omnidirectionally, throughout the hemisphere that is defined from the surface and the domain in front of it. Dalenbäck calls this source *secondary source* [6]. The energy of this source is equal to the incident energy attenuated by the diffuse reflection portion $s\rho$. The radiosity governing equation – eq. (2.9) – is itself an implementation of the concept of secondary sources. Each element serves as a source that emits energy towards all the other elements in the boundary. The way the energy moves around the meshed boundary is governed by Lambert’s law, which is applied through the form factors between all the element to element combinations.

In Dalenbäck’s approach, the diffuse surfaces in a room are divided in a number of square patches, functioning as the secondary sources. However, the whole method is ray tracing based. Initially, the original source sends a high number of rays that hit the room surfaces randomly. A ray can be reflected specularly and it continues its course, attenuated by the specular reflection fraction $(1 - s)\rho$. But whenever it encounters a diffuse patch, a record is made that the patch should act as a secondary source. Later on, the diffuse patch emits another bundle of rays that begin their own course in the room. Both the original source and the secondary sources work in a stochastic manner, that governs the ray tracing method. Every source sends a finite number of rays and we are never sure that they will hit all the patches on the surfaces. Moreover, the diffuse reflection is represented itself by a finite number of rays and not by a continuous function.

Radiosity seems to be much more accurate than this. There is a concrete equation for the energy exchange between the elements, the form factor integral. And if the form factor is evaluated accurately, then we can obtain a good overview of the diffuse energy behavior along the elements. Of course, the finer the mesh on the boundary the more accurate the result, because, as it was discussed in Sec. 2.2 the energy is assumed to be constant over an element, which is itself an approximation.

Now, let us adopt the concept of rays for a moment, as a useful tool to study the energy movement at the room. Figure 4.3 illustrates the mixed diffuse and specular case. The black ray follows the specular reflection path originating from the original source. Every time it is reflected on a partially diffuse surface, it gives rise to a secondary source of rays, representing the diffuse reflection. These secondary sources are placed at the center of the elements \mathbf{r} , \mathbf{r}' etc. But every new diffuse ray from the secondary sources, like the blue one, may follow its own path of specular reflections, accumulating energy to the surfaces it meets. If a ray (from a secondary source) meets a fully diffuse surface, its course is terminated.

Figure 4.4 shows schematically the energy flow in a room, when modeled with both specular and diffuse reflections. The upper and lower boxes emphasize the fact that the energy is supplied by the source and it is continuously absorbed by the surfaces, with no dependence on the kind of reflection. Thus, in terms of the total energy decay in the room, the middle boxes can be considered as a “black box”, where the energy is absorbed with the one or the other way. This is very crucial, for

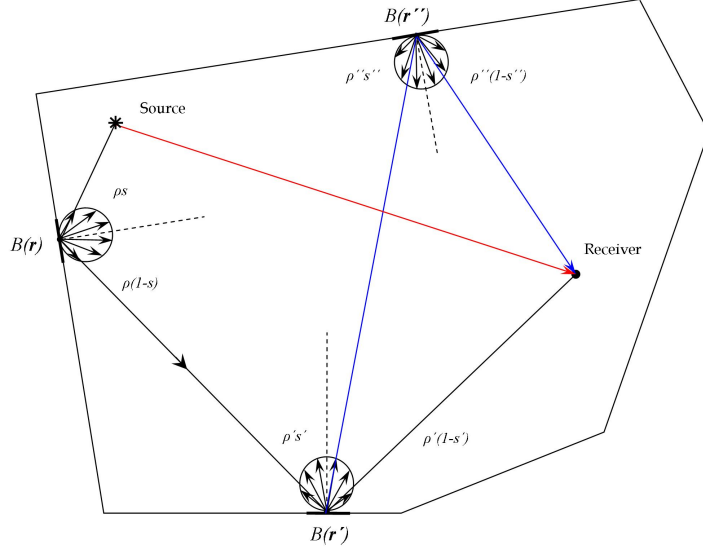


Figure 4.3: Geometry of diffuse and specular reflections in a room. —: Specular reflection path from the original source. —: Specular reflection path of a secondary ray, originating from a diffuse reflection. —: Direct contribution from the original source at the receiver.

the validation of the model. However, as it was discussed in Sec. 1.4, the assumption that the total energy of the room remains the same, is valid only when at least some of the surfaces lead to diffuse reflections [19, 20]. Later on, a direct comparison of the combined-model responses with the pure AR ones, will confirm that the energy flow is correct.

In radiosity we are not dealing with point sources but with whole elements in order to preserve the advantage of form factor relation between them. Thus, the study of subsequent specular reflections of the diffuse reflected energy can be realized by the notion of *image elements*, in a similar way to the image sources of the original source [37]. There are now two distinct differences to the Dalenbäck's approach. First, all the specular reflections, either from the original source or the elements, are represented by images and not rays, thus making the approach fully deterministic. Second, the diffuse part is handled by radiosity. Lewers [36] used beam tracing for the specular reflections and radiosity for the diffuse, but he did not account further for the specular reflections of the beams after the diffuse reflections. In other words, he ignored the interaction between his specular and diffuse models (the dotted arrow in Fig. 4.4).

Figure 4.5 illustrates the principle of specular reflection by an image element. The mirroring of the source element behind the wall, gives the full path of the first order reflection at the receiving element. A new form factor has to be calculated now to account for the diffuse relation between the image element and the receiving element. Let us now adopt the notation jm for an image element of the source element j , where m is the indexing of all image elements linked to the source element j . For convenience, as we did in Sec. 2.3, any receiving element will be symbolized by i .

The radiation density of each image element is the same as that of the source element. Therefore, the contribution of each image element to a real receiving element on the boundary is this radiation density, attenuated by $s\rho$ of the receiving element, and by the product of the $(1-s)\rho$ factors that were involved in all precedent mirror-

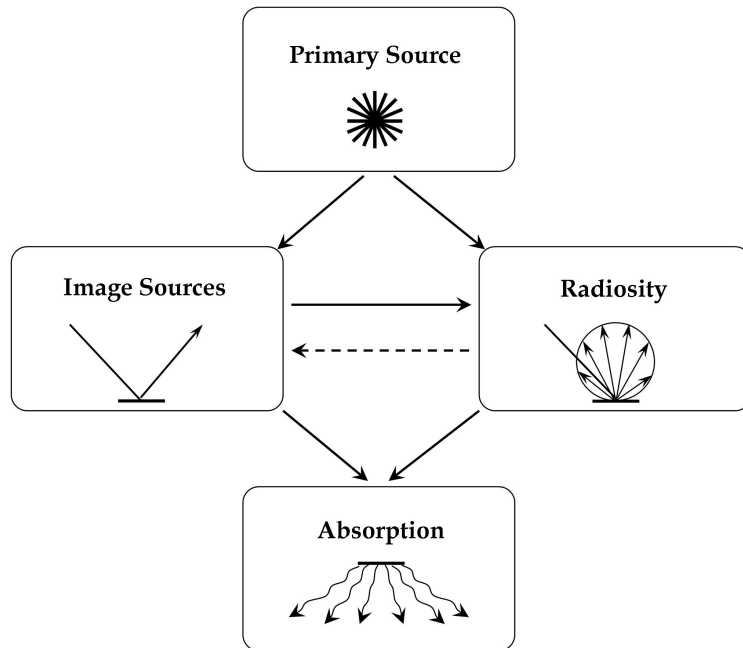


Figure 4.4: Flow of the energy supplied by the primary source in the **CARISM**. When a reflection of any kind takes place, energy is dissipated via the wall absorption. The dashed arrow indicates that the full problem involves a diffuse-specular coupling between the elements on the boundary.

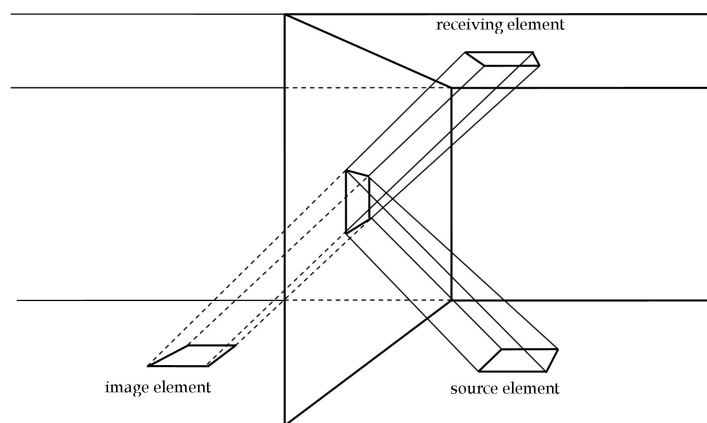


Figure 4.5: Principle of specular reflection by an image element. The diffusely reflected energy from the *source element* suffers several specular reflections afterwards that are represented by image elements.

ing of the image element; that is, in all specular reflections of the diffusely reflected energy from the source element. The attenuation due to the distance and the diffuse coupling between an image element and another receiving element on the boundary, is accounted for by the corresponding *extended form factor*, $F_{i,jm}$, between them. With these in mind and using eq. (4.4), the discretized AR equation (2.14) can now be extended to:

$$B_i(t) = s_i \rho_i \sum_{j=1}^N \sum_{m=0}^M r_{jm} B_j \left(t - \frac{R_{i,jm}}{c} \right) F_{i,jm} e^{-a_m R_{i,jm}} \\ + \frac{s_i \rho_i}{4\pi S_i} \sum_{k=0}^K r_{qk} W_Q \left(q_k, t - \frac{R_{i,qk}}{c} \right) H_{i,qk} e^{-a_m R_{i,qk}} \quad (4.6)$$

where r_{jm} is the source factor of the image element jm , up to an order o :

$$r_{jm} = (1 - s_{w_{j0}}) \rho_{w_{j0}} \cdot (1 - s_{w_{j1}}) \rho_{w_{j1}} \cdots (1 - s_{w_{jo}}) \rho_{w_{jo}} = \prod_{l=0}^o (1 - s_{w_{jl}}) \rho_{w_{jl}} \quad (4.7)$$

and w_{jl} is, as before, the index of the reflecting wall. Again, the product $(1 - s_{w_{j0}}) \rho_{w_{j0}} = 1$ corresponds to the direct contribution from the source element j . The *extended form factor* works similarly to the standard *form factor* from element i to element j , but now, element j is replaced by one of its image descendants:

$$F_{i,jm} = \frac{1}{S_i} \int_{S_i} \int_{S_{jm}} \frac{\cos \theta \cos \theta''}{\pi R_{i,jm}^2} ds'' ds \quad (4.8)$$

Apparently, $S_{jm} = S_j$.

A slightly similar kind of form factor, called *extra form factor*, has been used before in computer graphics [42]. But, it is used only for first order specular reflections, in a radically different approach, which is based on BRDFs and discretized incoming-outgoing angles. The *extended form factor*, introduced here, is a complete generalization of the standard form factor, in consistency with the ISM approach.

In contrast to the element to element evaluation of the standard form factor that was performed in Sec. 2.4, the double integration proves to be very time consuming, when we deal with all the images of each element. Since the images are placed further and further away from i , as the order of reflection is increased, the *extended form factor* is expected to become progressively smaller. Moreover, the *five-times rule* can be applied here, according to which an element can be modeled as a point source, as long as the distance to the receiver is at least five times the maximum projected dimension of the element [23]. In other words, it can be assumed that the energy does not vary over element i and thus eq. (4.8) can be approximated by the *extended configuration factor*:

$$F_{i,jm} \simeq \int_{S_{jm}} \frac{\cos \theta \cos \theta''}{\pi R_{i,jm}^2} ds'' \quad (4.9)$$

A straightforward evaluation of this single area integral is given by eq. (2.29). The distance $R_{i,jm}$ is now taken from the center of element i to the vertices of jm (see Sec. 2.4.2). The foregoing simplification makes the computations two to three times faster. Comparison of the results from equations (4.8) and (4.9) for the irregular room with 387 elements, showed a deviation between 3 and 5 %.

In an alternative way, eq. (4.6) can be written as:

$$\begin{aligned}
B_i(t) = & s_i \rho_i \sum_{j=1}^N B_j \left(t - \frac{R_{i,j}}{c} \right) F_{i,j} e^{-a_m R_{i,j}} \\
& + s_i \rho_i \sum_{j=1}^N \sum_{m=1}^M r_{jm} B_j \left(t - \frac{R_{i,jm}}{c} \right) F_{i,jm} e^{-a_m R_{i,jm}} \\
& + \frac{s_i \rho_i}{4\pi S_i} W_Q \left(Q, t - \frac{R_{i,Q}}{c} \right) H_{i,Q} e^{-a_m R_{i,Q}} \\
& + \frac{s_i \rho_i}{4\pi S_i} \sum_{k=1}^K r_{qk} W_Q \left(q_k, t - \frac{R_{i,qk}}{c} \right) H_{i,qk} e^{-a_m R_{i,qk}}
\end{aligned} \tag{4.10}$$

Now, the first summation corresponds to the classical diffuse to diffuse connection between the elements, i.e. pure **AR**. The second summation term accounts for the diffuse to specular and specular to diffuse reflections. i.e., for the concept of image elements. The third term is the direct contribution from the original source and the last term corresponds to pure specular to specular reflections, i.e., pure **ISM**. Clearly, the second is the most computationally heavy term, even though its contribution might not be large. Indeed, the main question to be answered at chapter 5 is whether the specular reflections of the diffusely reflected energy give any further information in the impulse response or they could be just neglected, judged as diffuse anyway. Note that eq. (4.6) is the compact form of eq. (4.10), where the indexes k and m start from 0, instead of 1.

In Figure 4.6 a group of image elements (together with their normals) is shown as an example. For the bold source element on the floor, the first and the second order images have been computed. The construction of the image elements follows the common rules for the construction of the image sources (chapter 3). An effective polyhedron, introduced in Sec. 3.3, originating from the centre of the image element can be used for defining the visible area. However, regarding the contribution of an image element to another one, an additional rule should be applied. Apparently, any element radiates energy towards the half space defined by its normal vector. In the same way, another element receives energy from the half space defined by its normal vector. As a result in order for an image element jm to be effective for a receiving element i , their normal vectors should point towards each other. Equivalently, we can demand that the center of each element is inside the plane defined by the other element.

4.1.4 Energy at the receiver

The energy density at the receiver can be calculated using the same concept as for eq. (4.6):

$$\begin{aligned}
E(t) = & \frac{1}{\pi c} \sum_{j=1}^N \sum_{m=0}^M r_{jm} B_j \left(t - \frac{R_{P,jm}}{c} \right) H_{P,jm} e^{-a_m R_{P,jm}} \\
& + \sum_{k=0}^K \frac{1}{4\pi c R_{P,qk}^2} r_{qk} W_Q \left(q_k, t - \frac{R_{P,qk}}{c} \right) e^{-a_m R_{P,qk}}
\end{aligned} \tag{4.11}$$

where in addition to the known symbols, $H_{P,jm}$ is the solid angle subtended by any element (source or image) at the receiver and $R_{P,qk}$ is the distance from any source

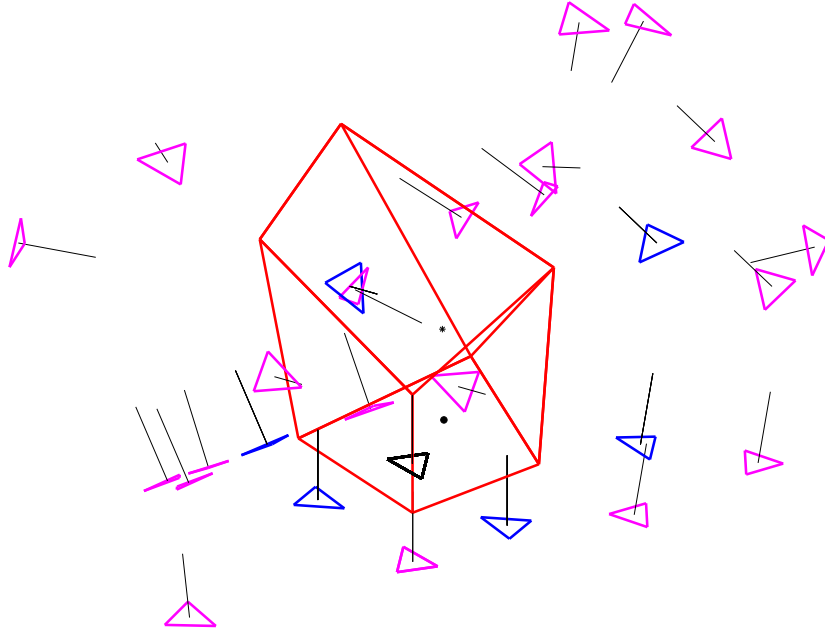


Figure 4.6: First (—) and second order (—) image elements for one of the real elements on the floor (black). The normal vectors are also shown.

(original or image) to the receiver. The double summation corresponds to the contribution from the elements and their images, while the single summation corresponds to the contribution from the the source and its images. Following eq. (4.10), we can split the summations as:

$$\begin{aligned}
E(t) = & \frac{1}{\pi c} \sum_{j=1}^N B_j \left(t - \frac{R_{P,j}}{c} \right) H_{P,j} e^{-a_m R_{P,j}} \\
& + \frac{1}{\pi c} \sum_{j=1}^N \sum_{m=1}^M r_{jm} B_j \left(t - \frac{R_{P,jm}}{c} \right) H_{P,jm} e^{-a_m R_{P,jm}} \\
& + \frac{1}{4\pi c R_{P,Q}^2} W_Q \left(Q, t - \frac{R_{P,Q}}{c} \right) e^{-a_m R_{P,Q}} \\
& + \sum_{k=1}^K \frac{1}{4\pi c R_{P,q_k}^2} r_{q_k} W_Q \left(q_k, t - \frac{R_{P,q_k}}{c} \right) e^{-a_m R_{P,q_k}}
\end{aligned} \tag{4.12}$$

where, as before, the first term corresponds to the direct diffuse contribution from the elements to the receiver, i.e., the gathering process in pure **AR**. The second term corresponds to the coupling between **AR** and **ISM**. That is, again a gathering process, but from all the image elements. The third term is the direct contribution from the original source, while the last corresponds to the contributions from its images, i.e., pure **ISM**.

4.2 Algorithm Implementation

The foregoing theoretical formulation of the problem is implemented in a multistep algorithm, similar to that Dalenbäck has proposed [6]. Dalenbäck distinguishes between a primary step and several successive steps. His primary step handles all the specular reflections caused by the original source, while the next ones serve for the distribution of the diffusely reflected energy. These subsequent steps can be seen as refinements of the initial solution, leading to a convergence towards the final response and a progressively saturated reflectogram.

In our case, a primary step is used only for the direct contribution from the original source. The next iteration steps handle both the specular and the diffuse reflections in a unified way, until the desired convergence is achieved. In every iteration step, a longer reflectogram is produced occupying progressively a larger part of the desired total duration. Hence, the convergence in our algorithm can be seen as an approach to a final reflectogram. This means that after some iterations, the reflectogram is stabilized and it does not change with further iterations, for the specific simulated duration. The same happens for the energy decay. After some iterations the curve has converged to a stabilized line.

The central point of our algorithm is the *radiation reflectogram* of each element on the boundary. We shall adopt this name henceforth in order to describe the values of the radiation densities as a function of time, that have been accumulated at an element, during an iteration step. These *radiation reflectograms* are similar to the *lists of reflections*, described by Dalenbäck [6] and the *plane impulse responses*, described by Lewers [36]. The reflectograms are realized as discretized time vectors¹. Similar to the radiation reflectograms, that are linked to the elements, we calculate the *energy density reflectogram*, related to the response at the receiver.

In the proposed algorithm the notions of the image and secondary sources are merged into a unified treatment. The algorithm is based strongly on the process of image source generation, described in Sec. 3.3.2. Recalling from this Section, the outer-most loop works over the order of reflection, o , for which all the valid image sources are generated. We can expand the scheme of this loop, so that in each iteration, not only the corresponding image sources are generated but the contribution from the secondary sources is also computed at the elements, simultaneously. In other words, both the specular and the diffuse model are treated together and now the orders of reflection become equivalent with the iteration steps. In that sense, the **AR** model is implemented in an iteration process, which produces a more accurate picture of the energy response at each step. Even a few steps are enough to reveal the trend of the whole response. This seems to be quite different with the time-dependent approach, followed by Nosal [28] and Miles [34], where **AR** is fully computed for every time step.

Calculating the **ISM** and **AR** simultaneously offers a great advantage. The termination order of the image sources can be unfixed, in contrast to the standard procedure followed [10, 11, 12]. At each iteration, the energy carried by the specular model (the image sources of the corresponding order) can be compared to the energy in the diffuse model, so that every image source chain can be terminated at an arbitrary order, as long as the energy contribution from the last image source is lower than the diffuse energy on the walls. At the same time, the specular energy of the terminated chain of image sources is transferred to the diffuse model. Consequently, as the iterations proceed, less and less remaining image sources contribute

¹In this chapter a *vector* is referred to a line matrix

specularly until the model has been converted totally from specular-diffuse to purely diffuse; which describes well the late part of a decay curve.

The algorithm is presented in two versions. In the first version – the main one – the coupling between **AR** and **ISM** is neglected. In other words, the dashed arrow in Fig. 4.4 is omitted, so that all the energy that is sent by an element is not reflected specularly afterwards and only the direct contribution to another element is taken into account. Thus, no image elements are involved. In the second version the full model is implemented by adding the coupling between the image elements, as a supplement to the main version. Strategies that reduce the computational cost are utilized. The primary step described in Sec. 4.2.3 is the same for both versions of the algorithm and only the diffuse part in the iteration steps is slightly different in each one.

4.2.1 Impulsive Original Source

Since the impulse response at the receiver is the major outcome from the whole method, the implementation of the formulas from Sec. 4.1 is greatly simplified by assuming an original source of unit impulse. In this case, the time-dependent power degenerates to:

$$W_Q(t) = \begin{cases} 1, & t = 0 \\ 0, & t \neq 0 \end{cases} \quad [W] \quad (4.13)$$

which means that there is no more need to include the power of the source in the formulas of this chapter. If the impulsive power of the source is other than one, then the real response at the receiver is obtained by multiplying with this value.

Moreover, the air absorption can be fully neglected until the end of the calculations. Once the energy density at the receiver has been computed without air absorption – let us call it $E_0(t)$ – the complete value is given by:

$$E_{a_m}(t) = E_0(t)e^{-a_m t c} \quad (4.14)$$

In accordance with this, the air absorption is neglected in this chapter. It will be included again during the experimental validation of the model.

4.2.2 Discretizing Time

The desired time duration t_{max} for the final impulse response is discretized by a sampling frequency f_s that results to equal time intervals dt . Each time step is now denoted by an integer n , so that the actual time at n is $t_n = n dt$. The length of the discretized time vector is denoted by T , so that the actual duration of the impulse response is expressed as $t_{max} = T dt$. Now, $t = 0$ corresponds to $n = 1$. Evidently, the higher the sampling frequency the more accurate the response is, but the computation time becomes longer. A compromise between the duration of the response, the accuracy desired and the computation time allowed should lead to an optimal selection of f_s . By this discretization all the delays between the elements, the source and the receiver can be expressed by a number of time steps, i.e., cell numbers in the energy vectors. We introduce:

- $T_{P,qk} = \lceil R_{P,qk}/(c dt) \rceil$, for the time steps between the receiver and any source.
- $T_{P,j} = \lceil R_{P,j}/(c dt) \rceil$, for the time steps between the receiver and element j .
- $T_{P,jm} = \lceil R_{P,jm}/(c dt) \rceil$, for the time steps between the receiver and image element jm .

- $T_{i,q_k} = \lceil R_{i,q_k}/(c dt) \rceil$, for the time steps between element i and any source.
- $T_{i,j} = \lceil R_{i,j}/(c dt) \rceil$, for the time steps between any element i and element j .
- $T_{i,jm} = \lceil R_{i,jm}/(c dt) \rceil$, for the time steps between any element i and image element jm .

where the operator $\lceil \cdot \rceil$ defines the ceiling function. Henceforth in this Section, in order to emphasize that the calculations are performed in discrete time, all time and element dependences will be denoted by $\lceil \cdot \rceil$, instead of (\cdot) ; for example $B_i(t)$ is transformed into $B[i, n]$.

4.2.3 Primary Step

The iteration process must be initiated by a primary step, where the direct contribution from the source to the receiver and the elements is calculated according to eq. (4.3) and eq. (4.4) – with $k = 0$. This contribution is stored at the radiation reflectograms and the energy density reflectogram of the receiver, according to the corresponding time delay.

It is convenient to implement the various delays involved in the equations of Sec. 4.1 as forward accumulations. That is, the known value of any kind of source at time step n is accumulated at any kind of receiver at time step $n + T_{delay}$, where T_{delay} is one of the possible delays discussed in Sec. 4.2.2. With this tactic, no initial data are required for time steps before $n = 1$.

During the primary step, all the first order image sources are generated and stored in a temporal table. However, in the next iteration steps we need to have control over the generation of new image sources for each wall. Hence, as will become apparent, it is crucial that we treat the AR expression in terms of walls and the corresponding wall elements, rather than in terms of elements directly, as we did so far. In addition, the energy contributed by a new image source should be compared with the purely diffuse energy being present on the wall.

For that purpose, we introduce the *diffuse radiation density*, $B_d[i, n]$, that records only the energy existing in the diffuse model, without adding the contribution from the image sources at every iteration. In the primary step, the energy is supplied only by the original source, so that $B[i, n]$ and $B_d[i, n]$ are identical. In general, knowing $B_d[i, n]$ we can compute the *diffuse radiation density of a wall*, $B_{dw}[w, n]$, as follows:

$$B_{dw}[w, n] = \frac{1}{S_w} \sum_{i=1}^{N_w} S_i B_d[i, n] \quad (4.15)$$

where S_w is the area of the wall and N_w is the number of elements i on the wall w . In a coarse approximation, but sufficient for our goal, we can ignore the delay variations among the different elements of the wall and the source. Instead, we assume that all the energy from the source arrives at the wall with a time delay corresponding to the distance from its center and the point source. Similarly to all other pairs in Sec. 4.2.2, the delay between the wall (its center) and the source is defined in time steps as T_{wQ} . Equation (4.4) can now be modified for the direct contribution from the source Q to a receiving wall w :

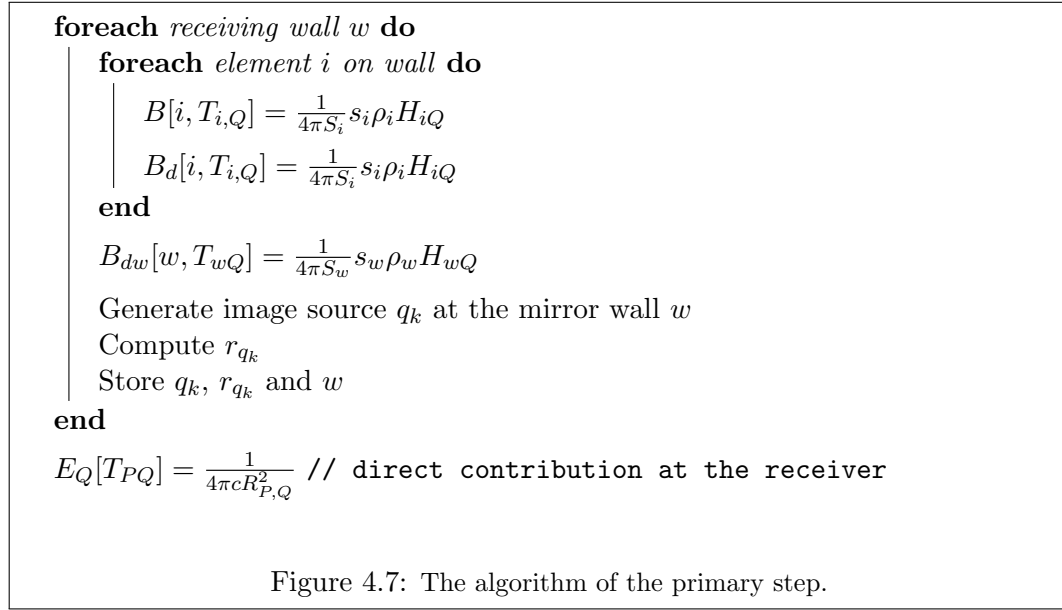
$$B_{dw}[w, T_{wQ}] = \frac{1}{4\pi S_w} s_w \rho_w H_{w,Q} \quad (4.16)$$

where $H_{w,Q}$ is the integral over the solid angle subtended by the wall at the original source. It is straightforward to see that:

$$H_{w,Q} = \sum_{i=1}^{N_w} H_{i,Q} \quad (4.17)$$

where $H_{i,Q}$ is the integral over the solid angle subtended by an element at the source.

It should be noted that the wall radiation density will be used only for the handling of the image source production. It is not a part of the actual solution, since this is still based on the element radiation densities. The algorithm of the primary step is summarized in Figure 4.7.



4.2.4 Main Algorithm - Iterations

At the end of the primary step, the radiation density vectors $B[i, 1 : T]$ and $B_d[i, 1 : T]$, have their initial values, corresponding to the diffuse fraction of the reflected energy. The remaining fraction is carried by the first order image source – behind the corresponding element’s wall – which has not yet sent its contribution. Now the first iteration step is ready to begin. Every step is divided into two parts; one for the diffuse model and one for the specular model.

4.2.4.1 Diffuse Model

The diffuse model is implemented by running through all the elements, that serve as secondary sources. Since in this section we assume no coupling between **AR** and **ISM**, all the energy from element j is reflected diffusely at element i . Thus, the total reflection coefficient ρ_i should be used.

Following Dalenbäck’s approach [6], we can “transfer” the radiation density vector $B[j, 1 : T]$ of a source element j to a new radiation vector $B'[i, 1 : T]$ of a receiving element i , filtered by the delay between them, the form factor and the reflection coefficient. The new radiation reflectogram for element i will be much more dense than the previous, since all the other elements j act as sources, contributing their reflectograms. For every element j , all elements i are run through and the diffuse

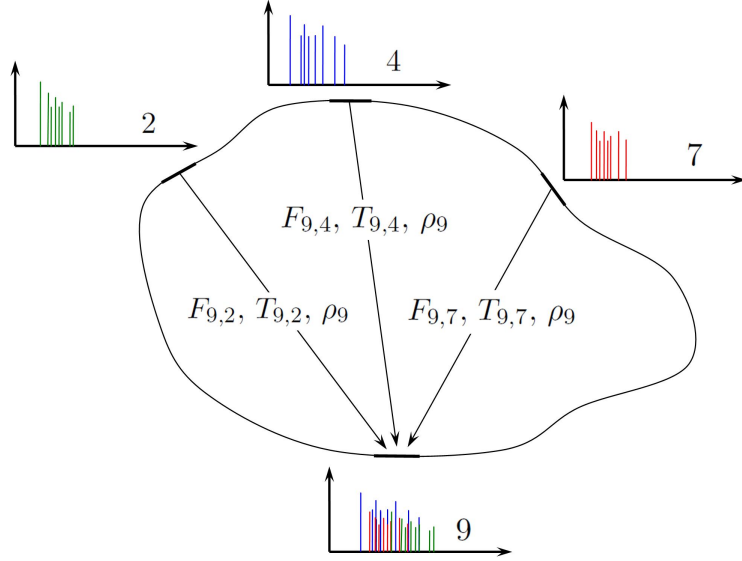


Figure 4.8: Demonstration of how the “new” radiation reflectograms work. During an arbitrary iteration the source elements 2, 4 and 7 contribute all their history to the receiving element 9, filtered by the form factors, the delay and the reflection coefficient of 9. Note that the “new” reflectogram of the 9th element consists of the information from 2, 4 and 7, without adding its own information. Its old reflectogram and thus any old information has been discarded in the previous iteration.

contribution is stored in the new radiation density vector, according to a *reduction assignment*², for every n :

$$B'[i, n + T_{i,j}] := B'[i, n + T_{i,j}] + \rho_i B[j, n] F_{i,j} \quad (4.18)$$

Note that this assignment implements the first term in eq. (4.10) but $\rho_i s_i$ has been replaced by ρ_i . For the present version of the algorithm, the second term in eq. (4.10) is neglected, or in other words, it has been merged with the first term. This process described by eq. (4.18) is similar to the *primary* and *secondary* lists used in [6]. According to this approach, the old radiation reflectograms, $B[j, 1 : T]$, should contribute first to all new ones, $B'[i, 1 : T]$, and then updated by them, $B := B'$. In the next iteration, the “new” radiation reflectograms have become “old” ones. Now the “new” radiation reflectograms are “empty”; that is, they do not contain any old information, since all the history of reflections has been transferred to the “old” reflectograms. The concept is illustrated schematically in Figure 4.8.

The iteration process seems to converge quite slowly with this approach. Instead, we can get inspired by a variant of the classical radiosity method, the *progressive radiosity* method, **PR**, widely used in computer graphics. Both methods deal with light, so they are time-independent, but the concepts are easily extended to time-dependent problems. A fundamental difference occurs between these two variations. The classical radiosity is based on the *gathering* operation, i.e., an element i collects energy from all other elements j . As a result, the picture of only one element, i , is improved at each iteration. In contrast, **PR** is based on the *shooting* operation, i.e., an element j acts as a source that sends energy to all other elements, simultaneously [43]. Thus, the energy of all the elements on the boundary is updated at each iteration³. Even if the two methods take almost the same time for a full solution, **PR**

²A reduction assignment is an accumulation across iterations of a loop (www.mathworks.com).

³This is the reason why this process is also called *progressive refinement*.

provides acceptable results from an early stage. It is not our intension to incorporate **PR** in our development, but we can adopt one of its key points. The *unshot* energy, which is the energy of the source element, j , that is going to be distributed to the rest of the elements. Once the energy has been transferred from j to the rest boundary, it should be reset to zero.

In our case, the radiation reflectogram of the source element, j , can be characterized as the *unshot* radiation density. Using the described concept, we can shoot this radiation density to all other elements, i . The contribution will be accumulated to the corresponding radiation reflectogram but without employing a “new” radiation density vector, in contrast to the previous idea. All we have to do is to make the current radiation density of element j zero, when it has shot all other elements. Equation (4.18) simply has to be transformed into:

$$B[i, n + T_{i,j}] := B[i, n + T_{i,j}] + \rho_i B[j, n] F_{i,j} \quad (4.19)$$

So far, it should be clear that two for-loops are used: the outer for the source elements j and the inner for the receiving elements i . Every receiving element i will act as a source j in a later stage of this double loop. If we had used the initial idea with the new radiation density, B' , the gathering and shooting operations would act separately. In other words a receiving element could shoot new information only during the next iteration of the whole algorithm. But now, during the same double loop, when a receiving element has turned to a source, it shoots all of its information collected so far. Consequently, the convergence of the diffuse model is much faster now, for the same number of iterations.

At every iteration, the receiver gathers energy from the elements in a view-independent manner, as in pure **AR**. Obviously, whichever approach from the previous two is adopted, the way the receiver collects the energy will be the same, depending on the radiation density of the source element j . Proceeding with the first term in eq. (4.12), we get for each j and for each n :

$$E[n + T_{P,j}] := E[n + T_{P,j}] + \frac{1}{\pi c} B[j, n] H_{P,j} \quad (4.20)$$

However, even if the way the receiver collects energy is the same, the rate of convergence to the desired solution depends on the convergence of $B[j, n]$. That is, if eq. (4.18) is used instead of eq. (4.19), the radiation densities of the elements will converge slower, affecting the convergence speed of the receiver’s energy.

Figures 4.9 and 4.10 illustrate the converging process for the energy density at the receiver, when only diffuse reflections are taken into account. In the first figure the initial approach – employing “new” radiation vectors – is applied using eq. (4.18). In the second, the variation from **PR** is adopted, by eq. (4.19). Evidently, after six iterations the last approach has given almost the full solution for the specific time duration, while the initial approach has converged only to the early part of the response.

Clearly using the concept of *unshot* energy the diffuse model is faster for the desired duration of the reflectogram. On the other hand we must be careful about the physical interpretation of the algorithm. The initial idea from eq. (4.18) was totally consistent with the physical behavior of the elements as secondary sources. As discussed in the beginning of this section, at every iteration the elements act as new sources, emitting the energy that they have received during the previous iteration. So, the process is very clear in terms of iterations – orders of reflections. With the improved approach, the orders of reflections are mixed in the same iteration. This

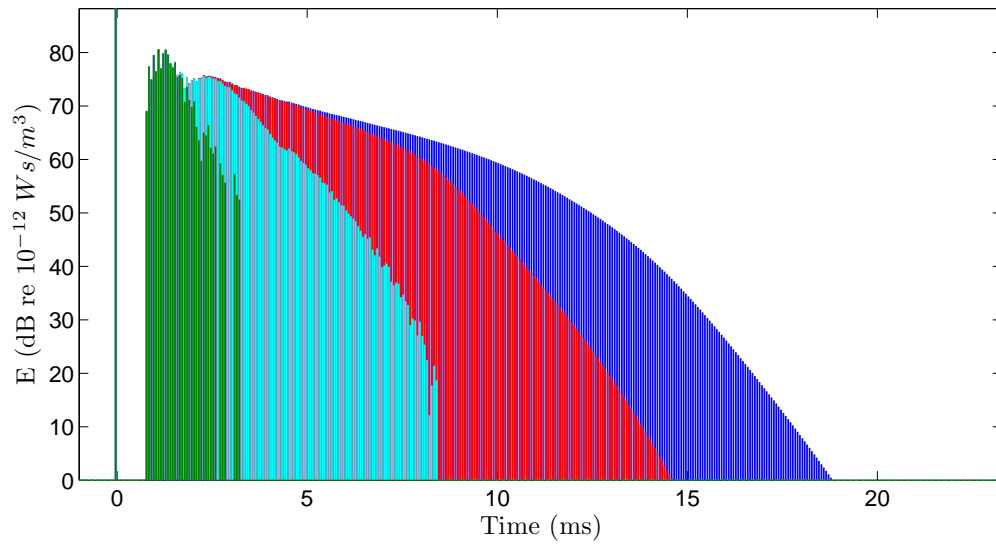


Figure 4.9: Convergence to the final solution applying the concept of “new” radiation vectors. —: After the first iteration. —: After two iterations. —: After four iterations. —: After six iterations.

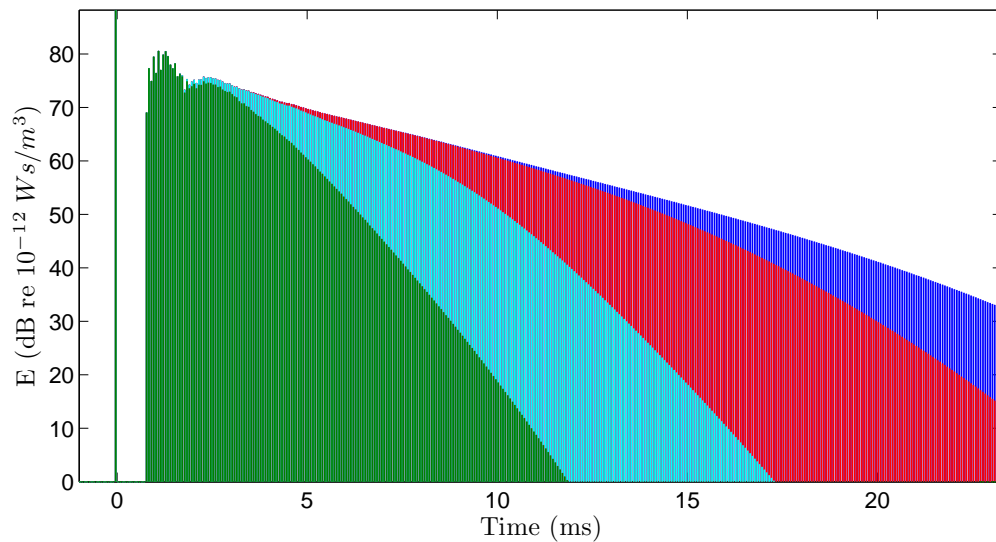


Figure 4.10: Convergence to the final solution applying the concept of unshot energy. —: After the first iteration. —: After two iterations. —: After four iterations. —: After six iterations.

has no impact at the final result, since the energy conservation is not violated, but we cannot apply the same concept for the purely *diffuse radiation density*, which is directly linked to each iteration. The reason will be more clear in the discussion about the specular model.

The purely diffuse radiation density, $B_d[i, n]$, must be accumulated in a new diffuse radiation vector, $B'_d[i, n]$ – and not the same – since the energy at the diffuse model at each iteration needs to be separated from the energy at the other iterations. The reduction assignment for every n reads:

$$B'_d[i, n + T_{ij}] := B'_d[i, n + T_{ij}] + \rho_i B_d[j, n] F_{i,j} \quad (4.21)$$

Summing up the new diffuse radiation densities from all elements on a wall, at every time step, we get the time vector of the total radiation density of each wall.

$$B_{dw}[w, 1 : T] = \frac{1}{S_w} \sum_{i=1}^{N_w} S_i B'_d[i, 1 : T] \quad (4.22)$$

This will be used later, during the specular part, for controlling the creation of a daughter image source.

4.2.4.2 Specular Model

In this part the contribution from the already determined first order image sources is computed and the next order group is created for use in the next iteration step.

Every image source “sees” some of the elements on the boundary, i.e., it is effective for them. As a result, the image source sends a specific amount of energy at a particular time on each visible element, which is then recorded at its *radiation reflectogram*. The same occurs for the receiver P . Once the contribution from the image source has been computed and all the valid daughter sources have been generated, the source is discarded. Hence, at every iteration only the sources of the corresponding order are stored. This alleviates the computational load, in contrast to the common methods, where all sources of all orders are stored and their contribution to the receiver is calculated at the last stage.

During the first iteration, the main loop of the specular model runs over the first order image sources. For each image source an *effective polyhedron* is created, defined by the planes that pass through the point source and the edges of the wall where it was reflected (Fig. 4.11, see also Sec. 3.3.1). It is now checked whether the receiver is inside the effective polyhedron by running through all its surfaces and checking if the inside criterion is fulfilled for all of them. If the receiver is outside from at least one surface, then the checking process is terminated and no contribution from the image source is added. In the opposite case, the energy reaching the receiver is calculated according to eq. (4.3).

$$E_q[n + T_{P,q_k}] := E_q[n + T_{P,q_k}] + \frac{1}{4\pi c} \frac{r_{q_k}}{R_{P,q_k}^2} \quad (4.23)$$

In the main phase of the specular part, the **ISM** and **AR** fully cooperate with each other. The algorithm works with each receiving wall individually. As seen in Figure 4.11, it is often likely that only part of a wall is visible by an image source (wall No 3 from the 2nd order image source). Thus, for each wall the visibility of each element is checked via the already determined *effective polyhedron*. For simplicity, only the center of the element is involved in the inside check. Thereupon, the integral over the

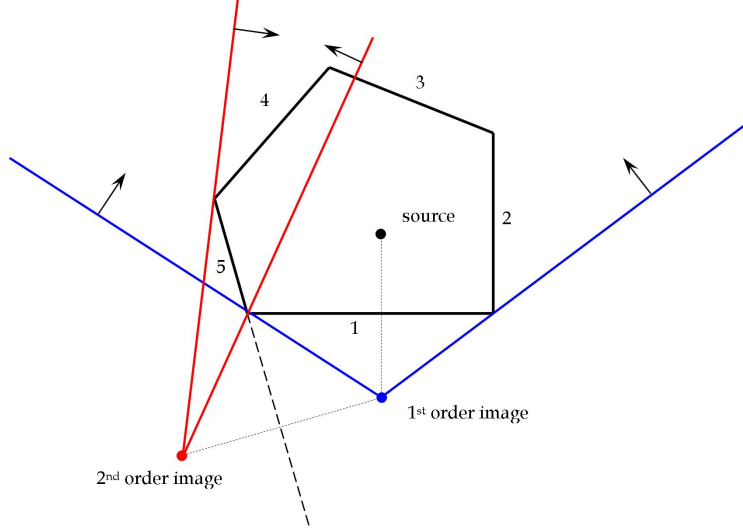


Figure 4.11: Two effective polyhedra as they appear in a ground plan of a room. —: For the first order image source. —: For the second order image source. The normal vectors define the inside region.

solid angle subtended by the element at the image source, H_{i,q_k} , is computed. The sum of these integrals for all elements gives an approximation of the corresponding integral for the visible part of the wall:

$$H_{w,q_k}^{vis} = \sum_{i=1}^{N_w} \begin{cases} H_{i,q_k}, & \text{if } i \text{ visible} \\ 0, & \text{if } i \text{ not visible} \end{cases} \quad (4.24)$$

The same holds for the visible area of the wall:

$$S_w^{vis} = \sum_{i=1}^{N_w} \begin{cases} S_i, & \text{if } i \text{ visible} \\ 0, & \text{if } i \text{ not visible} \end{cases} \quad (4.25)$$

Approximate Wall Visibility Criterion The visibility check for any wall, discussed in Sec. 3.3.1, can be facilitated by comparing S_w^{vis} with S_w . The fraction S_w^{vis}/S_w varies from 0% to 100%, so that a preset value between 0% and 100% can be specified in order for the condition of visibility of the wall to be valid. Apparently, if it is set to 100%, this means that the daughter source can be produced if and only if the *whole* wall is visible from the mother source. The criterion is very strict in this case and many of the daughter sources are missed. In the opposite case, when we demand that the fraction should be just larger than 0%, more sources are likely to be produced than the actual, because even a very small visible part of a wall leads to a daughter source that serves for the whole wall. If we had applied *dynamical* subdivision for the wall, this source would lead to fewer daughter sources after several reflections. It seems reasonable to assume that the fraction should be larger than 20%-50%, in order for the daughter source to be produced.

Precise Wall Visibility Criterion A more precise treatment is possible if we take advantage of the element positions, since the meshing of the wall already incorporates a sense of dynamical subdivision, described in Sec. 3.3.1. The indices of all visible elements on the wall can be recorded to a line vector, linked to the candidate daughter source. These elements can be called *active elements* for the

daughter source, because they will define the new valid region for this source. If all elements are visible from the mother source, the daughter source will be produced for the whole wall and no further information about the elements is required. In the other extreme case, when none of the elements is visible, the source is simply not produced. But if at least one element is visible, then the line vector is attached to the daughter source, for use in the next iteration. Then, when the daughter source becomes a mother source, the line connecting any receiver with the source is checked whether it intersects any of the *active elements*. If this happens, the checking process is immediately terminated and the receiver is considered visible. The effective polyhedron is not involved in this case. The accuracy of this visibility checking process is increased as the number of the elements on the boundary is increased. This happens because the valid region of the image source is built from the corresponding active elements, which act as “pixels” on the whole wall. When these are smaller the region is defined more precisely.

Obviously, the storing and scanning of the active elements raises the computational cost. Various combinations of the precise and the simple checking processes can lead to an optimal result. For example, we can apply the precise approach for the very first reflections, where the details are very important. Later on, the checking can be based on the percentage of the visible area. Another idea is to check if the number of visible elements is between an upper and a lower predefined limit. If quite few elements are visible, the daughter source is discarded. If almost all elements are visible, the daughter source is created being referred to the whole wall, without further information.

The generation of image sources, according to the previous considerations, can be validated using the well-known **ISM** for rectangular rooms, as described in Sec. 3.2. Let us use the room described in Sec. 2.5, with uniform absorption coefficient, equal to 0.4 and zero scattering coefficient. Apparently, when no diffuse reflections are taken into account, only the specular part of our algorithm contributes to the receiver’s response. The algorithm behaves as a pure **ISM** in an arbitrary room and the boundary subdivision does not play any role, except from its application at wall visibility tests. Let us assume source coordinates $Q = (3.0, 2.5, 2.0)$ m and receiver coordinates $P = (6.0, 1.25, 2.5)$ m. First, only the approximate wall visibility criterion is applied, for three different preset percentages of the whole wall area. All sources up to 10th order are used. In Figure 4.12 the resulting decay curves are compared with the decay curve obtained by the algorithm of Sec. 3.2. Let us call this *theoretical one*. For our general algorithm, allowing each daughter source to be generated behind any wall that is visible by 45%, a decay curve is generated that coincides well with the *theoretical one*. When the percentage decreases down to 40% more sources are created, elevating the curve. In the opposite case, for 50% visibility, we miss some sources and consequently some energy. After 0.08 s the curves drop suddenly because of the fixed maximum order of reflection. The precise wall visibility criterion is applied in Figure 4.13. The agreement with the theoretical curve is very good up to 0.04 s. Even if the same orders were used as before, the energy decay “converges” much slower than with the approximate criterion. This is because with the approximate criterion more sources are generated which are placed progressively far away from the original source, while with the precise one, more “gaps” are filled in the pattern of the theoretically expected sources. The precise criterion is much more computationally heavy than the approximate one. Its most important advantage though is the elimination of the arbitrary parameter about the wall visibility.

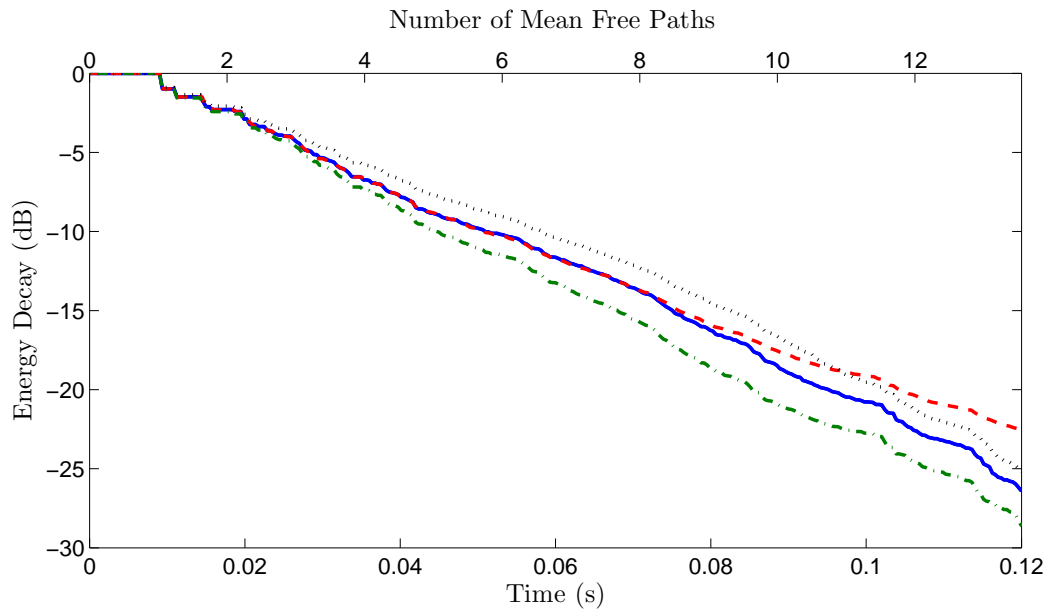


Figure 4.12: Generation of image sources according to wall visibility, applying the approximate criterion. Rectangular room. ---: Theoretical curve (algorithm from Sec. 3.2). —: appr. with 45% wall visibility. ⋯: appr. with 40% wall visibility. -·-: appr. with 50% wall visibility.

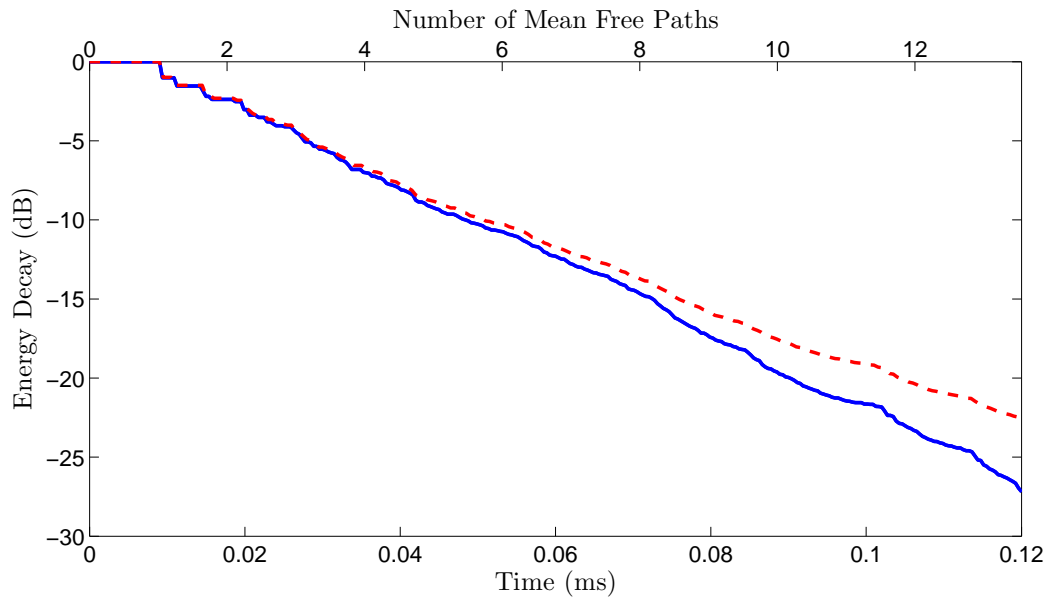


Figure 4.13: Generation of image sources according to wall visibility, applying the precise criterion. ---: Theoretical curve (algorithm from Sec. 3.2). —: Precise visibility according to surface elements.

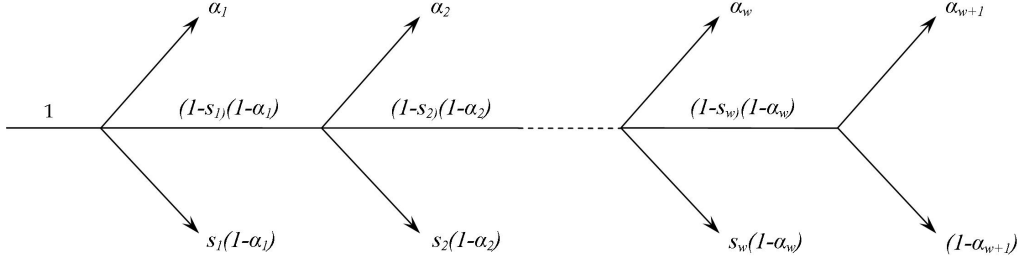


Figure 4.14: A single specular reflection path from the original source. When the path is terminated, the specular coefficient, $(1 - s)$, becomes zero and from now on, the energy is reflected totally diffusely.

Transition from Specular to Diffuse Reflections Once H_{i,q_k} is known, the *radiation density* of the visible elements, due to the source, can be calculated. However, the reflected energy heavily depends on whether the mother source is the last source of an image source sequence or it will produce a daughter source. In Figure 4.14, a sequence of reflections is presented, corresponding to a sequence of image sources. Each time a new image source is produced behind a wall, a fraction $(1 - s)(1 - \alpha)$ of the reflected energy is expected to be sent by the source, while the rest $s(1 - \alpha)$ is sent by the elements of the wall in a diffuse way. Evidently, when the mother source of wall w does not produce a daughter source behind wall $w + 1$, all the energy from the mother source will be reflected totally diffusely by wall $w + 1$.

Using the integral H_{w,q_k}^{vis} and the visible wall area, S_w^{vis} , the *specular radiation density of the wall*, B_{sw} , is also calculated. As we did in Sec. 4.2.3, we assume that the wall receives all of its energy within a unique time delay, T_{w,q_k} , related to the distance between its center and the image source.

$$B_{sw} = \rho_w \frac{1}{4\pi S_w^{vis}} r_{q_k} H_{w,q_k}^{vis} \quad (4.26)$$

With this compromise, the specular radiation density of the wall is compared to the corresponding diffuse radiation density at T_{w,q_k} .

In its simplest form, the condition for producing a daughter source reads $B_{sw} > B_{dw}[w, T_{w,q_k}]$. This means that as long as the energy contained in the specular model is higher than that in the diffuse model, the specular model can still be active. In this case, the *radiation density* of the visible elements on each wall, due to the mother source, is accumulated to the total radiation density of the visible elements as:

$$B[i, T_{i,q_k}] := B[i, T_{i,q_k}] + s_i \rho_i \frac{1}{4\pi S_i} r_{q_k} H_{i,q_k} \quad (4.27)$$

The simplest condition for terminating the image source chain reads $B_{sw} < B_{dw}[w, T_{w,q_k}]$ and then eq. (4.27) becomes:

$$B[i, T_{i,q_k}] := B[i, T_{i,q_k}] + \rho_i \frac{1}{4\pi S_i} r_{q_k} H_{i,q_k} \quad (4.28)$$

The termination condition can be subjected to a predefined margin. We could demand for example that it is enough for the specular energy to be higher than 50% of the diffuse energy, in order for the image source sequence to be continued. The lower the margin is, the later the image source sequence is terminated. Figure 4.15 demonstrates the relation between the specular and the diffuse radiation density of the ceiling in the irregular room of Section 2.5. After the first 7 ms the contribution

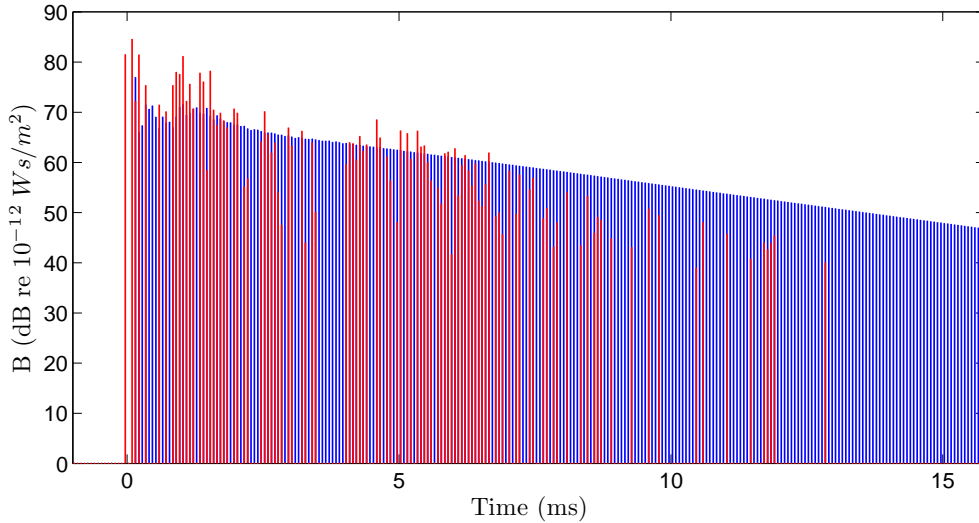


Figure 4.15: Demonstration of the transition from specular to diffuse model on a wall in the irregular room. After 7 ms the specular radiation density starts to become lower than the diffuse one, so that from now on the whole radiation density of the wall should start being converted to diffusely reflected. —: Diffuse radiation density. —: Specular radiation density.

from the image sources becomes smaller than the diffuse contribution from the wall. The image sources are then gradually discarded.

In the cases where the scattering coefficient for most of the walls is very low, the number of generated image sources would soon become too high, since the diffuse radiation density would remain very low to satisfy the inequalities. So, more and more image sources would be created at every iteration. This would have a dramatic effect on the algorithm’s performance. It seems reasonable to replace the diffuse radiation density by the total radiation density of the wall, which will contain both diffuse and specular reflections so far. This treatment can be allowed because of the fact that the number of specular reflections increases with the square of time. Thus, even if we had only specular reflections, we can assume that after some time they can be represented by diffuse reflections. The important early part of the impulse response is still not affected by this modification. As before, a predefined margin can be used for the comparison.

Another way to terminate the image source production is by the reflection order, following the classical **ISM** implementation (Sec. 3.3). In such a case, a maximum order of specular reflections should be predefined. Since the iterations of the algorithm are directly linked to the orders of specular reflections, we can simply demand that after a number of iterations all the energy from the specular model is transferred to the diffuse one according to eq. (4.28). This termination criterion can be effectively combined with the energy criterion. In this way, we ensure that the conversion from the specular-diffuse to purely diffuse model will take place after a certain number of iterations, but in the meantime if some of the sources contribute rather weakly they can be discarded by the energy criterion.

Apparently the *rendering* and the *gathering* processes have been merged together. The specular nature of the algorithm removes one of the advantages of the pure **AR** method for a view-independent solution, since the directional information

from the **ISM** has to be captured by the receiver. As a result, there is no sense to calculate first the energy at the boundary (rendering), extracting afterwards the energy at the receiver (gathering).

Once the first iteration step is finished, the diffuse and specular contributions have been added to the elements and the receiver. As mentioned in Sec. 4.2.4.1, there is no need for updating the primary radiation density by a new one, but this should be done for the diffuse radiation density, $B_d[i, n] := B'_d[i, n]$. Every new iteration step can now be run using the same procedure, with the elements serving as new sources together with the already generated image sources.

As the order of reflection is increased, there is an exponential growth of the number of reflections on each element, thus of the number of the arrival times. However, the constant time discretization of the reflectograms serves for lumping together reflections recorded within the same time interval, reducing the computational load and storage. The pseudocode of the entire described algorithm is presented in Figure 4.16.

4.2.5 Full Algorithm – Iterations

Now let us include the coupling between **AR** and **ISM**, by letting the energy emitted from the elements, suffer several specular reflections before distributed on the boundary. According to Sec. 4.1.3, these specular reflections are represented by image elements. Proceeding similarly to Sec. 4.2.4, both **AR** and **ISM** are used for the first reflections, but in the late reflections all the energy is carried by **AR** and the scattering coefficient shifts to 1. Figure 4.14 is now extended to include a typical specular reflection path from a source element. In the resulting Figure 4.17, the diffusely reflected energy from the first reflection is subsequently reflected specularly, until all the reflections become diffuse.

4.2.5.1 Impulse Response due to Image Elements

The indirect contribution from the images of the source element j to the radiation density of the receiving element i – second term in eq. (4.10) – is implemented as:

$$B[i, n + T_{i,jm}] := B[i, n + T_{i,jm}] + s_i \rho_i \sum_{m=1}^M r_{jm} F_{i,jm} B[j, n] \quad (4.29)$$

in this form the radiation density $B[j, n]$ can be removed outside from the inner summation:

$$B[i, n + T_{i,jm}] := B[i, n + T_{i,jm}] + s_i \rho_i B[j, n] \sum_{m=1}^M r_{jm} F_{i,jm} \quad (4.30)$$

This means that the way all the image elements of j contribute at element i – the pattern of the radiation strengths and the corresponding delays – is always the same. Thus, for the next iteration steps we do not need to generate from scratch the sequence of image elements. It is enough to store the radiation reflectogram of each element i when one of the other elements j is active, emitting a unit impulse ($B[j, 0] = 1$):

$$B_m[i, j, T_{i,jm}] := B_m[i, j, T_{i,jm}] + s_i \rho_i \sum_{m=1}^M r_{jm} F_{i,jm} \quad (4.31)$$

```

input : The radiation reflectograms and source table from the primary step

repeat
  DIFFUSE MODEL
  foreach source element j do
    foreach receiving element i do
      if  $w_j = w_i$  then skip calculations
       $B[i, T_{ij} + 1 : T] := B[i, T_{ij} + 1 : T] + \rho_i B[j, 1 : T - T_{ij}] F_{i,j}$ 
       $B'_d[i, T_{ij} + 1 : T] := B'_d[i, T_{ij} + 1 : T] + \rho_i B_d[j, 1 : T - T_{ij}] F_{i,j}$ 
    end
     $E[n + T_{Pj} + 1 : T] := E[n + T_{Pj} + 1 : T] + \frac{1}{\pi c} B[j, 1 : T - T_{Pj}] H_{P,j}$ 
     $B[j, 1 : T] := 0$  // Reset the unshot energy of  $j$ 
  end
  SPECULAR MODEL
  foreach mother image source  $q_k$  do
    Compute effective polyhedron for  $q_k$ 
    if  $P$  inside effective polyhedron then
       $E[T_{P,q_k}] := E[T_{P,q_k}] + \frac{1}{4\pi c} \frac{r_{q_k}}{R_{P,q_k}^2}$ 
    end
    foreach receiving wall  $w_i$  do
      foreach element  $i$  of receiving wall do
        if  $i$  inside effective polyhedron then
           $B'_d[i, T_{i,q_k}] := B'_d[i, T_{i,q_k}] + \frac{1}{4\pi S_i} (1 - s_i) \rho_i r_{q_k} H_{i,q_k}$ 
           $H_{w,q_k}^{vis} := H_{w,q_k}^{vis} + H_{i,q_k}$  // visible part of the wall
        end
         $B_{dw} := B_{dw} + \frac{1}{S_w} S_i B'_d[i, T_{w,q_k}]$ 
      end
       $B_{sw} = \frac{1}{4\pi S_w^{vis}} \rho_w r_{q_k} H_{w,q_k}^{vis}$ 

      // Checking whether to produce the daughter source
      if  $S_w^{vis} > 0.3 S_w$  then // wall visibility check
        if  $B_{sw} < B_{dw}$  then // energy check
           $B'[i, T_{i,q_k}] := B'[i, T_{i,q_k}] + \rho_i \frac{1}{4\pi S_i} r_{q_k} H_{i,q_k}$ 
        else
           $B'[i, T_{i,q_k}] := B'[i, T_{i,q_k}] + s_i \rho_i \frac{1}{4\pi S_i} r_{q_k} H_{i,q_k}$ 
          Generate daughter source  $q_{k+1}$  at the mirror wall  $w_i$ 
          Compute  $r_{q_{k+1}}$ 
          Store  $q_{k+1}$ ,  $r_{q_{k+1}}$  and  $w_i$ 
        end
      end
    end
  end
   $B_d := B'_d$  // Update diffuse radiation density
until convergence

```

Figure 4.16: Main version. The algorithm of the iteration steps.

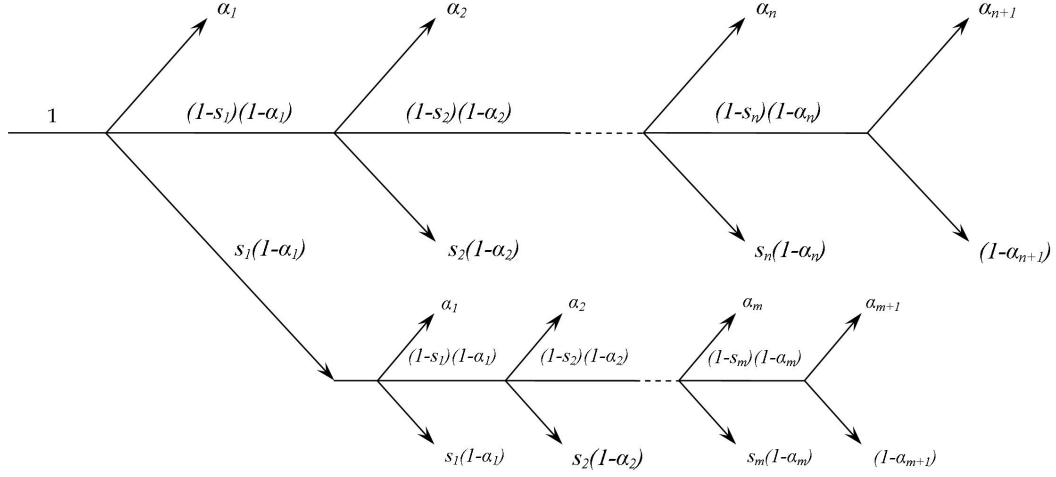


Figure 4.17: Flow of energy through specular reflections in the full algorithm. The upper path represents a single image source sequence for the original source, while the lower path represents a single image element sequence for one of the elements acting as a source. When any of the paths is terminated, the specular coefficient, $(1 - s)$, becomes zero and from now on, the energy is reflected totally diffusely.

For the construction of the image elements, a fixed reflection order can be used. All the energy received by the image elements of the last order will be diffusely radiated, so that eq. (4.31) for the last order becomes:

$$B_m[i, j, T_{i,jm}] := B_m[i, j, T_{i,jm}] + \rho_i \sum_{m=1}^M r_{jm} F_{i,jm} \quad (4.32)$$

The resulting $B_m[i, j, 1 : T]$ vector is essentially the *impulse response* of the element i with respect to source element j – Impulse Response due to the Image Elements (IRIE). When it is convolved with the real $B[j, n]$, it gives the real radiation density as a function of time:

$$B[i, n] = B_m[i, j, n] * B[j, n] = \sum_{\tau=n}^T B_m[i, j, \tau] \cdot B[j, \tau - n + 1] \quad (4.33)$$

Evidently, the computational cost is drastically reduced by storing the $B_m[i, j, 1 : T]$ vectors, but we have to consider that eq. (4.32) leads to a three dimensional matrix. For every element j as the source, every element i as the receiver and for every time step. Three dimensional matrices are very impractical and difficult to be stored. We need to transform it into a two dimensional one, but trying to keep it small. The strategy is to take a very low sampling frequency only for the $B_m[i, j, 1 : T]$ calculation. Thus, the reflectograms for the element to element coupling will be a bit coarse but this seems not to harm our result. The important thing is that many reflections can be grouped into one bin, once they arrive at the same time interval. Then it seems useful to store only the bins and their arrival times, not the whole time vectors $B_m[i, j, 1 : T]$, which contain usually a large number of zeros. Hence two 2-dimensional matrices should be created, one for the values of $B_m[i, j, 1 : T]$ and one for the corresponding arrival time steps. Their columns represent the receivers i , while the lines are divided into groups of element j and a number of arrival times. Table 4.1 shows the way of storing.

1		$B_m[1, 2, T_{min}^{1,2}]$	$B_m[1, 3, T_{min}^{1,3}]$...	$B_m[1, N, T_{min}^{1,N}]$
	0	\vdots	\vdots	...	\vdots
		$B_m[1, 2, T_{max}^{1,2}]$	$B_m[1, 3, T_{max}^{1,3}]$...	$B_m[1, N, T_{max}^{1,N}]$
2	$B_m[2, 1, T_{min}^{2,1}]$		$B_m[2, 3, T_{min}^{2,3}]$...	$B_m[2, N, T_{min}^{2,N}]$
	\vdots	0	\vdots	...	\vdots
	$B_m[2, 1, T_{max}^{2,1}]$		$B_m[2, 3, T_{max}^{2,3}]$...	$B_m[2, N, T_{max}^{2,N}]$
3	$B_m[3, 1, T_{min}^{3,1}]$	$B_m[3, 2, T_{min}^{3,2}]$...	$B_m[3, N, T_{min}^{3,N}]$
	\vdots	\vdots	0	...	\vdots
	$B_m[3, 1, T_{max}^{3,1}]$	$B_m[3, 2, T_{max}^{3,2}]$...	$B_m[3, N, T_{max}^{3,N}]$
\vdots	\vdots	\vdots	\ddots	\vdots	
N	$B_m[N, 1, T_{min}^{N,1}]$	$B_m[N, 2, T_{min}^{N,2}]$	$B_m[N, 3, T_{min}^{N,3}]$...	
	\vdots	\vdots	\vdots	...	0
	$B_m[N, 1, T_{max}^{N,1}]$	$B_m[N, 2, T_{max}^{N,2}]$	$B_m[N, 3, T_{max}^{N,3}]$...	

Table 4.1: A way of storing the bins of the element impulse responses. The left most column corresponds to the source elements j . The table contains the values of the bins, sorted with respect to the arrival times $T_{min}^{j,i} \dots T_{max}^{j,i}$. A similar table should be used for the values of the arrival times.

4.2.6 Energy at the Receiver

As happens for the receiving elements, the way the image elements of j contribute at the receiver P is always constant. We can thus compute the energy density reflectograms for every element as a unit impulse source –with $B[j, 0] = 1$ – and store the result in a matrix with j lines and n columns:

$$E_m[j, T_{P,jm}] := E_m[j, T_{P,jm}] + \frac{1}{\pi c} \sum_{m=1}^M r_{jm} H_{P,jm} \quad (4.34)$$

Here the problem of the three-dimensional matrix is removed, since we are dealing with one receiver. There is no need to distinguish between zeros and bins, unlike we did in Sec. 4.2.5.1. If more receivers are involved in the simulation simultaneously, care has to be taken for storing the data.

Once the matrix E_m has been computed, we can calculate the contribution to the real energy density, $E[n]$, due to the image elements of j , by discrete convolution with $B[j, n]$:

$$E[n] = E_m[j, n] * B[j, n] = \sum_{\tau=n}^T E_m[j, \tau] \cdot B[j, \tau - n + 1] \quad (4.35)$$

4.2.7 Reciprocity of Image Elements

A variation of the **ISM**, the *Image Receiver Model*, **IRM**, has been proposed for efficiently simulating the case of a room with multiple sources and a single receiver [44]. In this model instead of generating all the images for the original sources,

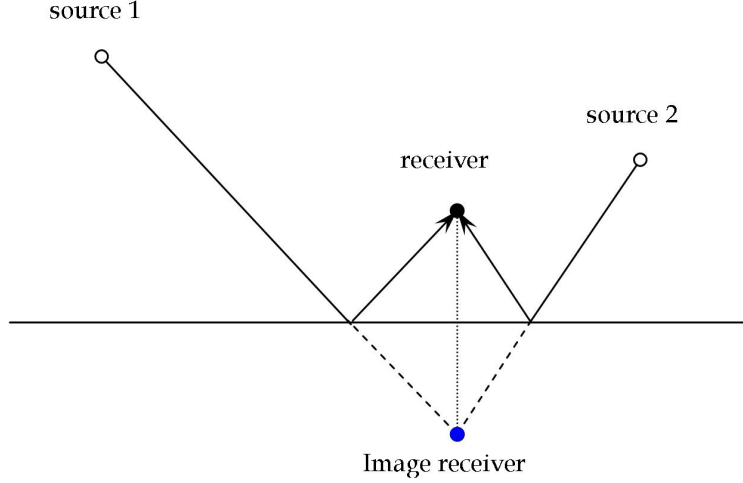


Figure 4.18: Principle of the IRM.

only the images of the receiver are created (Fig. 4.18). The resulting configuration is exactly the same as with the ISM (i.e., same distances, source factors etc.), but the mirroring operations have been reduced dramatically.

Applying the IRM to the case of image elements, we can realize that a reciprocity relation occurs between a source element j and a receiving element i , similar to the reciprocity of the form factors. Figure 4.19 illustrates an example. The source element j contributes directly at i and indirectly, via its images. Here only two of the images are shown. It can be seen that when element i is the source and element j is the receiver, the contributions from the images of i to element j are identical to the contributions from element i to the images of j (blue and red lines are mutually equal). Actually, since the elements are connected through the extended form factors and they are not point sources, the form factor reciprocity relation should be applied – eq. (2.12) – in order to compensate for the difference in the element areas:

$$B_m[j, i, 1 : T] = \frac{S_i}{S_j} B_m[i, j, 1 : T] \quad (4.36)$$

Obviously, applying the foregoing concept, not only the calculations can be halved, but the storage as well. Now, for every source element j only the receiving elements from j to N should be run through and not all of them from 1 to N . Now the storing of the impulse responses can be facilitated by joining the bin values and their arrival times in a unique matrix, as illustrated in Table 4.2.

The contribution to the receiver is not affected by these modifications, since it still collects the energy from the image elements of j . However, if the elements are made from more than three vertices, application of the IRM for the receiver would be extremely beneficial, reducing the mirroring operations and storage (Fig. 4.20). All the common validation tests can be applied as the image receiver was an image source and as the center of the source element was the receiver.

Once the $B_m[j, i, 1 : T]$ and $E_m[j, 1 : T]$ vectors have been computed, their convolutions with B should be imported in the main algorithm of Figure 4.16. For that reason, equation (4.19) is modified as:

$$B[i, n + T_{ij}] := B[i, n + T_{ij}] + s_i \rho_i B[j, n] F_{i,j} \quad (4.37)$$

1	0	$B_m[1, 2, T_{min}^{1,2}]$ \vdots $B_m[1, 2, T_{max}^{1,2}]$	$B_m[1, 3, T_{min}^{1,3}]$ \vdots $B_m[1, 3, T_{max}^{1,3}]$	\cdots \cdots \cdots	$B_m[1, N, T_{min}^{1,N}]$ \vdots $B_m[1, N, T_{max}^{1,N}]$
2	$T_{min}^{2,1}$ \vdots $T_{max}^{2,1}$	0	$B_m[2, 3, T_{min}^{2,3}]$ \vdots $B_m[2, 3, T_{max}^{2,3}]$	\cdots \cdots \cdots	$B_m[2, N, T_{min}^{2,N}]$ \vdots $B_m[2, N, T_{max}^{2,N}]$
3	$T_{min}^{3,1}$ \vdots $T_{max}^{3,1}$	$T_{min}^{3,2}$ \vdots $T_{max}^{3,2}$	\ddots	\ddots	\vdots
\vdots	\vdots	\vdots	\ddots	\ddots	$B_m[N-1, N, T_{min}^{N-1,N}]$ \vdots $B_m[N-1, N, T_{max}^{N-1,N}]$
N	$T_{min}^{N,1}$ \vdots $T_{max}^{N,1}$	$T_{min}^{N,2}$ \vdots $T_{max}^{N,2}$	\cdots \cdots \cdots	$T_{min}^{N,N-1}$ \vdots $T_{max}^{N,N-1}$	0

Table 4.2: A compact way of storing the element impulse responses results by joining together two triangular matrices. The lower triangular matrix contains the time steps of the bins, in increasing order. The upper triangular matrix contains the respective values of the bins for the reciprocal pairs.

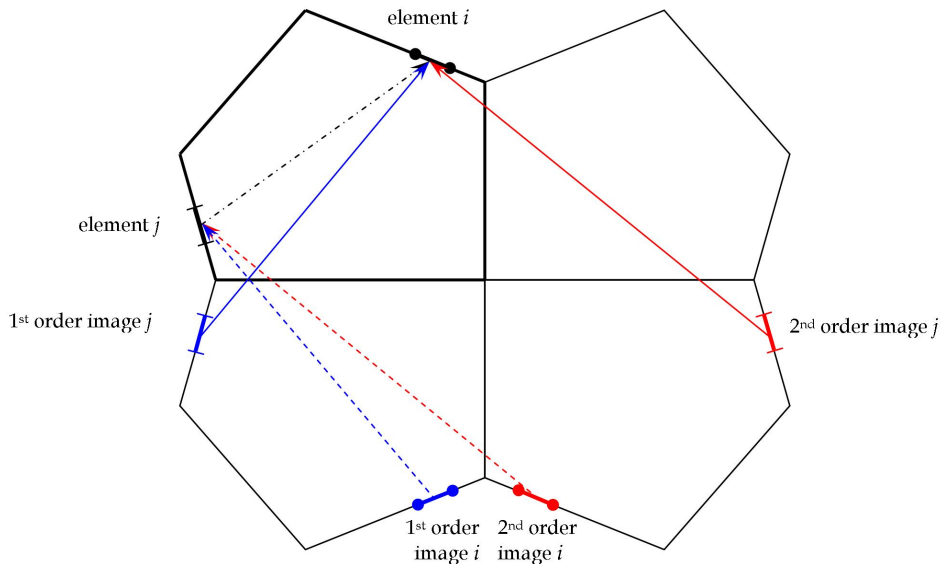


Figure 4.19: Reciprocity relation between the images of a source and a receiving element. Arrows — and - - - are mutually equal. The same happens with arrows — and - - - .

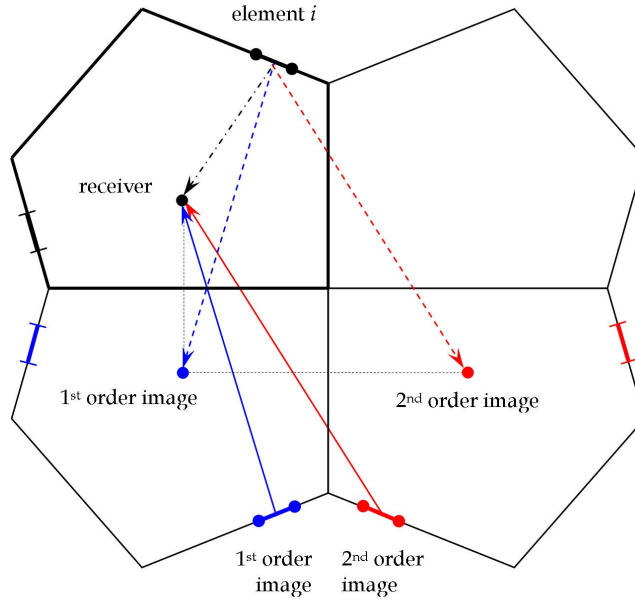


Figure 4.20: Using the images of the receiver, instead of the elements. The mirroring of the point receiver replaces the need of mirroring the whole source element. This is advantageous if polygonal elements are used. Arrows — and - - - are mutually equal. The same happens with arrows — and - - -.

because now a portion of the energy that element i receives is further specularly reflected – first term in eq. (4.10). To simplify the algorithm, the diffuse radiation density, B_d , that is used for the controlling of the image source production, can be still calculated as no further specular reflections occur for the diffuse portion of energy. That is, eq. 4.21 may be used as it is without changing the reflection coefficient.

Apparently, the reflection orders of the image elements work independently of the orders - iterations of the main algorithm. This allows setting a relative low number of reflections for the image elements, in order to keep the computational cost as low as possible. The modification in the diffuse part of the main algorithm is presented in Figure 4.21. Several examples and investigation of the benefits from the full algorithm are presented in Section 5.7.

DIFFUSE MODEL

```

foreach source element  $j$  do
  foreach receiving element  $i$  do
    if  $w_j = w_i$  then skip calculations
     $B[i, T_{i,j} + 1 : T] := B[i, T_{i,j} + 1 : T] + s_i \rho_i B[j, 1 : T - T_{i,j}] F_{i,j}$ 
     $B'_d[i, T_{i,j} + 1 : T] := B'_d[i, T_{i,j} + 1 : T] + \rho_i B_d[j, 1 : T - T_{i,j}] F_{i,j}$ 
  end
   $E[n + T_{P,j} + 1 : T] := E[n + T_{P,j} + 1 : T] + \frac{1}{\pi c} B[j, 1 : T - T_{P,j}] H_{P,j}$ 
  // Convolution with  $B_m$  to obtain contribution at element  $i$ 
  Read sequence of bins  $B_m[j, i, T^{j,i}]$  and arrival times  $T^{i,j}$  from Tab. 4.2
  foreach  $B_m[j, i, T^{j,i}]$  and  $T^{i,j}$  do
     $B[i, T^{j,i} + 1 : T] := B[i, T^{j,i} + 1 : T] + B[j, 1 : T - T^{j,i}] \cdot B_m[j, i, T^{j,i}]$ 
  end
  // Convolution with  $E_m$  to obtain contribution at the receiver
  foreach time step  $n$  do
     $E[n : T] := E[n : T] + B[j, 1 : T - n + 1] \cdot E_m[j, n]$ 
  end
   $B[j, 1 : T] := 0$  // Reset the unshot energy of  $j$ 
end

```

Figure 4.21: Full version for the diffuse part of main algorithm (Fig. 4.16)

Chapter 5

Investigation of the Combined Model

In this chapter we attempt to make a theoretical validation for the algorithms that implement the **CARISM**. The crucial aspect of the energy behavior in the room is investigated for the main algorithm, in order to ensure that it works in a reasonable way. Apart from that, the computational performance is discussed and the variation of several room acoustic parameters is investigated as a function of the scattering coefficient. Application of the main algorithm is performed for several cases of rooms.

Most important, the necessity of the coupling between the elements on the boundary, i.e., the necessity of the full algorithm, is examined. We will keep the reference used in the previous chapter for the two algorithms: The *main algorithm* is the one that does not take into account further specular reflections of the diffusely reflected energy by an element. The *full algorithm* includes these specular reflections.

5.1 Energy Conservation

The energy behavior in the room is studied using the main algorithm. Figure 5.1 presents a simple example for the response at the receiver in the rectangular room introduced in Sec. 2.5. As the scattering coefficient is increased uniformly from 0 to 1, the nonlinear exponential decay, approaches the linear one, justifying the arguments of Sec. 1.4 and Sec 3.2. Actually, only $s = 0.3$ is enough for this convergence. We will discuss again the required degree of scattering for the exponential decay in Section 5.2.

Let us now refer back to Figure 4.4. Considering the room and a particular group of absorption coefficients as a “black box”, we expect that the energy supplied by the source is absorbed always in the same way, no matter what type of reflections are applied. In other words, the scattering coefficient should not play any role for the **total** absorbed energy in the room, at every time step. Of course, the way each individual element absorbs the supplied energy will be different for different scattering coefficients. Hence, the response at the receiver will be different too.

Pure **AR** and our **CARISM** are expected to give the same *global* energy decay, as long as the absorption is not highly non-uniform and there is some scattering on the room boundary. If we calculate the irradiation density, $B_{irr}[i, n]$, of the elements, the energy density of the entire boundary, that has received at time step n , should

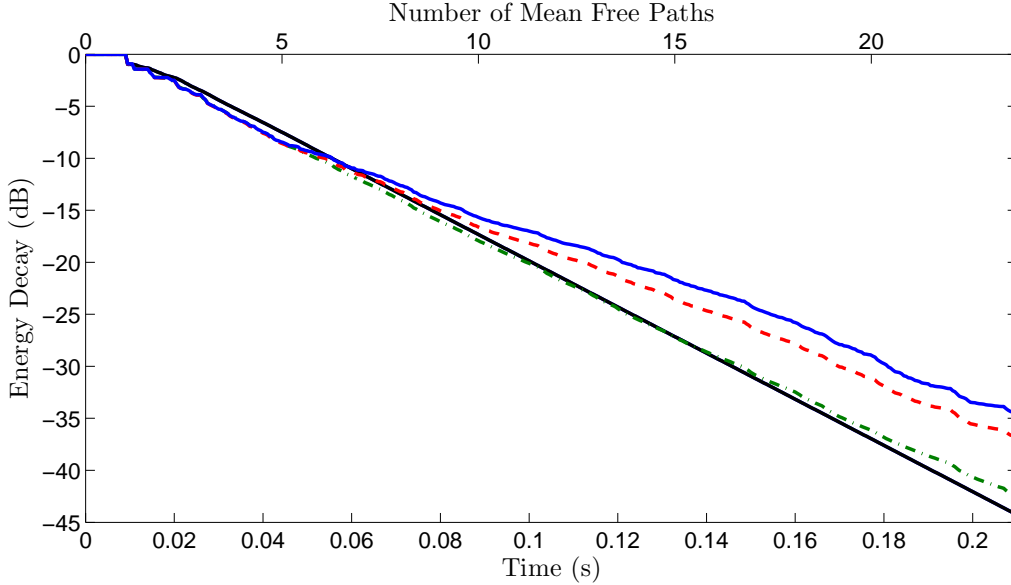


Figure 5.1: Energy decay at the receiver for the rectangular room and different uniform scattering coefficients. —: $s = 0$. - - -: $s = 0.05$. - · - · -: $s = 0.3$. —: $s = 1$. Source-receiver position and absorption coefficient as in Sec. 2.5.

be:

$$E_b[n] = \sum_{i=1}^N S_i B_{irr}[i, n] \quad (5.1)$$

The irradiation density can be easily calculated using equations (4.4), (4.19) and (4.27), without the reflection and scattering coefficients. By backward Schroeder integration (see App. A), we obtain the decay curve for the boundary energy density. The different prediction models result to different energy distribution along the elements of the boundary. Consequently, the corresponding reflectograms and the decay curves are different for each element. However, the weighted average energy for all the elements at every time step, $S_i B_{irr}[i, n]$, is expected to give an objective picture of the whole boundary energy decay, as $E_b[n]$ does. It can be calculated by:

$$E_{av}[n] = \frac{1}{\sum_{i=1}^N S_i} \sum_{i=1}^N S_i B_{irr}[i, n] \quad (5.2)$$

As for $E_b[n]$, $E_{av}[n]$ should be the same for different scattering coefficients, as long as the absorption is the same. More precisely, Hanyu states that it is sufficient to have the same average absorption coefficient in order for the total energy decay to be the same [19]. This means that the actual distribution of the absorption could be different for the different cases.

Three simulation cases in the irregular room are now examined. The sequence of absorption coefficients is the same for all cases, giving an average absorption coefficient $\bar{\alpha} = 0.4$. The sequence of scattering coefficients varies. In the first case the scattering coefficient is everywhere 1, corresponding to a pure AR simulation. In the other two cases a random sequence of scattering coefficients is applied and the simulations are run with the CARISM. All coefficients are summarized in Table 5.1, with the corresponding averaged ones. The source coordinates are $Q = (0.3, 0.2, 0.2)$ m and the receiver coordinates are $P = (0.4, 0.7, 0.5)$ m. The boundary is subdivided

	Walls	1	2	3	4	5	6	7	
	S_w (m ²)	0.54	0.41	0.49	0.65	0.34	0.54	0.65	
	α	0.8	0.3	0.7	0.1	0.0	0.2	0.6	$\bar{\alpha} = 0.40$
case 1	s	1.0	1.0	1.0	1.0	1.0	1.0	1.0	$\bar{s} = 1.00$
case 2	s	0.6	0.0	0.2	0.2	0.0	0.1	0.4	$\bar{s} = 0.24$
case 3	s	0.6	0.2	0.3	0.6	0.0	0.3	0.4	$\bar{s} = 0.38$

Table 5.1: Absorption and scattering coefficients for the three cases in Sec. 5.1. The area of each wall is also given.

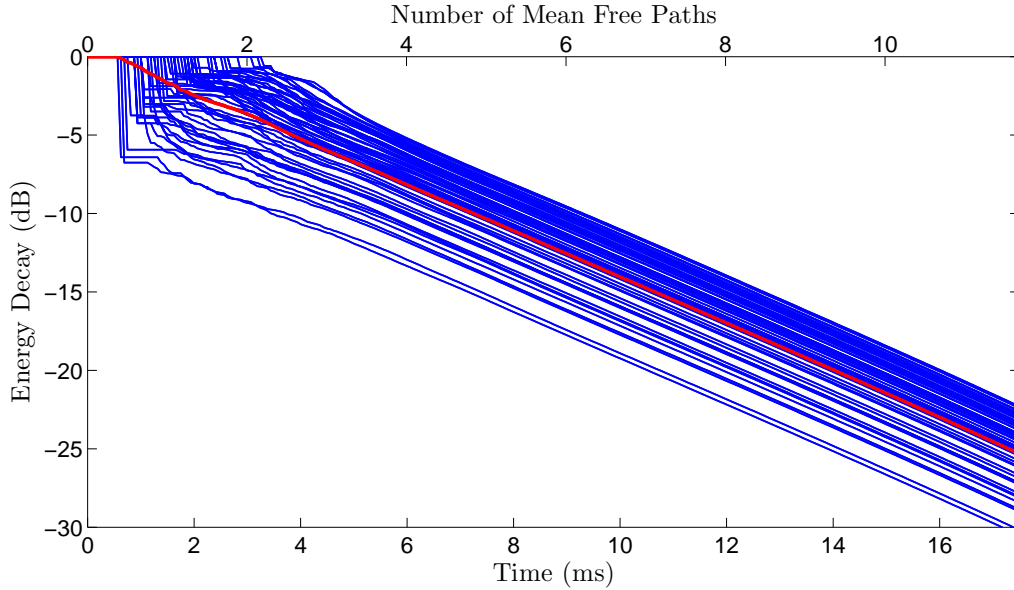


Figure 5.2: Case 1. Decay curves for 55 uniformly chosen elements on the boundary, obtained by AR. Coefficients from Tab. 5.1. —: Curve for each element. —: Decay curve of averaged energy for all 276 elements.

into 276 elements and a sampling frequency of 16 kHz is used for a total impulse response length of 25 ms. The sampling frequency is chosen relatively low in order to help for better visibility of the reflectograms.

Figures 5.2, 5.3 and 5.4 present the energy decay for 55 uniformly chosen elements on the boundary, for the three cases. Note that the figures focus on a slightly shorter length than the actually predicted impulse response. The red line is the average energy decay of all elements, obtained by eq. (5.2). The decay curves of the averaged energy (red lines) coincide. However, the individual transition times towards the exponential decay are longer when specular reflections are allowed by the CARISM. It is clear that the energy is differently distributed and the individual responses are different. For the receiver, the T_{30} reverberation time was calculated 402 ms for case 1, 404 ms for case 2 and 403 ms for case 3. The difference is small. However the EDT varies more, being 456 ms for case 1, 424 ms for case 2 and 452 ms for case 3. This shows that even if the late part of the decay is almost the same in the three approaches, the early one – the transition towards the exponential decay – is different. The longest transition is observed in the second case, where the lowest scattering is applied. In the third case the transition is shorter and the individual decays approach more the smooth lines of Figure 5.2.

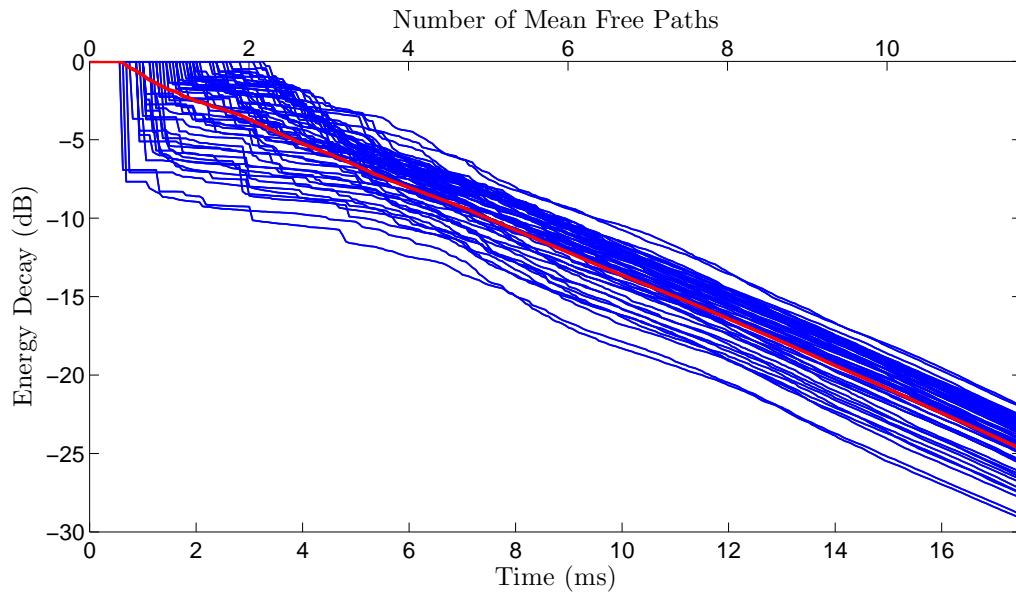


Figure 5.3: Case 2. Decay curves for 55 uniformly chosen elements on the boundary, obtained by the main algorithm of the **CARISM**. Coefficients from Tab.5.1. **—**: Curve for each element. **—**: Decay curve of averaged energy for all 276 elements.

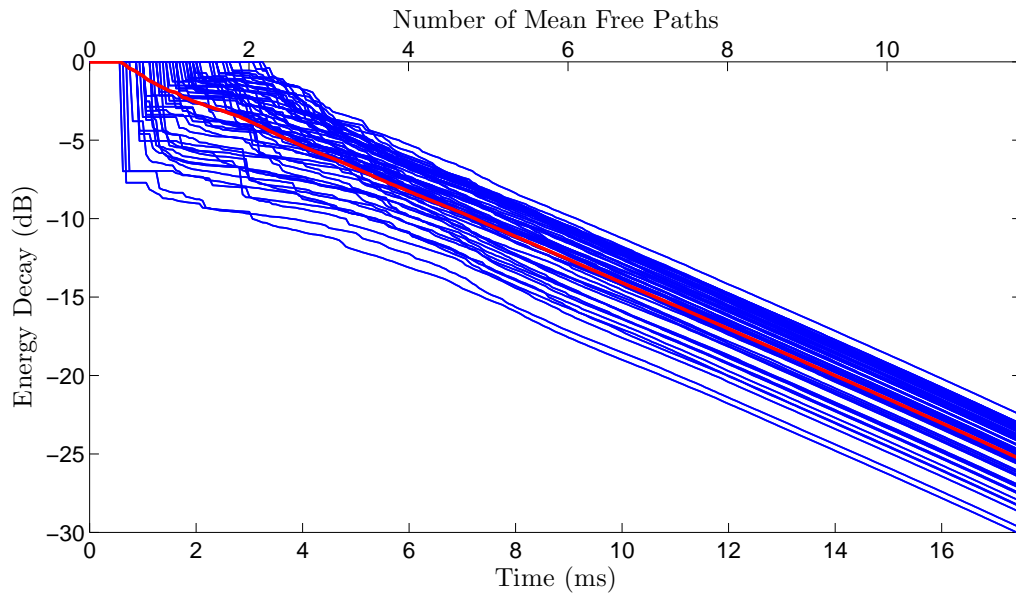


Figure 5.4: Case 3. Decay curves for 55 uniformly chosen elements on the boundary, obtained by the main algorithm of the **CARISM**. Coefficients from Tab.5.1. **—**: Curve for each element. **—**: Decay curve of averaged energy for all 276 elements.

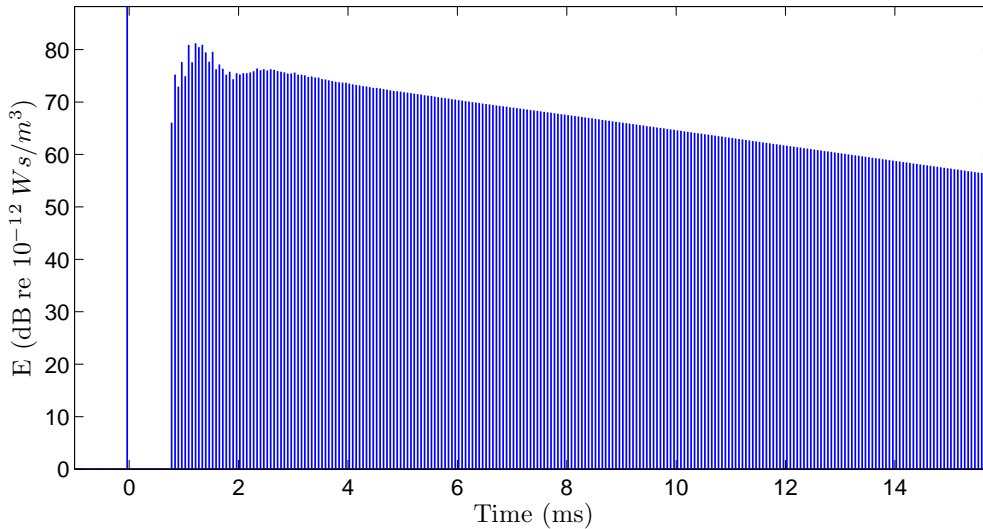


Figure 5.5: Case 1. Reflectogram at the receiver position obtained by **AR** in the irregular room. Coefficients from Tab. 5.1.

The reflectograms obtained by **AR** and the **CARISM** at the receiver, for the three cases, are illustrated in Figures 5.5, 5.6 and 5.7. The lower the scattering, the less smooth the reflectogram is. After 7 ms the response in the third case consists only of diffuse reflections, as we can conclude from the highly smooth reflectogram. Figure 4.15 was calculated with exactly the same parameters. We can now see the connection between the reflectogram and the transition from the **CARISM** to pure **AR**. After around 7 ms the specular reflections are much weaker than the diffuse ones.

Tables 5.2 and 5.3 give an idea of the image sources behavior and of the convergence towards the diffuse response. In both cases, 18 iterations are used in total. For each iteration the effective sources for the receiver are recorded. In the second case, the number of sources is reduced after the 8th iteration, because the diffuse model is dominant. In the third case, the number of effective image sources has started to be reduced earlier, after the first 5 iterations. Now, the specular model is used only up to the 10th iteration. Then the model has completely converted to **AR** and no further image sources are produced.

5.2 On the Degree of Scattering

In the foregoing examples the average scattering coefficient was chosen to be higher than 0.2 (Tab. 5.1). The resulted total boundary energy was the same in all configurations since the absorption remained constant. The progress of the total energy inside the room follows approximately the graph in Fig. 1.2. In such cases, as the case considered in this graph, the late part of the energy decays exponentially, being almost identical to that predicted by Eyring’s reverberation theory [1, 19, 20].

However, when the average scattering coefficient is too low, the specular model is dominant throughout the response and the reverberant tail is expected to be longer. In the following example, all simulation parameters are the same as in Sec. 5.1 but the scattering coefficients are taken from Table 5.4. Now, the average scattering

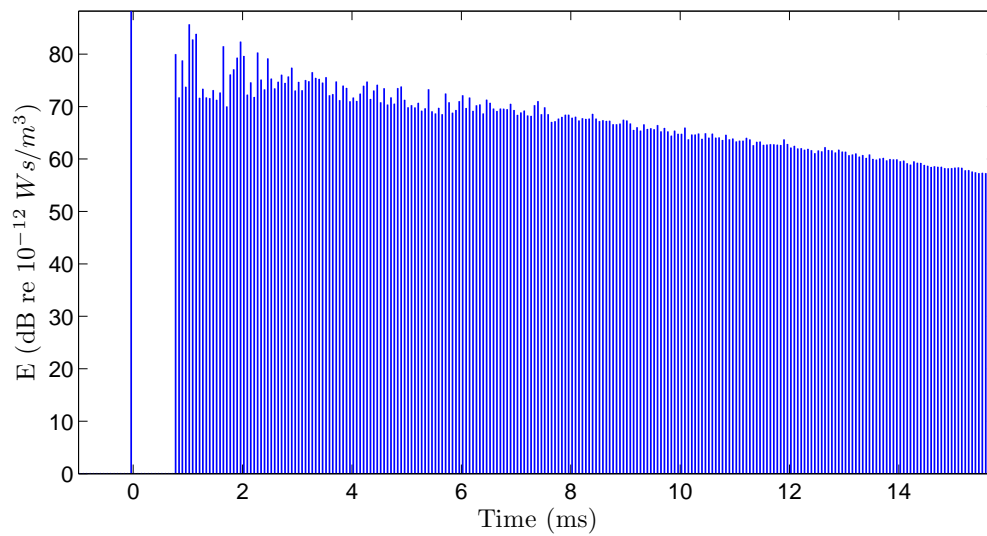


Figure 5.6: Case 2. Reflectogram at the receiver position obtained by the **CARISM** in the irregular room. Coefficients from Tab. 5.1.

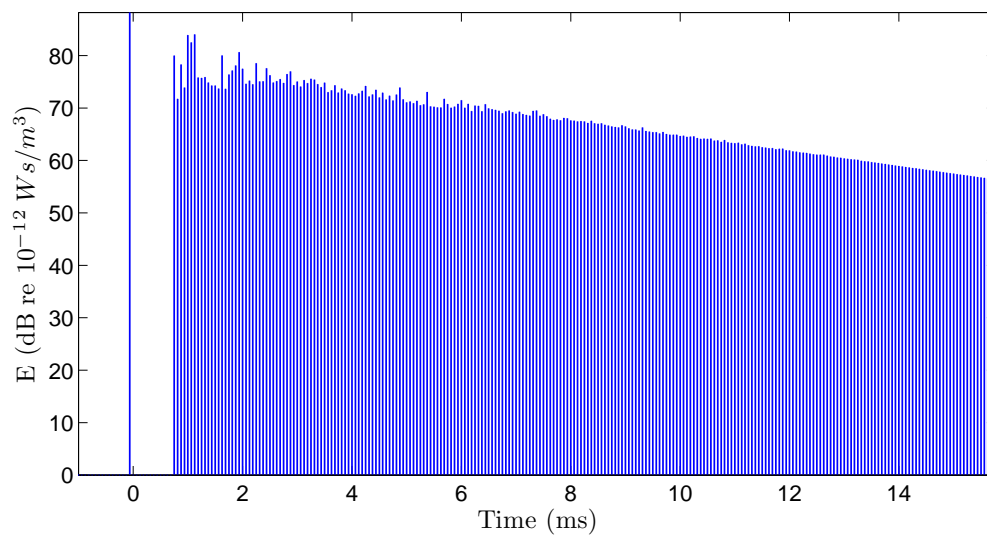


Figure 5.7: Case 3. Reflectogram at the receiver position obtained by the **CARISM** in the irregular room. Coefficients from Tab. 5.1.

Iteration	Eff. im. sources	Iteration	Eff. im. sources
1	7	10	289
2	25	11	224
3	58	12	165
4	124	13	101
5	217	14	50
6	306	15	24
7	385	16	7
8	391	17	1
9	373	18	-

Table 5.2: Case 2. Number of effective image sources for the receiver as a function of the iteration steps in the algorithm.

Iteration	Eff. im. sources	Iteration	Eff. im. sources
1	7	10	1
2	25	11	-
3	58	12	-
4	106	13	-
5	124	14	-
6	103	15	-
7	50	16	-
8	14	17	-
9	5	18	-

Table 5.3: Case 3. Number of effective image sources for the receiver as a function of the iteration steps in the algorithm.

coefficient is $\bar{s} = 0.10$. In Figure 5.8 the total energy decay predicted by AR and the CARISM is shown. The decay by AR is the same as before, but the decay by the CARISM is elevated because only 10 % of the energy is diffusely reflected. The individual decay curves for 55 elements are illustrated in Figure 5.9, together with the average-energy decay curve (red line). Now, the transition time is even longer compared to the second case of Sec. 5.1. The reflectogram at the receiver is shown in Figure 5.10.

The present example, in correlation with the cases in Sec. 5.1 reveal that there must be minimum value of the average scattering coefficient in the room, in order for the total and average energy decay to remain constant, for constant absorption. As Hanyu states [19], the degree of diffusion in a room does not only depend on the scattering but on the absorption as well.

Now, we consider o as the number of energy reflections, equally spaced in time. The probability that the energy in the room is not absorbed and it is specularly

Walls	1	2	3	4	5	6	7
S_w (m ²)	0.54	0.41	0.49	0.65	0.34	0.54	0.65
α	0.8	0.3	0.7	0.1	0.0	0.2	0.6
s	0.3	0.0	0.2	0.0	0.3	0.0	0.0

Table 5.4: Absorption and scattering coefficients for the simulations of Sec. 5.2. The area of each wall is also given. Average scattering coefficient: $\bar{s} = 0.10$.

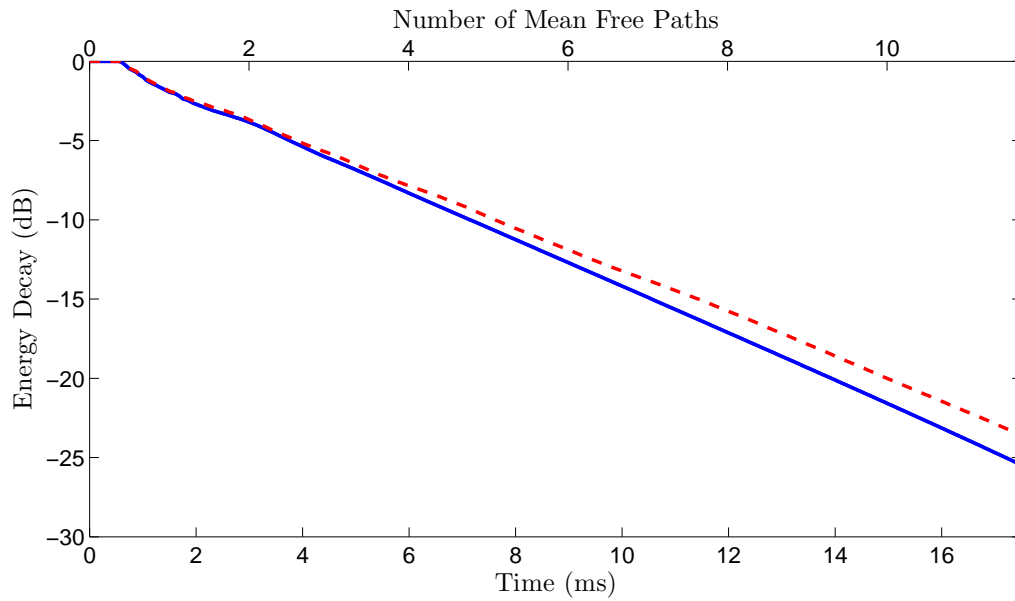


Figure 5.8: Decay curve of the total energy predicted by AR and the CARISM for the coefficients from Tab. 5.4. —: Result by AR. - - -: Result by the CARISM.

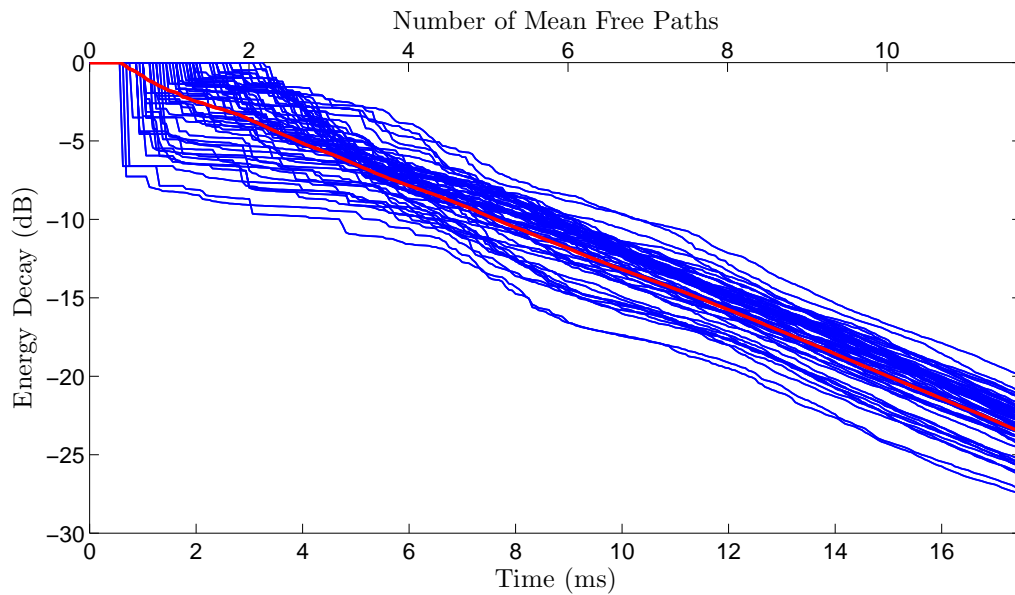


Figure 5.9: Decay curves for 55 uniformly chosen elements on the boundary, obtained by the main algorithm of the CARISM. Coefficients from Tab. 5.4. —: Curve for each element. —: Decay curve of averaged energy for all 276 elements.

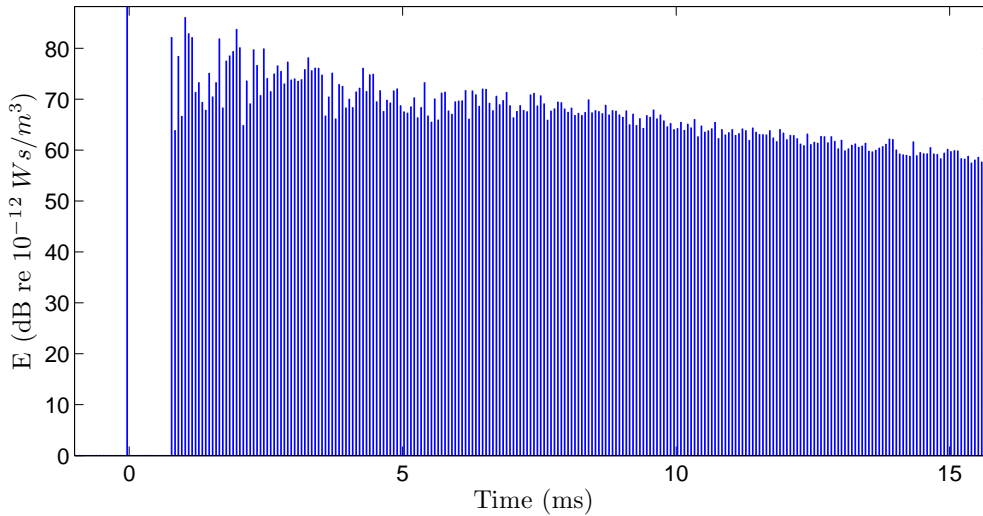


Figure 5.10: Reflectogram at the receiver position obtained by the **CARISM** in the irregular room. Coefficients from Tab. 5.4.

reflected after o reflections is given by:

$$P_{spec} = [(1 - \bar{s})(1 - \bar{\alpha})]^o \quad (5.3)$$

Now, we plot this simple formula, as a function of both the (average) scattering and absorption coefficient, with the number of reflections as the parameter. The result is illustrated in Figure 5.11. If we consider only the first reflection, it is obvious that only very high values of scattering and absorption could reduce the probability of specular reflections. Indeed, this happens with **AR**, where the scattering coefficient is 1 and diffuse reflections are dominant already from the first reflection. But when the number of reflections increases, the probability drops dramatically. Now, if we assume that the first four reflections are enough to reveal the trend of the decay in an irregular room, values of the average scattering and absorption coefficient higher than 0.2, seem enough to reduce the probability of specular reflections so much, so that the decay is expected to be very close to the one predicted by **AR**. This seems to be in consistence with the decays in Fig. 5.2, 5.3, 5.4 and 5.9, where the three first were derived with $\bar{s} > 0.2$ and the last one was derived with $\bar{s} < 0.2$.

On the other hand, as we will see in the next section, highly symmetrical rooms cannot be included in this coarse generalization, because the statistical nature of eq. (5.3) is lost.

5.3 Rectangular Room with High Absorption at the Ceiling

Rectangular rooms with high absorption at the ceiling and very low absorption at the walls and floor have been studied by Nilsson [45, 46]. Such cases are characterized by Nilsson as “non-Sabine” spaces, since the diffuse reverberation theory fails to give correct results.

We investigate one such case with our **CARISM**, by making the walls of the rectangular room almost hard ($\alpha = 0.1$), except from the ceiling which is assumed

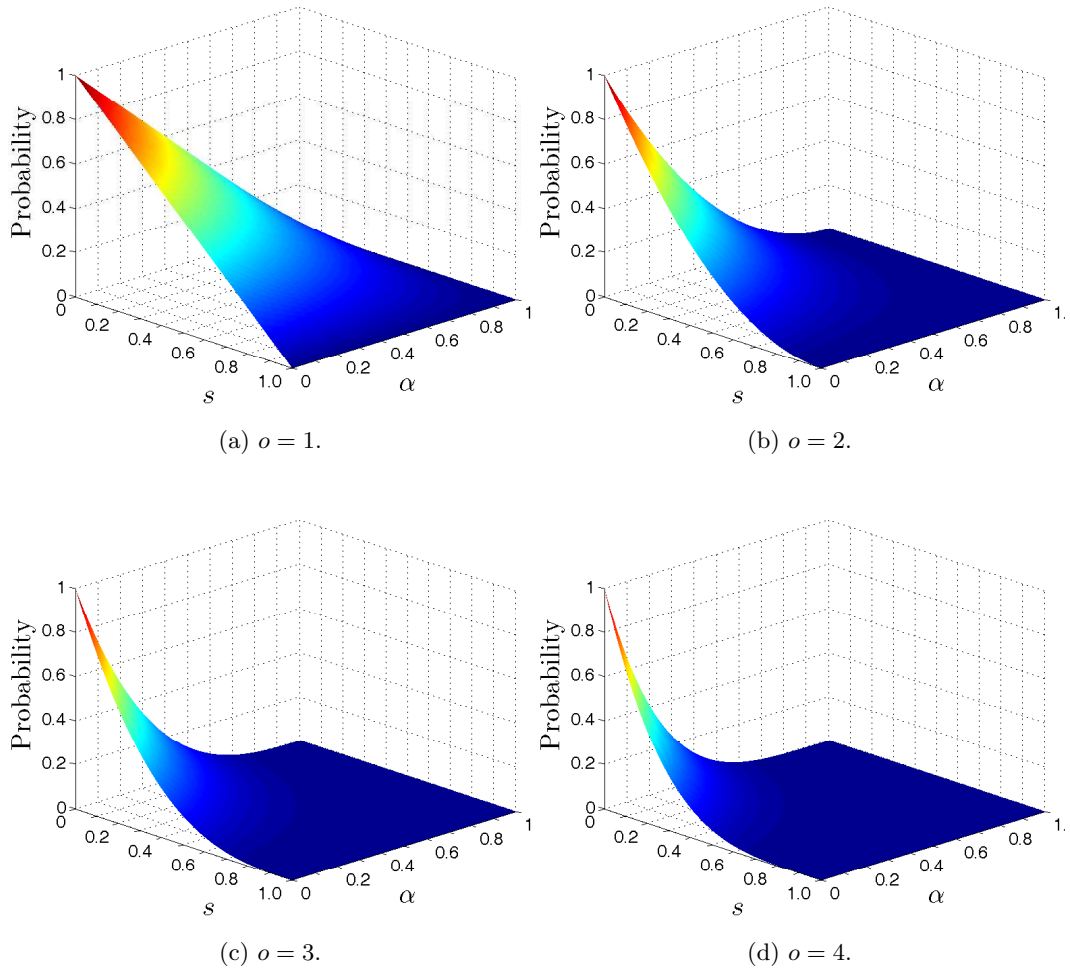


Figure 5.11: Probability that the total energy is specularly reflected after o reflections, as a function of the average scattering and absorption coefficient.

totally absorptive ($\alpha = 1.0$). Three simulations are run. For the first simulation all walls are specularly reflecting. For the second simulation one lateral wall is totally scattering and for the third simulation two lateral walls are totally scattering. Table 5.5 summarizes the cases. The source is placed at $Q = (3.0, 2.5, 2.0)$ m and the receiver is placed at $P = (6.0, 1.5, 2.0)$ m. The room is subdivided into 252 elements and a sampling frequency of 2 kHz is used for a 0.4 s impulse response length.

The early part of the reflectograms at P are illustrated in Figures 5.12 to 5.14, for the three cases. The corresponding decay curves are presented in Figure 5.15. The decay curve by AR is also plotted. The results are in consistence with the discussion in Sec. 5.2. As expected, the totally specular case leads to a non-exponential decay. The case with scattering at one lateral wall leads to a decay curve which has a “knee” point around 0.03 s, where the slope changes from a high to a lower value. Now the average scattering coefficient is around 0.1, still below the limit suggested in Sec. 5.2. The third case gives almost the same result with AR. Now the average scattering coefficient is 0.25, which seems enough for a linear decay in logarithmic scale. But the important point in the third case is that there is not any couple of parallel walls that could maintain a series of repeatable specular reflections. More specific, the ceiling is totally absorbing, so no image source is produced behind it.

	Walls	1	2	3	4	5	6	
	S_w (m ²)	40.0	40.0	15.0	15.0	24.0	24.0	
	α	0.0	1.0	0.0	0.0	0.0	0.0	$\bar{\alpha} = 0.25$
case 1	s	0.0	0.0	0.0	0.0	0.0	0.0	$\bar{s} = 0.00$
case 2	s	0.0	0.0	1.0	0.0	0.0	0.0	$\bar{s} = 0.09$
case 3	s	0.0	0.0	1.0	0.0	1.0	0.0	$\bar{s} = 0.25$

Table 5.5: Absorption and scattering coefficients for the simulations in Sec. 5.3. The area of each wall is also given.

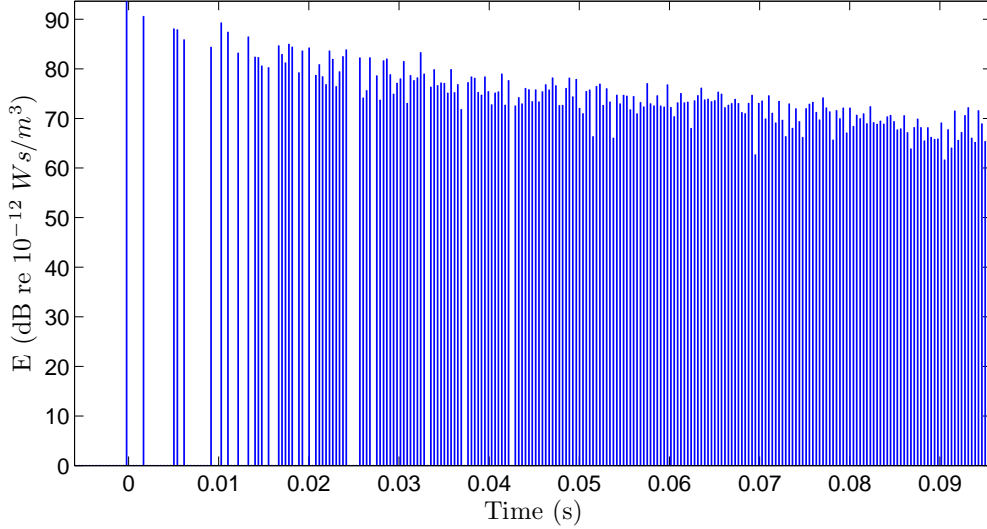


Figure 5.12: Case 1. Reflectogram at the receiver position obtained by the CARISM in the rectangular room with coefficients from Tab. 5.5.

Consequently, even if the floor is almost totally reflective, the sequence of image sources for this pair is terminated after the first order. The same happens for the pair of the lateral walls with one being totally scattering.

The decay curves from 50 elements on the boundary, for cases 2 and 3, are given in Figures 5.16 and 5.17. The red line is the decay curve of the average energy –eq. 5.2–. In the second case, the decay curves corresponding to elements on walls No 5 and No 6 are elevated and non-linear, because this walls are totally specular with low absorption. The rest of the curves, corresponding to the other walls, decay exponentially in a diffuse-like manner. In the third case, the curves decay more or less as in a typical AR prediction. The corresponding T_{30} and EDT values for the three cases are presented in Table 5.6. Their variation is in agreement with the curves in Fig. 5.15.

	T_{30} (s)	EDT (s)
case 1	0.77	0.59
case 2	0.60	0.40
case 3	0.29	0.32

Table 5.6: T_{30} and EDT values for the three cases in Sec. 5.3.

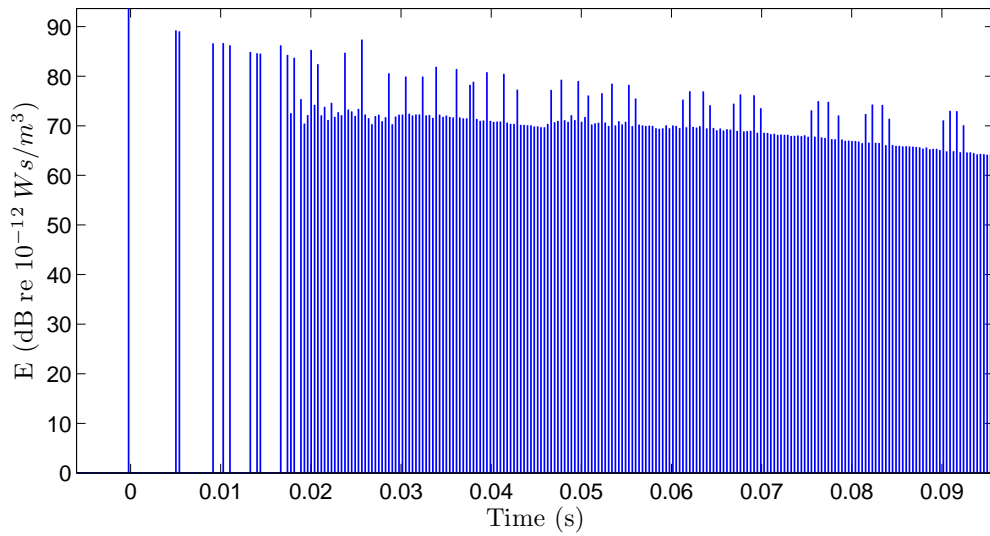


Figure 5.13: Case 2. Reflectogram at the receiver position obtained by the **CARISM** in the rectangular room with coefficients from Tab. 5.5.

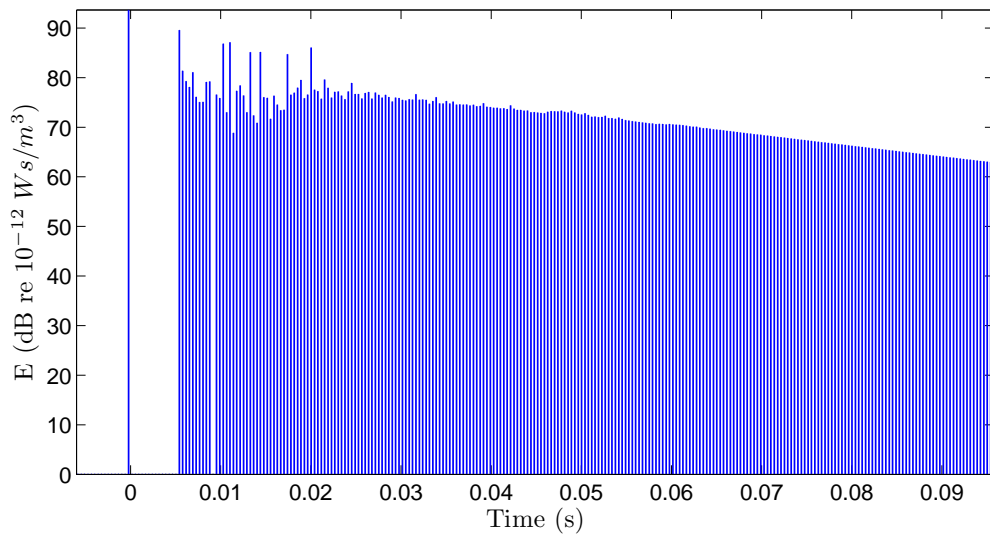


Figure 5.14: Case 3. Reflectogram at the receiver position obtained by the **CARISM** in the rectangular room with coefficients from Tab. 5.5.

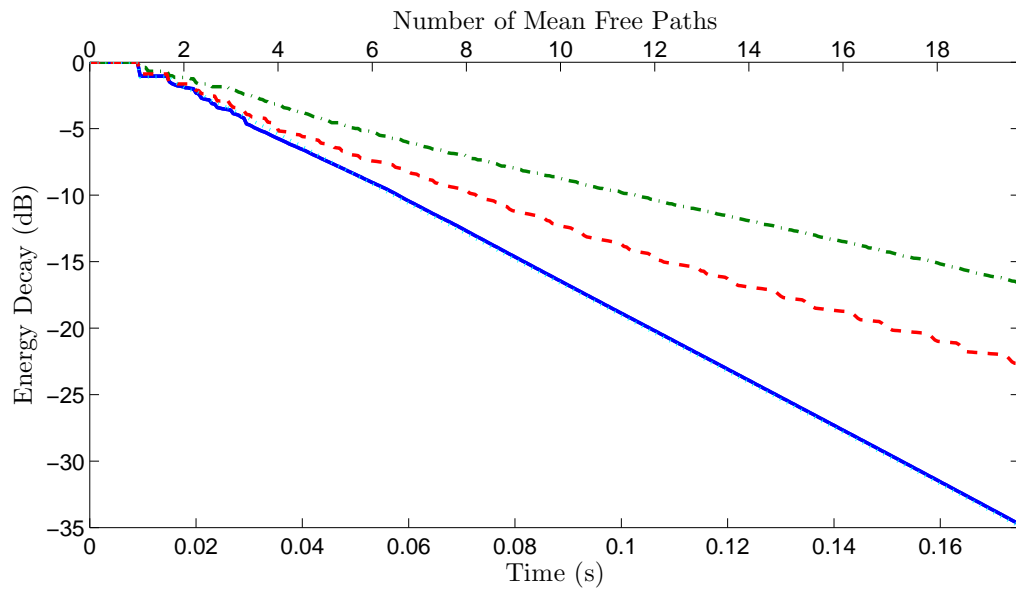


Figure 5.15: Decay curves for all cases at the receiver position obtained by the **CARISM** in the rectangular room with coefficients from Tab. 5.5. **— · — · —**: Case 1. **- - -**: Case 2. **—**: Case 3. **- · - · -**: Calculation with **AR**.

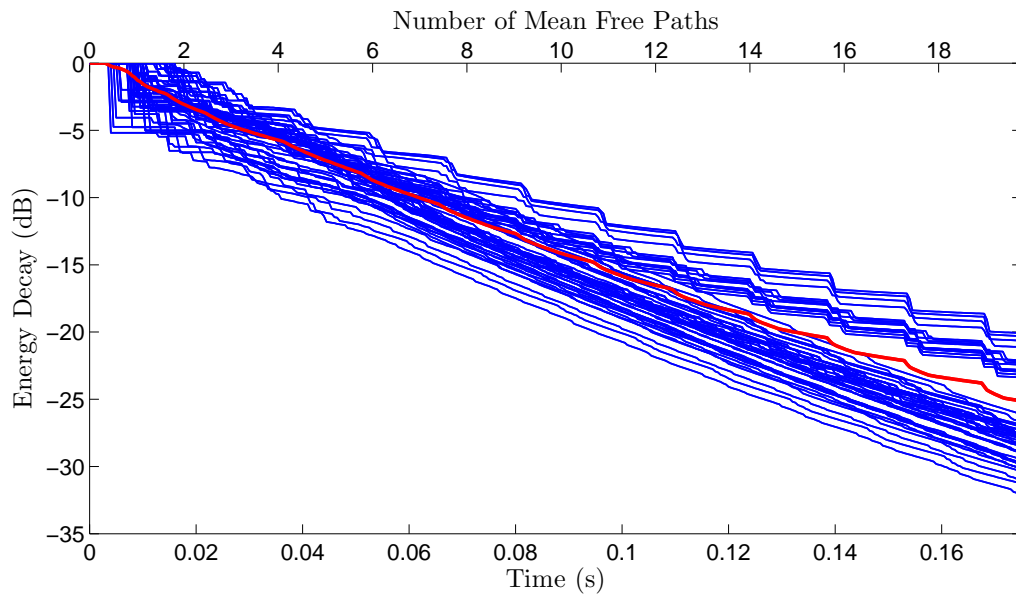


Figure 5.16: Case 2. Decay curves for 50 uniformly chosen elements on the boundary, obtained by the **CARISM**, in the rectangular room with coefficients from Tab. 5.5. **—**: Curve for each element. **—**: Curve for averaged energy over all 252 elements.

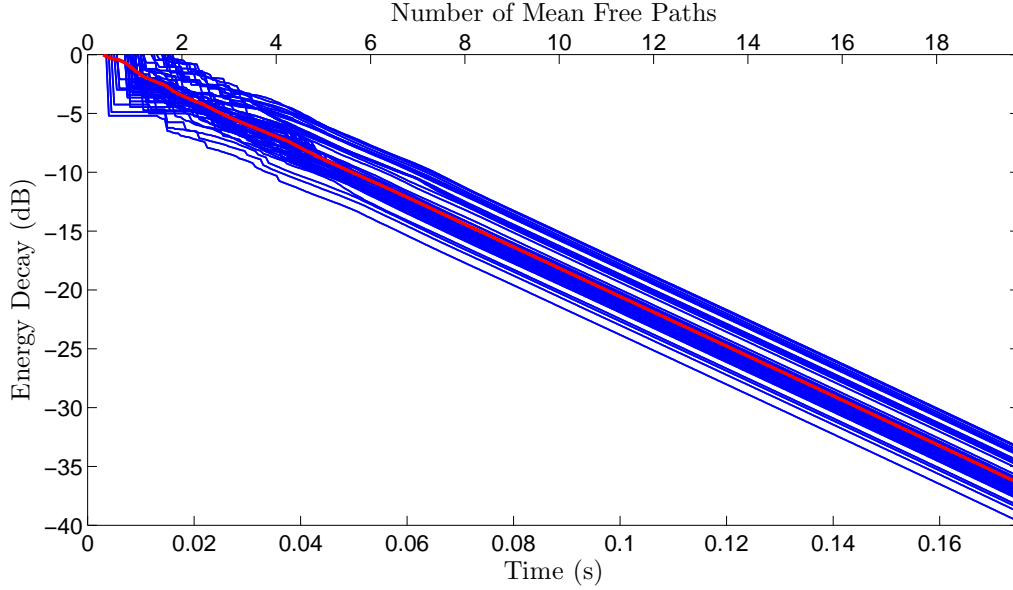


Figure 5.17: Case 3. Decay curves for 50 uniformly chosen elements on the boundary, obtained by the **CARISM**, in the rectangular room with coefficients from Tab. 5.5. **—**: Curve for each element. **—**: Curve for averaged energy over all 252 elements.

Walls	1	2	3	4	5	6
S_w (m ²)	40.0	40.0	15.0	15.0	24.0	24.0
α	0.8	0.8	0.8	0.8	0.2	0.2
s	1.0	1.0	1.0	1.0	0.0	0.0

Table 5.7: Absorption and scattering coefficients for investigation of flutter echo in the rectangular room. The area of each wall is also given.

5.4 Prediction of Flutter Echo

One interesting application of the main algorithm is the prediction of the so common flutter echo phenomenon, which cannot be simulated properly by ray tracing or **AR**. Consider a rectangular room consisting of highly scattering walls, except from two parallel lateral ones, which are highly specular. After some time from the direct contribution, only the sequence of image sources corresponding to these two walls will be maintained, since all other sequences will have transferred all of their energy to the diffuse model. This unique sequence of image sources, corresponding to the parallel specular reflecting walls, effectively represents the flutter echo.

The phenomenon is investigated with the rectangular room and the coefficients from Table 5.7. All walls are chosen to be totally diffuse, except from two parallel ones, which are totally specular. The absorption is quite low for the specular walls, while it is high for the rest. The boundary is subdivided into 252 elements. A sampling frequency of 2.7 kHz is used for an impulse response length of 0.15 s. The source is placed at the centre of the room, $Q = (4, 2.5, 1.5)$ m and the receiver is placed between the source and one of the specular reflecting walls, $P = (4, 1.25, 1.5)$ m. The simulation was run with 7 iterations. For each iteration, only two image sources are produced, corresponding to the pair of the specular parallel walls.

The reflectogram at the receiver is illustrated in Figure 5.18. It can be seen that equally spaced bins occur in the response with much higher amplitudes than

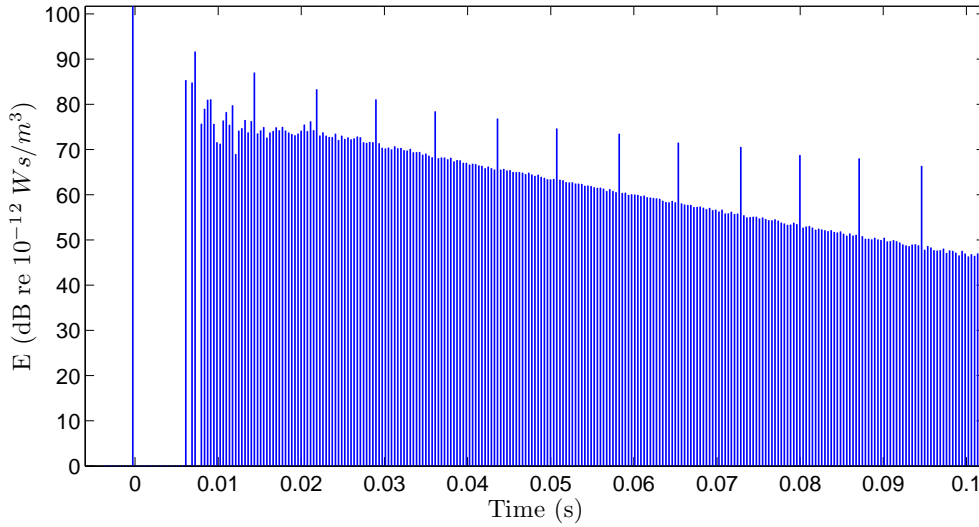


Figure 5.18: Demonstration of flutter echo. Reflectogram at the receiver position obtained by the **CARISM** in the rectangular room with coefficients from Tab. 5.7.

the rest stems. Starting from the first bin, just after the direct contribution, we can count 14 bins in total. A pair of bins corresponds to the contribution from the image sources during one iteration. Hence, 7 pairs of bins corresponds to the number of iterations used in the simulation. The advantage of the **CARISM** in the case of highly symmetrical problems, like flutter echo, is that the computational load is mitigated by the fact that only the important image source sequences are kept, while the rest of the problem is handled by the much faster **AR** part.

The decay curve at the receiver is shown in Figure 5.19. In the same Figure, the curve by **AR** is presented. Unlike the cases in Sec. 5.3, the average scattering coefficient is very high now ($\bar{s} = 0.7$), but the curve does not follow the exponential law. Evidently, the repeatable reflections between the parallel specular walls – that result to the flutter echo – prevent the energy to be dissipated in a diffuse way and raises the reverberation time ($T_{30} = 0.24$ s, instead of $T_{30} = 0.15$ s given by **AR**). The reverberation time by Sabine’s formula is 0.20 s, while by Eyring’s is 0.13 s.

The decay of the total boundary energy, as given by eq. (5.1) is illustrated in Figure 5.20. Both the results by the **CARISM** and by **AR** are presented. Similarly to Fig. 5.19, **AR** underestimates the energy at the late part, by assuming perfectly diffuse reflections.

Finally, in Figure 5.21 the decay curves from 50 elements on the boundary are given. The red line is the decay curve of the average energy, which is the same as the dashed line in Fig. 5.20. Evidently, the individual curves of the elements lying on the parallel specular walls have different shape and they are elevated above the average. The behavior of the energy at these elements is the reason for decreasing the slope at the late part of the total boundary energy in Fig. 5.20.

5.5 Performance of the **CARISM**

Clearly **AR** is faster than **ISM** when less elements are used for the same number of walls and **ISM** is faster than **AR** when less walls are used for the same number of

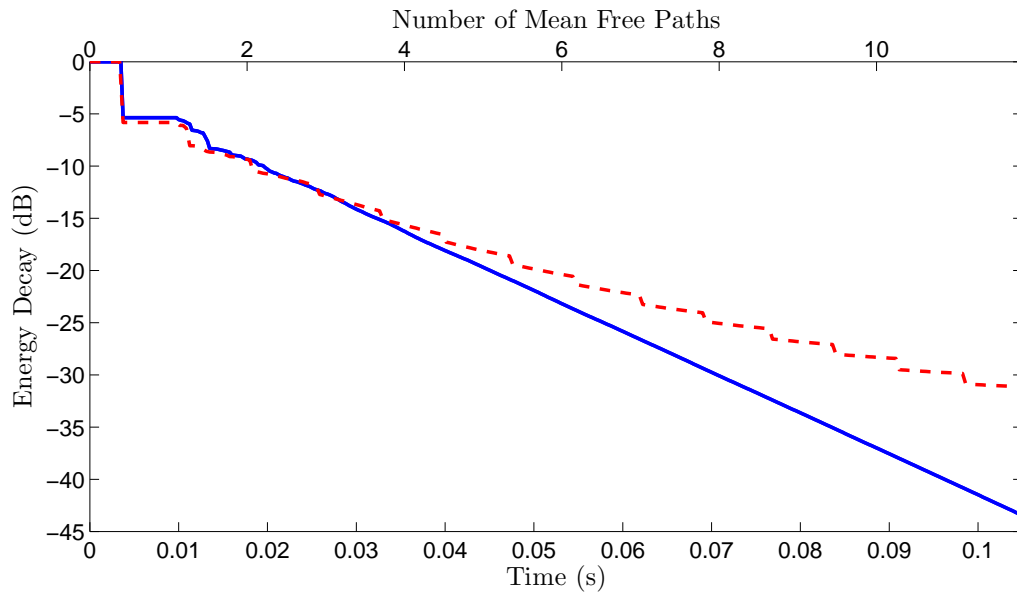


Figure 5.19: Demonstration of flutter echo. Decay curve at the receiver position in the rectangular room with coefficients from Tab. 5.7. ---: Result by the CARISM. —: Result by AR.

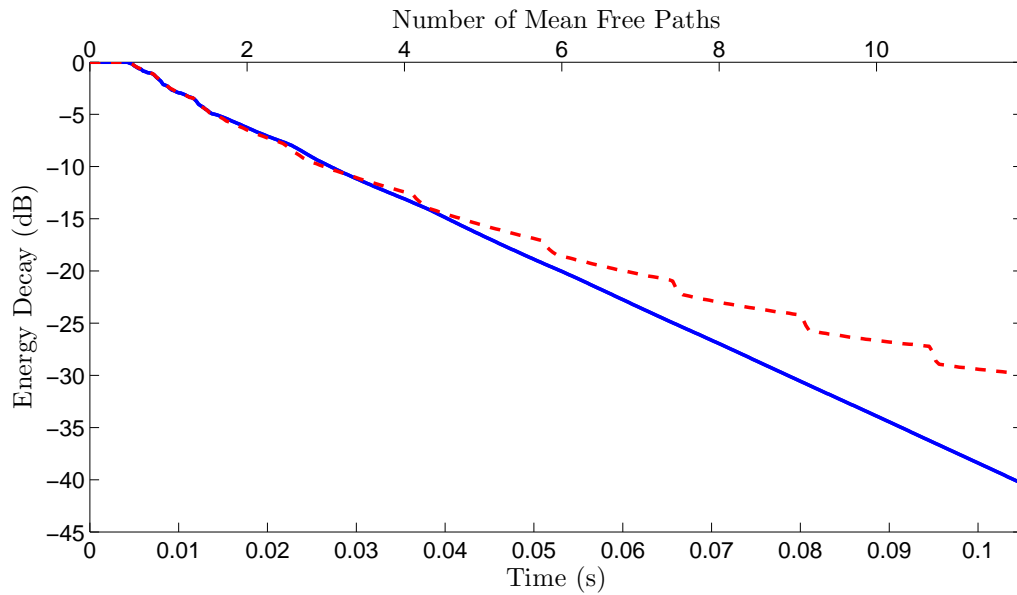


Figure 5.20: Demonstration of flutter echo. Decay curve of the total boundary energy in the rectangular room with coefficients from Tab. 5.7. ---: Result by the CARISM. —: Result by AR.

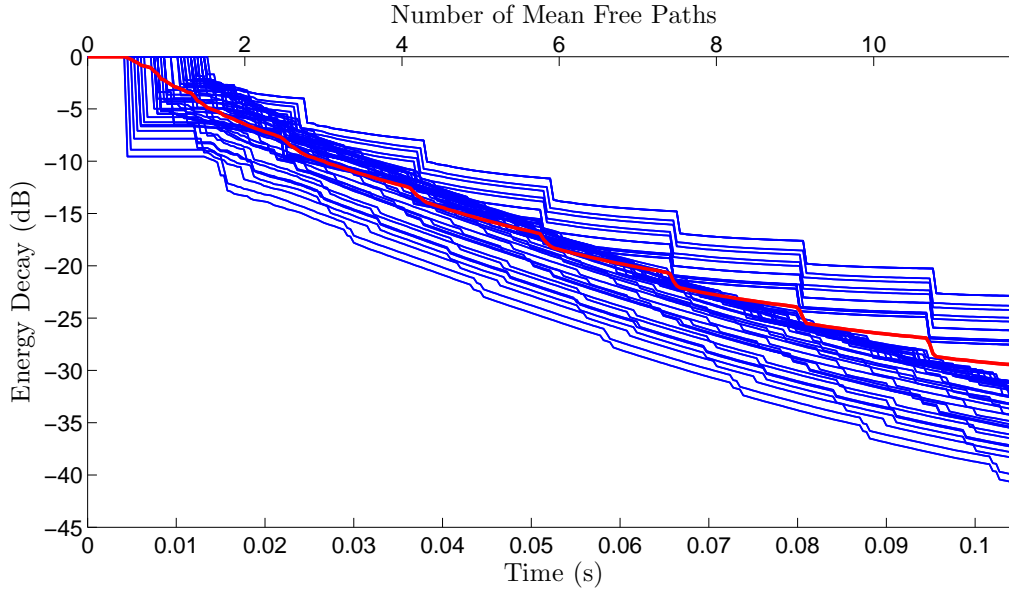


Figure 5.21: Demonstration of flutter echo. Decay curves for 50 uniformly chosen elements on the boundary, obtained by the **CARISM**, in the rectangular room with coefficients from Tab. 5.7. —: Curve for each element. —: Curve for averaged energy over all 252 elements.

elements. For our combined algorithm, the execution time depends highly on which of the two models is dominant.

In the following example, the room and its meshing are fixed with 7 walls and 276 elements, respectively. The irregular room is used with absorption according to Tab. 5.1. The **CARISM** is run with uniform scattering, varying from 0 to 1. 18 iterations are used with a sampling frequency of 20 kHz. The duration of the impulse response is 35 ms. Only the energy termination criterion is used for the image sources, as was described in Sec. 4.2.4.2. The execution cpu time is recorded for every iteration and the result is illustrated in Figure 5.22. The number of effective image sources per iteration is shown in Figure 5.23. Obviously, the execution time is proportional to the number of generated image sources. For pure specular reflections the execution time and the number of image sources increase monotonically. Applying $s = 0.1$ to all walls is enough to introduce a “peak” in the image source production, after which their number is gradually reduced, resulting to a bell-shaped curve for the computational time. For $s = 0.2$ the execution time has been dramatically reduced and for $s > 0.4$ it is almost the same as with $s = 1$, (lower black curve in Fig. 5.22). These facts are correlated well with the discussion in Sec. 5.2. The non-linear decrease of the total execution time, for increasing scattering, is illustrated in Figure 5.24.

5.6 Room Acoustic Parameters

According to Sec. 5.1, the total energy decay in a room remains the same for different scattering coefficients, in irregular rooms, as long as the absorption is constant and randomly distributed. As a result, the reverberation time remains the same as well. If it is evaluated by the slope of the late part of the decay curve, then it is the same not only for the whole energy in the room but also for energies at individual

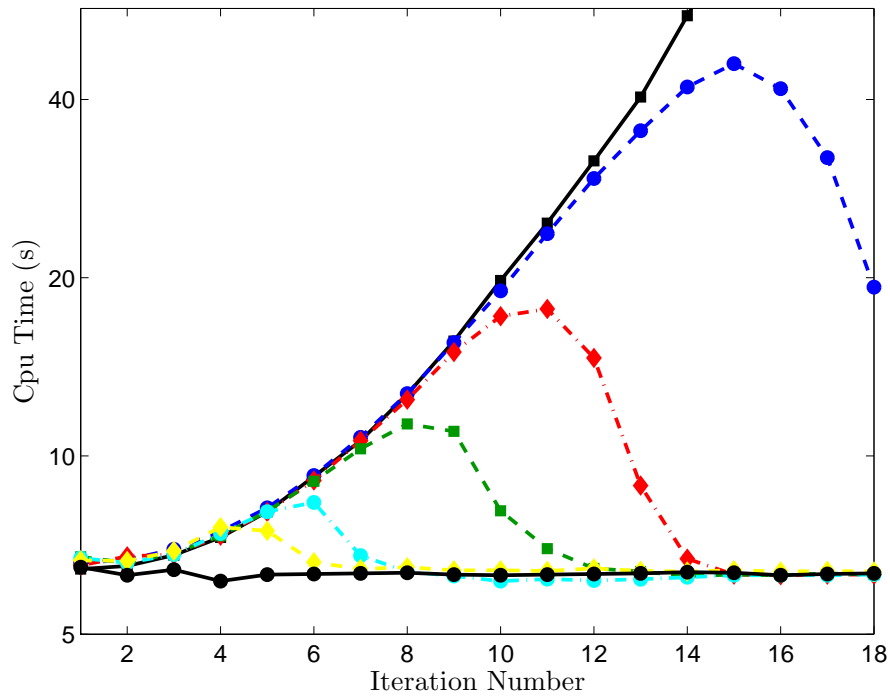


Figure 5.22: Cpu time per iteration for different uniform scattering coefficients.
 —■— : $s = 0$. —●— : $s = 0.1$. —◆— : $s = 0.15$. —■— : $s = 0.2$. —●— : $s = 0.3$.
 —◆— : $s = 0.4$. —●— : $s = 1$.

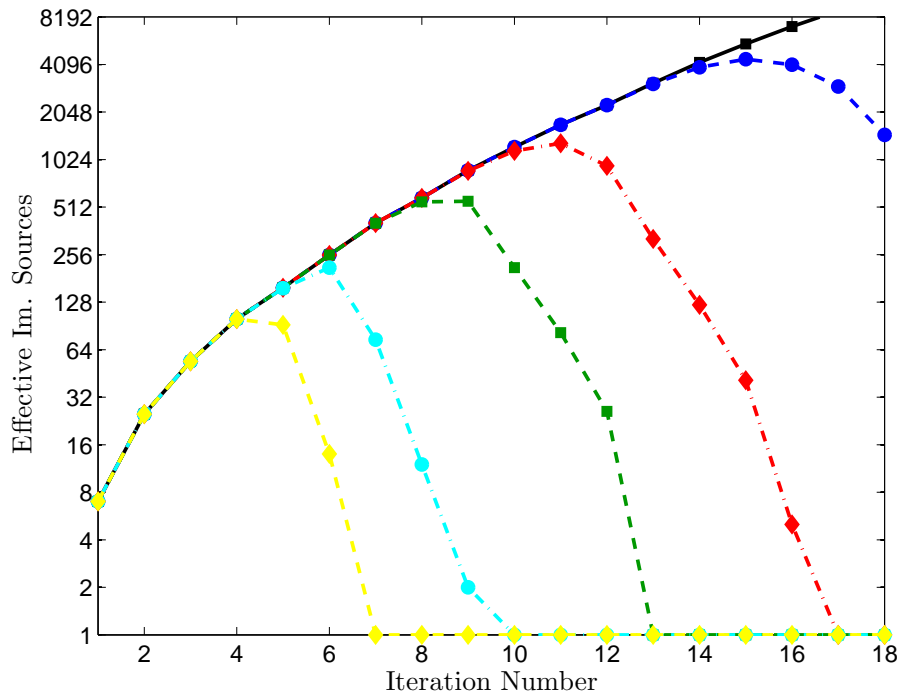


Figure 5.23: Number of effective image sources per iteration for different scattering coefficients.
 —■— : $s = 0$. —●— : $s = 0.1$. —◆— : $s = 0.15$. —■— : $s = 0.2$. —●— : $s = 0.3$.
 —◆— : $s = 0.4$.

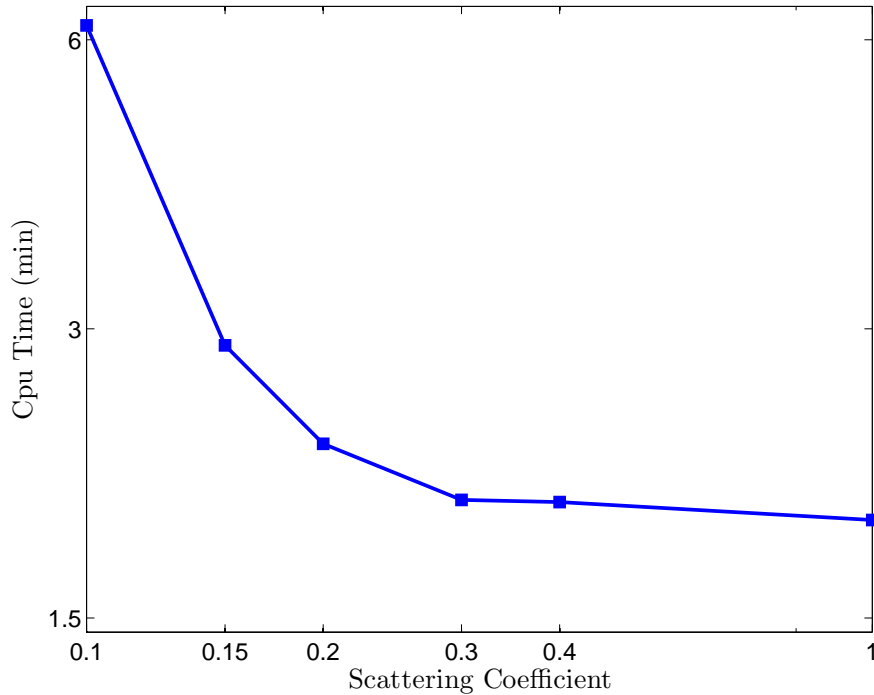


Figure 5.24: Total cpu time as a function of the scattering coefficient, corresponding to figure 5.22.

receivers, since the slope of the late part is constant everywhere in the room. On the other hand, evaluating the reverberation time by the early part of the curve – T_{25} , T_{30} or EDT – different values will be obtained, for varying scattering coefficients, because of the different transitions towards the exponential decay.

The influence of scattering is also prominent on other room acoustic parameters, which are based on the energy ratio between the early and the late part of the curve. Such parameters are clarity C_{80} , definition D_{50} , and center time TS (see App.A). We investigate the change in these three parameters and EDT , as a function of the scattering coefficient for two room cases: 1) Irregular room with uniform absorption. 2) Irregular room with highly non-uniform absorption. In both cases the scattering coefficient varies uniformly from 0 to 1, by a step of 0.1.

5.6.1 Irregular room with uniform absorption

For this case the absorption coefficient is everywhere 0.4. The sampling frequency is 20 kHz for an impulse response duration of 50 ms. 22 iterations are used. Figure 5.25 illustrates the change in the predicted EDT , C_{80} , D_{50} and TS as a function of the scattering coefficient. One source and three receiver positions are used, according to Table 5.8. The room is subdivided into 276 elements. Notice that since the room is really small ($V = 0.452 \text{ m}^3$), the reverberation time for $\bar{\alpha} = 0.4$ is very low (by Sabine formula we get 53 ms). It would be meaningless to apply the clarity and definition indexes for the usual early time limit of 80 ms and 50 ms, respectively. Otherwise, we would obtain infinite value for C_{80} and $\gg 100\%$ for D_{50} . According to Sec. 2.5, the room has been made for 1/10 scale measurements. However, in this study we use it as a very small full scale room, since we investigate its behaviour and not the real values. For this reason the early time limits of C_{80} and D_{50} can be scaled by 1/10, in order to obtain the same information as if we had applied the

	x (m)	y (m)	z (m)
Q	0.3	0.2	0.2
P_1	0.4	0.7	0.5
P_2	0.6	0.4	0.3
P_3	0.1	0.3	0.2

Table 5.8: Source-receiver positions for the investigation of room acoustic parameters in the irregular room.

scaling to the room itself.

As expected from the study so far, the level of scattering on the room surfaces affects the early part of the response, changing the value of the room acoustic parameters. Among the four parameters, the EDT shows the largest variation as a function of scattering. This variation can be seen by comparing Fig. 5.2, 5.3 and 5.4. The elements are considered as different receivers. For low degree of scattering in the room, the energy decays slowly between 0 and -10 dB. This results to a longer EDT . As the degree of scattering is increased, the values for P_2 and P_3 decrease with a progressively shallower slope. As for the first receiver, the EDT exhibits a dip around $s = 0.3$, increasing afterwards. It seems that the position of P_1 is responsible for such a non-monotonous behavior, because of different distribution of some late-early reflections.

Similar behavior is observed for the other parameters. Clarity and definition increase monotonically with increased scattering for both P_2 and P_3 . This increase can be explained both by the change in the slope of the decay curve and by concentration of energy in the early part of the response. For very low scattering values, the specular reflections are dominant and the minor portion of energy that is diffusely reflected is not enough to cause an exponential decay in the response. Thus, the energy decays much slower, for low scattering values, leading to a higher denominator in the expressions of C_{80} , D_{50} (see App.A). However, in consistency to the discussion in Sections 5.1 and 5.2, when the average scattering coefficient is more than around 0.2, the energy decay is close to the one predicted by AR and the change in the parameters is less abrupt. Of course, even if the global energy decay is approximately constant for different scattering coefficients larger than 0.2, the individual responses are different. For this reason, C_{80} and D_{50} continue to increase slightly up to $s = 0.6$ for P_2 and P_3 . After this value the parameters remain practically unchanged. The same occurs for TS , in the reverse direction. However, $s = 0.3$ is enough to fix TS to the final value. Similar to the case of EDT , the parameters do not behave monotonous for P_1 . Again, its position should be the reason for that. As the scattering coefficient increases, the slope of the energy decay decreases and the concentration of energy becomes higher at the early part (before 8 ms for C_{80} and 5 ms for D_{50}). This results to an increase of the parameters. But while the scattering coefficient increases further, more energy is concentrated at the late part (after 8 ms for C_{80} and 5 ms for D_{50}). This energy must have been radiated by distant elements or distant image sources. Similar arguments hold for TS at P_1 .

5.6.2 Irregular room with non-uniform absorption

Now the absorption in the irregular room is non-uniform, given in Table 5.9. All other simulation parameters are the same with Sec. 5.6.1. The predicted values of EDT , C_{80} , D_{50} and TS are presented in Figure 5.26. In general, the shape of the curves is similar to those in Sec. 5.6.1. Again EDT shows the largest variation. As

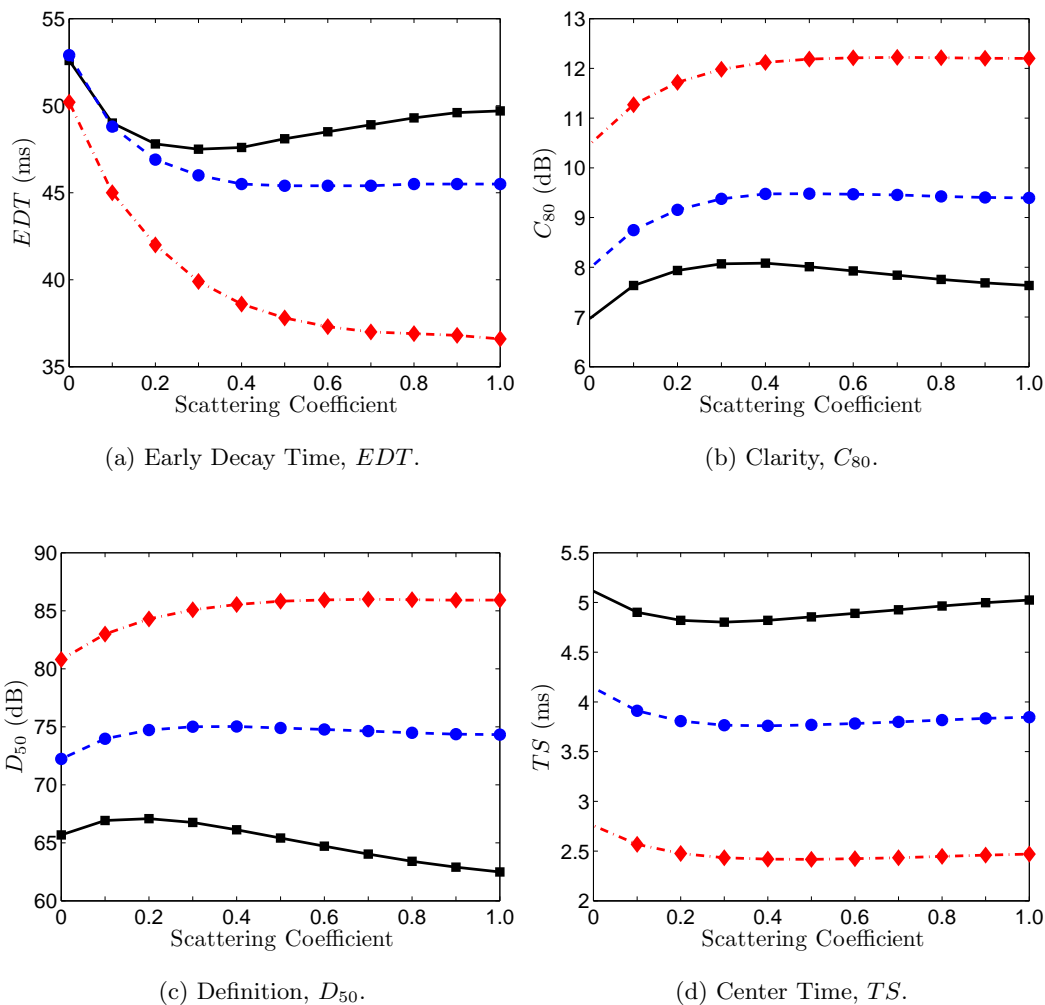


Figure 5.25: Room acoustic parameters at three receiver positions as a function of the scattering coefficient in the irregular room. Uniform absorption coefficient 0.4. \blacksquare : P_1 . $\text{---}\bullet\text{---}$: P_2 . $\text{---}\blacklozenge\text{---}$: P_3 . For clarity and definition a scaling of 1/10 was used for the early time limit, resulting to 8 ms and 5 ms respectively.

before, the curves for the first receiver are not monotonous and its position should be a reason for that.

5.7 Investigation of the Full Algorithm

So far, theoretical predictions were performed with the main algorithm of figure 4.16. In the next examples, the modifications corresponding to the full algorithm (Sec. 4.2.5) are included. Initially, simulations are run for 2, 3, 4 and 5 orders of image elements. The irregular room is used with the simulation parameters of Sec. 5.1 and coefficients for the second case of Tab. 5.1. Following the discussion in Sec. 4.2.5.1, a very low sampling frequency of 2 kHz is used for the $B_m[i, j, 1 : T]$ calculation. The concepts of Sec. 4.2.7 are applied to halve the computational cost. The execution time for the calculation of $B_m[i, j, 1 : T]$ and $E_m[j, 1 : T]$ for 2 orders is 1 min. For 3 orders it is 2 min, for 4 orders 6.5 min, while for 5 orders it is 9 min. The time required for the full algorithm to run was about 15 min. This is quite

Walls	1	2	3	4	5	6	7
S_w (m^2)	0.54	0.41	0.49	0.65	0.34	0.54	0.65
α	0.1	0.7	0.1	0.0	0.3	0.6	0.4

Table 5.9: Absorption coefficients for the investigation of room acoustic parameters in the irregular room. The area of each wall is also given.

large, compared with the execution time of the main algorithm (Sec. 5.5).

As an example, the decay curves obtained with 2 and 4 orders for the image elements are illustrated in Figures 5.27 and 5.28. The average energy decay (red line) is the same with Fig. 5.3, but even if the coefficients are the same, the individual energy decays are slightly different, because now the energy is differently distributed by the image elements. However the differences seem to be really small. Even between the different orders of image elements that were used (Fig. 5.27 and 5.28), is hard to identify the deviations by visual inspection. This is the case also when comparing the corresponding reflectograms at the receiver (Fig. 5.29 and 5.30).

Now, we will try to quantify these small deviations by comparing the decay curves obtained with the main algorithm (Fig. 5.3) with the results from the full algorithm with different orders of image elements. For that purpose, the *mean absolute percentage error* (*MAPE*) and its standard deviation are calculated for the decay curves of all elements N , at every time step. That is, if the decay curve of each element is EDT_i (see App. A), the mean absolute percentage error between the main and the full algorithm is obtained by:

$$MAPE(\%) = \frac{1}{N} \sum_{i=1}^N \left| \frac{(EDT_i)_{main} - (EDT_i)_{full}}{(EDT_i)_{full}} \right| \cdot 100 \quad (5.4)$$

Figures 5.31 to 5.34 show the results for the different orders. The *MAPEs* of Fig. 5.31 to 5.34 are summarized in Figure 5.35. Another picture of the deviation between the algorithms is obtained by calculating the *mean square percentage error*:

$$MSPE(\%) = \frac{1}{N} \sum_{i=1}^N \left[\frac{(EDT_i)_{main} - (EDT_i)_{full}}{(EDT_i)_{full}} \right]^2 \cdot 100 \quad (5.5)$$

The summarized result for all the used orders is illustrated in Figure 5.36. In both cases, the behavior is similar. There is a peak at the early part of the response around 5.5 ms and then the error becomes progressively smaller at the late part. Moreover, all curves coincide at this peak, revealing that the error in the very early part of the response depends on at least 2 orders of image elements. It is interesting to see that after the peak, the simulation with 2 orders produces more error than the simulation with more orders. It seems that when quite few orders of image elements are used, the specular nature of the full algorithm is more prominent and the deviation with the main algorithm is higher, because the latter uses only the diffuse interaction between the real elements. Increasing the orders of image elements the error curve converges to a final lower value. This is quite important, because the full algorithm tends to behave in a diffuse way when a large number of image elements are used, which are distributed unevenly around the room. Of course, the shape of the irregular room encourages such an “uneven” behavior, that leads to high diffusion. It is likely that results from regularly shaped rooms could lead to different conclusions.

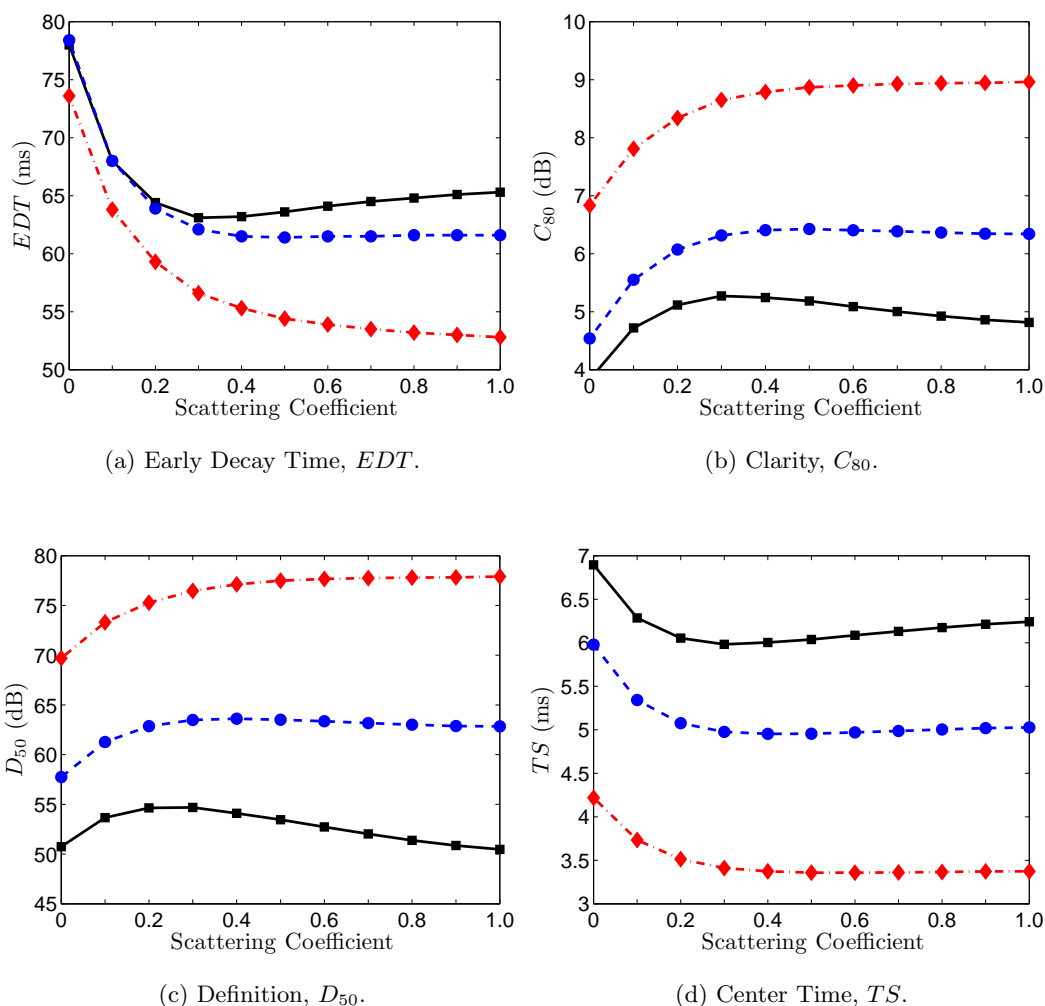


Figure 5.26: Room acoustic parameters at three receiver positions as a function of the scattering coefficient in the irregular room. Absorption coefficients are taken from Tab. 5.9. \blacksquare : P_1 . \bullet : P_2 . \blacklozenge : P_3 . For clarity and definition a scaling of 1/10 was used for the early time limit, resulting to 8 ms and 5 ms respectively.

The simulations are run once more for a longer impulse response length of 50 ms, with a lower sampling frequency of 1 kHz for the image elements. Now the orders are increased by one. Both the $MAPE$ and the $MSPE$ are computed for 3, 4, 5 and 6 orders of image elements. The results are illustrated in Figures 5.37 and 5.38. Again, the behavior is similar among the curves of different orders. In addition, the error is stabilized for the higher orders at the very late part of the response.

In any case, the error between the results of the main algorithm and the full one is very small. At this point we have some facts that justify the approach by Lewers [36], who did not account for further specular reflections in the **AR** part. The perfectly diffuse nature of **AR** seems powerful enough to blur any specular reflection of the diffusely reflected energy. Thus, it seems that there is no need to include the coupling discussed in Sec. 4.1.3, because whatever the course of the energy, it will remain more or less diffuse.

On the other hand, the ray tracing based algorithm by Dalenbäck [6], could not represent the diffuse reflections sufficiently if no secondary sources and further

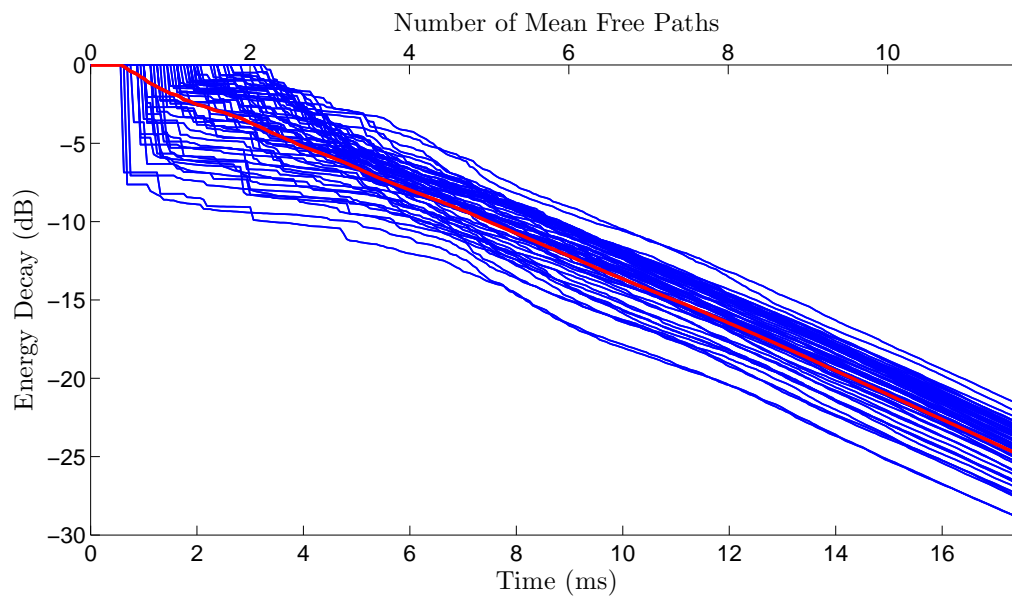


Figure 5.27: Decay curves for 55 uniformly chosen elements on the boundary, obtained by the full **CARISM** algorithm in the irregular room. Coefficients from Tab. 5.1, for case 2. **—**: Curves for each element. **—**: Curve for averaged energy over all 276 elements. Two orders of reflections were used for the image elements.

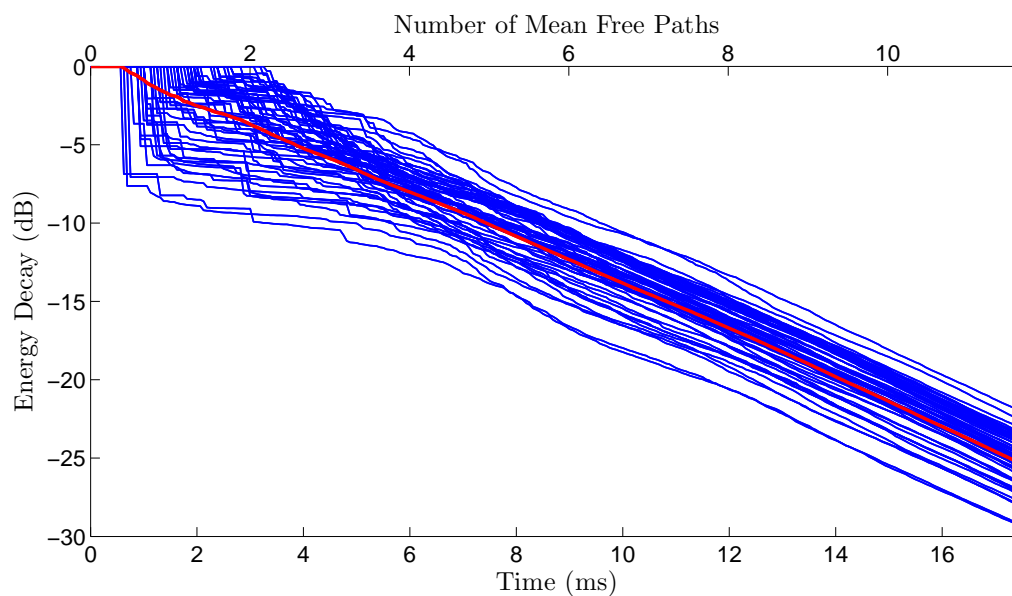


Figure 5.28: Decay curves for 55 uniformly chosen elements on the boundary, obtained by the full **CARISM** algorithm in the irregular room. Coefficients from Tab. 5.1, for case 2. **—**: Curves for each element. **—**: Curve for averaged energy over all 252 elements. Four orders of reflections were used for the image elements.

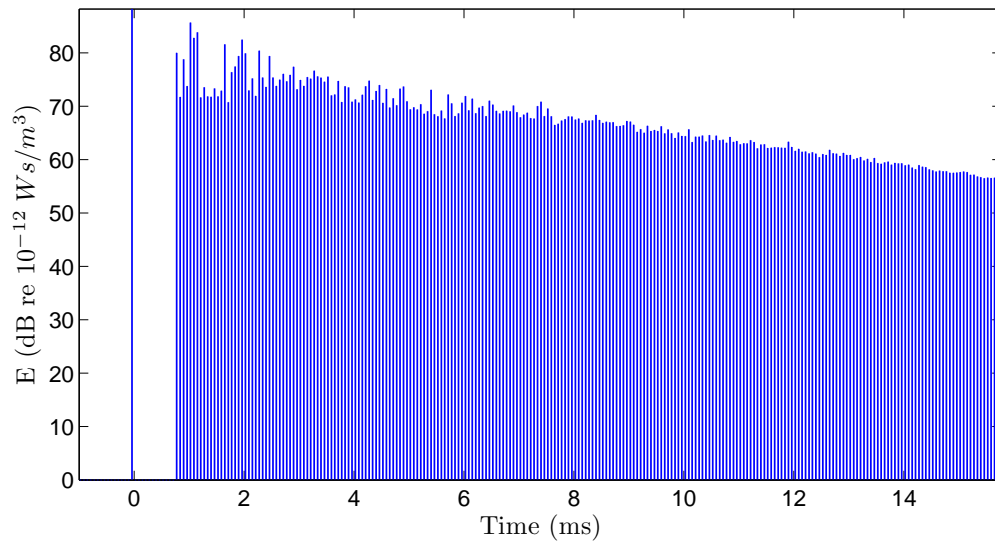


Figure 5.29: Reflectogram at the receiver position obtained by the full **CARISM** algorithm in the irregular room. Coefficients from Tab. 5.1, for case 2. Two orders of reflections were used for the image elements.

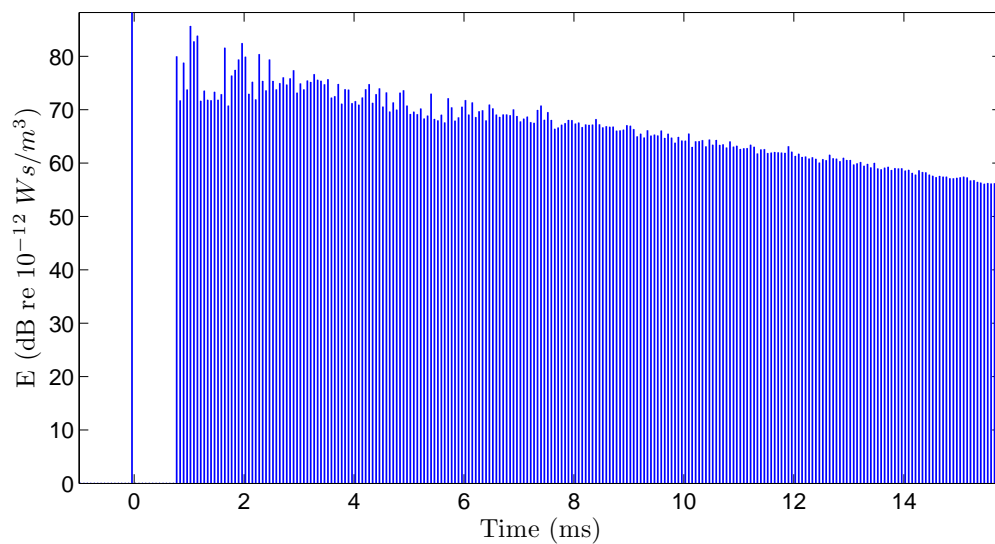


Figure 5.30: Reflectogram at the receiver position obtained by the full **CARISM** algorithm in the irregular room. Coefficients from Tab. 5.1, for case 2. Four orders of reflections were used for the image elements.

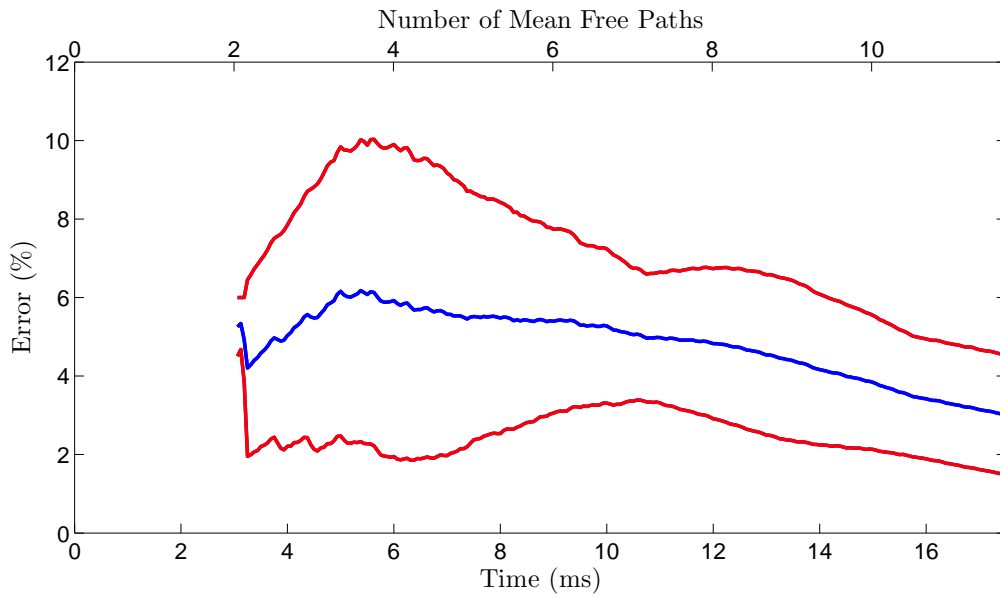


Figure 5.31: Mean absolute percentage error between the decay curves predicted by the main and the full **CARISM** algorithm in the irregular room. **—**: Mean value from all N decay curves. **—**: \pm standard deviation. Coefficients from Tab. 5.1, for case 2. Two orders of reflections were used for the image elements.

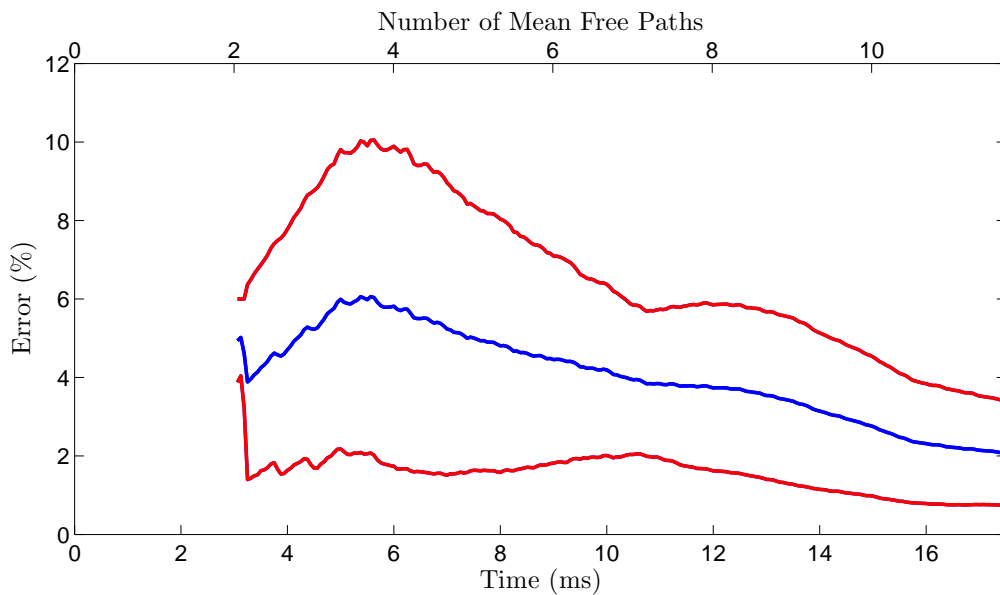


Figure 5.32: Mean absolute percentage error between the decay curves predicted by the main and the full **CARISM** algorithm in the irregular room. **—**: Mean value from all N decay curves. **—**: \pm standard deviation. Coefficients from Tab. 5.1, for case 2. Three orders of reflections were used for the image elements.

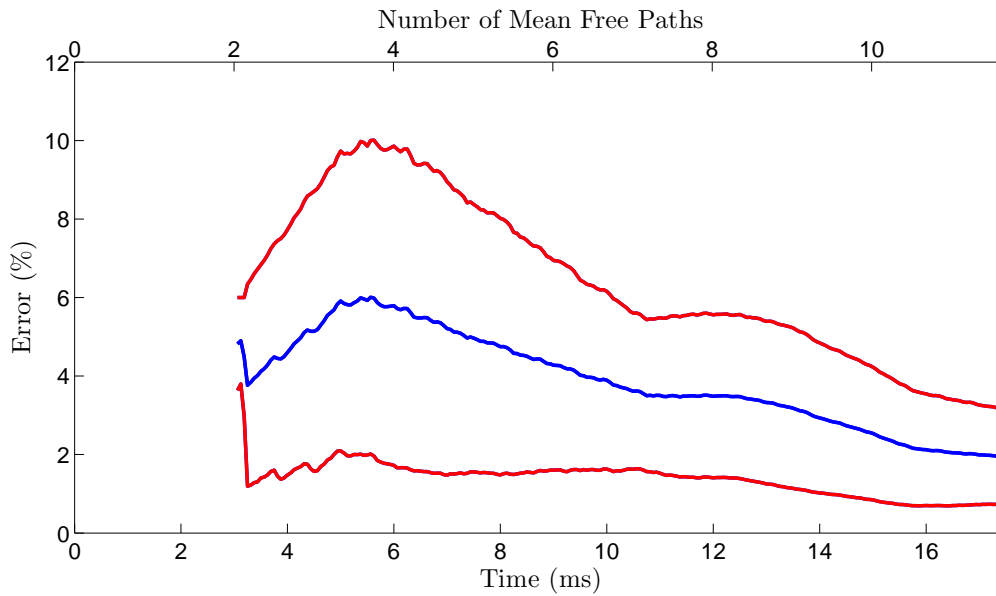


Figure 5.33: Mean absolute percentage error between the decay curves predicted by the main and the full **CARISM** algorithm in the irregular room. —: Mean value from all N decay curves. —: \pm standard deviation. Coefficients from Tab. 5.1, for case 2. Four orders of reflections were used for the image elements.

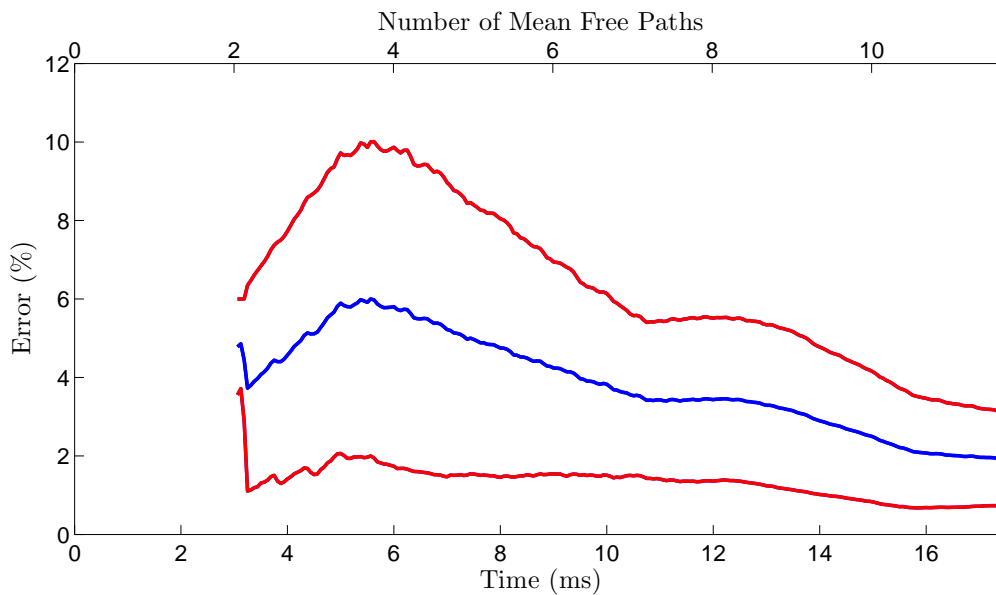


Figure 5.34: Mean absolute percentage error between the decay curves predicted by the main and the full **CARISM** algorithm in the irregular room. —: Mean value from all N decay curves. —: Standard deviation. Coefficients from Tab. 5.1, for case 2. Five orders of reflections were used for the image elements.

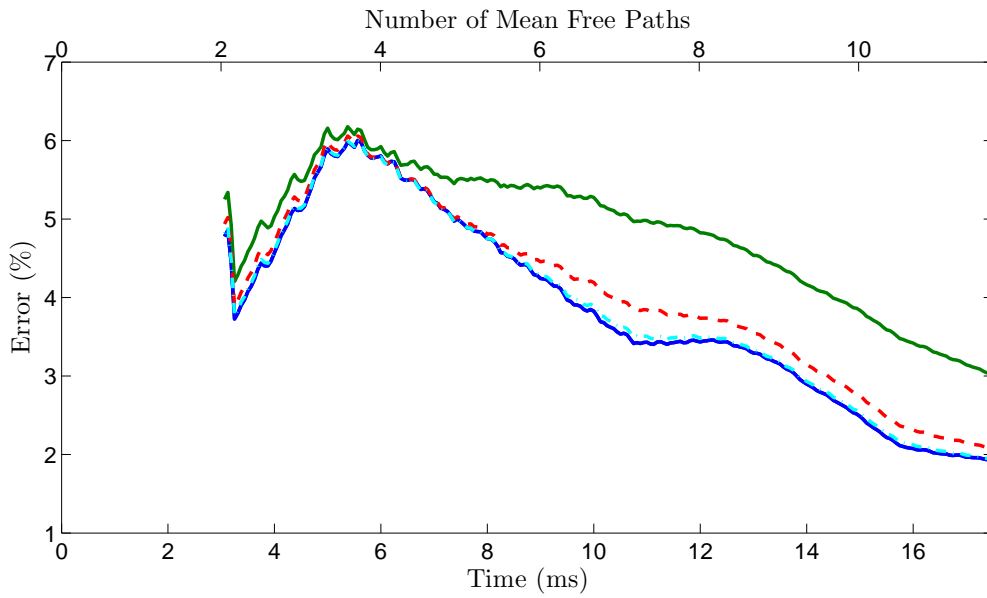


Figure 5.35: Mean absolute percentage error between the decay curves predicted by the main and the full **CARISM** algorithm in the irregular room. Coefficients from Tab. 5.1, for case 2. —: 2 orders of image elements. - - -: 3 orders of image elements. - · - · -: 4 orders of image elements. —: 5 orders of image elements.

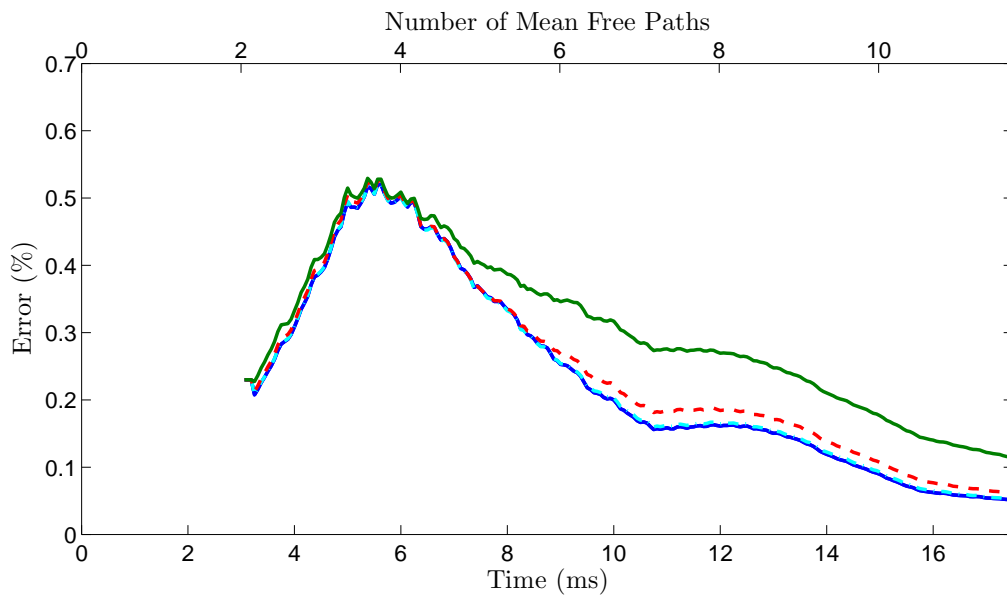


Figure 5.36: Mean square percentage error between the decay curves predicted by the main and the full **CARISM** algorithm in the irregular room. Coefficients from Tab. 5.1, for case 2. —: 2 orders of image elements. - - -: 3 orders of image elements. - · - · -: 4 orders of image elements. —: 5 orders of image elements.

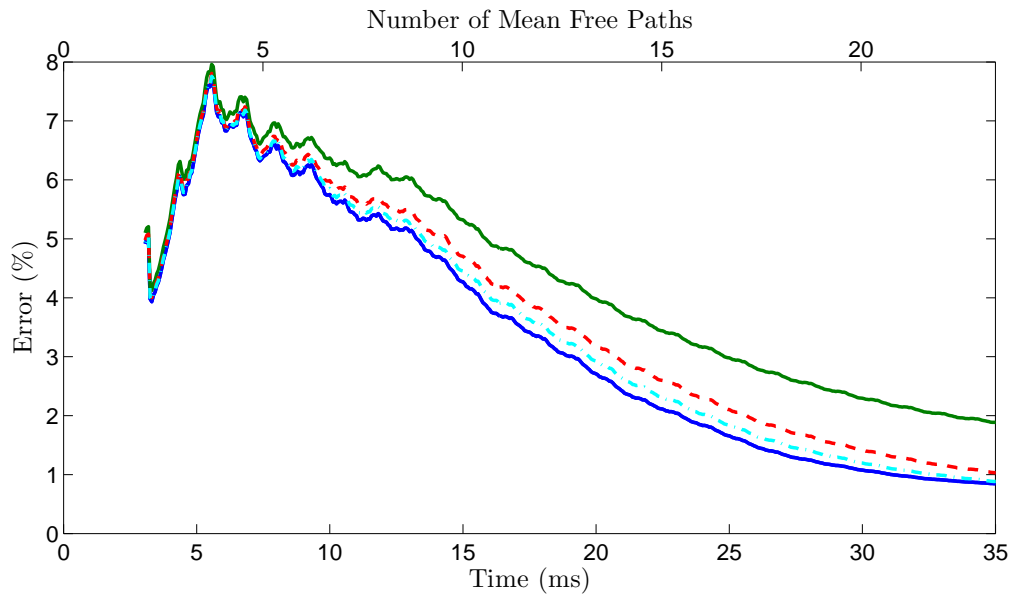


Figure 5.37: Mean absolute percentage error between the decay curves predicted by the main and the full **CARISM** algorithm in the irregular room. Coefficients from Tab. 5.1, for case 2. Now the length of the impulse response is 50 ms. —: 3 orders of image elements. - - -: 4 orders of image elements. - · - · -: 5 orders of image elements. —: 6 orders of image elements.

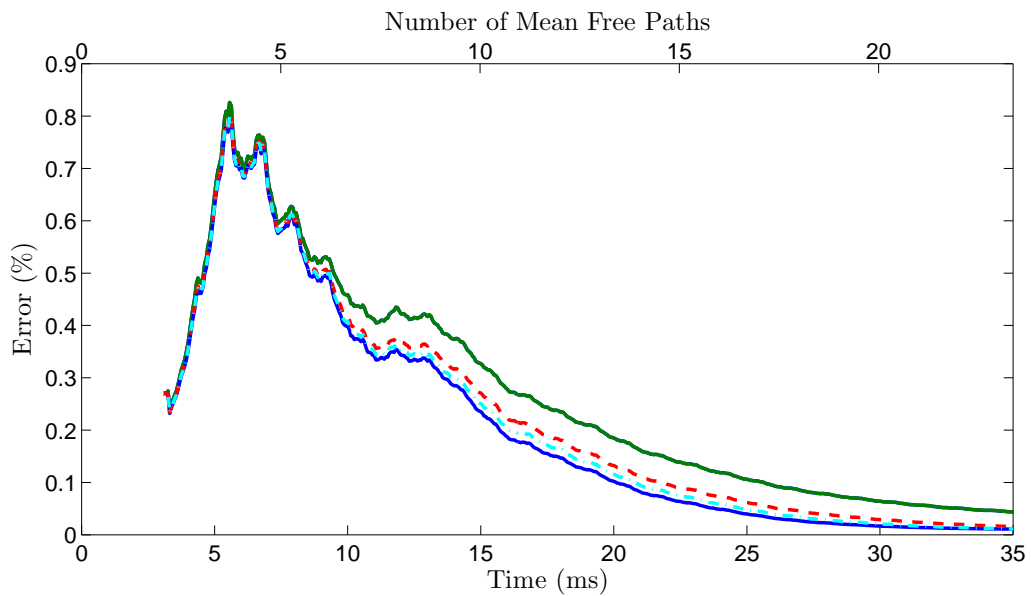


Figure 5.38: Mean square percentage error between the decay curves predicted by the main and the full **CARISM** algorithm in the irregular room. Coefficients from Tab. 5.1, for case 2. Now the length of the impulse response is 50 ms. —: 3 orders of image elements. - - -: 4 orders of image elements. - · - · -: 5 orders of image elements. —: 6 orders of image elements.

specular reflections were taken into account, as discussed in Sec. 4.1.3. This is the reason why his approach seems quite reasonable for the model he uses, which is fundamentally different to AR.

These claims seem very important, since the computational effort for the full algorithm is really high: 3 to 4 times higher than that of the main algorithm, plus the time for the calculation of image elements. In consistency with this discussion, the validations in Chapter 6 are performed only with the main algorithm.

Chapter 6

Experimental Validation

The theoretical predictions by the algorithm described in Section 4.2 are validated with experimental data. In the first stage a reverberation room for scale measurements is used as a very small full-scale one. In the second stage, the PTB Round Robin III geometry is used¹ [21, 22], for which there is available public measurement data, in addition to results by commercial room acoustic software.

6.1 Time Resolution

Clearly the discretization of time discussed in Sec.4.2.2 affects the quality of simulations. In Sec. 2.5 an example has been given for pure AR. Similar influence of time resolution is expected for the CARISM. As Nosal states for AR [47], the sampling frequency of the impulse response has nothing to do with the frequency of the signal, since phase information is not included. It is only used to define in which time interval the energy contributions are summed up. However we still need a rule to find the appropriate sampling frequency for our algorithm implementation, such as the Nyquist theorem, that holds for phase-supporting signals.

Following Nosal [47], the *Courant number* criterion is applied for all validations. The Courant number is expressed as $cdt/\Delta x_{min}$, where Δx_{min} is the minimum distance between the elements. The criterion states that this number should be less than one, so that the distance traveled at every time step is not more than the (minimum) distance between the elements.

6.2 Irregular Room Measurements

The room introduced in Section 2.5 is used for the experimental validation of the proposed algorithm. A circular scattering surface of diameter 35.4 cm is placed in the bottom of the room. Since the surface does not occupy the whole bottom area but only a part of it, a new wall has to be considered in the virtual model of the room, as illustrated in Figure 6.1. Table 6.1 presents the areas of the 8 walls. The first wall represents the bottom and the second one represents the scattering surface. The original walls of the room are made of acrylic glass and can be assumed to be specularly reflective.

Three types of scattering surfaces are used: a sinusoid, a wave and a hexagonal one (Fig. 6.2). The surfaces are made for 1/10 scale measurements. In this study they are treated as full scale ones, since the room itself is treated as a full scale too.

¹<http://www.ptb.de/en/org/1/16/163/roundrobin/roundrob3.1.htm>

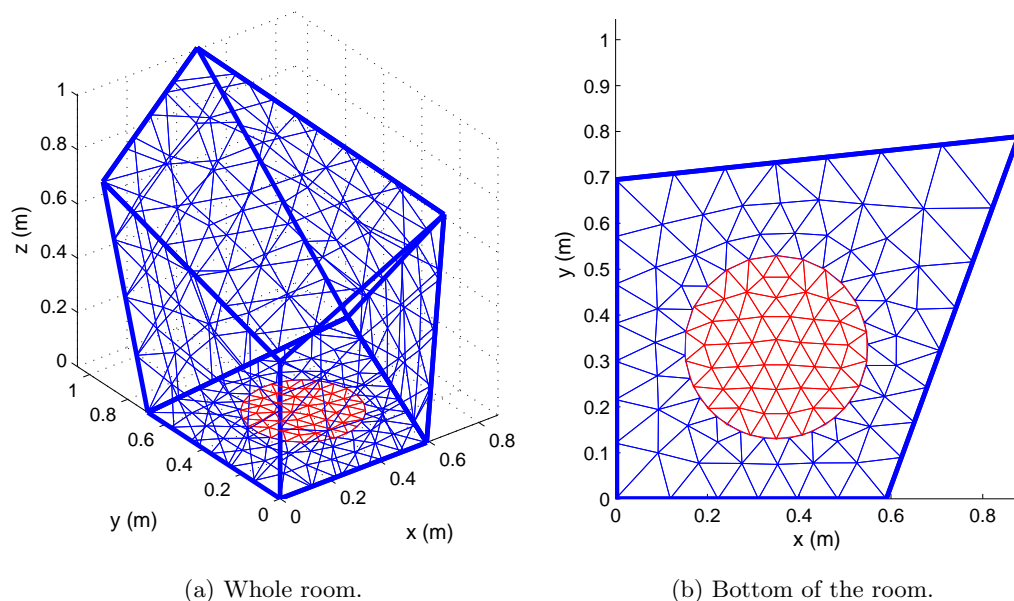
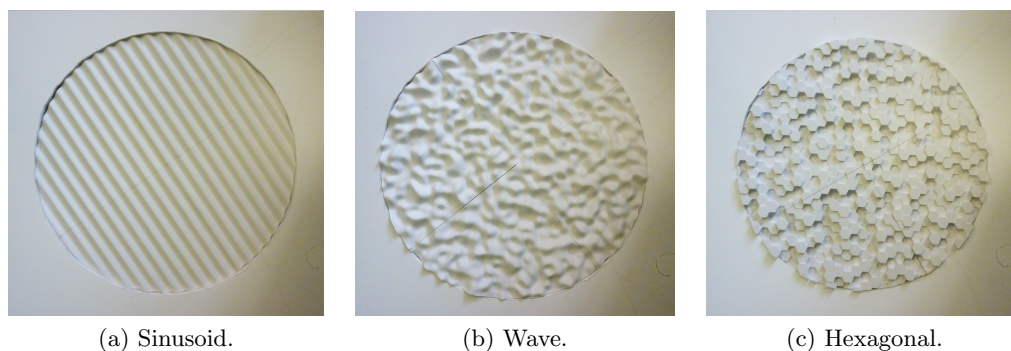


Figure 6.1: The meshed irregular room with the scattering surface (—) placed on the bottom.



(a) Sinusoid. (b) Wave. (c) Hexagonal.

Figure 6.2: The three scattering surfaces used in the irregular room.

Their average thickness is about 10 mm. Placing them directly at the acrylic bottom of the room would lead to diffraction by-products around their free edge. For that reason, the bottom of the room was treated by adding a paper-faced foam board of 10 mm thickness. A disc with the same diameter as the scattering surfaces was removed, so that the surfaces could be placed in face with the rest of the bottom board. Two of the walls were covered with a porous absorber of 2.2 cm approximate thickness.

A spark source was used for producing impulses and a free field 1/2-inch B&K microphone was used as the receiver. The microphone recorded the pressure impulse response, that is, a response including phase information, in contrast to the results

Walls	1	2	3	4	5	6	7	8
S_w (m ²)	0.42	0.09	0.40	0.49	0.57	0.34	0.52	0.56

Table 6.1: Wall areas for the simulated irregular room of fig. 6.1.

	x (m)	y (m)	z (m)
Q_1	0.180	0.148	0.075
Q_2	0.205	0.180	0.213
Q_3	0.475	0.200	0.213
P_1	0.295	0.585	0.310
P_2	0.320	0.550	0.315

Table 6.2: Source-receiver positions at the irregular room.

produced by the **CARISM**. All impulse response measurements were performed with the aid of DIRAC software, developed by *Acoustics Engineering* company². For every position, five impulse responses were averaged in order to improve the signal to noise ratio. The various positions of the source and the receiver are presented in Table 6.2. Three combinations were treated: Q_1 - P_1 , Q_2 - P_2 and Q_3 - P_2 . For the position Q_1 the source was placed through a hole on the foam board, in order to eliminate unwanted reflections. A picture of the setup is presented in Figure 6.3. The room has a Schroeder's frequency limit of 3070 Hz. The measurements are taken at three octave bands above this limit: 4 kHz, 8 kHz and 16 kHz. A sampling frequency of 96 kHz was used.

Obviously, the empty room is not perfectly reverberant, with its walls being not fully reflective. Thus, the empty room has an equivalent absorption area different from zero and it is crucial that we know the corresponding average absorption coefficient which should be attached afterwards to the original walls during the simulation, even if it is rather small. The equivalent absorption area of the empty room was estimated by measuring the reverberation time and using Sabine's formula, $A = 0.16V/T$, with $V = 0.452 \text{ m}^3$. Afterwards, the averaged absorption coefficient for the walls was derived by division with the total inside surface, $S_t = 3.64 \text{ m}^2$.

The random incidence statistical absorption coefficients of the paper-faced foam board and the porous absorber were measured by the reverberation chamber method in the empty irregular room. The reverberation time of the empty room, T_{em} , was measured first. Afterwards, the reverberation time with a specimen of the material inside, T_{sp} , was measured. If S_{sp} is the area of a specimen and V the volume of the room, the absorption coefficient can be calculated by Sabine's formula [2]:

$$\alpha = \frac{0.161V}{S_{sp}} \left(\frac{1}{T_{sp}} - \frac{1}{T_{em}} \right) \quad (6.1)$$

Absorption and scattering data for the wave and hexagonal scattering surfaces were taken directly from the work by Olesen [48], who used the same surfaces. As for the sinusoidal surface, the absorption coefficient was measured with the reverberation chamber method, while the scattering coefficient was taken from the theoretical study by Embrechts *et al.* [41]. The absorption data for all materials used at the frequencies of consideration, are presented in Table 6.3. The scattering coefficients for the three surfaces are given in Table 6.4. Apparently, the volume of the room after installing the new bottom and the porous absorbers was decreased, becoming $V = 0.423 \text{ m}^3$. Apart from the scattering surface, it would be quite unreasonable to assume perfectly specular reflecting walls. An arbitrary low value of 0.02 was assumed for the scattering coefficient for all walls in the room.

The temperature in the room was 20 °C, the relative humidity was 55 % and static air pressure was 101.325 kPa. For these parameters, the air absorption coef-

²<http://www.acoustics-engineering.com>

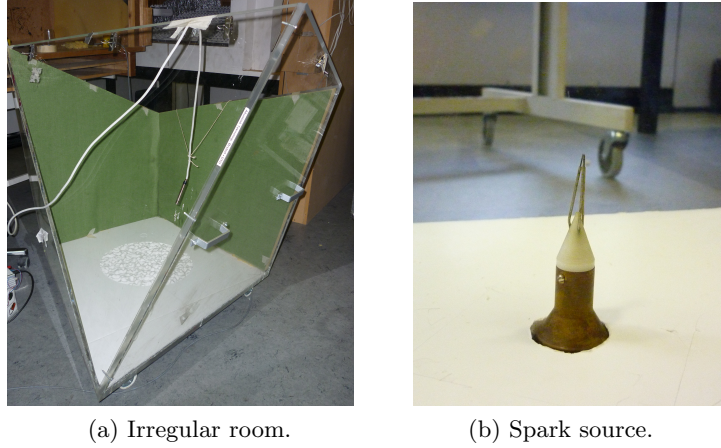


Figure 6.3: The irregular room with the paper-faced foam bottom and the porous material on two of its walls. The wave-type scattering surface is placed in the circular opening of the bottom. For one of its positions, the spark source was placed through a hole on the foam board in order to eliminate unwanted reflections.

material	4 kHz	8 kHz	16 kHz
original walls	0.02	0.03	0.04
paper-faced foam board	0.30	0.35	0.38
porous absorber	0.85	0.91	0.93
sinusoid surface	0.18	0.25	0.20
wave surface	0.25	0.60	0.85
hexagon surface	0.30	0.45	0.50
α_{air} (dB/1 Km)	27.410	96.320	339.95
α_m (10^{-3} m^{-1})	6.311	22.179	78.276

Table 6.3: Absorption coefficients for the materials used in the irregular room measurements.

ficient, α_{air} , was calculated using the formulas from [49]. Then, the air absorption exponent was obtained by [28]:

$$\alpha_m = \frac{\alpha_{air}}{10 \log_{10}(e)} \quad (6.2)$$

material	4 kHz	8 kHz	16 kHz
sinusoid surface	0.04	0.15	0.43
wave surface	0.06	0.49	0.81
hexagon surface	0.29	1.00	0.89

Table 6.4: Scattering coefficients for the surfaces used in the irregular room measurements.

6.2.1 Results

Simulations were run with the main algorithm of the **CARISM** for direct comparison of the impulse responses with the measured ones and for comparison of five room acoustic parameters, T_{30} , EDT , C_{80} , D_{50} and TS .

For the simulations, the room was subdivided into 240 elements. A high sampling frequency of 96 kHz was used for the early impulse responses, in order to match with the experimental data. For the derivation of the room acoustic parameters, a lower sampling frequency of 20 kHz was used, for an impulse response length of 40 ms. Approximately 30 iterations were used in both simulations.

The energy impulse responses from the simulations is compared to the squared pressure impulse responses from the measurements. Figures 6.4 to 6.11 show the early part of the response for the source-receiver combination Q_1-P_1 , at 8 kHz, as well as the energy decay down to -35 dB. Each pair of impulse response and decay curve corresponds to a different scattering surface. The last pair corresponds to purely specular walls. For the last case, a flat surface made from the same material as the sinusoidal one was placed in the circular opening on the bottom – instead of a scattering surface.

Regarding the squared impulse responses, it can be seen that most of the first reflections are quite well predicted by the **CARISM**. Some disagreement exist in their amplitudes, probably due to errors in the adopted absorption coefficients. Evidently, these first reflections are represented by the **ISM**, which is highly involved in the early part of the simulation. However, after the first milliseconds it is hard to find coincidence between the predicted and the measured bins, even if the overall graphs look quite similar. It is important to notice that inevitably we have to compare two elementary different responses. The measured graph is the square of the pressure impulse response, which initially includes phase information. On the other hand, the simulated graph is the energy impulse response, derived without any phase information taken into account. Although the very first reflections can be predicted, the stochastic nature of the late ones prevent them to be correctly simulated. Some errors in the geometry and possible unwanted reflections due to the microphone and the source should also be taken into account for the disagreement.

The results state another important thing, regarding the setup of the experiment. According to Tab. 6.1, the area of the scattering surface is very small to produce clear differences among the different types. The average scattering coefficient in the room was $\bar{s} = 0.023$ when the sinusoidal surface was used, $\bar{s} = 0.031$ for the wave and $\bar{s} = 0.045$ for the hexagonal (the scattering coefficient 0.02 for the walls was also included here). For the case of specular reflections (Fig. 6.10 and 6.11), only the adopted scattering of the walls was used, so that $\bar{s}=0.02$. With these average scattering coefficients it is very difficult to see prominent differences in the the results of the four cases. However, the bins are differently spaced, when the surface is changed. Moreover, the response of Fig. 6.10 seems to be less blurred than the others, revealing the absence of scattering surface inside the room. At this point it should be stressed that the Lambert's scattering law adopted in the **CARISM** is just an empirical approximate model for describing the diffuse reflections. Hence, the complicated reflection phenomena occurring on a scattering surface cannot be properly described in the algorithm. Obviously, the combined nature of the **CARISM** is not visible in these figures, since the specular reflections are dominant and the diffuse model does not play a major role.

According to Figures 6.5, 6.7, 6.8 and 6.11, the energy decay is well predicted by the **CARISM**, for the four cases.

It should be emphasized that the impulse responses of Figures 6.4, 6.6, 6.8 and 6.10 were simulated with a high sampling frequency of 96 kHz, while the decay curves were calculated with a lower sampling frequency and for a longer duration of 40 ms (the curves are plotted for the first 35 ms). Figure 6.12 shows an example of the impulse response which was used for the derivation of the decay curve in Fig. 6.7.

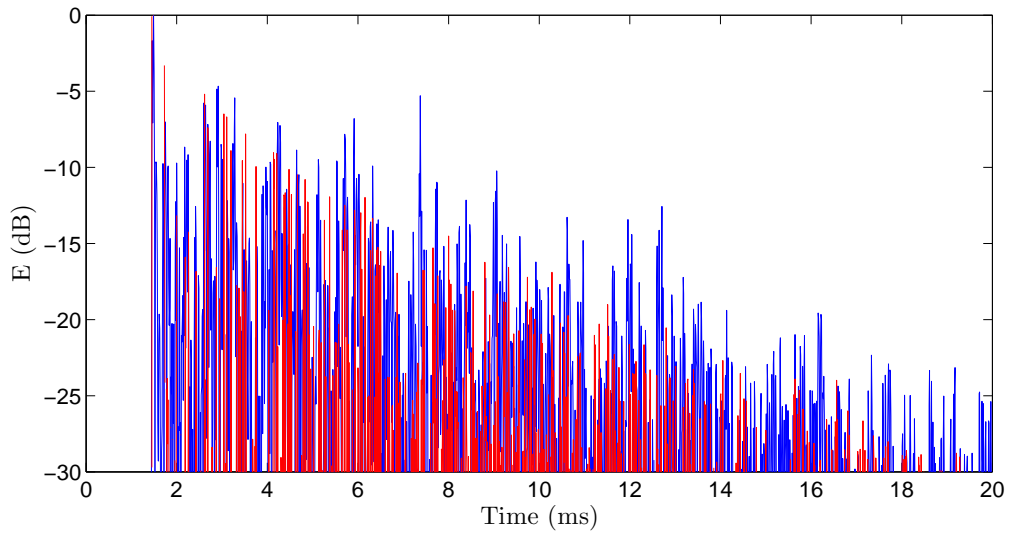


Figure 6.4: Squared impulse response for the combination Q_1 - P_1 with the sinusoidal scattering surface at 8 kHz. —: Measurement. —: Simulation.

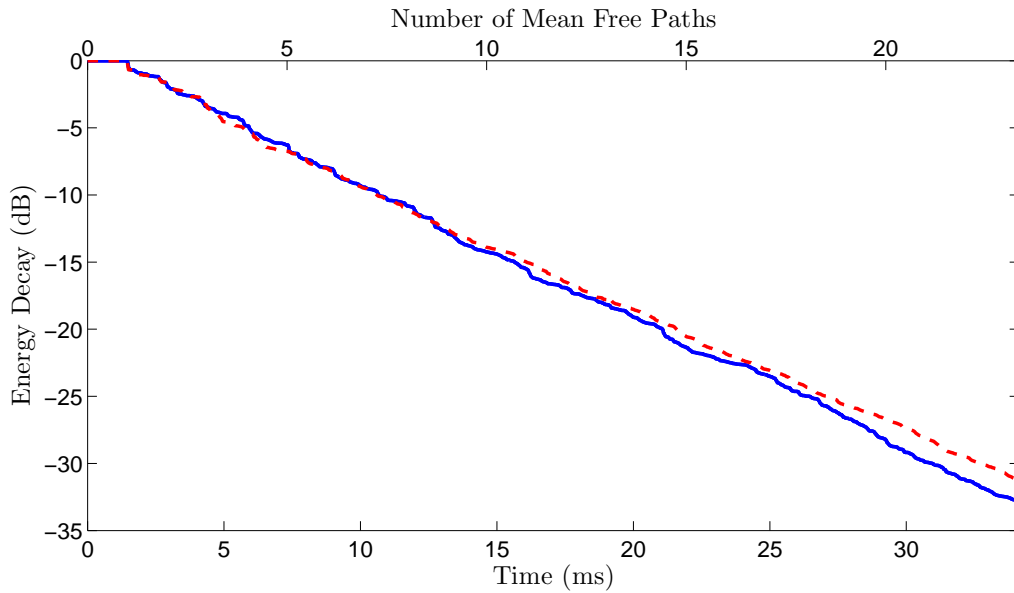


Figure 6.5: Energy decay for the combination Q_1 - P_1 with the sinusoidal scattering surface at 8 kHz. —: Measurement. - - -: Simulation.

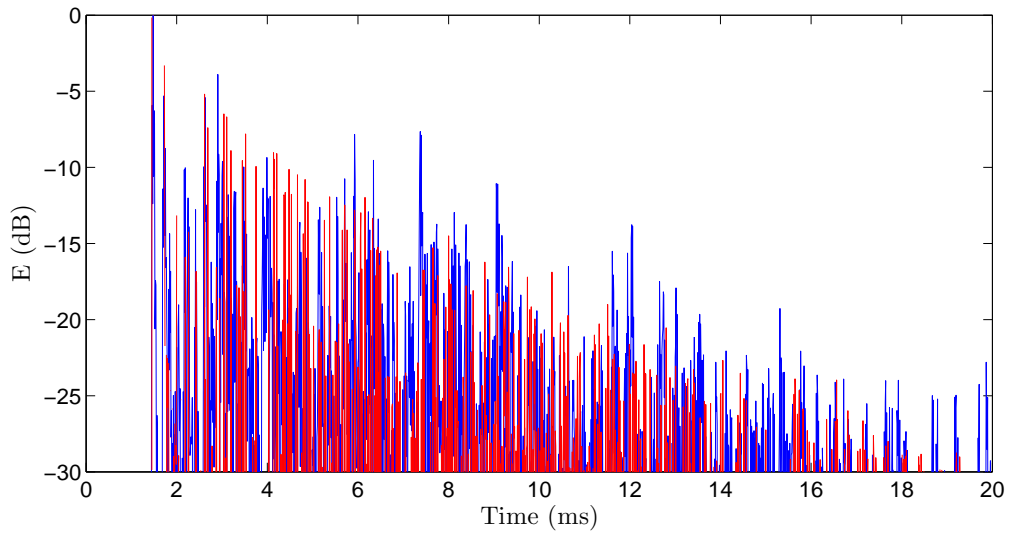


Figure 6.6: Squared impulse response for the combination Q_1-P_1 with the wave scattering surface at 8 kHz. —: Measurement. —: Simulation.

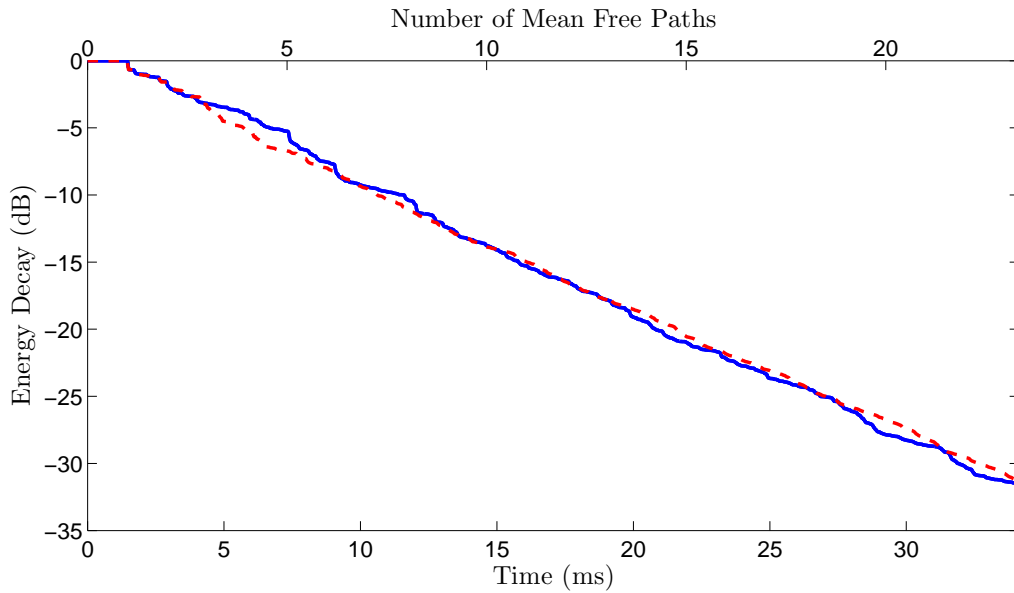


Figure 6.7: Energy decay for the combination Q_1-P_1 with the wave scattering surface at 8 kHz. —: Measurement. - - -: Simulation.

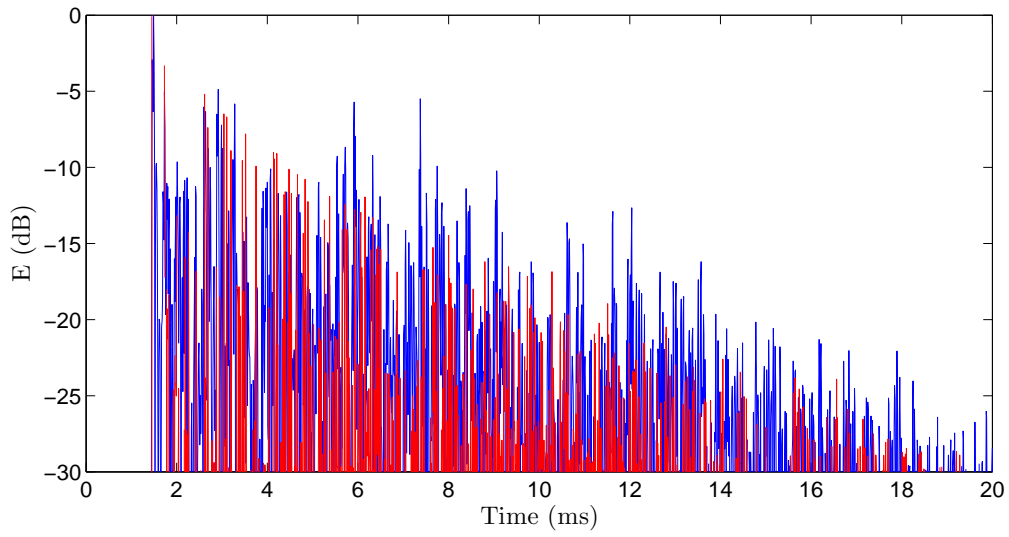


Figure 6.8: Squared impulse response for the combination Q_1 - P_1 with the hexagonal scattering surface at 8 kHz. —: Measurement. —: Simulation.

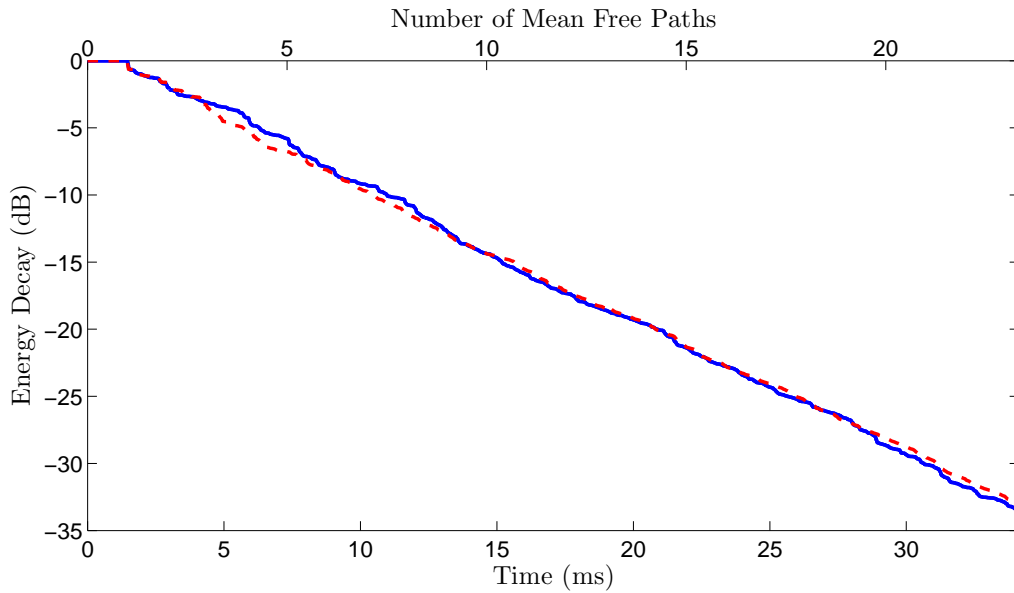


Figure 6.9: Energy decay for the combination Q_1 - P_1 with the hexagonal scattering surface at 8 kHz. —: Measurement. - - -: Simulation.

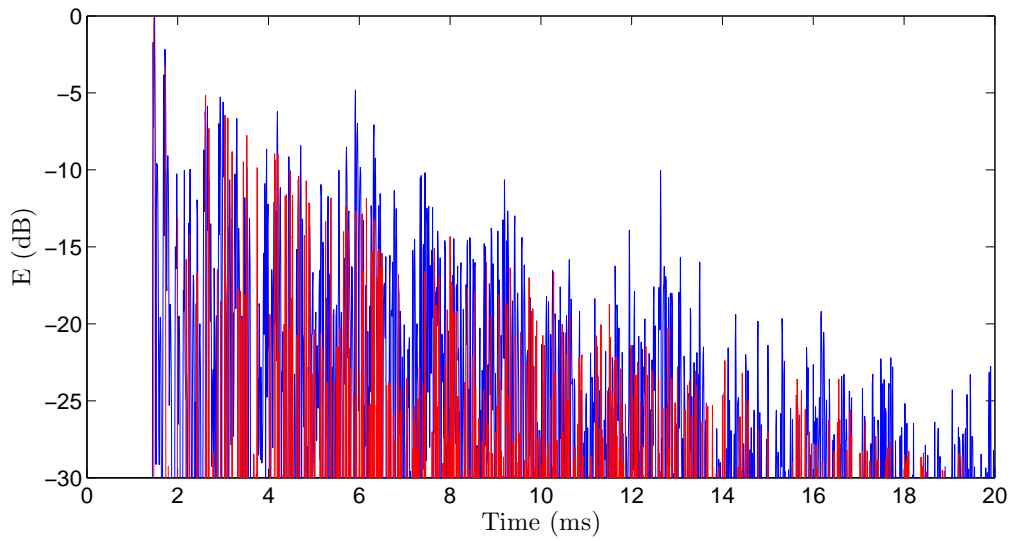


Figure 6.10: Squared impulse response for the combination Q_1 - P_1 without scattering surfaces at 8 kHz. —: Measurement. —: Simulation.

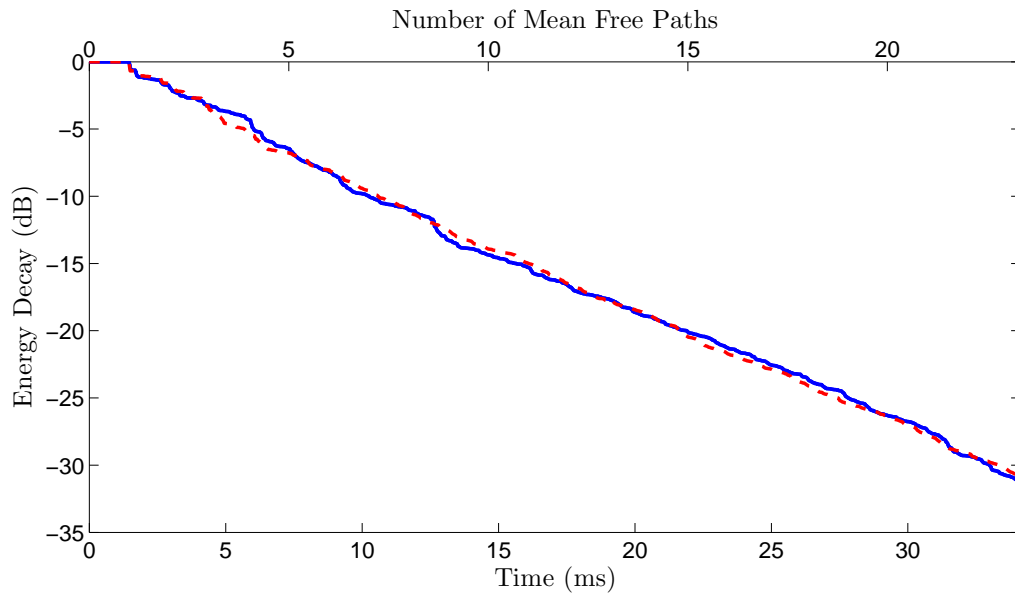


Figure 6.11: Energy decay for the combination Q_1 - P_1 without scattering surfaces at 8 kHz. —: Measurement. - - -: Simulation.

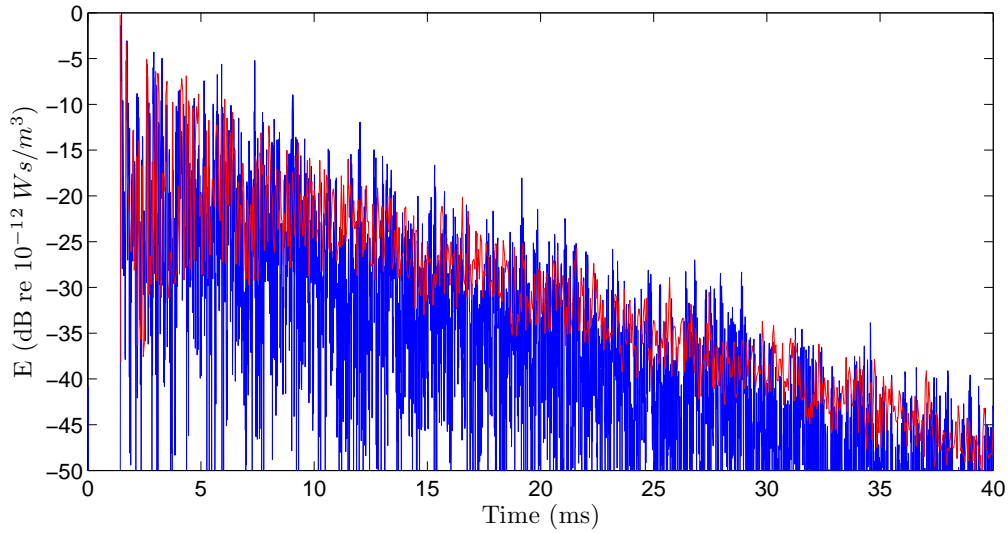


Figure 6.12: Squared impulse response for the combination Q_1-P_1 with the wave scattering surface at 8 kHz. Sampling frequency of 20 kHz. —: Measurement. —: Simulation.

$Q-P$	Sinusoid			Wave			Hexagon		
	4 kHz	8 kHz	16 kHz	4 kHz	8 kHz	16 kHz	4 kHz	8 kHz	16 kHz
Q_1-P_1 (M)	60.6	61.4	62.7	63.0	63.8	64.0	59.4	59.8	59.0
Q_1-P_1 (S)	66.5	65.9	56.7	69.8	65.6	58.5	62.7	61.7	59.0
Q_2-P_2 (M)	64.2	64.0	62.9	64.1	62.5	60.2	62.0	62.3	60.3
Q_2-P_2 (S)	70.0	66.7	59.5	69.9	66.4	58.8	61.7	59.8	59.1
Q_3-P_2 (M)	63.7	64.9	64.1	64.5	67.4	64.0	59.9	61.4	63.0
Q_3-P_2 (S)	69.8	65.5	57.9	69.6	64.9	57.0	63.0	61.1	57.5

Table 6.5: Irregular room. Measured (M) and simulated (S) reverberation time T_{30} (ms).

Now, it is clear that the diffuse part in the **CARISM** plays a major role after the first 20 ms. However, instead of accurately predicting the bins of the measured response, it actually follows its envelope. The reason, apart from the diffuse reflections adopted in the **CARISM**, is the larger discretization step, which results to different summing up of the various reflections, that arrive at same time interval.

Tables 6.5 to 6.9 present the measured and predicted room acoustic parameters for all positions for the 4 kHz, 8 kHz and 16 kHz octave bands. In general the agreement is good. The main reason for the deviations is the possible errors in the measured absorption and scattering coefficients.

6.3 Round Robin III Music Studio

The Round Robin in general is a process aiming to help room acousticians evaluating their simulations. It consists of absorption-scattering data and measurements on three different types of rooms: one concert hall, one auditorium and one music studio. Theoretical predictions can be directly compared to the published measured data. We will focus on the last room, which is considerably simpler than the others and its measured results are considered quite reliable [21, 22].

Three phases are available for this room, corresponding to different levels of

Q - P	Sinusoid			Wave			Hexagon		
	4 kHz	8 kHz	16 kHz	4 kHz	8 kHz	16 kHz	4 kHz	8 kHz	16 kHz
Q_1 - P_1 (M)	53.8	58.5	60.0	54.4	58.0	61.6	56.1	60.5	61.3
Q_1 - P_1 (S)	61.6	57.8	50.6	63.9	58.0	51.5	59.3	57.0	53.2
Q_2 - P_2 (M)	55.8	60.0	63.1	54.1	55.9	61.9	55.4	57.5	61.6
Q_2 - P_2 (S)	64.4	58.4	52.7	64.4	58.6	51.2	58.4	56.2	52.8
Q_3 - P_2 (M)	60.0	64.4	67.2	68.4	69.3	67.3	69.3	69.6	66.7
Q_3 - P_2 (S)	70.9	65.9	60.5	70.9	66.1	59.3	62.8	62.3	60.6

Table 6.6: Irregular room. Measured (M) and simulated (S) early decay time EDT (ms).

Q - P	Sinusoid			Wave			Hexagon		
	4 kHz	8 kHz	16 kHz	4 kHz	8 kHz	16 kHz	4 kHz	8 kHz	16 kHz
Q_1 - P_1 (M)	8.97	8.28	8.38	9.07	8.73	8.36	8.81	8.21	8.27
Q_1 - P_1 (S)	7.58	8.02	9.61	7.32	8.21	9.50	7.97	8.40	9.16
Q_2 - P_2 (M)	8.96	8.37	8.01	9.26	8.86	8.10	8.87	8.59	8.08
Q_2 - P_2 (S)	8.00	7.80	9.03	7.07	7.97	9.34	7.95	8.37	9.02
Q_3 - P_2 (M)	7.89	7.80	7.63	6.75	6.79	7.34	6.76	6.86	7.33
Q_3 - P_2 (S)	6.12	6.87	7.78	6.13	6.84	8.01	7.34	7.39	7.77

Table 6.7: Irregular room. Measured (M) and simulated (S) clarity C_{80} (dB).

Q - P	Sinusoid			Wave			Hexagon		
	4 kHz	8 kHz	16 kHz	4 kHz	8 kHz	16 kHz	4 kHz	8 kHz	16 kHz
Q_1 - P_1 (M)	76.2	73.7	68.9	75.8	72.2	67.2	74.2	70.3	67.1
Q_1 - P_1 (S)	73.9	76.1	81.0	73.2	76.7	80.5	75.0	76.9	79.4
Q_2 - P_2 (M)	74.1	73.9	68.8	76.7	76.8	69.3	74.8	74.4	68.2
Q_2 - P_2 (S)	70.7	74.4	77.9	70.7	74.3	78.9	73.9	75.5	77.8
Q_3 - P_2 (M)	77.7	74.9	72.4	71.4	67.2	66.8	70.6	67.6	65.0
Q_3 - P_2 (S)	67.2	70.6	73.7	67.2	70.4	74.6	71.5	72.3	73.6

Table 6.8: Irregular room. Measured (M) and simulated (S) definition D_{50} (%).

Q - P	Sinusoid			Wave			Hexagon		
	4 kHz	8 kHz	16 kHz	4 kHz	8 kHz	16 kHz	4 kHz	8 kHz	16 kHz
Q_1 - P_1 (M)	5.16	5.32	5.38	5.17	5.35	5.57	5.21	5.43	5.50
Q_1 - P_1 (S)	5.53	5.34	4.73	5.66	5.25	4.82	5.36	5.18	4.92
Q_2 - P_2 (M)	5.26	5.29	5.53	5.18	5.24	5.65	5.21	5.23	5.64
Q_2 - P_2 (S)	5.50	5.07	4.65	5.50	5.08	4.55	5.08	4.90	4.66
Q_3 - P_2 (M)	5.21	5.25	5.31	5.58	5.67	5.56	5.29	5.61	5.67
Q_3 - P_2 (S)	5.86	5.45	5.00	5.85	5.46	4.90	5.52	5.21	5.01

Table 6.9: Irregular room. Measured (M) and simulated (S) center time TS (ms).

Freq. (Hz)	125	250	500	1000	2000	4000
α_{air} (dB/1 Km)	0.4486	1.3210	2.7161	4.6496	9.9950	30.3081
α_m (10^{-3} m^{-1})	0.1033	0.3042	0.6254	1.0706	2.3014	6.9787

Table 6.10: Air absorption coefficient and corresponding air absorption exponent for use in the Round Robin simulations.

detail. The first one consists of 7 plane walls forming only convex corners between them³. The second phase consists of around 70 walls and provides a higher geometric accuracy, but without all the surface details. The higher level of detail is achieved in the third phase of the room, which is not considered here.

6.3.1 First Phase

The first phase is quite straightforward to be evaluated, because the room consists of convex corners. This means that all elements are visible from the others and no special treatment is required for including obscuring checks. Our algorithm can be applied directly to this geometry. The meshed room is illustrated in Figure 6.13. $N = 324$ elements were used. All walls are given uniform absorption and scattering coefficients by PTB, both equal to 0.1, for six octave bands: 125 Hz, 250 Hz, 500 Hz, 1 kHz, 2 kHz and 4 kHz. The source is placed at two positions and the receiver at three, giving six source-receiver combinations as shown in Table 6.11. The response at the three receivers is calculated simultaneously for each source. In the algorithm of Figure 4.16 each of the three receivers is checked whether it is inside the effective polyhedron, so that a contribution to be added.

Since the absorption and scattering is the same for all bands, simulations are performed only once for each source and the three receivers. Only the air absorption is different at each frequency. Thus, initially the impulse responses are calculated without air absorption and the final ones are obtained by eq. (4.14). As specified by PTB, the temperature in the room is 20 °C, the relative humidity is 50 % and static air pressure is 1000 hPa. For these conditions the air absorption coefficient is calculated using the formulas from [49] and the air absorption exponent is obtained from eq. (6.2). Table 6.10 shows the values of α_{air} and α_m used in the simulations.

The simulations by the CARISM are compared with the mean of 20 predictions by other room acoustic software. These predictions are available by PTB. There is no point to compare the estimations directly to the available measurements, since the first phase of the music studio is extremely simplified and the absorption and scattering data are approximately attached to the walls. As we will see in Section 6.3.2, the measured data are quite far from the predicted ones for this phase. The actual role of the first phase is to examine the agreement between the various room acoustic models and not between them and the real data. The room has an approximate volume of 400 m^3 and the average real reverberation time is about 0.95 s. Hence, the Schroeder’s frequency is approximately 98 Hz. As we will see in Sec. 6.3.2, the simulated results for the lower frequency band (125 Hz) deviate much from the measured data, since this octave band is quite close to the Schroeder’s frequency.

³*Convex* is a corner with internal angle less than 180 degrees, while *concave* is a corner with internal angle more than 180 degrees. Sometimes the terms are used in the reverse way [11].

	x (m)	y (m)	z (m)
Q_1	1.5	3.5	1.5
Q_2	-1.5	5.5	1.5
P_1	-2.0	3.0	1.2
P_2	2.0	6.0	1.2
P_3	0.0	7.5	1.2

Table 6.11: Source-receiver positions at the Round Robin III room.

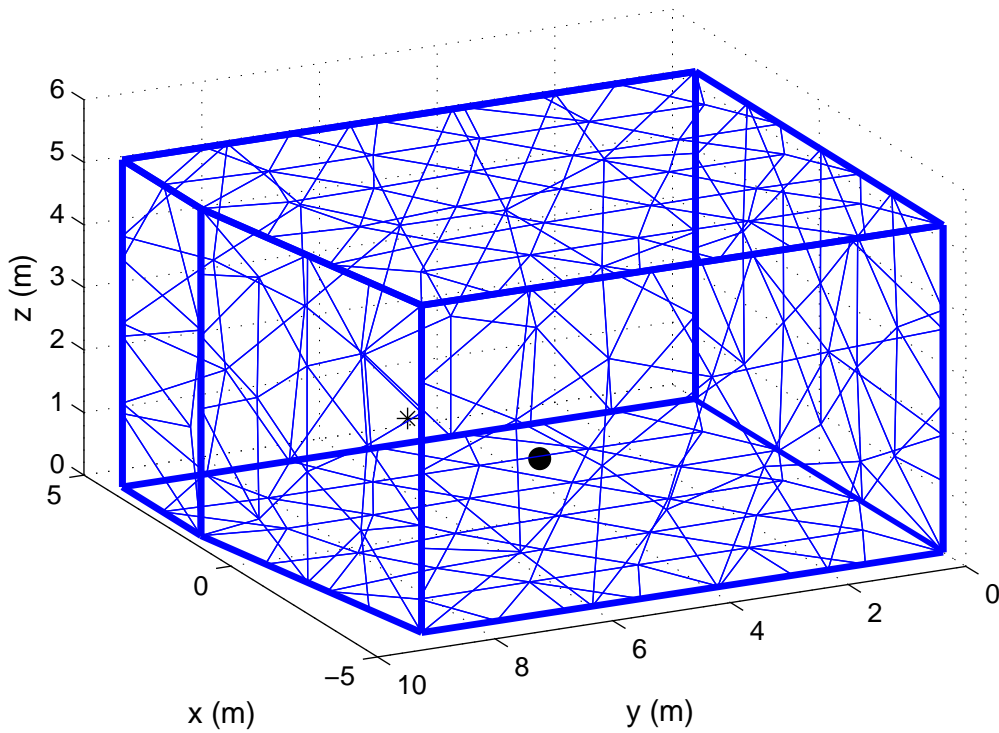


Figure 6.13: First phase of Round Robin III, consisting of 7 uniformly absorptive and scattering walls. Meshing with $N = 324$ elements.

6.3.1.1 Results

Figures 6.14 to 6.19 present the calculated T_{30} , EDT , C_{80} , D_{50} , TS and G values for each source-receiver combination at each octave band.

In general, the estimations by the proposed algorithm are very close to the mean values from other prediction software. The shape of the curves is similar, revealing the common assumptions used by all geometrical acoustics models. Clearly, the air absorption is responsible for the variations throughout the frequency range, since the absorption and scattering of the surfaces are constant. In some cases the results by the **CARISM** deviate from the mean of the other software but they are still within the corresponding standard deviation.

6.3.2 Second Phase

The second phase of the Round Robin III room has two versions: one with open and one with closed curtains. We will focus on the second one, consisting of about 65 walls and being slight simpler than the first one. Some couples among the walls form concave corners, which complicates the **ISM** in a way that more validation criteria should be included. Mechel [11] gives a thorough description of the **ISM** in concave rooms, so that only a few basic rules will be revised here. Apart from convex corners, the room contains curtains which form apertures between them and the walls. Handling of the apertures is a really important task because sound rays can enter the cavity behind the aperture, leading to complex reflections.

One of the major modifications that has to be done in the existing algorithm is the inclusion of an *obstacle test*, since any obstacle, such as a convex corner or a curtain, may prevent an image source or a surface element of “seeing” part of a wall behind them. This obstacle test has to be performed from the very early stage of the form factor calculation. If an element is not visible by another one, their form factor is zero. Calculating all form factors in this way, we do not need to include the obstacle test again during the diffuse part of our algorithm, since it will have been already done for the form factors. As in computer graphics, the form factor expression –eq. (2.19)– can be generalized including a visibility term:

$$F_{i,j} = \frac{1}{S_i} \int_{S_i} \int_{S_j} V_{i,j} \frac{\cos \theta \cos \theta'}{\pi \mathbf{R}^2} ds' ds \quad (6.3)$$

where $V_{i,j} = 1$, if the line between i and j is unobstructed and $V_{i,j} = 0$, otherwise.

Even if the room is relatively simple comparing to the other two phases of Round Robin, it is still quite complicated for our unoptimized algorithm. For that reason, some of the initial complexities were removed for the simulations. An initial picture of the room is illustrated in Figure 6.20, where the two closed curtains have been noted by 1 and 2. The large curtain, no 1, covers almost all the wall behind it leaving only a small gap of 5 cm height from the floor –along z axis. We can simplify the room model by assuming that the curtain is stretched down to the floor, covering the small gap. In this way, the whole wall behind the curtain can be ignored. Apparently, we cannot do the same for the smaller curtain, no 2, because the aperture that it forms is quite large both in the x and z axis. Apart from the complexity due to the curtains, the original room contains several concave polygonal walls which are difficult to be handled by our primitive algorithm. Instead, these walls are split into convex polygons. The modified room is meshed with 660 triangular elements, as illustrated in Figure 6.21.

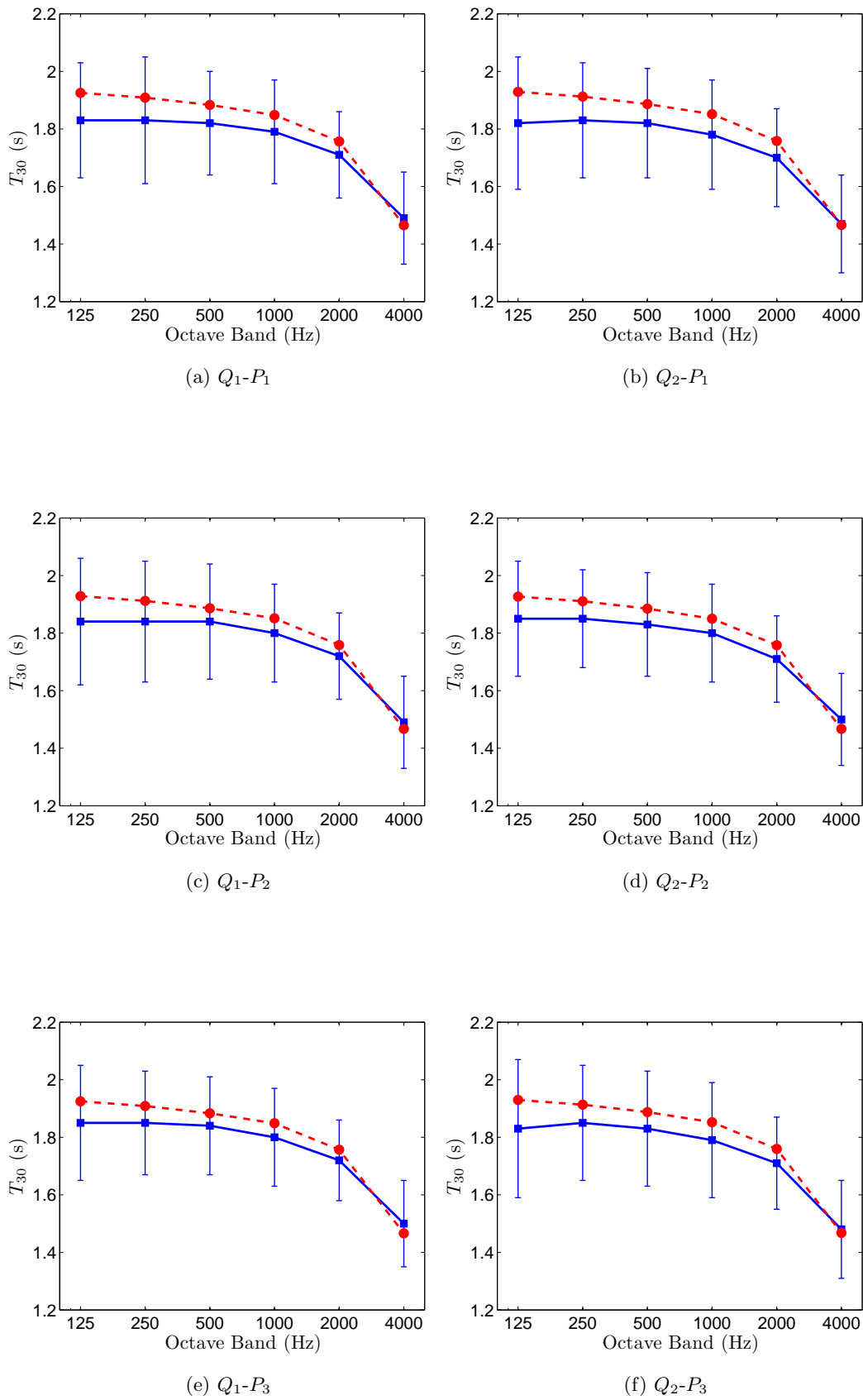


Figure 6.14: First phase of Round Robin III. Reverberation time T_{30} . \blacksquare —: Mean value and \pm standard deviation from 20 participants. \bullet - - - : Results by CARISM.

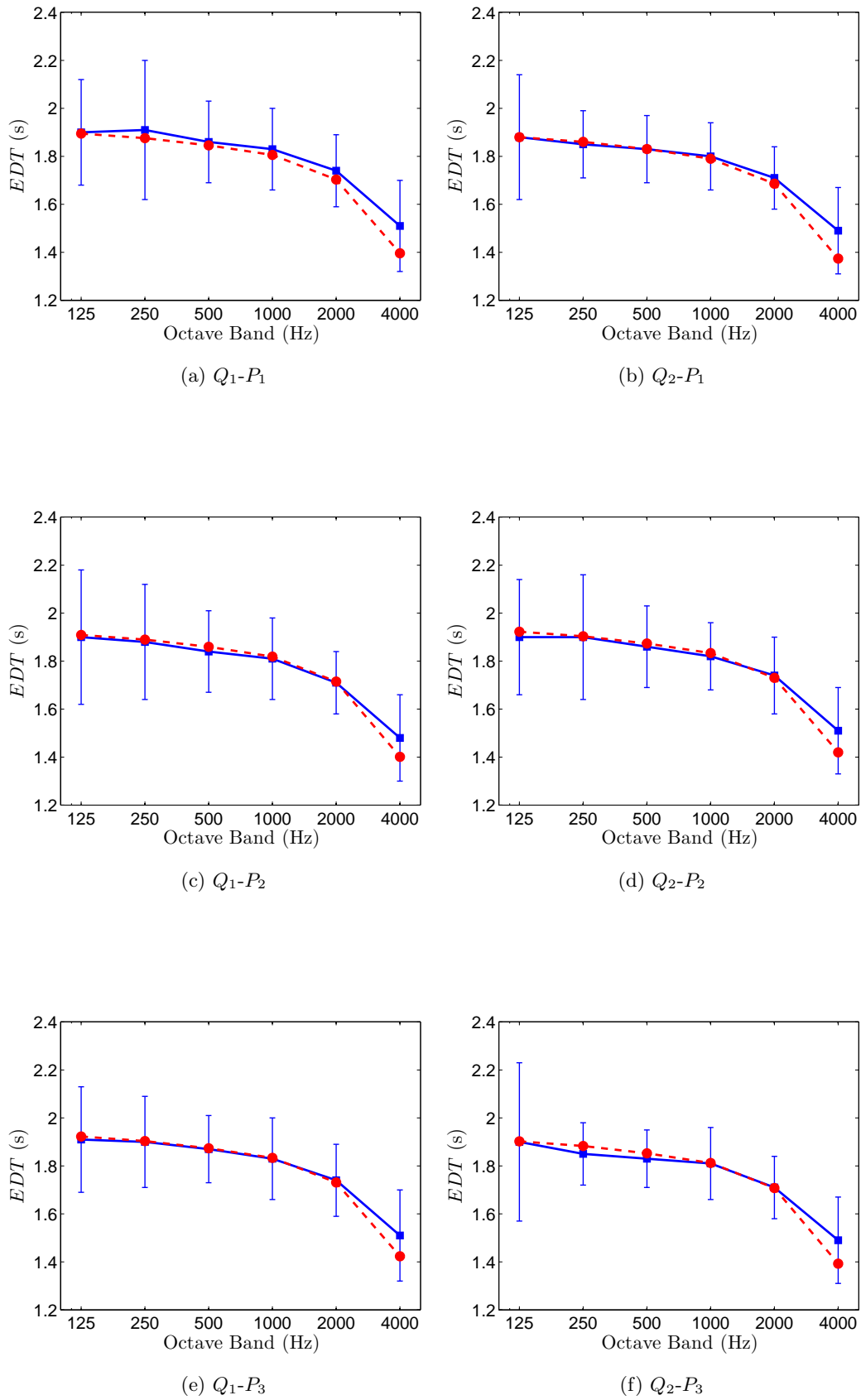


Figure 6.15: First phase of Round Robin III. Reverberation time EDT . $\text{---}\blacksquare\text{---}$: Mean value and \pm standard deviation from 20 participants. $\text{-}\bullet\text{-}$: Results by CARISM.

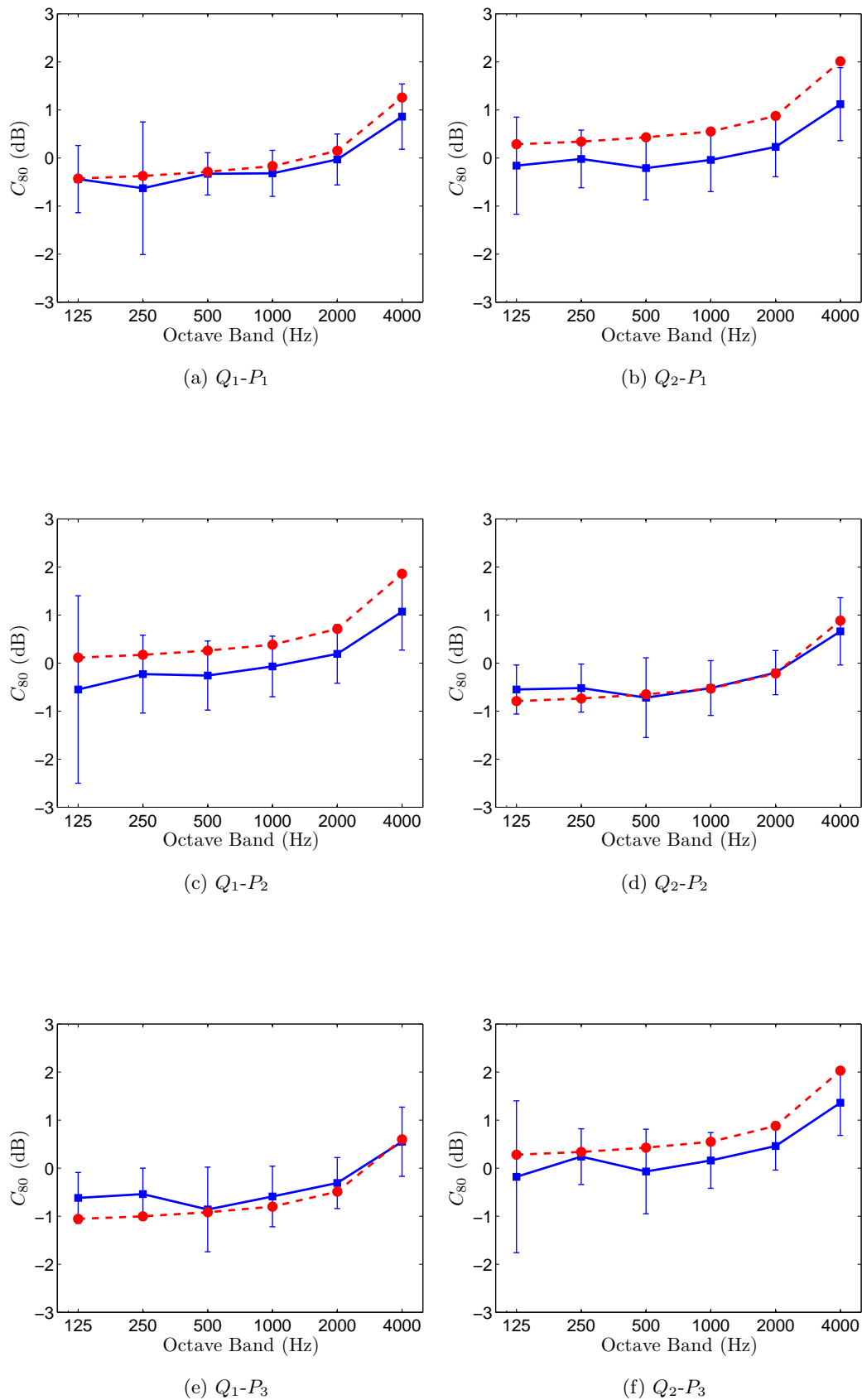


Figure 6.16: First phase of Round Robin III. Clarity C_{80} . \blacksquare : Mean value and \pm standard deviation from 20 participants. $-\bullet-$: Results by CARISM.

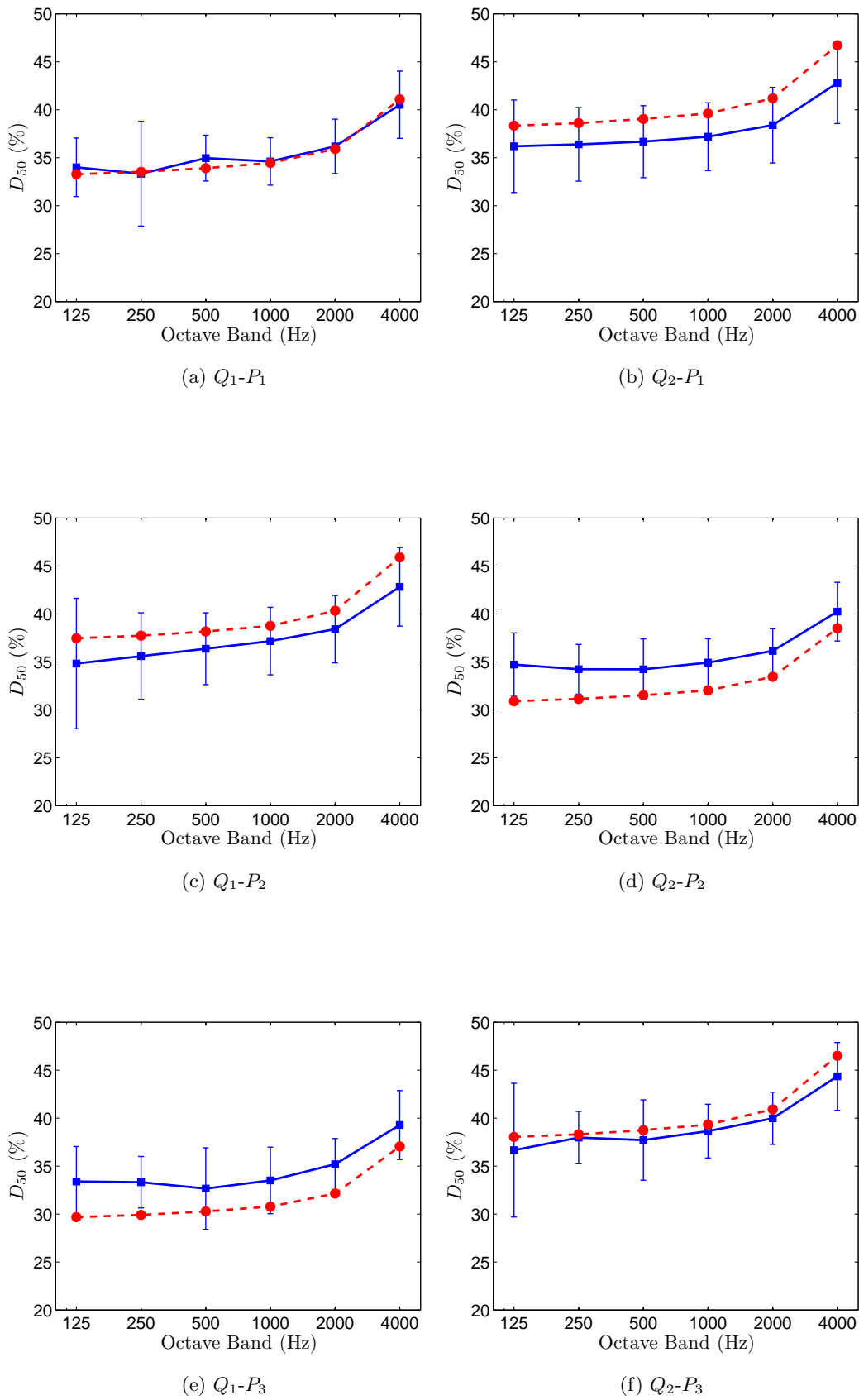


Figure 6.17: First phase of Round Robin III. Definition D_{50} . \blacksquare —: Mean value and \pm standard deviation from 20 participants. $-\bullet-$: Results by CARISM.

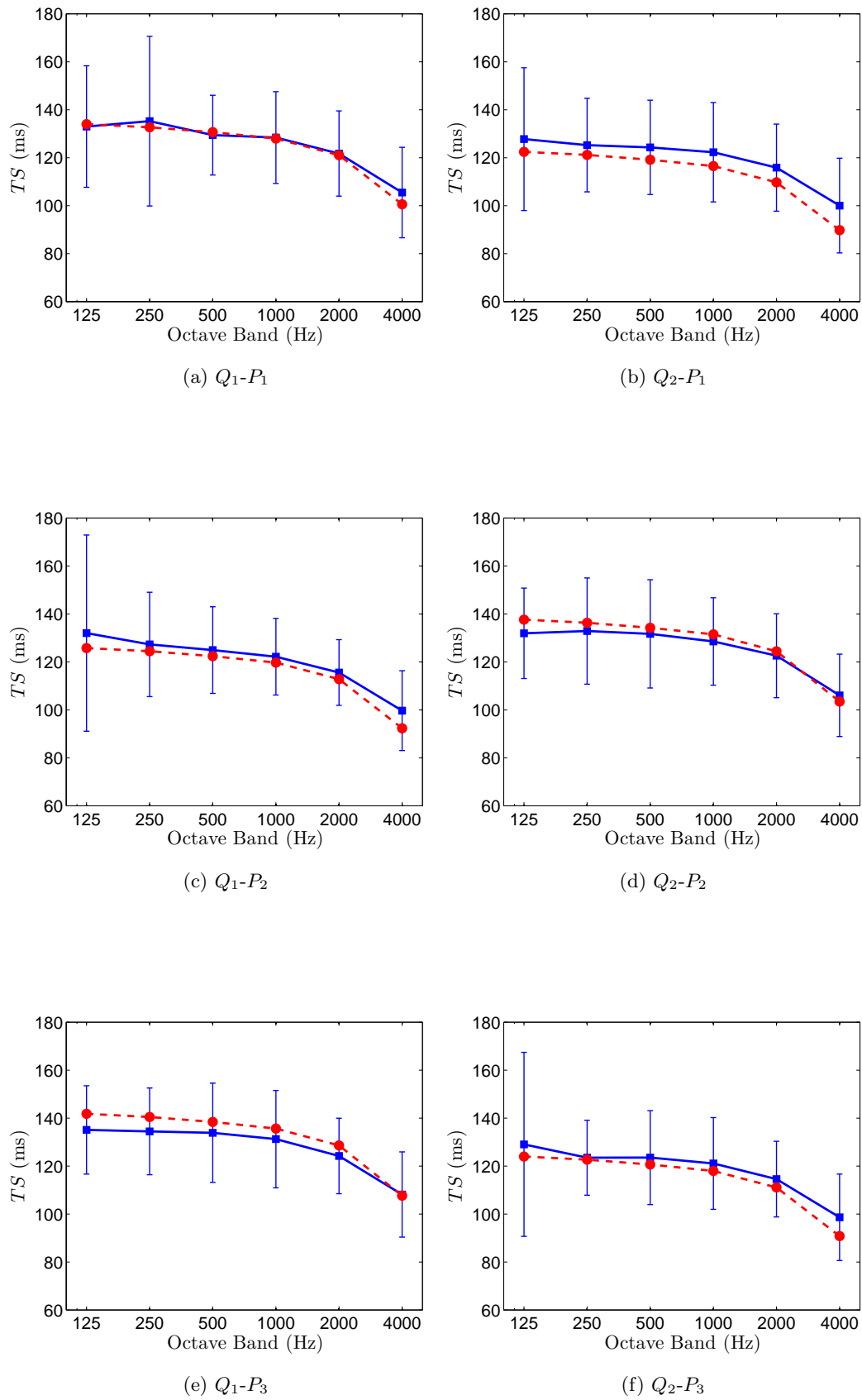


Figure 6.18: First phase of Round Robin III. Center time TS . \blacksquare —: Mean value and \pm standard deviation from 20 participants. \bullet - - : Results by CARISM.

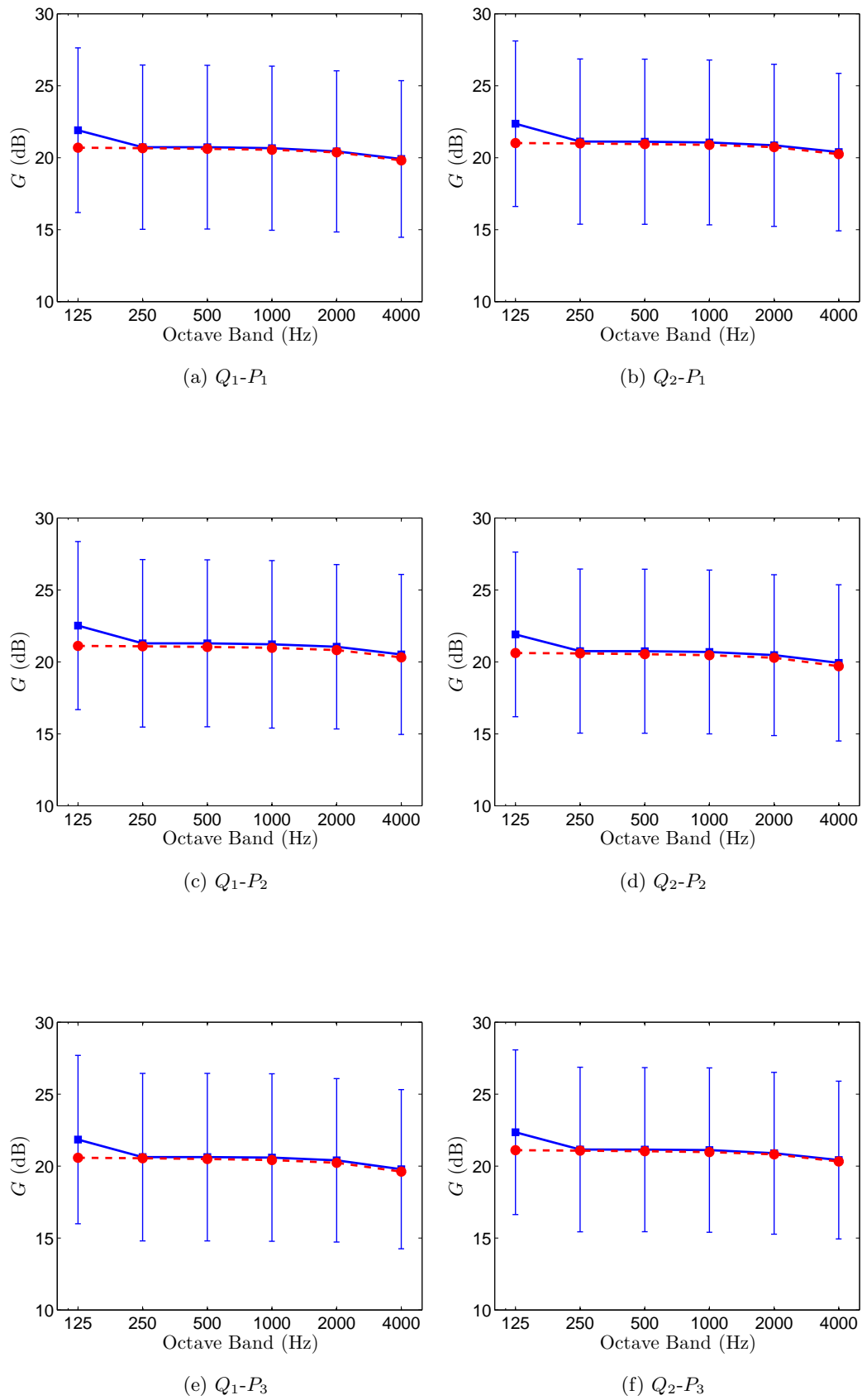


Figure 6.19: First phase of Round Robin III. Sound strength G . \blacksquare —: Mean value and \pm standard deviation from 20 participants. \bullet - - : Results by CARISM.

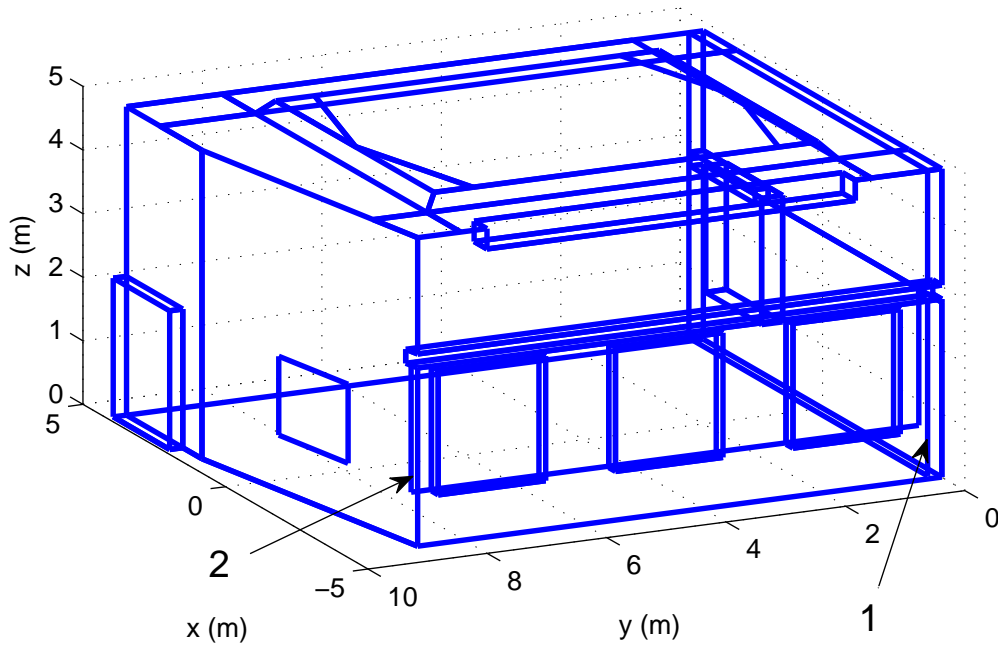


Figure 6.20: Second phase of Round Robin III. Original room with closed curtains consisting of 65 polygonal walls. Curtains are marked with 1 and 2. Curtain 1 covers 98.9 % of the wall behind it, so that this wall can be totally removed.

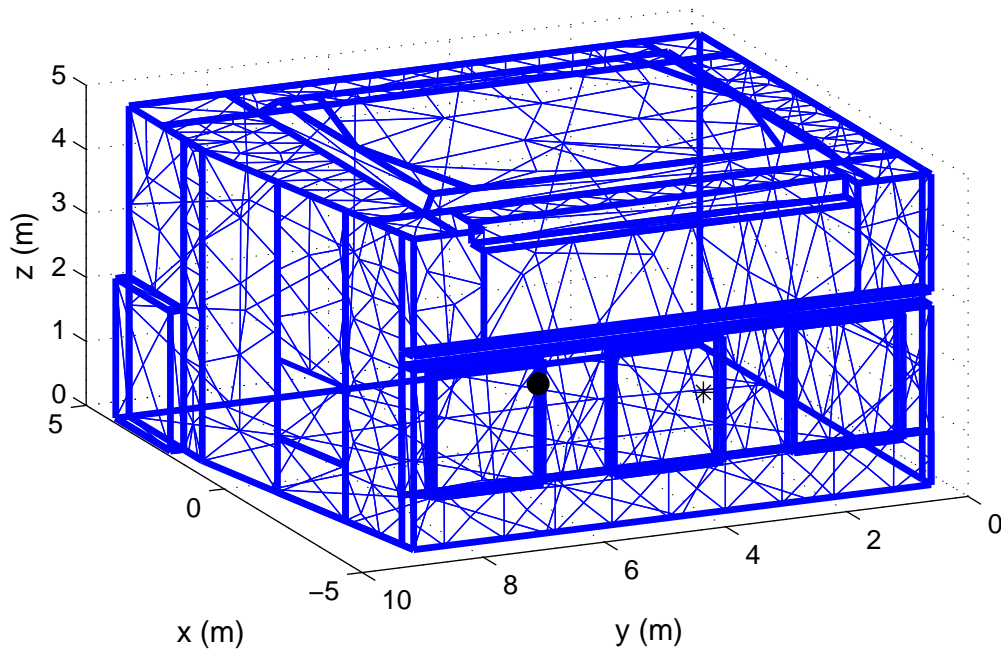


Figure 6.21: Second phase of Round Robin III. Modified room consisting of 70 convex polygonal walls. Meshing with $N = 660$ elements.

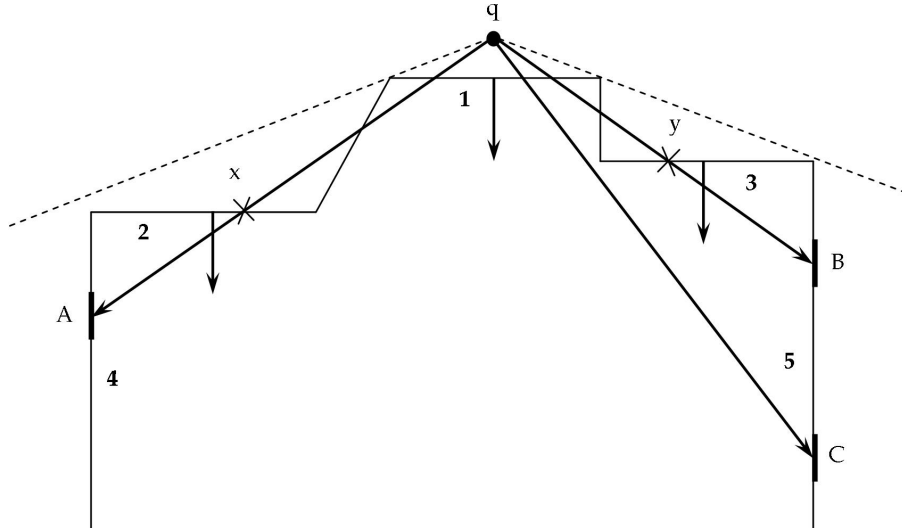


Figure 6.22: An example of a concave room with corners up to 270° . The image source q , corresponding to wall No 1, is effective only for element C. The element is inside the source effective polyhedron (dashed line) and the connection line between the element and source is not obscured.

List of Parallel Walls The fact that the angle of all convex corners does not exceed 270° is very useful for facilitating the obstacle test. If the angle exceeds 270° , there is a sequence of tests that should be performed in order for an image source to be accepted. These are described in [11] and they are not repeated here.

However, in our case we only need to proceed as follows: For each wall, let us call it *reference wall*, we find all the others that have the same unit normal vectors. So we essentially find all the parallel walls pointing towards the room interior. These walls are also checked if they are *inside* the reference wall. Every line formed by the source behind the reference wall and the receiver has to be checked if it intersects any of these parallel walls. Each of these walls should be further checked whether it lies between the source and the receiver. If both criteria are fulfilled, the wall can be considered as obstacle and the receiver is not visible by the source. Figure 6.22 gives an example where the reference wall is 1. Walls no 2 and 3 are parallel and inside 1. The effective polyhedron of the source q is denoted by the dashed line. Elements A and B are not visible by the source even if they are inside the effective polyhedron, because the lines connecting them with the source intersect walls 2 and 3, at x and y respectively. On the other hand, element C is visible, because it is both inside the effective polyhedron and the line connecting the element with the source does not intersect any of the parallel walls.

6.3.2.1 Results

The main algorithm of the **CARISM** was run separately for each frequency band and for each source of Table 6.11. Time was discretized with a sampling frequency of 2 kHz and the length of the impulse response was 0.9 s. 30 iterations were used. The same room acoustic parameters as in Sec. 6.3.1.1 were calculated. The simulation results are presented in Figures 6.23 to 6.28, together with the mean of the published measured data and the mean of 20 predictions by other room acoustic software.

The behavior of the simulated curve is similar to the mean of the 20 predictions. This can be explained by the common limitations of the various geometrical acoustic

models. In most of the cases, the results by **CARISM** are within the standard deviation of the predictions, that is, within $\pm 34\%$ of the predictions above and below the mean value. The lowest octave band is close to the Schroeder's frequency ($\simeq 98$ Hz) and all models (including **CARISM**) have difficulties in simulating properly the sound field. Hence in most of the cases the deviation between simulations and measurements is large.

The T_{30} values by **CARISM** are higher than the mean of the 20 predictions at all positions, but lower than the measured data at high frequencies. The positional dependence of T_{30} is very small for the predictions by **CARISM** and the other software. This seems to happen again due to similar assumptions about the behavior of sound waves. However the results for bands 1 kHz and 2 kHz, provided by **CARISM**, are very close to the measured data. In general, the differences in the T_{30} very much depend on the air absorption model used. For our **CARISM** prediction, the values from Table 6.10 were used.

The EDT values by **CARISM** are lower in general than the mean of the 20 predictions at all positions. In some positions and some frequency bands the agreement is very good with the measured data.

As for clarity, C_{80} , the predictions by **CARISM** are close to the measured data at the middle frequencies (500 Hz and 1 kHz), but they are much higher at 4 kHz. Surprisingly, at the positions Q_2-P_1 and Q_2-P_3 there is a nice agreement between our simulations and the measured data at 125 Hz.

The case is similar for definition, D_{50} . Above 250 Hz the agreement with the measured data is satisfying. As for the center time TS and the sound strength G the simulations by the **CARISM** are very close to the mean of the 20 predictions, in most of the cases. The agreement with the measured data is good above 1 kHz for TS and between 250 Hz and 1 kHz for G .

Tables 6.12 and 6.13 present the averaging for the 250 Hz, 500 Hz, 1 kHz and 2 kHz octave bands at every source-receiver combination. The measured data and the results by **CARISM** are shown. The maximum error for T_{30} is 8.5 % with respect to the measured value. The highest agreement between simulation and measurements is observed for G and D_{50} where the error is around 1 to 4 %. The TS predictions are also quite good.

Evidently, the modified room model treated by the **CARISM** is rather simplified to give predictions very close to the measured data. The second phase of the Round Robin III is itself an approximation of the real geometry, better represented by the third phase. In order to increase the speed of form factor calculation, the *configuration factors* were used instead of the full form factor between two elements (Sec. 2.4.2). This also introduces some errors in the prediction. Finally, the boundary subdivision could be more dense and the sampling frequency could be larger, increasing the accuracy.

6.3.3 Computational Performance

The speed of execution of the **CARISM** algorithm very much depends on the number of walls, the number of surface elements and the level of time discretization. Evidently, the number of image sources increases in a non linear way as a function of the number of walls, as was mentioned in Sec.3.3. As for the **AR** part, the algorithm has a second order dependency with the number of elements, N^2 .

The time required for each iteration is not constant but depends strongly on the number of image sources that are created. In the usual behavior, the iterations are very fast at the beginning, very slow at the peak of the image-source production and

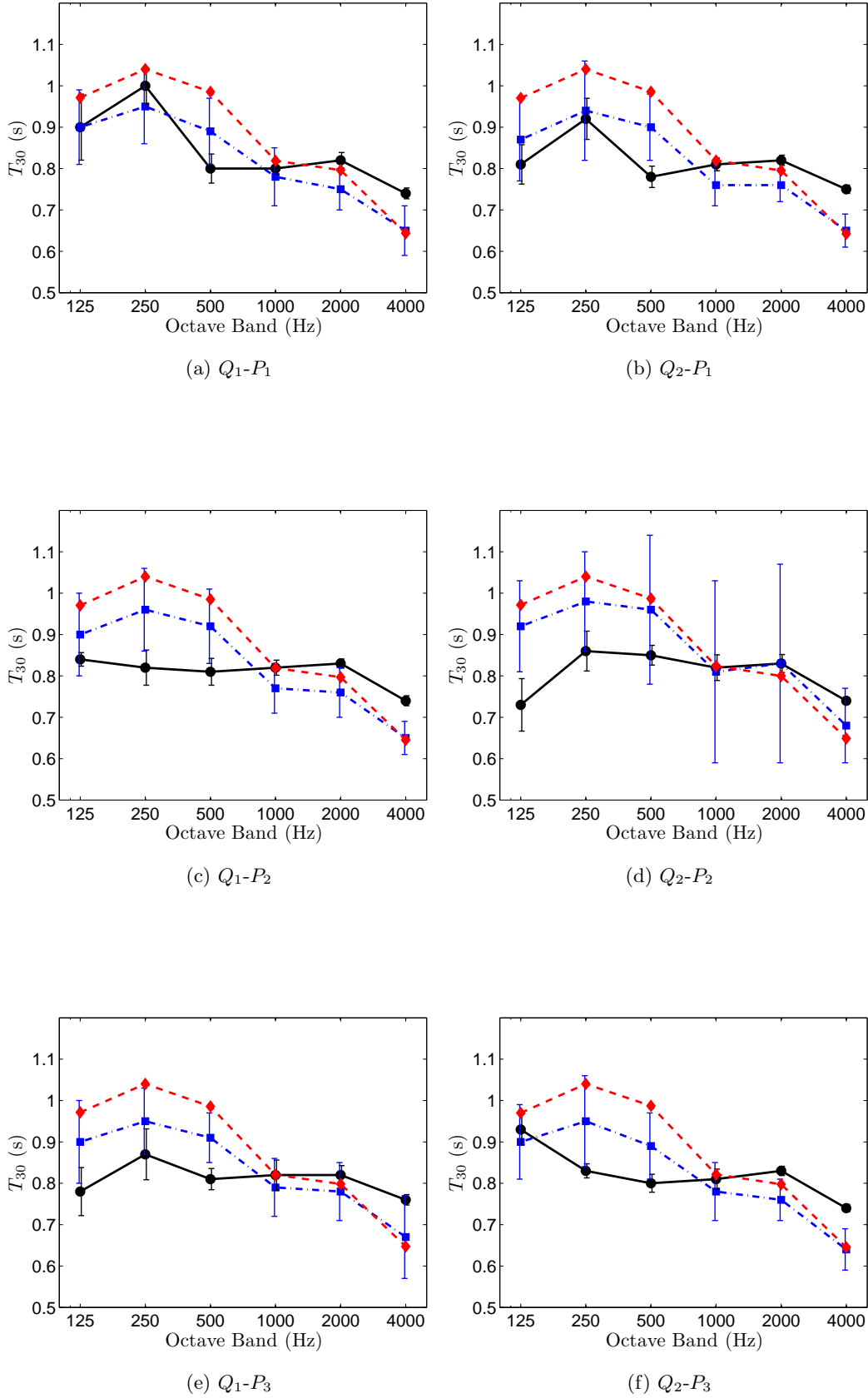


Figure 6.23: Reverberation time T_{30} . —●—: Mean value and \pm standard deviation from measured data. -·-■-·-: Mean value and \pm standard deviation from 20 participants. - -◆- - : Results by CARISM.

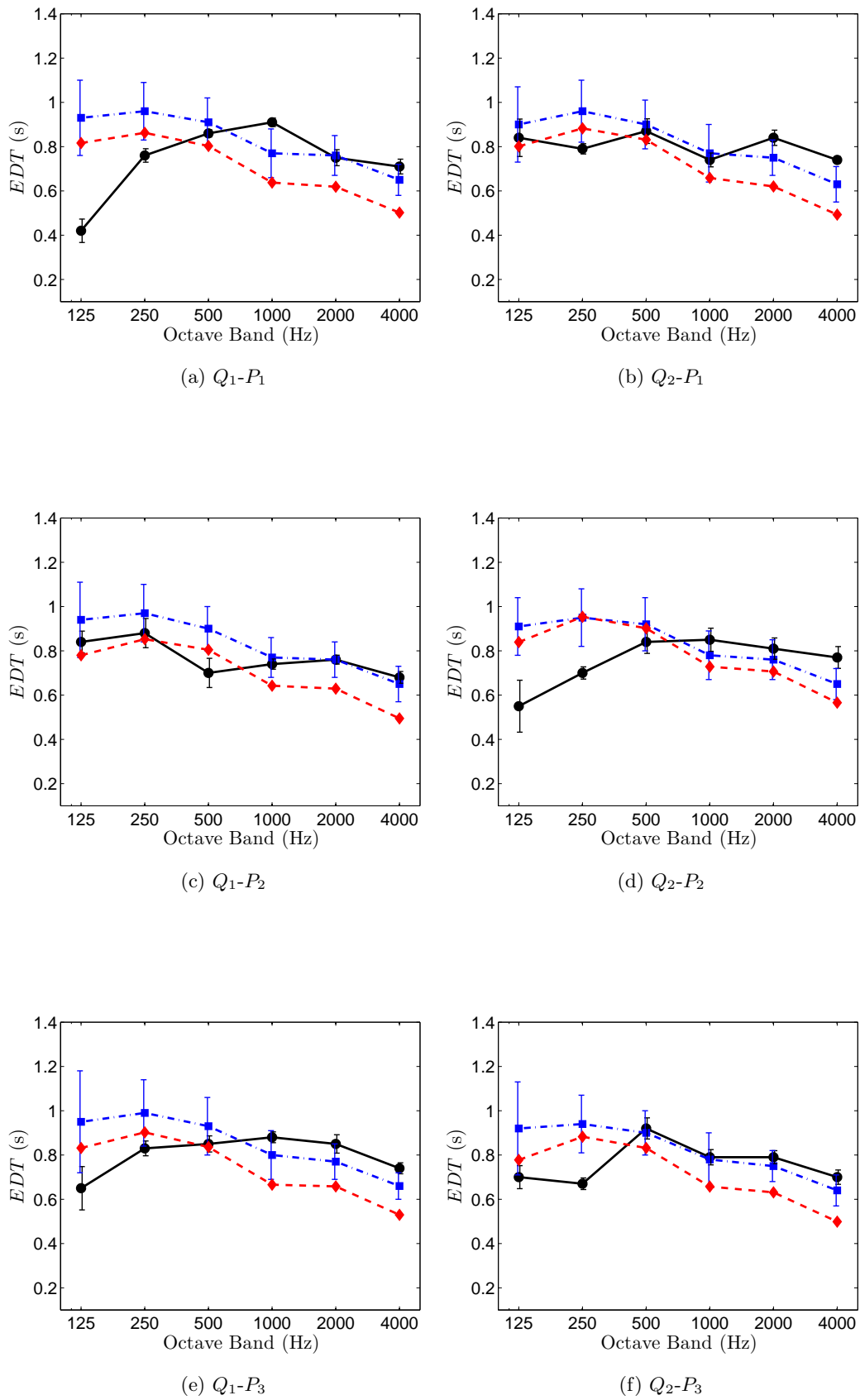


Figure 6.24: Reverberation time EDT . \bullet —: Mean value and \pm standard deviation from measured data. \blacksquare - - : Mean value and \pm standard deviation from 20 participants. \blacklozenge - - : Results by CARISM.

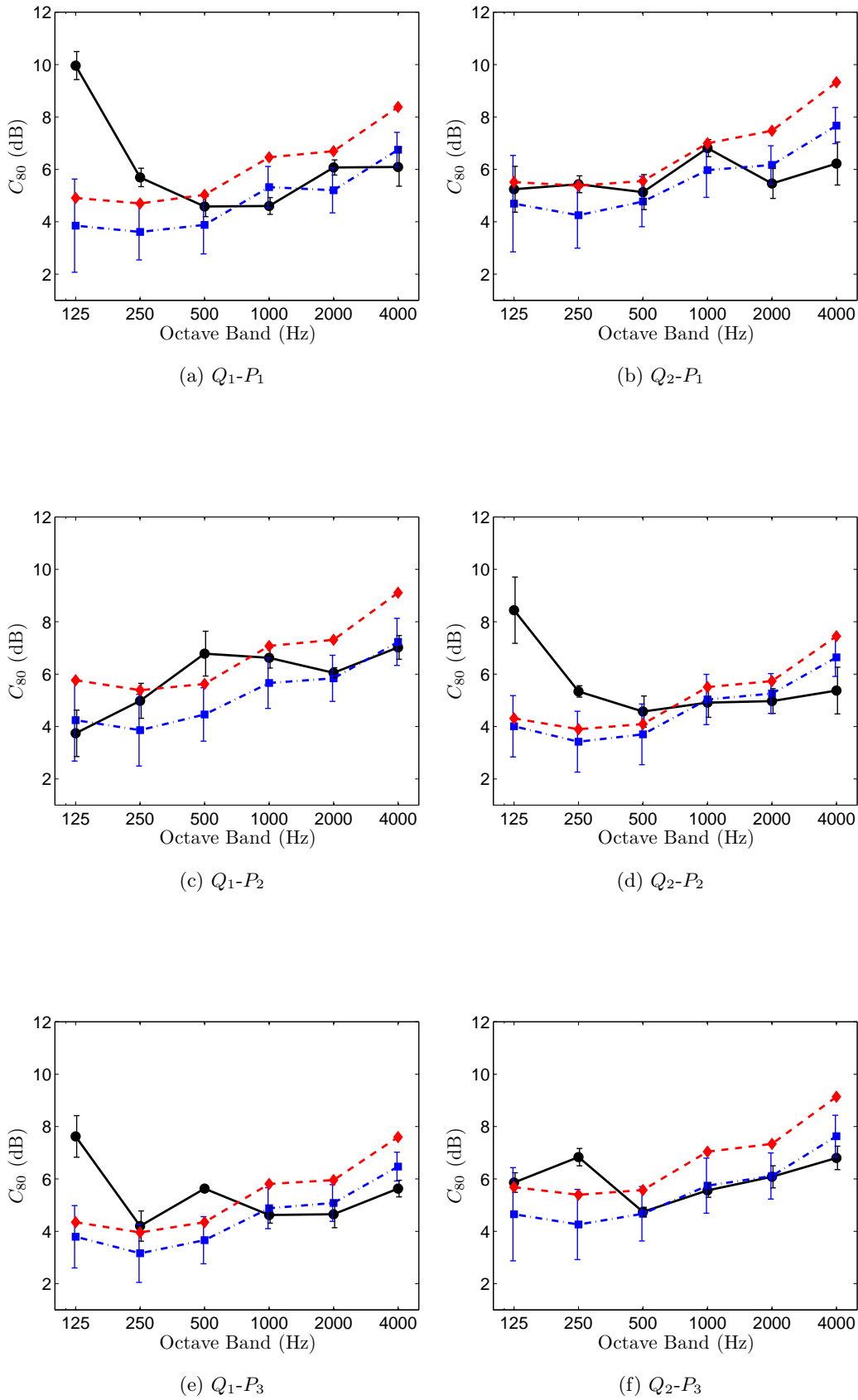


Figure 6.25: Clarity C_{80} . —●—: Mean value and \pm standard deviation from measured data. - -■- - : Mean value and \pm standard deviation from 20 participants. - -◆- - : Results by CARISM.

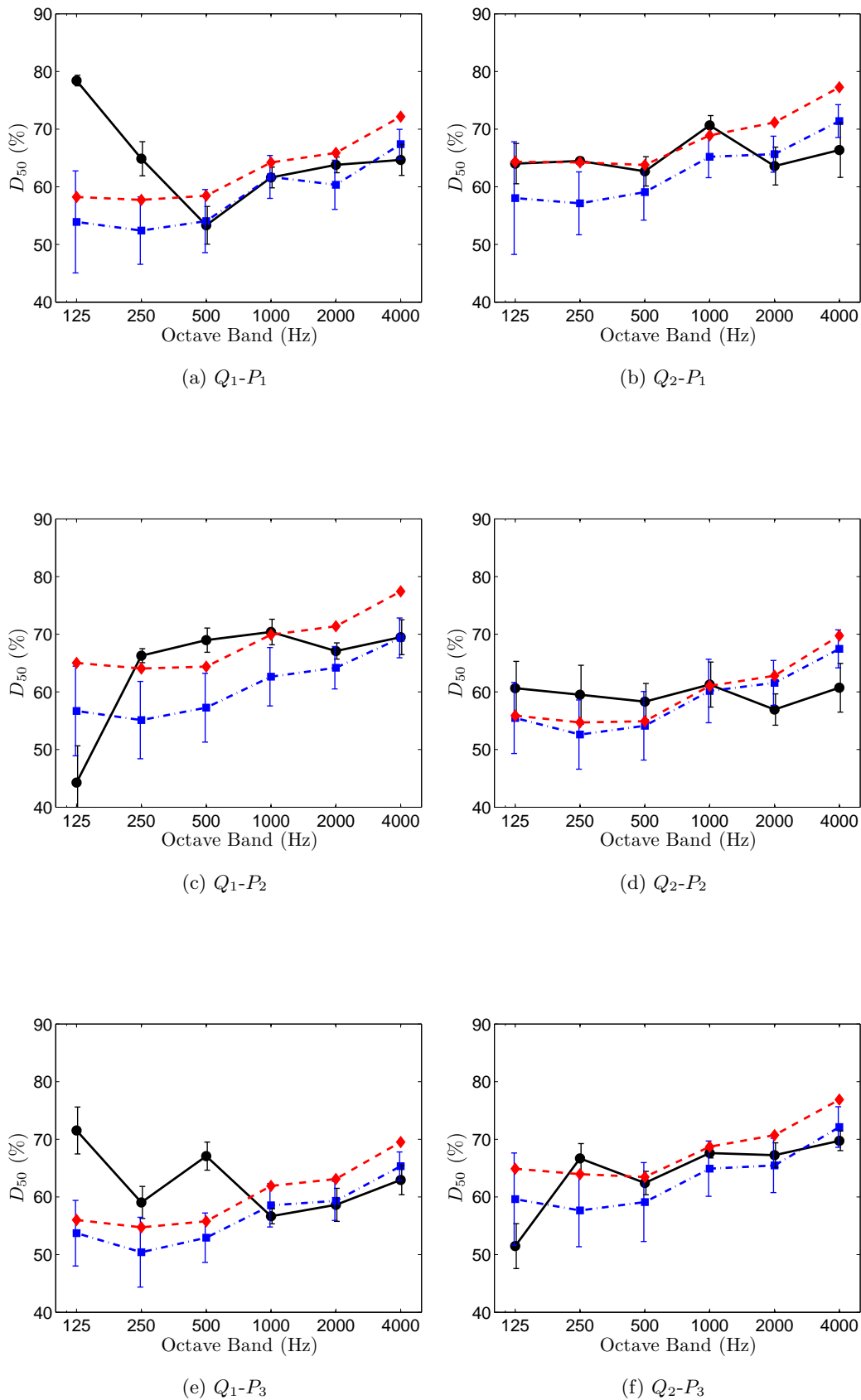


Figure 6.26: Definition D_{50} . —●—: Mean value and \pm standard deviation from measured data. - -■- - : Mean value and \pm standard deviation from 20 participants. - -◆- - : Results by CARISM.

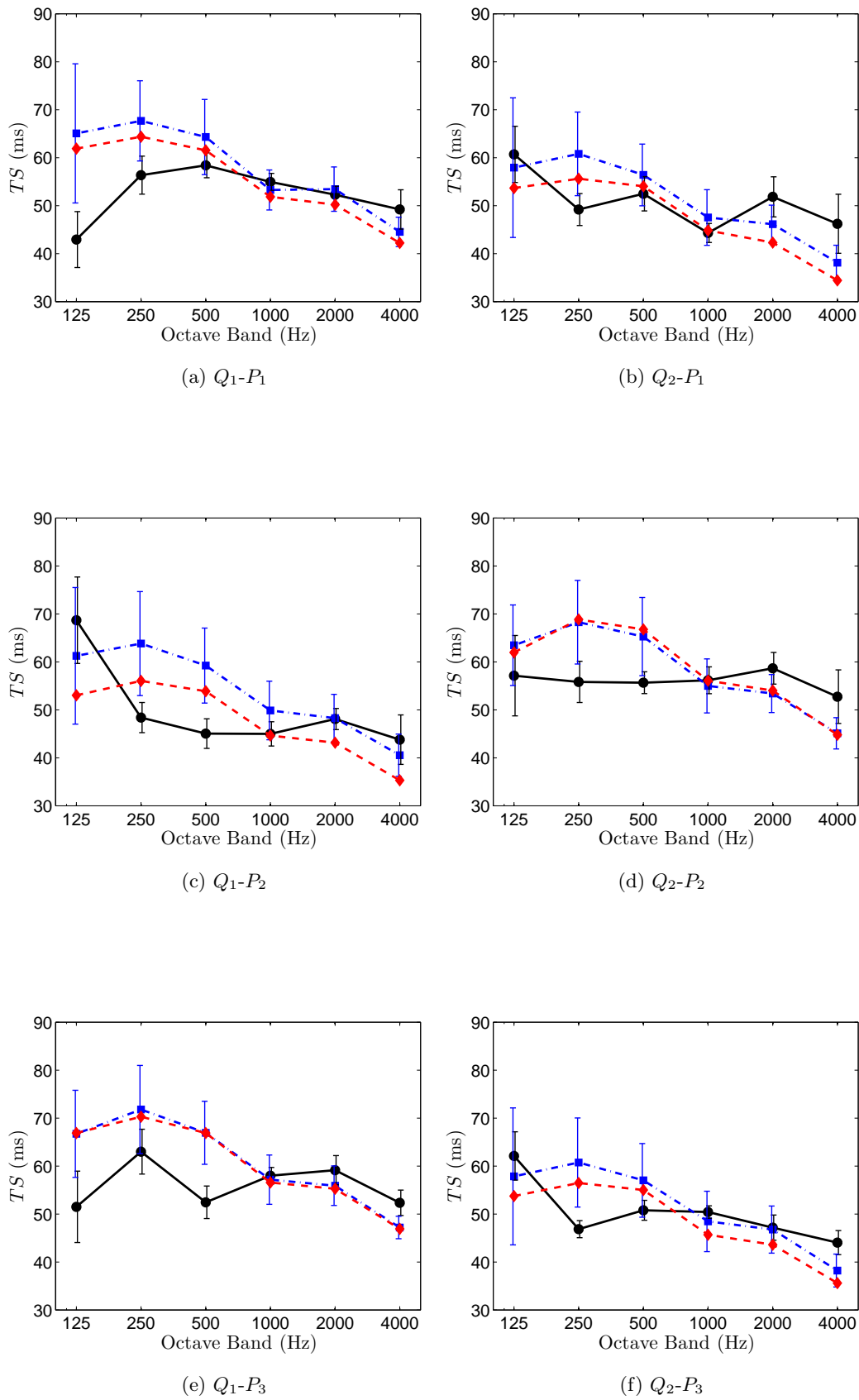


Figure 6.27: Center time TS . —●— : Mean value and \pm standard deviation from measured data. - -■- - : Mean value and \pm standard deviation from 20 participants. - -◆- - : Results by CARISM.

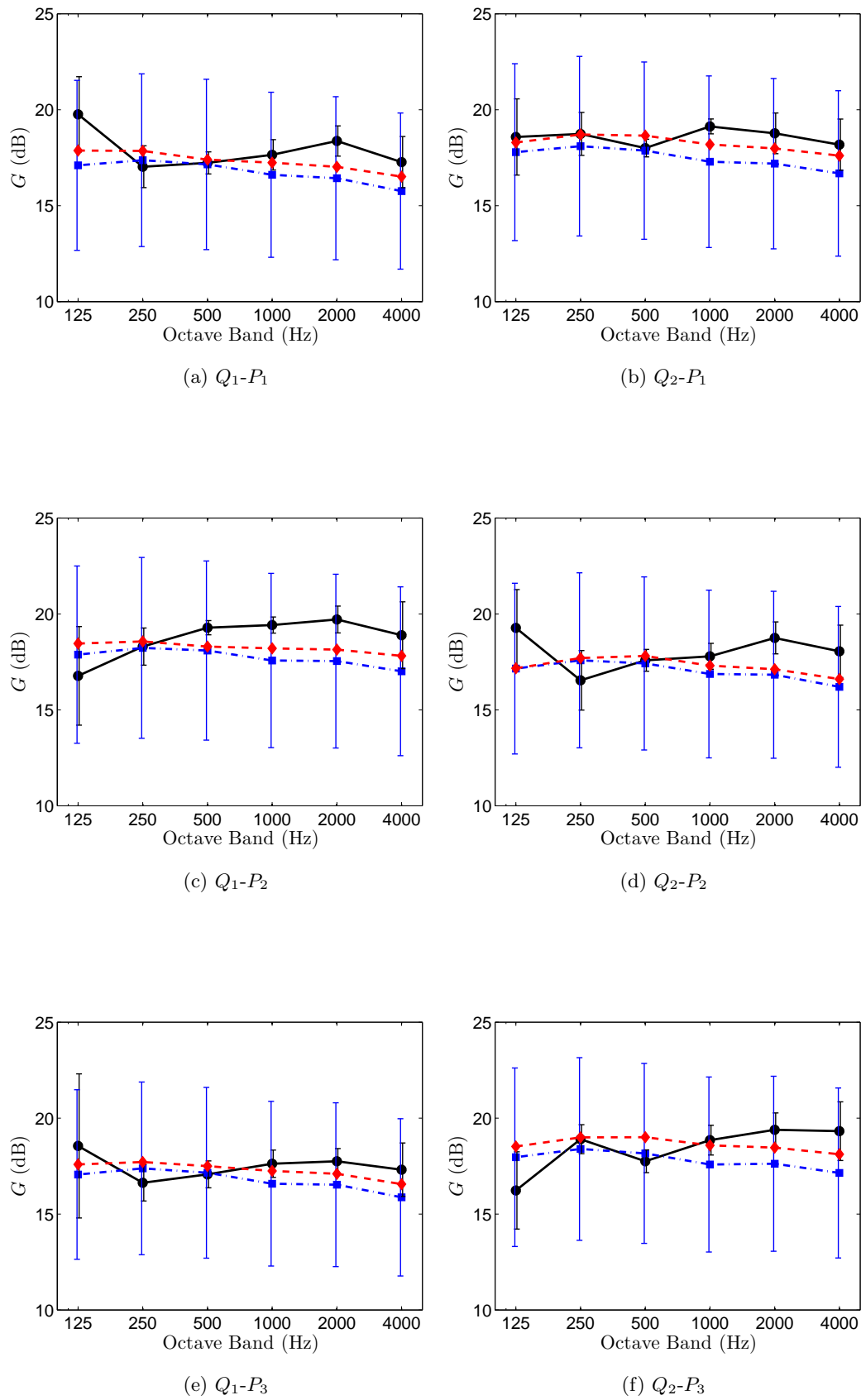


Figure 6.28: Sound strength G . \bullet —: Mean value and \pm standard deviation from measured data. \blacksquare - - - : Mean value and \pm standard deviation from 20 participants. \blacklozenge - - - : Results by CARISM.

		T_{30} (s)			EDT (s)			G (dB)		
Q	P	M	S	Err. (%)	M	S	Err. (%)	M	S	Err. (%)
Q_1	P_1	0.86	0.89	3.5	0.82	0.75	-8.5	17.57	17.37	-1.1
Q_1	P_2	0.82	0.89	8.5	0.77	0.75	-2.6	19.18	18.30	-4.6
Q_1	P_3	0.83	0.89	7.2	0.85	0.78	-8.2	17.27	17.39	0.7
Q_2	P_1	0.83	0.89	7.2	0.81	0.77	-4.9	18.66	18.38	-1.5
Q_2	P_2	0.84	0.89	5.9	0.80	0.83	3.8	17.67	17.48	-1.1
Q_2	P_3	0.82	0.89	8.5	0.79	0.77	-2.5	18.73	18.76	0.2

Table 6.12: Second phase of Round Robin III. Measured (M) and simulated (S) T_{30} , EDT and G values for all source-receiver combinations, averaged for the 250 Hz, 500 Hz, 1 kHz and 2 kHz octave bands.

		C_{80} (dB)			D_{50} (%)			TS (ms)		
Q	P	M	S	Err. (%)	M	S	Err. (%)	M	S	Err. (%)
Q_1	P_1	5.24	5.72	9.2	60.91	61.57	1.0	55.50	56.99	2.7
Q_1	P_2	6.11	6.34	3.8	68.18	67.43	-1.1	46.63	49.42	6.0
Q_1	P_3	4.78	5.01	4.8	60.36	58.89	-2.4	58.15	62.25	7.1
Q_2	P_1	5.71	6.34	11.0	65.36	67.03	2.6	49.46	49.19	-0.6
Q_2	P_2	4.95	4.81	-2.8	59.01	58.36	-1.1	56.58	61.42	8.6
Q_2	P_3	5.80	6.33	9.1	66.00	66.71	1.1	48.80	50.19	2.8

Table 6.13: Second phase of Round Robin III. Measured (M) and simulated (S) C_{80} , D_{50} and TS values for all source-receiver combinations, averaged for the 250 Hz, 500 Hz, 1 kHz and 2 kHz octave bands.

fast again at the end, where the **ISM** is gradually converted to **AR** (see Sec. 5.5). All algorithms were implemented in MATLAB for research purposes and they are only slightly optimized. Hence it seems reasonable that their performance is poor. It is believed however that a commercial implementation of the suggested method could be highly efficient, for the detailed impulse responses that it provides.

The first phase of the music studio, consisting of 324 elements and only convex walls, was very simple to implement. The main **CARISM** algorithm was run for each of the two sources, for one frequency band. The execution time was 10 minutes for the first source and 11 minutes for the second one. Since the absorption and scattering coefficients were the same for all frequency bands, only one calculation

Freq. (Hz)	Time (min)	
	Q_1	Q_2
125	23.88	23.45
250	23.78	23.38
500	22.70	22.45
1000	23.63	23.50
2000	22.85	22.40
4000	22.56	21.90

Table 6.14: Computational Times of the **CARISM** main algorithm for the second phase of Round Robin III, with closed curtains. For every source, each frequency band was calculated separately. The room was subdivided into 660 elements. A sampling frequency of 2 kHz was used for an impulse response length of 0.9 s.

was performed. Afterwards, the impulse responses at the receivers were filtered by the air absorption for each band. The calculation time for the form factors was 17 s.

The second phase of the music studio, consisting of 660 elements and concave walls, was much more difficult to implement. The obstacle test is very time consuming, raising the algorithm computational effort abruptly. The absorption and scattering coefficients were different for each frequency band, so that the algorithm was run for each source and each band separately, that is, for 12 times. The duration of each simulation is presented in Table 6.14. The calculation time of the form factors was 10 min.

Chapter 7

Conclusion

7.1 Summary and Discussion

This study was devoted on developing a combined room acoustic model treating diffuse and specular reflections. The model is based on the acoustic energy propagation and incorporates two other well known models: acoustical radiosity (**AR**) and image source model (**ISM**). The former deals with purely diffuse, while the later deals with purely specular reflections.

Initially, the principles of **AR** and the **ISM** are presented. As for **AR**, the main equations are presented in analytical and discretized form. Emphasis is given on the calculation of form factors for the particular case of a pair of triangular elements. The form factor integrals are transformed using the parametric equation of a plane, so that they can be easily integrated numerically. The application of the **ISM** in rectangular rooms and in arbitrary polyhedral rooms is presented. The important topic concerning the validity of the generated image sources in polyhedral rooms is discussed and several criteria for accepting or discarding a source are presented.

In the main chapter of the thesis (Chap.4), the **AR** discretized equations are reformulated to account for the specular part represented by the **ISM**. The group of final equations constitutes the combined model, which was given the name **CARISM** (Combined Acoustical Radiosity – Image Source Model). The model is implemented in two multi-iteration algorithms. In the proposed model, the concept of iteration is equivalent to the reflection order, so that image sources from the **ISM** and source elements from **AR** are treated in a unified way. The first algorithm, the *main* one, neglects any specular reflections of the diffuse portion of energy and thus it neglects the coupling between **AR** and the **ISM**. The second one, the *full* algorithm, takes this coupling into account.

Both the main and the full algorithm are studied through several examples in Chapter 5. The results produced by the two algorithms are compared with each other. The deviation is small, leading to the conclusion that the error arising from neglecting the specular reflections of the diffuse energy is not large. The direct diffuse contribution between the elements – applied in the main algorithm – seems to be enough for the distribution of energy, since the important specular reflections are still preserved by the image sources.

The **CARISM** in its unoptimized implementation is computationally costly, since its main components, **AR** and the **ISM** are already costly methods themselves. **AR** is heavy because the boundary of the room has to be subdivided into a large number of elements and the impulse response on each element has to be calculated. For a large room, thousands of elements would be required, raising the computational

cost proportionally to the square of the number of elements. The **ISM** is also a computational heavy method, because the number of image sources grows exponentially as a function of the order of reflections taken into account and the number of walls. It was shown that the execution time for the **CARISM** depends strongly on the scattering coefficient, that determines which of the two models is dominant. Initially, more energy is handled by the **ISM** than **AR**, so that image sources are generated with an exponential rate. Depending on the scattering coefficient, the image source production per iteration exhibits a peak after which their number per order is reduced and the energy is gradually transferred to **AR**.

Application of the **CARISM** to concave rooms is very time consuming because of the obstacle tests that should be performed. An example of a concave room was treated in Section **6.3.2**.

Simulations by the **CARISM** were validated with experimental data in chapter **6**. Initially, measurements in a small polyhedral reverberant room were carried out using three circular scattering surfaces placed on its bottom. Some absorption material was added on the walls in order to obtain a reasonable energy decay. The measured squared impulse responses were quite different from the simulated energy impulse responses, clearly because of the principal violations of the wave nature by our algorithm. As in all geometrical acoustic models, the concept of sound wave is extremely simplified and all interference phenomena between waves in an enclosure cannot be modeled properly. Apart from that, the measured pressure impulse response includes phase information, while the energy impulse response from the **CARISM** does not. Hence, even if the measured impulse response is squared, the outcome is expected to be similar to the predicted energy impulse response only in the very early part. Besides the expected disagreement in the impulse responses, their backward integration, i.e., the energy decay curves, were close to each other. Moreover, the predicted room acoustic parameters were close to the measured ones. Some deviations can be attributed at errors in the measurements of the absorption and scattering coefficients. Uncertainties are involved in the air absorption model used as well.

The model was also applied in prediction of room acoustic parameters for a real music studio, located at the German National Metrology Institute (PTB). Absorption and scattering coefficients are provided by PTB. The simulations were compared with published measured data and results from other room acoustic prediction software. The agreement was satisfying in most of the cases.

The proposed model falls into the common limitations of the geometrical acoustic models. Less deviation from the measured data is obtained above Schroeder's frequency, where a high modal overlap occurs. The model does not take phase information into account, since it is energy based. Hence, wave fields and eigenmodes cannot be predicted.

At this point it should be clear that all geometrical acoustic models do not attempt to replace the full wave equation solution, which in general gives a more physically correct interpretation of the complicated real acoustic phenomena. Finite element or boundary element methods deal with numerical solutions of the wave equation, but their range of application is limited to small enclosures. Consequently, the approximations adopted by geometrical acoustic models are inevitable for practical applications in large and complicated rooms, such as concert halls.

One of the known problems in room acoustics literature is the difficulty in experimentally validating the theoretical results. Indeed, as discussed in Sec. **6.2**, the lack of phase information in some models –like the **CARISM**– gives ambiguous predictions of the impulse response. Still, even models with phase information included are

not able to predict well the response, because of their physically incorrect assumptions about waves. Nevertheless, the energy decay can be predicted quite well by room acoustic models, as long as the degree of absorption and scattering have been determined correctly. Since most room acoustic parameters of interest are based on energy ratios, the room acoustic models are very useful for predicting these parameters. This is the reason why geometrical acoustic modeling is the widely accepted tool for room acoustic studying and designing.

In this study, an attempt to validate the model experimentally took place. However, many of the ideas have been only theoretically validated, mainly because of time limitations. The study introduces a new model and serves more as an initiation for further development.

7.2 Future Work

Probably the most important extension of the project would be a series of carefully designed experiments for validation of the model. Clearly, investigating scattering in real rooms is a rather difficult task, due to the fact that the scattering coefficients themselves are difficult to determine and much more error is involved in their measurement in comparison with the absorption coefficients. Apart from that, even if the measured energy decay for a room, partially covered with scattering surfaces, is approximately exponential, the measured impulse responses are quite similar to the case with only specular surfaces. In the experiments of Sec. 6.2, the average scattering coefficient was too low to lead to clearly distinguishable differences between the responses with and without scattering. A more carefully designed experiment should involve a much larger portion of scattering in the room. Moreover, regular geometries, such as rectangular rooms, can provide clearly different results with and without scattering, as we saw in Sec. 5.3 and 5.4.

The algorithms implementing the **CARISM** could be rewritten in efficient computer languages and optimized, so that complicated concave room geometries could be treated.

The wall visibility criterion for the image source generation in the **CARISM** could be improved. In this study, a highly precise criterion and an approximate criterion were proposed. However, the first one is excessively time consuming for a practical application, while the second one involves errors in determining the actual number of image sources per iteration and gives rise to some statistical behaviour in the algorithm.

Further investigation of the role of image elements is required. Several specific cases can be studied where the specular reflections of the diffuse portion of energy could be important. In such cases, the coupling between **AR** and the **ISM** should not be omitted.

Bibliography

- [1] H. Kuttruff, *Room Acoustics*, Applied Science Publishers LTD, London, 1973.
- [2] A. C. Gade, *Room Acoustic Engineering*, DTU Electro, Acoustic Technology, Technical University of Denmark, 2008, Lecture Note 4213.
- [3] M. R. Schroeder and K. H. Kuttruff, “On frequency response curves in rooms: Comparison of experimental, theoretical and monte carlo results for the average frequency spacing between maxima.”, *J. Acoust. Soc. Am.*, vol. 34, pp. 76–80, 1962.
- [4] A. Krokstadt, S. Strm, and S. Srsdal, “Calculating the acoustical room response by the use of a ray tracing technique.”, *J. Sound Vib.*, vol. 8, pp. 118–125, 1968.
- [5] M. Vorländer, *Auralization. Fundamentals of Acoustics, Modelling, Simulation, Algorithms and Acoustic Virtual Reality*, Springer-Verlag, Berlin, 2008.
- [6] B. L. Dalenbäck, “Room acoustic prediction based on a unified treatment of diffuse and specular reflection.”, *J. Acoust. Soc. Am.*, vol. 100, pp. 899–909, 1996.
- [7] B. Kapralos, *The sonel mapping acoustical modeling method*, York University, Toronto, Ontario, Canada, 2006, PhD thesis.
- [8] H. W. Jensen, *Realistic image synthesis using photon mapping*, A.K. Peters, Natick, MA, 2001, PhD thesis.
- [9] J. B. Allen and D. A. Berkley, “Image method for efficiently simulating small-room acoustics”, *J. Acoust. Soc. Am.*, vol. 65.
- [10] J. Borish, “Extension of the image model to arbitrary polyhedra”, *J. Acoust. Soc. Am.*, vol. 75, pp. 1827–1836, 1984.
- [11] F. P. Mechel, “Improved mirror source method in room acoustics”, *J. Sound Vib.*, vol. 256, pp. 873–940, 2002.
- [12] H. Lee and B. H. Lee, “An efficient algorithm for the image source technique”, *Applied Acoustics*, vol. 24, pp. 87–115, 1988.
- [13] M. Vorländer, “Simulation of the transient and steady state sound propagation in rooms using a new combined ray-tracing / image-source algorithm”, *J. Acoust. Soc. Am.*, vol. 86, pp. 172–178, 1989.
- [14] C. W. Kosten, “The mean free path in room acoustics”, *Acustica*, vol. 10, pp. 245–250, 1960.

- [15] C. Jeong, J. Brunskog, and F. Jacobsen, “Room acoustic transition time based on reflection overlap (1)”, *J. Acoust. Soc. Am.*, vol. 127, pp. 2733–2736, 2010.
- [16] M. Hodgson, “Evidence of diffuse surface reflections in rooms”, *J. Acoust. Soc. Am.*, vol. 89.
- [17] H. Kuttruff, “On the dependence of reverberation time on the “wall diffusion” and on room shape”, *Acustica. Acta Acustica*, vol. 45, pp. 246–255, 1980.
- [18] T. J. Cox, B. L. Dalenbäck, P. D’Antonio, J. J. Embrechts, J. Y. Jeon, E. Mommertz, and M. Vorländer, “A tutorial on scattering and diffusion coefficients for room acoustic surfaces”, *Acustica. Acta Acustica*, vol. 92, pp. 1–15, 2006.
- [19] T. Hanyu, “A theoretical framework for quantitatively characterizing sound field diffusion based on scattering coefficient and absorption coefficient of walls”, *J. Acoust. Soc. Am.*, vol. 128, pp. 1140–1148, 2010.
- [20] H. Kuttruff, “A simple iteration scheme for the computation of decay constants in enclosures with diffusely reflecting boundaries”, *J. Acoust. Soc. Am.*, vol. 98, pp. 288–293, 1995.
- [21] I. Bork, “Report on the 3rd round robin on room acoustical computer simulation - part i: Measurements”, *Acustica. Acta Acustica*, vol. 91, pp. 740–752, 2005.
- [22] I. Bork, “Report on the 3rd round robin on room acoustical computer simulation - part ii: Calculations”, *Acustica. Acta Acustica*, vol. 91, pp. 753–763, 2005.
- [23] I. Ashdown, *Radiosity: A Programmer’s Perspective*, Wiley, New York, 1994.
- [24] H. C. Hottel and A. F. Sarofim, *Radiative transfer*, McGraw-Hill, New York NY, 1967.
- [25] L. P. Franzoni and J. W. Rouse, “An intensity-based boundary element method for analyzing broadband high frequency sound fields in enclosures”, *in Proceedings of the Forum Acusticum Sevilla in Seville*, September 16-20, 2002, Spain.
- [26] H. Kuttruff, “Energetic sound propagation in rooms”, *Acustica. Acta Acustica*, vol. 83, pp. 622–628, 1997.
- [27] H. Nironen, *Diffuse Reflections in Room Acoustics Modelling*, Helsinki University of Technology - Department of Electrical and Communications Engineering, Helsinki, 2004, MSc Thesis.
- [28] E. M. Nosal, M. Hodgson, and I. Ashdown, “Improved algorithms and methods for room sound-field prediction by acoustical radiosity in arbitrary polyhedral rooms”, *J. Acoust. Soc. Am.*, vol. 116, pp. 970–980, 2004.
- [29] U. Gross, K. Springer, and E. Hahne, “Shape-factor equations for radiation heat transfer between plane rectangular surfaces of arbitrary position and size with rectangular boundaries”, *Lett. Heat Mass Transfer*, vol. 8, pp. 219–227, 1981.
- [30] P. Schröder and P. Hanrahan, “A closed form expression for the form factor between two polygons”, Tech. rep. cs-404-93, Department of Computer Science, Princeton University, 1993.
- [31] L. Lewin, *Dilogarithm and Associated Functions*, Mcdonald, London, 1958.

- [32] G. N. Walton, *Calculation of obstructed view factors by adaptive integration*, National Institute of Standards and Technology, Department of Commerce, USA, 2002.
- [33] M. F. Cohen and J. R. Wallace, *Radiosity and Realistic Image Synthesis*, Academic Press Professional, New York, 1995.
- [34] R. N. Miles, “Sound field in a rectangular enclosure with diffusely reflecting boundaries”, *J. Sound Vib.*, vol. 92, pp. 203–226, 1984.
- [35] S. G. McGovern, “A model for room acoustics”, <http://www.2pi.us/rir.html>.
- [36] T. Lewers, “A combined beam tracing and radiant exchange computer model of room acoustics”, *Appl. Acoust.*, vol. 38, pp. 161–178, 1993.
- [37] H. Kuttruff, “Stationary propagation of sound in flat enclosures with partially diffuse surface reflection”, *Acustica. Acta Acustica*, vol. 86, pp. 1028–1033, 2000.
- [38] N. C. Baines, *An investigation of the factors which control non-diffuse sound fields in rooms*, University of Southampton, PhD thesis.
- [39] N. Korany, *A model for the simulation of the sound fields in enclosures integrating the geometrical and the radiant approaches*, University of Alexandria, 2000, PhD thesis.
- [40] S. Siltanen, T. Lokki, S. Kiminki, and L. Saviola, “The room acoustic rendering equation.”, *J. Acoust. Soc. Am.*, vol. 122, pp. 1624–1635, 2007.
- [41] J. Embrechts, L. De Geetere, G. Vermeir, M. Vorlander, and T. Sakuma, “Calculation of the random-incidence scattering coefficients of a sine-shaped surface”, *Acustica. Acta Acustica*, vol. 92.
- [42] J. R. Wallace and M. F. Cohen, “A two-pass solution to the rendering equation: A synthesis of ray-tracing and radiosity methods”, *Comput. Graph.*, vol. 21, pp. 311–320, 1987.
- [43] F. Cohen, S. E. Chen, J. R. Wallace, and D. P. Greenberg, “A progressive refinement approach to fast radiosity image creation”, *Comput. Graph.*, vol. 22, pp. 75–84, 1988.
- [44] C. Tsakostas, *Image Receiver Model: An efficient variation of the Image Source Model for the case of multiple sound sources and a single receiver*, Greek Acoustic Conference, National Technical University of Athens, 2004.
- [45] E. Nilsson, “Decay processes in rooms with non-diffuse sound fields. part i: Ceiling treatment with absorbing material”, *Building Acoustics*, vol. 11.
- [46] E. Nilsson, “Decay processes in rooms with non-diffuse sound fields. part ii: Effect of irregularities”, *Building Acoustics*, vol. 11.
- [47] E. M. Nosal, *Room sound field prediction by acoustical radiosity*, The University of British Columbia, Vancouver, 2002, MSc Thesis.
- [48] T. Olesen, “Predicting sound scattering performance of complex architectural surfaces”, Project report, Department of Electrical Engineering, Technical University of Denmark, 2010.

- [49] H. E. Bass, L. C. Sutherland, A. J. Zuckerwar, D. T. Blackstock, and D. M. Hester, “Atmospheric absorption of sound: Further developments”, *J. Acoust. Soc. Am.*, vol. 97.
- [50] M. R. Schroeder, “New method of measuring reverberation time”, *J. Acoust. Soc. Am.*, vol. 37, pp. 409–412, 1965.
- [51] ISO 3382-1, *Acoustics - Measurement of room acoustic parameters - Part 1: Performance spaces*, 2009.
- [52] ISO 3382-2, *Acoustics - Measurement of room acoustic parameters - Part 2: Reverberation time in ordinary rooms*, 2008.

Appendix A

Room Acoustic Parameters

Definitions and practical way of calculation are presented for the room acoustic parameters used in this study. The starting point for all following calculations is the squared pressure impulse response.

A.1 Energy Decay Curve

The energy decay curve describes the rate of the energy attenuation due to absorption in the room. It can be considered as a smooth version of the reflectogram –its envelope–, normalized with the total energy throughout the impulse response duration. In this way, the maximum energy corresponds to 0 dB. The energy decay curve can be obtained by the Schroeder’s integration method [50]:

$$EDC(t) = 10 \log_{10} \left(\frac{\int_t^{\infty} p(\tau)^2 d\tau}{\int_0^{\infty} p(\tau)^2 d\tau} \right) \quad (\text{A.1})$$

In practice, when the impulse response has been computed for discretized time, we can approximate the integration by a sum over all time steps:

$$EDC[n] = 10 \log_{10} \left(\frac{\sum_{q=n}^{q=T} p(q)^2}{\sum_{q=1}^T p(q)^2} \right) \quad (\text{A.2})$$

where n is the current time step and T is the whole duration of the discretized impulse response. Any of the commonly used reverberation times, T_{20} , T_{30} and EDT is obtained from the decay curve by a least squares linear fitting, according to ISO 3382 [51, 52].

A.2 Clarity

Clarity measures the balance between early and late arriving energy. The early part is defined as the part between the arrival time of the direct sound plus 80 ms. The late part is taken to be after these 80 ms. Clarity is most used for characterizing the music quality of a room. It is given by:

$$C_{80} = 10 \log_{10} \left(\frac{\int_0^{80 \text{ ms}} p(t)^2 dt}{\int_{80 \text{ ms}}^{\infty} p(t)^2 dt} \right) \quad (\text{dB}) \quad (\text{A.3})$$

where $t = 0$ refers to the direct sound. In discretized form, eq. (A.3) is expressed as:

$$C_{80} = 10 \log_{10} \left(\frac{\sum_{q=n_d}^{q=n_d+n_{80 \text{ ms}}} p(q)^2}{\sum_{q=n_d+n_{80 \text{ ms}}}^T p(q)^2} \right) \quad (\text{dB}) \quad (\text{A.4})$$

where n_d is the time step corresponding to the direct sound and $n_{80\text{ms}}$ is the time step corresponding to 80 ms after the direct sound. According to ISO 3382 [51, 52], the total duration T should be sufficient for the energy to have decayed by 30 dB. Only then ∞ can be replaced by T .

A.3 Definition

Definition gives the ratio between the early arriving energy, up to 50 ms after the direct sound, and the total one:

$$D_{50} = \frac{\int_0^{50\text{ms}} p(\tau)^2 d\tau}{\int_0^{\infty} p(\tau)^2 d\tau} 100 \text{ (\%)} \quad (\text{A.5})$$

Definition is used most for characterizing the speech quality of a room. In discretized form, eq. (A.5) is expressed as:

$$D_{50} = 10 \log_{10} \left(\frac{\sum_{q=n_d}^{q=n_d+n_{50\text{ms}}} p(q)^2}{\sum_{q=n_d}^T p(q)^2} \right) \text{ (dB)} \quad (\text{A.6})$$

where as before $n_{50\text{ms}}$ is the time step corresponding to 50 ms after the arrival time step n_d of direct sound. As with clarity, the total duration T should be enough for the energy to have decayed by 30 dB.

A.4 Center Time

The center time is the time-weighted average of the squared pressure impulse response:

$$TS = \frac{\int_0^{\infty} t p^2(t) dt}{\int_0^{\infty} p^2(t) dt} \text{ (ms)} \quad (\text{A.7})$$

In discretized form it can be written as:

$$TS = \frac{\sum_{q=1}^{q=T} t(q) p^2(q)}{\sum_{q=1}^{q=T} p^2(q)} \text{ (ms)} \quad (\text{A.8})$$

A.5 Sound Strength

The sound strength describes the perceived loudness. It is given by:

$$G = 10 \log_{10} \frac{\int_0^{\infty} p^2(t) dt}{\int_0^{\infty} p_{10}^2(t) dt} = L_{pE} - L_{pE,10} \text{ (dB)} \quad (\text{A.9})$$

where L_{pE} is the sound pressure exposure level of $p(t)$:

$$L_{pE} = 10 \log_{10} \left(\frac{1}{T_0} \int_0^{\infty} \frac{p^2(t) dt}{p_0^2} \right) \text{ (dB)} \quad (\text{A.10})$$

and $L_{pE,10}$ is the sound pressure exposure level of the sound pressure 10 m away from the source in free field $-p_{10}(t)$:

$$L_{pE,10} = 10 \log \left(\frac{1}{T_0} \int_0^{\infty} \frac{p_{10}^2(t) dt}{p_0^2} \right) \text{ (dB)} \quad (\text{A.11})$$

In the foregoing equations, $p_0 = 20 \mu\text{Pa}$ and $T_0 = 1 \text{ s}$.

For calculating the sound strength from simulations, a simplified formula can be used for the denominator, based on the power of the source, W_Q . According to the sphere propagation law, the energy density at 10 m away from the source is:

$$E = \frac{W_Q}{4\pi c 10^2} e^{-\alpha_m 10} \quad (\text{A.12})$$

at a specific time, given by the distance (10 m) divided by the sound speed c . α_m accounts for the air absorption. The square of the average sound pressure can be given in terms of energy density $E(t)$ as:

$$p^2(t) = E(t) \rho_0 c^2 \quad (\text{A.13})$$

where ρ_0 is the density of air. For an impulsive source, only one value arrives at the receiver, so that the integration in the denominator of eq. (A.9) simply becomes:

$$\int_0^\infty p_{10}^2(t) dt = \frac{W_Q \rho_0 c}{4\pi 10^2} e^{-\alpha_m 10} \quad (\text{A.14})$$

The sound strength can be written now in discretized form as:

$$G = 10 \log \left(\frac{\sum_{q=1}^T p(q)^2}{\frac{W_Q \rho_0 c}{4\pi 10^2} e^{-\alpha_m 10}} \right) \quad (\text{dB}) \quad (\text{A.15})$$

Index

- air absorption exponent, 12
- beam tracing, 3
- bidirectional reflectance distribution functions, 31
- Boundary Element Method, 1
- center time, 132
- clarity, 131
- combined model, 31
- concave corners, 102
- cone tracing, 3
- configuration factor, 12
- convex corners, 102
- daughter source, 23
- definition, 132
- diffuse radiation density, 42
- diffuse radiation density of a wall, 42
- diffuse reflections, 4
- diffuse reflections, 9
- echograms, 2
- effective polyhedron, 47
- eigenmode analysis, 1
- energy decay, 5
- energy decay curve, 131
- energy density reflectogram, 40
- Energy Integral Equation, 9
- extended form factor, 37
- Eyring's reverberation theory, 5
- Finite Element Method, 1
- flutter echo, 6, 74
- form factor, 12
- gathering, 9, 52
- image elements, 34
- Image Source Model, 23
- Impulse Response due to Image Elements, 53
- mean free path, 4
- mother source, 23
- obstacle test, 104
- radiation density, 11
- radiation reflectogram, 40
- radiosity, 9
- ray tracing, 3
- reflectograms, 2
- rendering, 9, 52
- reverberation time, 131
- Round Robin, 7, 100
- Sabine's reverberation theory, 5
- scattering coefficient, 32
- Schroeder's integration method, 131
- Schroeder's large room limit, 2
- secondary source, 34
- solid angle, 13
- sonel mapping technique, 4
- sound strength, 132
- specular reflections, 4, 23

www.elektro.dtu.dk

Department of Electrical Engineering
Acoustic Technology (AC)
Technical University of Denmark
Orsted's Plads, building 352
DK-2800 Kgs. Lyngby
Denmark
Tel: (+45) 45 25 39 49
E-mail: info@elektro.dtu.dk